Dissertation
submitted to the
Combined Faculties of the Natural Sciences and Mathematics
of the Ruperto-Carola-University of Heidelberg, Germany
for the degree of
Doctor of Natural Sciences

Put forward by
Andre Niklas Wenz
Born in: Stuttgart
Oral examination: 19.12.2013

From Few to Many: Ultracold Atoms in Reduced Dimensions

Referees:	**Prof. Dr. Selim Jochim** **Prof. Dr. Matthias Weidemüller**

Abstract:

This thesis reports on experimental studies exploring few and many-body physics of ultracold Bose and Fermi gases with reduced dimensionality. These experiments illustrate the versatility and great amount of control over the particle number, the interaction and other degrees of freedom, like the spin, that these generic quantum systems offer. In the first part of this thesis, we use quasi one-dimensional few-particle systems of one to ten fermionic atoms to investigate the crossover from few to many-body physics. This is achieved by measuring the interaction energy between a single impurity atom in a state $|\downarrow\rangle$ which repulsively interacts with an increasing number of majority atoms in a state $|\uparrow\rangle$. We find that the system quickly approaches the results from the many-body theory, which describes the behavior of a single impurity immersed in a Fermi sea of an infinite number of majority particles. The second part of this thesis presents studies of the time evolution of a bosonic F=1 spinor BEC of ^{87}Rb atoms. In this system, we investigate the emergence and coarsening of ferromagnetic spin textures from initially unmagnetized samples. While the ferromagnetic domains grow, we observe the development of a spin space anisotropy which is in agreement with the predicted phase-diagram. The last part of this thesis presents our first steps towards the investigation of phase coherence of quasi two-dimensional quantum gases in the crossover from bosonic molecules to fermionic atoms.

Zusammenfassung:

Diese Arbeit beschreibt Experimente, die Wenig- und Vielteilchenphysik mit ultrakalten Bose- und Fermigasen in reduzierten Dimensionen untersuchen. Die Experimente zeigen die Flexibilität und Kontrolle, die diese generischen Quantensysteme über die Teilchenzahl, die Wechselwirkung und andere Freiheitsgrade, wie den Spin, bieten. Im ersten Teil dieser Arbeit verwenden wir quasi-eindimensionale Wenigteilchensysteme, bestehend aus ein bis zehn fermionischen Atomen, um den Übergang zwischen Wenig- und Vielteilchenphysik zu untersuchen. Hierfür messen wir die Wechselwirkungsenergie eines repulsiv wechselwirkenden Systems, welches aus einem Minoritätsteilchen im Zustand $|\downarrow\rangle$ und einer wachsenden Anzahl von Majoritätsteilchen im Zustand $|\uparrow\rangle$ besteht. Die Ergebnisse zeigen, dass sich das System schnell den Vorhersagen der Vielteilchentheorie nähert, die das Verhalten eines einzelnen Minoritätsatoms beschreibt, welches sich in einem Fermisee von unendlich vielen Majoritätsteilchen befindet. Der zweite Teil dieser Arbeit stellt unsere Untersuchungen über die zeitliche Entwicklung eines bosonischen F=1 Spinor Bose-Einstein Kondensats aus ^{87}Rb-Atomen vor. Mit einem solchen System untersuchen wir, wie aus anfangs nicht magnetizierten Systemen ferromagnetische Spinbezirke entstehen und sich verbinden. Während des Wachstums der ferromagnetischen Bereiche beobachten wir die Bildung einer Anisotropie in der Ausrichtung der Magnetisierung. Diese Beobachtung steht in Übereinstimmung mit dem vorhergesagten Phasendiagramm. Im letzten Teil dieser Arbeit präsentieren wir erste Schritte auf dem Weg zur Untersuchung von Phasenkohärenz in quasi-zweidimensionalen Quantengasen im Crossover zwischen bosonischen Molekülen und fermionischen Atomen.

Contents

1 Introduction

The Short History of Ultracold Quantum Gases

The first achievement of Bose-Einstein condensation with dilute atomic vapors in 1995 [And95, Dav95] marks the birth of the field of ultracold quantum gases. These seminal experiments, which led to the Nobel prize in physics for E.A. Cornell, W. Ketterle and C. E. Wieman in 2001, were made possible through advances in cooling and trapping of atoms with lasers and magnetic fields [Met99]. They introduced a new way to access, prepare and investigate quantum matter in laboratories [Ket99]. These systems are comparatively simple, well-controlled and easy to model for theorists [Dal98, Dal99]. The first in-depth studies were still performed in magnetic traps and investigated the mean-field regime and excitations of Bose-Einstein condensates (BECs) [Mat98, Sta99]. The results were very well-described by mean-field theories like the Gross-Pitaevskii equation (GPE). These experiments showed for example the phase coherence of condensed atoms [And97, Hal98] and superfluid behavior like the formation of quantized vortices for rotating systems [Mat99, Mad00, Sha01]. The success of relatively simple Hamiltonians for the description of these quantum many-body systems can be attributed to several elementary facts. First, due to their creation inside ultra-high vacuum chambers, ultracold atom clouds are extremely well isolated and decoupled from the environment. Second, the interactions of ultracold gases can be easily modeled. The interaction term in ultracold atom Hamiltonians is completely described by a two-body interaction and in most cases depends only on a single parameter, the s-wave scattering length a. Additionally, this term is well approximated by a δ-function pseudo potential of zero range [Dal98, Dal99, Wei99].

The next milestone in the field of ultracold quantum gases was the possibility to trap ultracold atom clouds in optical dipole traps (ODTs) [Sta98a, Gri00]. Using such optical potentials allowed to trap atoms independent of their spin state and at various magnetic offset fields. Thus, it became possible to perform experiments where the spin is an additional degree of freedom (see chapter 5 and references therein). Furthermore, applying magnetic offset fields enabled researchers to access so-called Feshbach resonances [Ino98, Chi10]. These scattering resonances permit to tune the single interaction parameter a of ultracold systems to arbitrary positive and negative values. This means one could then change the interactions of the cloud from repulsive to attractive and even produce both resonantly interacting as well as non-interacting systems.

The first realization of a degenerate Fermi gas of ultracold atoms was achieved in 1999 [DeM99]. This paved the way to study a whole new class of systems which obey the Fermi-Dirac statistics [Gio08, Ket08]. While bosonic quantum gases become very unstable close to the newly available Feshbach resonances, i.e. for strong interactions, two-component Fermi gases remain unexpectedly stable [Joc03a, Reg03, Pet04, Pet05]. This allows to create strongly interacting Fermi gases and molecular BECs (mBECs) of diatomic bosonic molecules that consist of two fermionic atoms [Joc03b, Gre03, Zwi04]. By investigating these systems close to a Feshbach resonance, experimentalists were able to study the BEC-BCS crossover, which connects bosonic superfluidity of molecules to the fermionic superfluidity of cooper pairs [Bar04, Chi04, Zwi05, Gre05, Gio08]. In between these two limits, one reaches the unitary limit where the scattering length diverges and the diatomic pairs are strongly correlated [Sch08b]. At the time, there were only theoretical speculations about this connection between bosonic and fermionic superfluidity [Eag69, Leg80] but in no previous system, one could so beautifully connect and investigate all regimes of this crossover.

For bosonic systems, the instability of the system for large scattering lengths inhibited to access the strongly interacting regime. However, using the interference of several retroreflected far-detuned laser beams one can create periodic trapping potentials. In these systems, the atoms are confined to the interference maxima (for red-detuned trapping beams) and this leads to an effective discretization of the three-dimensional space. These so-called optical lattices, which were first proposed in [Jak98], were experimentally realized with ultracold bosonic systems in 2002 [Gre02]. In these spatially discretized systems, one could then reach the regime of strong interactions without being limited by the strong losses associated with large scattering lengths in bulk bosonic systems.

After each of these groundbreaking experiments, an initial fear that the pace of new achievements in the field of ultracold atoms would slow down turned out to be unfounded. With the large number of different bosonic and fermionic ultracold atom experiments around the globe, the impact and influence of research with cold gases for different fields of physics even continued to increase. This raises the question what drives this growing interest of both theorists and experimentalists to work with ultracold atoms.

Ultracold Gases: A Generic Quantum System

The just presented seminal achievements in the field of ultracold atoms show that the fascination and appeal of this area is to model and investigate simple Hamiltonians in a very pure form. The Hamilton operator used to describe most physical systems has the form

$$\hat{H} = \hat{K} + \hat{V}_{\text{trap}} + \hat{V}_{\text{int}}, \tag{1.1}$$

where $\hat{K}$ is an operator describing the kinetic energy, $\hat{V}_{\text{trap}}$ is the term that describes some sort of trapping potential and $\hat{V}_{\text{int}}$ describes the interparticle interactions. For general systems, for example in condensed matter physics, this Hamiltonian is often only an effective description which neglects many unwanted effects. The interaction term, for instance, can become inhibitively difficult to write down and solve.

The success of the field of cold atoms can be attributed to several facts. First, for ultracold atoms this effective Hamiltonian describes the systems almost perfectly. Additionally, for cold gases most of the terms are remarkably simple and thus often allow calculations of the ground state, low-lying excited states and sometimes even the dynamics of the systems. But that is not all: What really makes these systems outstanding is that unlike most other systems ultracold atoms allow to add, remove and control almost all terms and parts of this Hamiltonian. The experiments therefore allow to "emulate" quantum mechanical behaviors and phenomena that can be described by these Hamiltonians. The versatility and simplicity of these systems can be attributed to a limited number of main ingredients that make ultracold atoms so well-suited for these kinds of investigations:

1. The control over the internal degree of freedom of the atoms enables to prepare bosonic and fermionic gases with a controllable number of states and atoms. This controls and determines the wave function, its symmetry and the statistics that the particles obey.

2. The control over the trapping potential by means of optical and magnetic fields allows to realized various trapping geometries and potentials. In this way, one can prepare quasi two-dimensional (2D) systems, quasi one-dimensional (1D) systems or optical lattice systems. This means that we can tailor the external potential term $\hat{V}_{\mathrm{trap}}$ in the Hamiltonian. For discrete systems, e.g. optical lattices, this also influences the way in which the many-body wave functions are constructed.

3. Through the application of a homogeneous offset field one can precisely tune and control the interactions of the systems by means of scattering resonances. Furthermore, the description of the interactions of these systems is theoretically easy to model. This knob grants full control over the interaction term of the Hamiltonian.

New Directions

With this vast amount of new possibilities at hand, the development of ultracold quantum gases in recent years can be roughly divided in three main trends.

One major direction of the current research with ultracold atoms is to investigate lower dimensional systems (e.g. [Kin04, Had06, Cla09, Hal09, Hal10a, Krü10, Tun10, Mar10b, Fel11, Frö12, Vog12, Kos12, Som12, Zür12b]). The change in the Hamiltonian for these systems is very subtle and fewer dimensions should in principle simplify the description of a system. However, it turns out that in lower dimensions fluctuations play a greater role [Pet03]. Thus, as laid out in [Mer66, Hoh67], long-range order cannot be established in these systems for any finite temperature. As a consequence, Bose-Einstein condensation does not occur in reduced dimensions. There are however other, more complicated superfluid phases for these systems at ultralow temperatures [Had06].

A second trend for the research with ultracold atoms is to use systems with full control over the spin states and in extreme cases to control the number and state of the atoms on the single particle level. One can for example study multi-component Fermi gases or mixtures of different bosonic and fermionic species (e.g.[Had02, Sim03, Sta04, Wil08, Ott08, Huc09, Voi09, Sol11, Pas13]) or investigate imbalanced and highly polarized Fermi gases (e.g.[Shi06, Zwi06c, Par06, Zwi06b, Sch07, Nas09, Lia10, Ku12, Sch09, Kos12]). It also becomes possible to control and measure the behavior of systems on the single particle level using optical lattices (e.g.[Bak09, Wil10, Bak10, Wei11]) or single small volume optical dipole traps (e.g.[Sch01, Grü10, Ser11b, Kau12]).

The third major field of research with ultracold atoms, which recently developed, is to study non-equilibrium physics and thermalization of ultracold systems (e.g. [Rig08]). These studies investigate the evolution and the dynamics when systems are perturbed or driven out of equilibrium. Often these measurements are performed in lower dimensions [Ott04, Hof07, Kin06, Sch12b, Gri12] or they investigate the spin of the system [Sad06b, Som11, Guz11].

Clearly, the boundaries between these different directions of research with ultracold quantum gases are blurred and many experiments combine different settings, techniques and phenomena which can be assigned to several of these main topics.

Outline

In this thesis, the contributions to the development of the field of ultracold atoms made by the investigations with three different systems and experimental setups are presented. The measurements study the behavior, the interactions, the dynamics, the equilibration and the fluctuations of fermionic and bosonic cold atom systems. This shows that ultracold bosonic and fermionic systems can be used to study a multitude of interesting phenomena, particularly in reduced dimensions.

In chapter 2, we introduce the theoretical description of ultracold bosonic and fermionic systems, their interaction and describe the role of the dimensionality of the system. Afterwards, we present the different experimental setups and techniques used to produce ultracold quantum gases in chapter 3. We then investigate few-fermion systems of ^{6}Li atoms in a quasi one-dimensional setting in chapter 4. Here, we focus on the crossover from few to many-body physics by studying quantum impurity systems where a single atom in a state $|\downarrow\rangle$ repulsively interacts with a growing number of atoms in a different state $|\uparrow\rangle$. In chapter 5, we then investigate the dynamics of a spinor BEC of ^{87}Rb with a system which is quasi two-dimensional for the spin degree of freedom. Finally, chapter 6, summarizes our ongoing efforts to study the crossover between diatomic bosonic molecules and fermions in a quasi two-dimensional system of ^{6}Li atoms.

2 Ultracold Quantum Gases

In this chapter, we will establish the theoretical framework used to describe ultracold bosonic and fermionic quantum gases. The specific details for the description of the investigated systems are given in the respective chapters. Thus, we will here only give a broad overview on the theoretical methods.

We start with a general introduction to quantum statistics, quantum many-body systems and the second quantization framework of bosons and fermions. Then we derive the bosonic and the fermionic distribution functions from the grand canonical potential. Subsequently, we use the distribution functions to calculate the density distributions and properties of ultracold Fermi and Bose gases. For a large part of these derivations we will follow the reasoning and notation used in [Fet03, Zwi06a, Wil11, Wei09]. Then we investigate how ultracold atoms interact and how we can tune these interactions. This will be done according to standard cold atoms literature (e.g. [Dal98, Ket99, Pit03, Pet02, Gio08, Ket08, Chi10]). At the end of the chapter we show how changing the dimensionality of a system affects the interactions and thus the physics in ultracold systems.

2.1 Quantum Statistics and Thermodynamics

In the macroscopic world, all particles and bodies are considered to be distinguishable from each other. This means we can label and keep track of the movement and behavior of each individual particle. Such systems are described by classical mechanics which has proven to be a very powerful tool for calculating the equations of motion of macroscopic particles and systems. It has, however, been shown that as soon as one enters the realm of quantum mechanics the classical description breaks down and it needs to be replaced by a quantum mechanical framework.

This transition from the classical to the quantum world occurs when the description of particles as point-like objects breaks down because the wave functions of different particles start to overlap. We know that due to the wave-particle duality, a wavelength $\lambda_{dB} = h/p$ [Bro23] can be associated to each particle, where h is Planck's constant and p is the momentum of the particle. By relating the momentum of the particle in a gas to the temperature T we obtain the thermal de Broglie wavelength

$$\lambda_{th} = \frac{h}{\sqrt{2\pi m k_B T}}, \tag{2.1}$$

where m is the mass of the particle, k_B is Boltzmann's constant and T is the temperature of the gas. We now need to compare this quantity to the interparticle spacing $d = 1/(n)^{1/3}$, where n is the density of the system. For regular classical systems the de Broglie wavelength is minuscule compared to the interparticle distance. Therefore, quantum effects can be neglected for most macroscopic systems that we experience in everyday life. In order to observe phenomena related to quantum statistics one needs to drastically increase the density or decrease the temperature of the gas. The field of ultracold gases makes use of the second approach and cools atomic and molecular gases down to the mK to nK regime[1]. In this temperature regime the wave functions of the individual particles start to overlap. Hence, the particles become indistinguishable and non-classical behavior emerges.

The indistinguishability has far-reaching consequences because if one cannot distinguish two systems where we interchanged two identical particles, then all observables should remain unchanged. Consequently, that the probability density, i.e. the modulus square of the wave function $|\Psi|^2$ has to stay invariant under the following transformation which exchanges two particles located at x_i and x_j

$$|\Psi(x_1, \dots, x_i, \dots, x_j, \dots, x_N)|^2 = |\Psi(x_1, \dots, x_j, \dots, x_i, \dots, x_N)|^2. \tag{2.2}$$

Here $\Psi(x_1, \dots, x_N)$ is the many-body wave function of N indistinguishable particles and x_i represents the spatial coordinate and discrete quantum numbers like the z component of the spin [Fet03]. There are two possibilities for the many-particle wave function Ψ to fulfill equation 2.2: Either Ψ has to transform symmetrically or antisymmetrically under the aforementioned exchange of two particles. According to the spin statistics theorem (see e.g. [Fie39, Pau40]) this property divides all particles into two types: fermions and bosons.

Fermions All particles with a spin of a half-integer times the reduced Planck's constant $\hbar$ [2] transform antisymmetrically under the exchange of two particles, i.e.

$$\Psi(\dots, x_i, \dots, x_j, \dots) = -\Psi(\dots, x_j, \dots, x_i, \dots). \tag{2.3}$$

These particles are called fermions and if two particles occupy the same quantum state we obtain $\Psi(\dots, x_i, \dots, x_i, \dots) = -\Psi(\dots, x_i, \dots, x_i, \dots)$. This is only possible for a vanishing wave function $\Psi(\dots, x_i, \dots, x_i, \dots) = 0$. We thus recover the Pauli exclusion principle [Pau25] which states that identical fermions cannot occupy the single-particle level E_i. If we want to construct a fermionic many-particle wave function, we have to completely antisymmetrize it. This is generally ensured by defining Ψ using the Slater determinant of single-particle wave functions $\psi_{E_i}(x_i)$. Here, E_i denotes a complete set of single-particle quantum numbers like the momentum p in a system of spinless

---

[1] There are also various other systems where these quantum effects play a crucial role, e.g. the electrons in a conductor or the nucleons in an atomic nucleus.

[2] When we will use half-integer or integer spin in the following we will not always explicitely mention $\hbar$ but it is implicitly included.

particles in a box. Due to the characteristic properties of the determinant, the many-body wave function constructed in such a way then automatically fulfills the necessary antisymmetry.

Bosons Particles that carry an integer spin are called bosons. They behave symmetrically under the exchange of two particles

$$\Psi(\ldots, x_i, \ldots, x_j, \ldots) = +\Psi(\ldots, x_j, \ldots, x_i, \ldots). \tag{2.4}$$

Due to the symmetric wave function, there is no restriction on the number of bosonic particles occupying the same single-particle state. We will see in the next section that this has strong implications for the difference in structure of the ground state for harmonically trapped bosonic and fermionic ensembles.

Generally, all elementary matter particles like electrons, quarks and neutrinos have half-integer spin and are thus fermions. All force carriers on the other hand like for example photons, W and Z particles and the graviton are bosons. For composite particles the distinction into those two classes still holds and the total angular momentum is obtained by the sum of the angular momenta of the constituents. Every composite particle with half integer spin or angular momentum will be a fermion and every particle with integer spin or angular momentum will be a boson. Thus a proton (odd number of quarks) is also a fermion whereas all mesons (even number of quarks) are bosons. This is also true for larger and more complicated structures like neutral atoms: A ^{6}Li atom consists of an odd number of fermions (3 neutrons, 3 protons and 3 electrons) and is therefore a fermion. ^{87}Rb consists of 37 protons, 50 neutrons and 37 electrons which results in a total number of 124 fermions. Therefore, it is a boson.

Due to the extremely low energies scales in ultracold gas experiments, the inner structure of the atoms will never be resolved in any of our experiments. We can therefore treat all atoms as a single particle in a certain quantum state. Hence, we do not have to consider their composite nature except to determine if they are bosons or fermions.

2.1.1 Second Quantization Description

It is useful to represent many-particle systems using the occupation number representation. In this framework the system is described by the number n_i of particles in the orthogonal single-particle states ψ_{E_i} denoted by the quantum numbers E_i. The desired basis states can be written as the direct product of the single-particle eigenstates of the number operator

$$|n_1 n_2 \ldots n_N\rangle = |n_1\rangle\, |n_2\rangle \ldots |n_N\rangle. \tag{2.5}$$

Starting from the vacuum state $|0\rangle$ it is convenient to construct and change occupation number states using creation $\hat{a}_i^\dagger$ and annihilation $\hat{a}_i$ operators for each single-particle mode E_i [Fet03].

For bosons these operators satisfy the following commutation relations

$$\left[\hat{a}_i^\dagger, \hat{a}_j^\dagger\right] = [\hat{a}_i, \hat{a}_j] = 0 \quad \text{and} \quad \left[\hat{a}_i, \hat{a}_j^\dagger\right] = \delta_{ij}, \tag{2.6}$$

where the commutator is defined by $[A, B] \equiv AB - BA$. These operators are defined by raising and lowering the occupation number in the single-particle state i in the following way $\hat{a}_i|n_i\rangle = \sqrt{n_i}|n_i - 1\rangle$, $\hat{a}_i^\dagger|n_i\rangle = \sqrt{n_i + 1}|n_i + 1\rangle$ with the limiting case $\hat{a}_i|0\rangle = 0$. We can define the number operator $\hat{n}_i \equiv \hat{a}_i^\dagger \hat{a}_i$ whose eigenvalue is the number of atoms in the single-particle state with the quantum number E_i.

We noted earlier that for fermions the occupation number n_i is limited to 0 and 1 due to the antisymmetric wave function. This is taken into account if the fermionic creation $\hat{b}_i^\dagger$ and annihilation operators $\hat{b}_i$ fulfill the following anticommutation relations

$$\left\{\hat{b}_i^\dagger, \hat{b}_j^\dagger\right\} = \left\{\hat{b}_i, \hat{b}_j\right\} = 0 \quad \text{and} \quad \left\{\hat{b}_i, \hat{b}_j^\dagger\right\} = \delta_{ij}, \tag{2.7}$$

where the anticommutator is defined by $\{A, B\} \equiv AB + BA$. The following relations are the same as for the bosonic case $\hat{b}_i^\dagger|0\rangle = |1\rangle$, $\hat{b}_i|1\rangle = |0\rangle$ and $\hat{b}_i|0\rangle = 0$. However, due to the limited occupation number we also obtain $\hat{b}_i^\dagger \hat{b}_i^\dagger|0\rangle = \hat{b}_i^\dagger|1\rangle = 0$, which is another way to formulate the Pauli exclusion principle.

2.1.2 Bosonic and Fermionic Ground State in a Harmonic Oscillator

With the formalism introduced above it becomes now rather simple to obtain the $T = 0$ ground state of a non-interacting many-body system both for bosons and for fermions in a harmonic oscillator.

For Bosons we construct the many-body wave function in occupation number basis. For N non-interacting bosons without spin, the energy of the system is minimized when all particles are created in the lowest possible single-particle state ψ_{E_0}. This state is the single-particle ground state of the harmonic oscillator and we obtain the following many-body wave function

$$|\Phi_{\text{bosons}}\rangle = |N, 0, \ldots, 0\rangle = \frac{1}{\sqrt{N!}} \left(\hat{a}_0^\dagger\right)^N |0, 0, \ldots, 0\rangle. \tag{2.8}$$

This means that all particles occupy the lowest accessible single-particle state and we will later see that this many-body state constitutes a Bose-Einstein condensate (BEC)[3].

---

[3] When we later investigate BECs in this thesis, we will notice that the interesting phenomena associated with Bose-Einstein condensation is not the macroscopic occupation of the ground state but rather the constant phase and macroscopic wave function ψ of the condensate.

For Fermions the occupation number of each single-particle state is limited to 1. Therefore, the many-body ground state of a non-interacting fermionic system with $T = 0$ in a harmonic oscillator potential is given by the following many-body wave function

$$|\Phi_{\text{fermions}}\rangle = |\overbrace{1, \ldots 1}^{\text{N times}}, 0, \ldots, 0\rangle = \prod_{\{i\}_{E_i < E_F}} \hat{b}_i^\dagger |0, \ldots, 0\rangle. \tag{2.9}$$

Here, the quantum number i denotes the i-th single-particle level of the harmonic oscillator potential. It runs from the ground state $i = 0$ to the $(N-1)$-th excited harmonic oscillator state with the energy E_{N-1}. This is the highest occupied single-particle level and we call its energy the Fermi energy E_F.

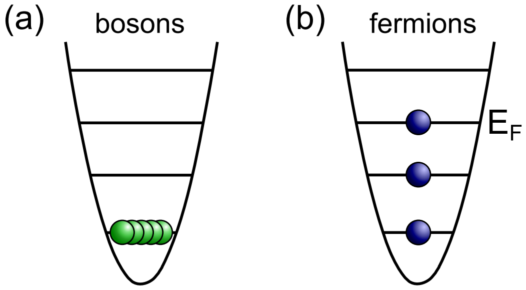

Figure 2.1: Ground state of non-interacting bosons (a) and non-interacting fermions (b) at $T = 0$ in a harmonic trapping potential. While the bosons accumulate in the ground state and form a Bose-Einstein condensate (BEC), the fermions occupy all single-particle levels up to the Fermi energy E_F with a single particle per state.

Figure 2.1 shows how these systems arrange inside the harmonic oscillator potential. The bosons all accumulate in the ground state and form a so-called BEC while the fermions build a Fermi sea by filling the single-particle levels up to the Fermi energy with one fermion per state.

2.1.3 Field Operators and the Hamiltonian

For the systems that we experimentally investigate, the general Hamilton operator in first quantization usually can be written as

$$\hat{H} = \sum_{i=1}^{N} \hat{T}(x_i) + \sum_{i=1}^{N} \hat{V}_{\text{trap}}(x_i) + \sum_{i \neq j}^{N} \hat{V}_{\text{int}}(x_i, x_j), \tag{2.10}$$

where $\hat{T}(x_i)$ is the kinetic energy operator, $\hat{V}_{\text{trap}}(x_i)$ is the operator that describes the trapping potential and $\hat{V}_{\text{int}}(x_i, x_j)$ denotes the two-body interaction operator. There are also interaction terms involving more than two particles but most of them can be approximated by a combination of two-body interactions or are not relevant for the systems we investigate.

Using the second quantization formalism we can rewrite the many-body Hamilton operator given in equation 2.10 in terms of the creation $\hat{c}_i^\dagger$ and annihilation $\hat{c}_i$ operators[4] in the following way (see [Fet03])

$$\hat{H} = \sum_{i,j}^{N} \hat{c}_i^\dagger \, \langle i|T|j\rangle \, \hat{c}_j + \sum_{i,j}^{N} \hat{c}_i^\dagger \, \langle i|V_{\text{trap}}|j\rangle \, \hat{c}_j + \frac{1}{2} \sum_{i,j,k,l}^{N} \hat{c}_i^\dagger \hat{c}_j^\dagger \, \langle ij|V_{\text{int}}|kl\rangle \, \hat{c}_l \hat{c}_k, \tag{2.11}$$

where the states $|i\rangle$ are the occupation number states with the energy E_i. One can now define the so-called field operators as linear combinations of the creation and annihilation operators

$$\hat{\psi} \equiv \sum_i \psi_i(x)\hat{c}_i \quad \text{and} \quad \hat{\psi}^\dagger \equiv \sum_i \psi_i^*(x)\hat{c}_i^\dagger. \tag{2.12}$$

With this definition one can write the matrix elements $\langle i|T|j\rangle = \int dx \, \psi_{E_i}^*(x) \, T(x)\psi_{E_j}(x)$, where one should note that these matrix elements which are defined by this integral are simply complex numbers.

Rewriting the Hamilton operator 2.11 using the field operators we obtain

$$\begin{aligned} \hat{H} = &\int dx \, \hat{\psi}^\dagger(x) \, T(x) \, \hat{\psi}(x) + \int dx \, \hat{\psi}^\dagger(x) \, V_{\text{trap}}(x) \, \hat{\psi}(x) \\ &+ \frac{1}{2} \int dx \, dx' \, \hat{\psi}^\dagger(x) \, \hat{\psi}^\dagger(x') \, V_{\text{int}}(x, x') \, \hat{\psi}(x') \, \hat{\psi}(x). \end{aligned} \tag{2.13}$$

Note that in this description $\hat{\psi}$ and $\hat{\psi}^\dagger$ are operators and not wave functions and the potential and kinetic energies are just complex coefficients, not operators.

This Hamiltonian will be used on several occasions throughout this thesis and it is useful to also define how other operators are described in this framework. A general operator that has the following form in first quantization $J = \sum_{i=1}^{N} J(x_i)$ becomes the following quantity in second quantization

$$\hat{J} = \sum_{ij} \langle i|J|j\rangle \, \hat{c}_i^\dagger \hat{c}_j = \int dx \, \hat{\psi}^\dagger(x) J(x) \hat{\psi}(x). \tag{2.14}$$

This leads for example to a very useful notation for the number-density operator which in its second quantized form can be written as $\hat{n}(x) = \hat{\psi}^\dagger(x) \, \hat{\psi}(x)$. As a result, the total number operator becomes $\hat{N} = \sum_i \hat{n}_i = \int dx \, \hat{\psi}^\dagger(x)\hat{\psi}(x)$.

---

[4] We use a general notation $\hat{c}$ for the operators since the following equations hold for both bosonic ($\hat{a}$) and fermionic ($\hat{b}$) operators.

2.1.4 Thermodynamic Quantities and the Distribution Functions

After introducing the second quantization description of many-particle bosonic and fermionic systems we will now turn to statistical mechanics and thermodynamic relations to obtain information about systems in the thermodynamic limit. This is done since in most cases systems of ultracold atoms have large particle numbers and finite temperatures and therefore a quantum statistical description of their properties is useful. Generally, one uses the grand canonical ensemble to describe ultracold systems. The macroscopic variables of the grand canonical ensemble are the volume V, the chemical potential μ, which is the energy necessary to add a particle to the system, and the temperature T, which is often implicitly defined by the Lagrange multiplier $\beta \equiv 1/(k_B T)$, where k_B is the Boltzmann constant.

We know from statistical mechanics (see e.g. [Fet03, Sch00, Lan96]) that the grand canonical partition function of a non-interacting system is given by

$$Z_G = \mathrm{Tr}\left(e^{-\beta\left(\hat{H}_0 - \mu\hat{N}\right)}\right), \tag{2.15}$$

where $\hat{H}_0$ is the non-interacting part of the Hamiltonian defined in equation 2.11. We can now use the previously introduced occupation number states $|n_i\rangle$, where E_i is the eigenenergy of the single-particle states and $E_{\text{total}} \equiv \sum_i E_i$ is the total energy of the many-body state $|n_1 \dots n_N\rangle$. These states are eigenstates of both the Hamilton operator $\hat{H}_0$ and the number operator $\hat{N}$ and thus one obtains

$$Z_G = \prod_i \mathrm{Tr}_i\left(e^{-\beta(E_i-\mu)\hat{n}_i}\right) = \prod_i \sum_n \left(e^{-\beta(E_i-\mu)}\right)^n . \tag{2.16}$$

We can now evaluate the sum over n which for bosons runs over all integers and for fermions is limited to 0 or 1. This results in the following bosonic and fermionic partition function

$$Z_{\text{bosons}} = \prod_i \frac{1}{1-e^{-\beta(E_i-\mu)}} \quad \text{and} \quad Z_{\text{fermions}} = \prod_i \left(1+e^{-\beta(E_i-\mu)}\right). \tag{2.17}$$

From the derivative of the grand canonical potential with respect to μ, the mean number of particles can be calculated to be

$$N = \sum_i \langle n_i\rangle = -\left(\frac{\partial\Omega}{\partial\mu}\right)_{T,V}, \tag{2.18}$$

where $\Omega(T,V,\mu) = -k_B T \ln Z_G$ is the grand canonical potential. Using the logarithm of equation 2.17 and the derivation with respect to μ we obtain the Bose-Einstein and Fermi-Dirac distribution functions

$$f_B \equiv \langle n_i\rangle_{\text{bosons}} = \frac{1}{e^{\beta(E_i-\mu)}-1} \quad \text{and} \quad f_F \equiv \langle n_i\rangle_{\text{fermions}} = \frac{1}{e^{\beta(E_i-\mu)}+1}. \tag{2.19}$$

These functions $\langle n_i \rangle = f_{B/F}$ give the expected mean occupation number of a non-interacting system in the i-th state. One can now use them to derive various interesting observables like the density distribution in a harmonic trap.

In the same way that we obtained the mean number of particles and the distribution functions from the grand canonical potential Ω we can also derive other macroscopic variables like the mean entropy per particle or the pressure of the system.

Boltzmann Distribution Function For high temperatures or low densities, quantum statistical effects become negligible and thus one should recover the classical distribution function. This means the particles should obey the Maxwell-Boltzmann statistics. In this limit, one can show that $e^{\beta(E_i-\mu)} \gg 1$ and therefore the additional 1 in the denominator of both the Fermi-Dirac and the Bose-Einstein distribution function is negligible. For both bosonic and fermionic systems one then obtains the Boltzmann distribution function

$$f_{\mathrm{cl}} = e^{-\beta(E_i-\mu)}. \tag{2.20}$$

2.1.5 Density Distributions in a Harmonic Trap

We will now consider non-interacting bosonic, fermionic and classical gases in a three-dimensional harmonic trapping potential, which is experimentally for example created by an optical dipole trap. To describe these systems we will use three-dimensional vectors like $\mathbf{r}$ with the components x, y and z for the spatial coordinate, the vector $\mathbf{p} = \hbar\mathbf{k}$ for the momentum coordinate and the vector $\mathbf{k}$ for the wave vector. The trapping potential is then given by

$$V_{\mathrm{trap}} = \frac{1}{2} m \left(\omega_x^2 x^2 + \omega_y^2 y^2 + \omega_z^2 z^2\right), \tag{2.21}$$

where the trapping frequencies ω_i range from a couple of Hz to a couple of kHz depending on the setup and the measurement. According to [Lan81, Wil11] the energies of the single-particle levels in such a system is given by

$$E_{n_x,n_y,n_z} = \hbar \sum_\alpha \omega_\alpha \left(n_\alpha + \frac{1}{2}\right), \tag{2.22}$$

where $\alpha = x, y, z$.

If the thermal energy $k_B T$ is significantly larger than the energy spacing $\hbar\omega_i$ between the levels[5], the sum over the discrete levels of the harmonic oscillator can be approximated by an integral over the phase space. For the following derivations we will use a semi-classical approach. This approach includes on one hand the quantum statistically derived distribution functions. But on the other hand the energies of the single-particle levels E_i in the partition function are described by the classical Hamiltonian $H = \frac{\hbar^2 k^2}{2m} + V_{\mathrm{trap}}(\mathbf{r})$. In this semi-classical approximation, which is usually called

---

[5] We will later see that for the finite systems described in chapter 4, this is not a good approximation.

Thomas-Fermi approximation [But97, Fer28, Tho27], the density distribution functions are given by

$$f_{B/F}(\mathbf{r},\mathbf{k}) = \frac{1}{e^{\beta\left(\frac{\hbar^2k^2}{2m}+V(\mathbf{r})-\mu\right)} \mp 1} \quad \text{and} \quad f_{\mathrm{cl}}(\mathbf{r},\mathbf{k}) = e^{-\beta\left(\frac{\hbar^2k^2}{2m}+V(\mathbf{r})-\mu\right)}. \tag{2.23}$$

Using these functions and a density of states of $1/(2\pi\hbar)^3$ per unit volume in the six-dimensional phase space $\{\mathbf{r},\mathbf{p}\}$ we define the following normalization condition for the number of particles N which implicitly defines the chemical potential μ

$$N = \frac{1}{(2\pi\hbar)^3}\int \mathrm{d}\mathbf{r}\,\mathrm{d}\mathbf{k}\, f(\mathbf{r},\mathbf{k}). \tag{2.24}$$

The real-space density distribution for bosonic (without the condensed part), fermionic and classical systems is given by

$$n(\mathbf{r}) = \frac{1}{(2\pi\hbar)^3}\int \mathrm{d}\mathbf{k}\, f(\mathbf{r},\mathbf{k}). \tag{2.25}$$

Carrying out this integration for the classical Boltzmann distribution $f_{\mathrm{cl}}(\mathbf{r},\mathbf{k})$ one obtains a Gaussian real-space density distribution

$$n_{\mathrm{cl}}(\mathbf{r}) = \frac{N}{(2\pi)^{3/2}\,\sigma_x\sigma_y\sigma_z}\, e^{\left(\frac{1}{2}\sum_i x_i^2/\sigma_i^2\right)},\ \text{where } \sigma_i^2 = \frac{k_BT}{m\omega_i^2};\ (i = x,y,z). \tag{2.26}$$

Recording this density distribution is the most common way to extract information from the ultracold atomic sample. Often we also record the momentum distribution $n_{\mathrm{cl}}(\mathbf{p})$ by switching off the trap and letting the atoms expand for a time-of-flight (tof). This distribution can be obtained is a similar way by integrating over the position coordinate instead of the integration over the wave vector (see e.g. [Sta00]). Usually, when using absorption imaging, the shadow cast on a CCD camera by the cloud is proportional to the integrated column density $n_{\mathrm{cl}}^{(col)}(x,y) = \int n_{\mathrm{cl}}(\mathbf{r})\,\mathrm{d}z$. By fitting Gaussian functions to these images we can extract the number of particles N and the temperature of the systems T. This technique, however, only gives reliable results for non-degenerate, non-interacting systems. Therefore, we now will try to extract the density distributions for degenerate fermionic and bosonic systems at non-zero temperature and afterwards we will give some basic ideas how to include interactions.

The Polylogarithmic Function $\mathrm{Li}_\nu(\mathrm{z})$

To simplify the definition of the density distributions it is useful to define the polylogarithmic function in its integral and power series form [6]

$$Li_\nu(z) = \frac{1}{\Gamma(\nu)} \int \frac{t^{\nu-1}}{\frac{1}{z}e^t - 1} dt = \sum_{k=1}^{\infty} \frac{z^k}{k^\nu}, \tag{2.27}$$

where $\Gamma(\nu)$ is the Gamma function. This polylogarithm can be used to easily define quantities related to the Bose gas. For fermions one uses

$$-Li_\nu(-z) = \frac{1}{\Gamma(\nu)} \int \frac{t^{\nu-1}}{\frac{1}{z}e^t + 1} dt = \sum_{k=1}^{\infty} (-1)^{k+1} \frac{z^k}{k^\nu}. \tag{2.28}$$

For $z = e^x$, these functions have a particular property[7] [Pit03, Wen08]

$$z \frac{d}{dz} Li_{\nu+1}(z) = Li_\nu(z). \tag{2.29}$$

This greatly simplifies the derivation of the singly or doubly integrated column densities $n^{(col)}(x)$ and $n^{(col)}(x, y)$ which are obtained in the experiments using the absorption imaging technique (see chapter 3).

2.2 Degenerate Fermi Gases

We will now investigate the properties and characteristics of ultracold fermionic clouds by using the Fermi-Dirac distribution function and the Thomas-Fermi approximation introduced earlier. We will consider the fermions trapped in a harmonic trapping potential defined by equation 2.21 and it is useful to introduce the mean trapping frequency $\bar{\omega} = (\omega_x \omega_y \omega_z)^{1/3}$. In this case, we can rewrite equation 2.24 for fermions in terms of the energy (see e.g. [Wei09]) and obtain

$$N = \frac{1}{(2\pi\hbar)^3} \int \mathrm{d}\mathbf{r}\, \mathrm{d}\mathbf{k}\, f_F(\mathbf{r}, \mathbf{k}) = \frac{1}{2(\hbar\bar{\omega})^3} \int_0^\infty \frac{E^2}{exp\left[(E-\mu)/(k_B T)\right] + 1} \mathrm{d}E. \tag{2.30}$$

For the limit of $T \to 0$ the Fermi-Dirac distribution function becomes unity for states with an energy smaller than E_F and vanishes for states with an energy larger than E_F. We can then carry out the integration in equation 2.30 and obtain a definition of the Fermi energy E_F that is more accessible in experiments

$$E_F = (6\,N)^{1/3}\, \hbar\bar{\omega} \equiv \mu(T = 0, N). \tag{2.31}$$

---

[6] This form is only well defined for $|z| < 1$.

[7] This relation holds for all real x and ν.

It makes sense to use the Fermi energy as a natural scale of the system and define other characteristic quantities like the Fermi temperature T_F, the Fermi momentum p_F, the Fermi wave vector k_F and the Fermi radii $x_{i,F}$ by the following formula

$$E_F = k_B T_F = \frac{p_F^2}{2m} = \frac{\hbar^2 k_F^2}{2m} = \frac{1}{2} m \omega_i^2 x_{i,F}^2. \tag{2.32}$$

To obtain the real-space density distribution for fermions in a harmonic trap we can integrate the first part of equation 2.30 over the wave vector $\mathbf{k}$. Using the chemical potential $\mu(T=0,N) = E_F$ and the just defined Fermi radii, we obtain

$$n_F(\mathbf{r}, T=0) = \frac{8\,N}{\pi^2 x_F y_F z_F} \left(1 - \sum_{i=x,y,z} \frac{x_i^2}{x_{i,F}^2}\right)^{3/2}. \tag{2.33}$$

The density cannot become negative and therefore $n_F(\mathbf{r}, T=0) = 0$ for the region where $V(\mathbf{r}) > E_F$. In the same way we can also obtain the momentum distribution of such a system by integrating equation 2.30 over $\mathbf{r}$ [Wen08].

2.2.1 Fermi Gases for Non-Zero Temperature

For Fermi gases with non-zero temperature we cannot give an explicit expression for the chemical potential μ. Therefore, we use the polylogarithmic functions to give the density distribution in that case [Wei09]. Starting from equation 2.25 and using the definition of the polylogarithm in equation 2.28 we obtain

$$n_F(\mathbf{r}, T) = -\frac{1}{\lambda_{th}^3} Li_{3/2}\left(-\exp\left\{\frac{\mu - V(\mathbf{r})}{k_B T}\right\}\right), \tag{2.34}$$

where $\lambda_{th} = \sqrt{\frac{2\pi\hbar^2}{m k_B T}}$ is the thermal deBroglie wavelength. The normalization condition is given by

$$N = -\left(\frac{k_B T}{\hbar\bar{\omega}}\right)^3 Li_3\left(-\exp\left\{\frac{\mu}{k_B T}\right\}\right). \tag{2.35}$$

We can now express N in terms of the Fermi temperature T_F using equations 2.31 and 2.32 and thus obtain the following implicit definition of the chemical potential in terms of the degeneracy temperature T/T_F

$$Li_3\left(-\exp\left\{\frac{\mu}{k_B T}\right\}\right) = -\frac{1}{6\,(T/T_F)^3}. \tag{2.36}$$

This equation can now be numerically solved for arbitrary values of T/T_F, which is done for example in [Wei09, Wen08]. For $T/T_F \ll 1$, i.e. small temperatures we can approximate the chemical potential using the Sommerfeld expansion. For $T/T_F \gg 1$, i.e. large temperatures, one can use the classical value for the chemical potential.

With the chemical potential $\mu(T/T_F)$ one can now calculate the density distribution of a Fermi gas in a harmonic trapping potential (see figure 2.2).

One should note that there is no drastic change in the density distribution when the temperature is lowered below T_F. This means that for a fermionic system the phase space density grows continuously and there is a smooth transition from a Gaussian density distribution to a Fermi density distribution as defined in equation 2.34. Due to the complexity of the polylogarithmic functions we usually use Gaussian functions to determine N and T/T_F for such non-interacting Fermi gases with $T/T_F \gtrsim 0.5$. In figure 2.2 and [Wen09], it is shown that the results obtained by a Gaussian fit still give reasonable results down to $T/T_F \approx 0.5$ (see figures 2.2(a) and (b)). For $T/T_F \ll 0.5$ one has to use a more sophisticated fitting routine using the Fermi function. Due to the finite resolution of the imaging system, however, it becomes increasingly difficult to distinguish samples with degeneracies lower than $T/T_F \lesssim 0.1$ (see figure 2.2(c)).

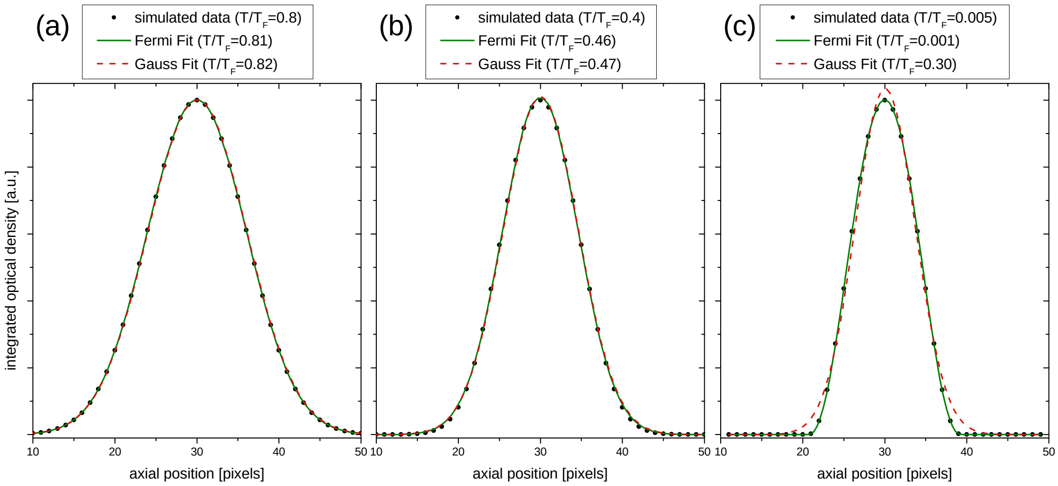

Figure 2.2: Simulated doubly integrated density distribution of a non-interacting Fermi gas with $T/T_F = 0.8$ (a), $T/T_F = 0.4$ (b) and $T/T_F = 0.005$ (c) as black points. Additionally we fitted the simulated data with a Gaussian (dashed red line) and a Fermi fit (solid green line). There is no drastic change in the density distribution for degenerate Fermi gases. Down to approximately $T/T_F \approx 0.5$ the Gaussian fit obtains reasonable results.

2.2.2 Interacting Fermi Gases

We just showed that it is quite complex to calculate the expected density distribution for a non-interacting Fermi gas with $T \neq 0$. It is even more complicated to incorporate interactions in such a description. We will therefore refrain from doing this in detail at this point. Still, one should note that, due to Pauli blocking the scattering cross section between identical fermions vanishes for $T \to 0$. Therefore, a one-component Fermi gas is a very good realization of a non-interacting system for ultracold temperatures ($T \lesssim 1\,\mu$K).

For the preparation of degenerate fermionic systems we need collisions between the atoms in the cloud to ensure thermalization during the evaporative cooling stage. Therefore, we use two-component Fermi gases that consist of atoms in two different Zeeman sublevels. Atoms in these states are then distinguishable and can scatter even at low temperatures. In this regime, complex many-body phenomena like can superfluidity occur. These effects are very interesting, but they also make the description of interacting two-component Fermi gases very complex. It therefore took until 1957 [Bar57] to establish a theory for such superfluid two-component systems for weak attractive interactions. In section 2.5.3, we will qualitatively explain what happens in such interacting two-component fermionic systems.

2.3 Degenerate Bose Gases

There are significant differences in the behavior of ultracold bosonic and fermionic clouds. In particular, describing a weakly interacting Bose gas is considerably simpler than describing a weakly interacting Fermi gas. After introducing the density distribution of non-interacting Bose gases we will thus study weakly interacting bosonic systems.

2.3.1 Non-Interacting Bose Gas

The Bose-Einstein distribution function as a function of the energy was derived to be

$$f_B(E_i) = \frac{1}{e^{\beta(E_i-\mu)} - 1}. \tag{2.37}$$

We can set the energy of the lowest single-particle ground state E_0 to zero without loss of generality. It would be unphysical for the distribution function f_B to become negative. This implies that $E_i - \mu > 0$ for all i and therefore the chemical potential must be $\mu \leq 0$. We know from earlier considerations that for $T = 0$ the ground state is macroscopically occupied and this phenomenon is called Bose-Einstein condensation.

Due to this exceptional weight of the macroscopically occupied single-particle ground state level, it makes sense to treat it separately from the rest of the sum ($i \geq 1$) for which we still perform the transition to an integral. For bosons trapped in a three-dimensional harmonic oscillator potential and with the appropriate density of states $g(E) = \frac{E^2}{2(\hbar\bar{\omega})^3}$ we obtain the following equation for the total number of particles N minus the ones in the macroscopically occupied ground state which we will label N_c

$$N - N_c = \frac{1}{2(\hbar\bar{\omega})^3}\int_0^\infty \frac{E^2}{exp\left[(E-\mu)/(k_BT)\right] - 1}\mathrm{d}E = \left(\frac{k_BT}{\hbar\bar{\omega}}\right)^3 Li_3\left(\exp\left\{\frac{\mu}{k_BT}\right\}\right). \tag{2.38}$$

This then constitutes the bosonic version of equation 2.35. Setting the chemical potential μ and the number of particles in the condensate N_c to zero we obtain the critical temperature for Bose-Einstein condensation

$$k_B T_c = \hbar\bar{\omega}\left(\frac{N}{Li_3(1)}\right)^{1/3} \approx 0.94\,(\hbar\bar{\omega})\,N^{1/3}, \tag{2.39}$$

where we used that $Li_3(1) \approx 1.202$. With this result and equation 2.38, we obtain the following relation for the fraction of atoms in the condensate

$$\frac{N_c}{N} = 1 - \left(\frac{T}{T_c}\right)^3 . \tag{2.40}$$

Using the polylogarithm, we can similar to the fermionic case, write down the density distribution of the thermal (uncondensed) part

$$n_{B,th}(\mathbf{r},T) = \frac{1}{\lambda_{th}^3}\,Li_{3/2}\left(\exp\left\{\frac{\mu - V(\mathbf{r})}{k_B T}\right\}\right). \tag{2.41}$$

This means that the density distribution of ultracold bosonic gases above T_c is slightly more peaked at the center than a Gaussian distribution. According to [Sta00], this effect can be understood by the bosonic enhancement at low momenta.

The maximum reachable density before condensation sets in is given when the chemical potential approaches 0 and it can be obtained from equation 2.41 to be $n_{B,th}^{max} = \frac{1}{\lambda_{th}^3}\,Li_{3/2}(1) \approx 2.6/\lambda_{th}^3$. This confirms the qualitative argument given in the beginning of this chapter that quantum effects become visible and relevant when the interparticle spacing $d = (1/n_{B,th}^{max})^{1/3}$ becomes similar to the size of the thermal de Broglie wavelength λ_{th}. This phase transition shows that there is an abrupt change in behavior when bosonic gases reach quantum degeneracy. This is fundamentally different from the fermionic behavior where the transition into the quantum degenerate regime occurs smoothly.

2.3.2 Weakly Interacting Bose Gas

So far, we have only considered non-interacting systems. Opposed to the fermionic case where the incorporation of interaction is theoretically challenging it is a lot simpler for the bosonic case. This is mainly due to the fact that in a Bose-Einstein condensate all atoms are in the same single-particle state. This significantly simplifies the theoretical treatment of the interactions. Let us consider the Hamitonian given in equation 2.13

$$\begin{aligned}\hat{H} \;&=\; \int d\mathbf{r}\,\hat{\psi}^\dagger(\mathbf{r})\,\left[T(\mathbf{r}) + V_{\text{trap}}(\mathbf{r})\right]\,\hat{\psi}(\mathbf{r}) \\ &\quad + \frac{1}{2}\int d\mathbf{r}\,d\mathbf{r}'\,\hat{\psi}^\dagger(\mathbf{r})\,\hat{\psi}^\dagger(\mathbf{r}')\,V_{\text{int}}(\mathbf{r},\mathbf{r}')\,\hat{\psi}(\mathbf{r}')\,\hat{\psi}(\mathbf{r}),\end{aligned} \tag{2.42}$$

where $T(\mathbf{r}) = \frac{-\hbar^2\nabla^2}{2m}$ is the kinetic energy, $V_{\text{trap}}(\mathbf{r})$ is the harmonic trapping potential and $V_{\text{int}}(\mathbf{r}, \mathbf{r}')$ is the two-particle interaction potential. To simplify the description we use a point-like pseudo interaction potential of the following form

$$V_{\text{int}}(\mathbf{r}, \mathbf{r}') = V_{\text{int}}(\mathbf{r} - \mathbf{r}') = g_{3D}\,\delta(\mathbf{r} - \mathbf{r}') = \frac{4\pi\hbar^2 a}{m}\,\delta(\mathbf{r} - \mathbf{r}'), \tag{2.43}$$

where g_{3D} is the three-dimensional coupling strength and a is the three-dimensional scattering length which will be introduced in section 2.4.1. We will limit our considerations to repulsive interactions ($g_{3D} > 0$) because attractively interacting BECs can become unstable and because we will not investigate such systems in this thesis.

If we assume that the macroscopic occupation of the single-particle ground state $\psi(\mathbf{r})$ still persist even with weak interactions, we can follow [Bog47, Zwi06a] and write the field operator in the following way $\hat{\psi}(\mathbf{r}) = \psi(\mathbf{r}) + \delta\hat{\psi}(\mathbf{r})$. Here, $\psi(\mathbf{r})$ is the thermal average of $\langle\hat{\psi}(\mathbf{r})\rangle_{th}$ and $\delta\hat{\psi}(\mathbf{r})$ describes the fluctuations around the mean field. When we now neglect these fluctuation and use the Hamiltonian given in equation 2.42 we obtain the time-dependent Gross-Pitaevskii equation for the macroscopically occupied single-particle ground state $\psi(\mathbf{r})$

$$i\hbar\frac{\partial}{\partial t}\psi(\mathbf{r}, t) = \left(-\frac{\hbar^2\nabla^2}{2m} + V_{\text{trap}}(\mathbf{r}) + g\left|\psi(\mathbf{r}, t)\right|^2\right)\psi(\mathbf{r}, t). \tag{2.44}$$

This has the form of a non-linear Schrödinger equation for the wave function $\psi(\mathbf{r}, t)$. Therefore, this quantity is sometimes called "condensate wave function"[8] and it plays the role of the order parameter for the BEC phase transition. All atoms described by this function $\psi(\mathbf{r})$ are in the ground state (with $E_0 = 0$) and its time evolution can be written as $\psi(\mathbf{r}, t) = e^{-i\mu t/\hbar}\,\psi(\mathbf{r})$. Using this, we obtain the time independent Gross-Pitaevskii equation

$$\left(-\frac{\hbar^2\nabla^2}{2m} + V_{\text{trap}}(\mathbf{r}) + g\left|\psi(\mathbf{r})\right|^2 - \mu\right)\psi(\mathbf{r}) = 0. \tag{2.45}$$

In the regime where the interaction term ($\approx g\left|\psi(\mathbf{r})\right|^2$) is significantly larger than the kinetic term, we can neglect the kinetic contribution[9]. It is then easy to obtain the density distribution for the condensed part $n_c(\mathbf{r}) \equiv \left|\psi(\mathbf{r})\right|^2$

$$n_c(\mathbf{r}) = \frac{\mu - V(\mathbf{r})}{g} = n_{c,0}\left(1 - \sum_i \frac{x_i^2}{R_i}\right), \tag{2.46}$$

where we use the shape of the harmonic trapping potential, $R_i \equiv \sqrt{\frac{2\,u}{m\omega_i}}$ are the Thomas-

---

[8] This name is somewhat misleading since $\psi(\mathbf{r}, t)$ is an approximation to the field operator not a regular wave function in the first quantization framework.

[9] This approach is called Thomas-Fermi approximation.

Fermi radii and $n_{c,0} = \frac{\mu}{g}$ is the central condensate density. This equation is only valid for $(\mu - V(\mathbf{r})) \geq 0$. In the case of $(\mu - V(\mathbf{r})) < 0$, we set $n_c(\mathbf{r}) = 0$. This result is very similar to the result obtained for fermionic systems with $T = 0$ in equation 2.33.

We can now also determine the chemical potential which is set by the normalization condition $N = \int n_c(\mathbf{r}) d\mathbf{r}$ and obtain

$$\mu = \frac{\hbar\bar{\omega}}{2}\left(\frac{15Na}{\bar{a}_{ho}}\right) \quad \text{and} \quad R_i = a_i \left(\frac{15Na}{\bar{a}_{ho}}\right)^{1/5}, \tag{2.47}$$

where $\bar{a}_{ho} \equiv \sqrt{\hbar/(m\bar{\omega})}$ is the harmonic oscillator length of the mean trapping frequency $\bar{\omega}$ (see e.g. [Zwi06a]).

Interacting Bose Gases at Non-Zero Temperatures

We can now combine our knowledge of the thermal phase above the critical temperature T_c and the Bose-Einstein condensate which emerges for $T \leq T_c$ to obtain the complete density distribution of a weakly interacting Bose gas. At $T = T_c$ the condensate forms and for even lower temperatures the condensate fraction N_c/N grows according to equation 2.40. In such a partly condensed system, the thermal part is described by the polylogarithmic density distribution given in equation 2.41 and the condensed part can be approximated by the parabolic density distribution given in equation 2.46. We thus obtain a bimodal density distribution n_{tot} which consists of a denser and smaller central part, the condensate, and a thermal cloud with significantly lower density that is larger in size

$$n_{tot}(\mathbf{r}, T) = n_{B,th}(\mathbf{r}, T) + n_c(\mathbf{r}). \tag{2.48}$$

By fitting such a density distribution to images of partly condensed clouds, one can now determine the condensate fraction N_c/N, the temperature T and other quantities (e.g. according to [Sta00]). Such a bimodal fit to experimentally obtained partly condensed clouds can be found in figure 2.3.

For weakly interacting systems the interactions in the thermal cloud and their effect on the condensate can be neglected since the density of the thermal part is relatively low [Zwi06a]. Therefore, such a description works very well for the relatively weakly interacting bosonic systems, which are described in chapter 5 where ultracold clouds of ^{87}Rb are studied. One can describe the excitations of the Bose condensate by adding the fluctuations of the field operators according to [Bog47]. This is often done using the Bogoliubov transformation which greatly simplifies the derivation of the excitation spectrum of the weakly interacting Bose gas. From the structure of this excitation spectrum one can then show that the BEC is in a superfluid state which has been confirmed e.g. by the observation of quantized vortices in rotating BECs [Pet02, Pit03].

For stronger interactions, the condensate has a strong effect on the thermal cloud due to its larger density and pushes the thermal part out of the center of the trap [Joc04]. This means that one should then use a self-consistent mean-field treatment to

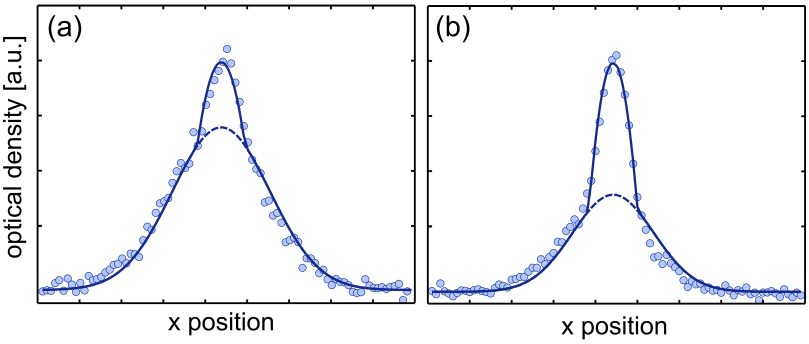

Figure 2.3: Bimodal doubly-integrated density distribution obtained from an absorption image of a partly Bose-condensed molecular cloud of ^{6}Li. For higher temperature (a) the condensate fraction is smaller than for lower temperature (b). The fit (solid line) consists of the thermal part which is indicated by the dashed line and a parabola for the condensate.

obtain the complete density distribution (see e.g. [Wil11]). In this regime, it becomes considerably more challenging to observe a bimodal distribution because the strong repulsion enlarges the size of the condensate part and thus it becomes similar in size to the thermal part.

2.4 Interactions in Ultracold Gases

Interactions strongly affect the characteristics and properties of ultracold gases. They are not only crucial for the preparation of degenerate gases but also determine the phases, shapes and dynamics of such systems. In this section, we will therefore introduce how one usually describes and models interactions in ultracold gases in more detail. We will show that for most ultracold systems the interactions can be described by a single parameter, the s-wave scattering length a. One peculiar property that makes ultracold gases such a great generic quantum system is that this single interaction parameter can be tuned over a large range using so-called Feshbach resonances. At the end of this section, we will then investigate the behavior of a two-component Fermi gas in the vicinity of such a Feshbach resonance. For these considerations we will follow basic cold atom scattering theory as presented for example in [Sak94b, Dal98, Gio08].

2.4.1 Elastic Collisions of Ultracold Atoms

To derive the properties of interacting ultracold gases we first have to examine the collisions between ultracold atoms. Due to the diluteness of ultracold systems it is sufficient for most cases to only consider binary (two-body) collisions[10].

Using fundamental quantum mechanics (see e.g. [Lan81, Gio08]), the elastic two-body scattering process is described by the stationary Schrödinger equation for the relative coordinates [11]

$$\left(\frac{-\hbar^2\nabla^2}{2m_r} + V_{\text{int}}(\mathbf{r}) - E_k\right)\psi_k = 0. \tag{2.49}$$

Here $\mathbf{r} = \mathbf{r}_1 - \mathbf{r}_2$ is the relative distance between the particles at $\mathbf{r}_1$ and $\mathbf{r}_2$, $m_r = \frac{m_1 m_2}{m_1+m_2}$ is the reduced mass, $E_k = \hbar^2\mathbf{k}^2/(2m_r) > 0$ is the energy of the eigenstate of the Hamiltonian with a well-defined wave vector $\mathbf{k}$ and $V_{\text{int}}(\mathbf{r})$ is the two-particle interaction potential with a finite range r_0 that vanishes for $r \equiv |\mathbf{r}| \gg r_0$. In such a potential we obtain the following asymptotic wave function at large distances ($r \gg r_0$)

$$\psi_k(\mathbf{r}) \propto e^{ikz} + f_k(\theta)\frac{e^{ikr}}{r}, \tag{2.50}$$

which consists of an incoming plane wave e^{ikz}, an outgoing spherical wave $\frac{e^{ikr}}{r}$ and a factor $f_k(\theta)$ that is called the scattering amplitude and depends on the angle θ between

---

[10] We will give some information about higher order collision terms when necessary but for most of our investigations these types of collisions are usually unwanted since they are inelastic and therefore limit the lifetime of the studied systems.

[11] In this description we neglect relativistic spin interactions [Gio08].

z and $\mathbf{r}$. Using this wave function one obtains the differential and total cross section

$$\frac{d\sigma_k}{d\Omega} = |f_k(\theta)|^2 \quad \text{and} \quad \sigma_{k,\text{tot}} = \int_\Omega |f_k(\theta)|^2 \, d\Omega, \quad \text{where} \quad 0 \leq \theta < \pi. \tag{2.51}$$

Effect of quantum statistics

Earlier we showed that the wave function of identical bosons (fermions) has to be totally (anti-)symmetric under particle exchange. This also applies to the scattering problem that we are studying and therefore the wave function given in equation 2.50 has to be correctly symmetrized. One thus obtains the following differential cross section for identical bosons and fermions

$$\left(\frac{d\sigma_k}{d\Omega}\right)_{\text{bosons}} = |f_k(\theta) + f_k(\pi - \theta)|^2 \quad \text{and} \quad \left(\frac{d\sigma_k}{d\Omega}\right)_{\text{fermions}} = |f_k(\theta) - f_k(\pi - \theta)|^2 \,, \tag{2.52}$$

where $0 \leq \theta < \pi/2$.

Partial Wave Expansion and Low Energy Behavior

We will now assume that the interparticle potential only depends on the interparticle distance and is spherically symmetric. In this case it is helpful to expand the wave function into partial waves with different angular momenta l and a radial wave function $\chi_{k,l}(r)$ that only depends on the radius. For each of these angular momentum states $\chi_{k,l}(r)$, we can obtain the following radial Schrödinger equation from equation 2.49

$$\left[\partial_r^2 - \frac{2m_r}{\hbar^2}\left(V_{\text{int}}(r) + \frac{\hbar^2 l(l+1)}{2m_r r^2}\right) + k^2\right] \chi_{k,l}(r) = 0. \tag{2.53}$$

The term $E_C = \hbar^2 l(l+1)/(2m_r r^2)$ originates from the spherical part of the ∇^2 operator and can be interpreted as a centrifugal barrier. For vanishing scattering energies ($k \to 0$) this barrier inhibits scattering for all states with $l > 0$. For ^{6}Li atoms this centrifugal barrier is $E_C \sim k_B \, 7\,\text{mK}$ [Jul92]. Therefore, collisions in systems with $T \ll 7\,\text{mK}$ can only occur via the isotropic s-wave ($l = 0$) channel. We also notice by examining the asymptotic behavior of the incident and outgoing wave at large radial distance $r \gg r_0$ that the only effect that an elastic collision has on the wave function is to add a phase shift δ_l to each spherical wave. Due to this fact one can write the scattering amplitude in terms of these phase shifts δ_l and obtains [Sak94a]

$$\sigma_{k,\text{tot}} = \sum_l \sigma_{k,l} = \frac{4\pi}{k^2} \sum_{l=0}^{\infty} (2l+1)(\sin(\delta_l))^2, \quad \text{with} \quad \delta_l \propto k^{2l+1}. \tag{2.54}$$

For low momenta ($k \to 0$) only the s-wave term contributes due to the reasons mentioned above[12] and therefore the scattering amplitude can be approximated by the s-wave term

$$f_k \approx f_{k,l=0} = \frac{1}{2ik}\left(e^{2i\delta_0} - 1\right), \tag{2.55}$$

where one should note that this scattering amplitude is independent of the angle θ. It then makes sense to define the so-called s-wave scattering length a by

$$a = -\lim_{k \to 0} \frac{\tan \delta_0}{k}, \tag{2.56}$$

which allows us to rewrite the scattering amplitude in terms of a [Zwi06a]. We thus obtain the following result for the total cross section

$$\sigma_{k,\mathrm{tot}} = \frac{4\pi a^2}{1 + k^2 a^2} \tag{2.57}$$

for distinguishable particles. This means that in the limit $ka \ll 1$ the scattering cross section is energy independent and

$$\sigma_{k,\mathrm{tot}} = 4\pi a^2. \tag{2.58}$$

In the limit of $ka \gg 1$ the total cross section is given by

$$\sigma_{k,\mathrm{tot}} = \frac{4\pi}{k^2}. \tag{2.59}$$

This regime is called the unitarity limit.

We already mentioned that for identical bosons and fermions we need to symmetrize the wave function according to quantum statistics. For indistinguishable particles there are two different scattering processes that cannot be distinguished (see e.g. [Dal98]). These two contribution lead to an interference in the scattering amplitude (see equation 2.52). Thus, one obtains the following total cross sections for the collisions of identical bosons and identical fermions in the limit of $ka \ll 1$

$$\sigma_{k,\mathrm{tot,bosons}} = 8\pi a^2 \quad \text{and} \quad \sigma_{k,\mathrm{tot,fermions}} = 0. \tag{2.60}$$

This shows that identical fermions do not scatter at ultracold temperatures [DeM99] and they are therefore well described by an ideal Fermi gas.

Pseudo-Potential Description and Mean Field Interaction Energy

For everything that was derived so far the only conditions for the interaction potential $V_{\mathrm{int}}(\mathbf{r})$ was that it only depends on the relative distance of the two particles, that it has

---

[12] This is true in the absence of scattering resonances in the other channels ($l > 0$).

a finite range r_0 and that it is spherically symmetric. The interactions between neutral atoms is usually described by a van-der-Waals interaction whose interparticle potential fulfills all of the aforementioned criteria, it has for example a finite range r_{vdW}.

When the energy of the colliding particles is so small that the de Broglie wavelength $\lambda_{dB} = 2\pi/k$ is much larger than the range of the interaction potential $r_0 = r_{vdW}$, the details of the interparticle potential are not resolved in the scattering process. In this case the description can be significantly simplified by assuming a contact interaction potential that correctly reproduces the s-wave scattering length a. Using the first Born approximation [Sak94a, Zwi06a] one can show that this is achieved by a pseudo-potential of the following form

$$V_{\text{int}}(\mathbf{r}) = g_{3D}\,\delta(\mathbf{r}) = \frac{2\pi\hbar^2 a}{m_r}\,\delta(\mathbf{r}). \tag{2.61}$$

This delta potential, however, produces divergences for three dimensional systems and therefore one usually regularizes it. This means that the delta function $\delta(\mathbf{r})$ is replaced by $\delta(\mathbf{r})\partial_r r$ [Hua87, Bus98, Wil11] which eliminates the divergences at short distances r [Gio08]. This pseudo potential approach is employed in most theoretical models describing ultracold atoms. The corrections to this approximation are suppressed by a factor r_{vdW}/a and are thus in most cases negligible. We will later also use such a pseudo potential to describe the interactions of the quasi one-dimensional few-fermion systems discussed in chapter 4.

Using this pseudo-potential it is easy to obtain the mean-field interaction energy for a weakly interacting system with $na^3 \ll 1$. According to [Joc04], one needs to consider N particles in a volume V at a density $n = \frac{N}{V}$. By summing the contributions of the interaction between a certain atom and all other particles, one can derive the mean-field interaction energy experienced by this atom and one obtains

$$E_{\text{int,mf}} = \lim_{V\to 0} \frac{1}{V} \sum_{i=1}^{N} \int g\,\delta(\mathbf{r}-\mathbf{r}_i)\,d\mathbf{r} = g\,n = \frac{4\pi\hbar^2}{m}\,a\,n. \tag{2.62}$$

We obtain the same result for $E_{\text{int,mf}}$ if we replace the interaction potential in the Hamiltonian given in equation 2.42 by the just introduced zero-range pseudo-potential and make use of the Bogoliubov approximation. A closer look at the definition of the mean-field energy also shows that the sign of the scattering length determines whether the mean-field energy is positive or negative. For $a > 0$, the mean-field energy is positive ($E_{\text{int,mf}} > 0$) which increases the total energy of the system. In this case the mean field repels the single test particle and we call such a system repulsively interacting. For $a < 0$, the mean-field energy is negative and lowers the total energy of the system. This means that the mean field attracts the test particle and we obtain an attractive mean-field interaction. One should bear in mind though that this does not mean that the microscopic interparticle interaction is repulsive for $a > 0$. It just tells us what happens to the interaction energy of the complete system interacting with such a scattering length. The microscopic scattering event which is described by a van-der-Waals interaction is always attractive, no matter which sign the scattering length has.

2.4.2 From Weakly to Strongly Interacting Systems

Following [Wil11], we can determine the regime of the interactions for a given system by comparing the size of the interaction energy $|E_{\text{int}}| \approx |E_{\text{int,mf}}| = |g|n$ to the density-dependent kinetic energy $E_{\text{kin}} \approx h^2 n^{2/3}/(2m)$ [Zwe03, Wil11]. Using these quantities we can define a dimensionless interaction parameter

$$\gamma = \frac{E_{\text{int}}}{E_{\text{kin}}} \approx n^{1/3} a. \tag{2.63}$$

For $\gamma \ll 1$, the system is weakly interacting and for bosonic systems the Gross-Pitaevskii equation gives an appropriate description of the relevant physical properties. For $\gamma \geq 1$, the system becomes strongly interacting and one obtains a strongly correlated many-body system. Here, simple mean-field approaches like the Gross-Pitaeksii equation break down and more involved theoretical techniques have to be employed to describe such systems.

Note that for degenerate Fermi systems γ can be written as $k_F a$, where k_F is the Fermi wave vector. This is an important quantity to describe the interaction strength of fermionic systems and it will later be extensively used. We will later see that such a dimensionless interaction scale γ also exists for one and two-dimensional systems.

2.4.3 Universality

Universality is a concept that is commonly used in physics. It describes the fact that certain physical behavior is independent of the exact details of the particular system (see e.g. [Bra06, Wen08, Lom11]). This concept was initially introduced to classify the critical behavior of systems at phase transitions. Universal behavior usually originates from the separation between different scales (in our case long- and short-range physics) of a physical system. One can use effective parameters to describe the macroscopic properties independently from the details of the short-range physics if this separation between the scales is sufficiently large. All quantities that are solely dependent on this effective description are called universal. We already introduced the scattering between ultracold atoms which constitutes a great example for universality. For such systems the de Broglie wavelength λ_{dB} is much larger than the range of the interaction potential $r_0 = r_{vdW}$. Thus, the scattering is independent of the exact details of the short-range potential and the only important quantity, necessary to describe the interactions, is the s-wave scattering length a. This implies that quantities like the critical temperature for the Bose-Einstein condensation or the mean field energy per particle only depend on the scattering length and are thus universal.

If the scattering length is significantly larger that r_0, we obtain even more universal behavior. One can generally show that a large and positive scattering length is always associated with a weakly bound dimer state whose binding energy is given by $E_B = \frac{\hbar^2}{ma^2}$ (see e.g. [Lan81]). This universality is not limited to the two-body sector but can even be extended to the three-body sector where universal three-body bound states, called Efimov trimers [Efi70, Bra06, Fer11], emerge at diverging scattering lengths. Until recently it was thought that the description of these Efimov states needs an additional non-universal three-body parameter but the comparison of recent experiments suggests that this might not even be necessary [Fer11].

In the unitary regime ($a \to \infty$), the diverging scattering length can no longer serve as a relevant scale of the system since this would lead to unphysical divergences, e.g. in the scattering cross section. The only remaining length scale is then the interparticle spacing which, for a fermionic system, is proportional to the inverse Fermi wave vector k_F and the only remaining energy scale is then the Fermi energy E_F. Thus, the system can be fully described by these quantities rescaled with numerical factors [Car03, Ku12]. This means that all fermionic systems in the unitary regime can be mapped onto each other and the underlying short-range physics becomes irrelevant. Consequently, results obtained with an ultracold, unitary interacting Fermi gas can be translated to various other unitary fermionic systems at completely different scales like in a neutron star or in high-T_c superconductors. This is particularly interesting since ultracold gases offer a very controlled environment and there is a simple way to reach the unitary regime by tuning the s-wave scattering length using magnetic Feshbach resonances. In the next section we will therefore introduce the concept of such resonances and then show how we can tune the scattering length a for a Fermi gas of ^{6}Li atoms.

2.5 Tuning the Interactions

We will now show how we can change the scattering length and thus the interaction strength using Feshbach resonances. Afterwards, we will present the resonances that occur for systems consisting of ^{6}Li atoms in different Zeeman sublevels. At the end of this section we will investigate the consequences on the many-body physics of a two-component Fermi gas in the vicinity of such a Feshbach resonance.

2.5.1 Feshbach Resonances

As mentioned before, we know from low-energy scattering theory that the scattering length and thus the cross section is resonantly enhanced if a bound state of the interparticle potential is close to the continuum. Generally, a weakly bound dimer state leads to a large and positive scattering length [Lan81] that diverges when the bound state reaches the continuum threshold. If we could change the interparticle potential such that the energy of the bound state would cross the continuum, then the scattering length would change sign and become negative and large in absolute value $|a|$ when the bound state is slightly above the continuum threshold. This is pretty easy to see from the definition of the scattering length given in equation 2.56 which is proportional to $\propto \tan(\delta_0)$. This accidental fine tuning to a strongly interacting system occurs for certain systems like for example neutron-neutron scattering.

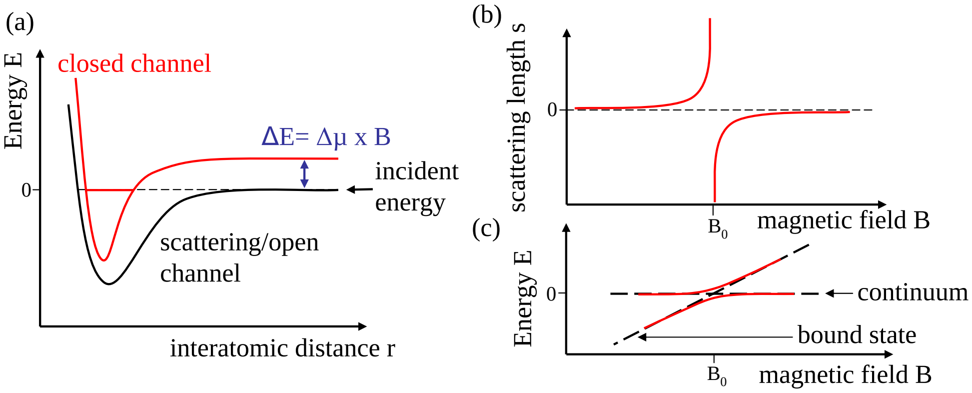

Figure 2.4: (a) Illustration of the open and closed channel in a scattering event close to a magnetic Feshbach resonance. If a bound state in the closed channel coincides with the continuum of the scattering/open channel and if there is a coupling between the two channels, the scattering length diverges as shown in (b). This coupling leads to an avoided crossing between the molecular state and the free scattering state and thus the scattering state is adiabatically connected to the molecular state (c). Taken from [Wen08].

There is another way to use the same principle but in a more controlled and tunable manner called magnetic Feshbach resonance. This concept has already been extensively investigated in both theoretical [Fes58, Moe95, Pet02, Pit03] and experimental publications [Ino98, Chi10]. We will therefore follow their reasoning and give a qualitative description of this effect. It relies on the fact that the structure of neutral atoms is usually more complex and there are different scattering channels with different hyperfine configurations. Imagine a low-energy scattering event in a certain channel (called open channel, see figure 2.4(a)), where the atoms have an incident energy slightly above the continuum threshold. If there is another scattering channel for example in a different hyperfine state that has a higher continuum threshold, then one calls this a closed channel. Due to the different magnetic moments of the channels, one can tune their relative energy ΔE by applying a magnetic offset field. At a certain magnetic offset field the closed channel is tuned such that one of its bound states exactly coincides with the continuum threshold of the open channel. A hyperfine coupling between the two channels can now lead to the possibility that the scattering atoms virtually enter the closed channel during the scattering event. This leads to a resonant enhancement of the scattering length and thus of the scattering cross section. These scattering resonances are called Feshbach resonances [Fes58]. A more careful analysis as for example performed in [Moe95] shows that the scattering length a as a function of the magnetic field B in the vicinity of such a Feshbach resonance can be described in the following way

$$a(B) = a_{\mathrm{bg}} \left(1 + \frac{\Delta}{B - B_0}\right), \tag{2.64}$$

where a_{bg} is the background scattering length, Δ is the width of the resonance and B_0 is the magnetic field value where the resonance occurs. A plot of $a(B)$ is shown in figure 2.4(b). As explained above, each Feshbach resonance is associated with a bound state which is slightly below the continuum for $a > 0$ and crosses the continuum for $a \to \infty$. This bound state has a universal binding energy $E_B = \hbar^2/(ma^2)$ for $a \gg r_0$ and a sketch of this binding energy is shown in figure 2.4(c).

In this thesis we will extensively use the Feshbach resonances occurring in systems of ^{6}Li atoms to tune the scattering length and thus the interaction of such ultracold systems. Therefore, we will now introduce the hyperfine states and the Feshbach resonances in the different scattering channels for this particular system.

2.5.2 Hyperfine States and Feshbach Resonances for ^{6}Li

Fermionic ^{6}Li has an electron spin $S = 1/2$ and a nuclear spin $I = 1$ which lead to a total spin of $F = 1/2$ or $F = 3/2$. These two hyperfine states are separated by $h \times 228\,\mathrm{MHz}$ at zero magnetic offset field [Geh03]. The Zeeman energy for the different states can be found in figure 2.5. For magnetic fields much larger than 30 Gauss we enter the high-field regime and the electron and nuclear spin decouple. This leads to two triplets (one with $S = 1/2$ and one with $S = -1/2$) that only differ by their nuclear spin. For the sake of simplicity we label the Zeeman sublevels $|1\rangle$ to $|6\rangle$ according to their energy in a magnetic offset field (see figure 2.5).

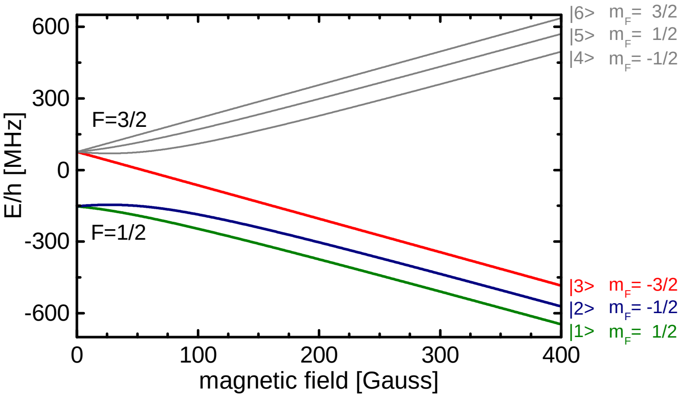

Figure 2.5: Magnetic field dependence of the energy of the Zeeman sublevels of the electronic ground state of ^{6}Li. The states are labeled $|1\rangle$ to $|6\rangle$ according to their energy from lowest to highest. The three lowest Zeeman sublevels are used for most of the experiments we perform with ^{6}Li.

Earlier we explained that identical ultracold fermions do not interact with each other due to their antisymmetric wave function. We therefore usually evaporate a two-component Fermi gas consisting of atoms in states $|1\rangle$ and $|2\rangle$. Most of our experiments are performed with binary mixtures of atoms in two different spin states of the lower triplet $|1\rangle$, $|2\rangle$ and $|3\rangle$. The scattering between atoms in these different Zeeman sublevels is described by the s-wave scattering lengths a_{12}, a_{13} and a_{23} for the scattering channels $|1\rangle|2\rangle$, $|1\rangle|3\rangle$ and $|2\rangle|3\rangle$.

The broad Feshbach resonances for the different scattering channels of ^{6}Li are shown in figure 2.6. The exact positions and widths of the resonances are given in table 2.1. They are determined by a combination of very precise radio-frequency spectroscopy of the bound states responsible for the Feshbach resonances and a complex coupled channel calculation that optimizes the exact potential shape to reproduce the measured spectroscopy data (more details in section 4.4.3).

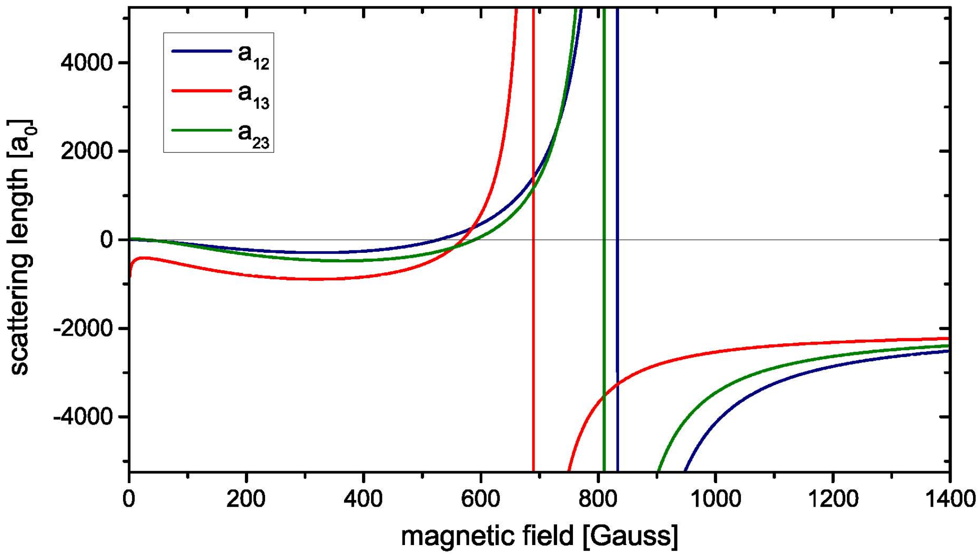

Figure 2.6: Scattering lengths for the different interaction channels in Bohr radii as a function of the magnetic field. The resonance positions and widths are given in table 2.1. The data for this plot is taken from [Zür13a].

The reason the scattering lengths a_{12}, a_{13} and a_{23} in figure 2.6 are not symmetric around the position of the Feshbach resonance is a change of the background scattering length in the region of the resonances. The open or scattering channel changes from a superposition of a triplet and singlet state at low fields to an almost complete triplet scattering process at magnetic fields larger than 600 Gauss. Therefore, the background scattering lengths change from very small values for low magnetic fields to large and negative values of about $-2000\,a_0$ above the resonance. This means that there is no zero crossing in the region above the Feshbach resonances (at least in the magnetic field range accessible with our magnetic field coils). We will see that this unfortunate fact has two major implications. Due to the collisional behavior close to the resonances, we can only create non-interacting Fermi gases after an evaporation at low magnetic fields of about 300 Gauss [Lom11]. Second, there is a range of intermediate negative scattering lengths that can not be accessed with ^{6}Li gases which ranges from about $-1000\,a_0$ to $-2000\,a_0$.

The large width of the three resonances shown in figure 2.6 make it comparatively simple to control the scattering length on a precise level. To be able to tune the scattering lengths over the full accessible range, we need magnetic offset fields ranging up to about 1400 Gauss. This is challenging but possible using the magnetic field coils described in section 3.3.1.

Scattering channel	Position [Gauss]	Width [Gauss]
$\|1\rangle\|2\rangle$	832.2	262.3
$\|1\rangle\|3\rangle$	689.7	166.6
$\|2\rangle\|3\rangle$	809.8	200.2

Table 2.1: Broad Feshbach resonances in the three lowest scattering channels of ^{6}Li with the resonance position and the corresponding width [Zür13a].

2.5.3 BEC-BCS Crossover

We will now briefly discuss the many-body physics occurring for strongly interacting two-component Fermi gases in the vicinity of such a Feshbach resonance. We will see that for such a system two limiting cases of fermionic superfluidity are continuously connected through the unitary regime in the so-called BEC-BCS crossover. First, we will discuss both limiting cases and then show how these two regimes can be connected by a resonantly interacting superfluid. We will discuss this topic more qualitatively since it has already been extensively studied and analyzed in various review articles [Ket08, Gio08], books [Pet02, Pit03, Zwe11] and theses [Joc04, Zwi06a]. For more details and the exact derivation of the important quantities, we will thus refer to these publications.

The Molecular BEC limit

In the previous section we showed that there is a weakly bound two-body bound state on the repulsive side ($a > 0$) of the Feshbach resonance. If the temperature is on the order or lower than the binding energy of the dimer state that consists of one atom in each of the two components, then molecules are formed through three-body recombination [Joc03a, Reg03, Pet04]. Close to the Feshbach resonance these molecules are relatively stable with lifetimes exceeding several seconds. It was shown that the molecules interact with a scattering length $a_{\text{mol}} = 0.6\,a$, i.e. a fixed fraction of the scattering length for two interacting atoms [Pet04]. These molecules consist of two fermionic atoms and are thus bosonic (have an interger spin). Hence, they can form a Bose-Einstein condensate of molecules, also called molecular BEC (mBEC) if the temperature is low enough.

In the limit of weak repulsive interaction ($k_F a \to 0_+$), these diatomic molecules behave exactly like bosons and we thus obtain the well-known BEC description as it was discussed earlier in section 2.3. This means all formulas like the critical temperature or the condensate fraction derived then can be applied. The only change is that the mass of the diatomic molecules is twice the mass of a free atom ($m_{\mathrm{mol}} = 2\,m$). In this limit, the system can be described with the Gross-Pitaevskii equation (2.44 and 2.45) and the condensate is superfluid for non-zero interaction.

The BCS limit

For attractively interacting two-component Fermi gases, there is no dimer state available. There is however another way to form diatomic pairs, which then also form a superfluid.

We consider a two-component Fermi gas at zero temperature with a weak attractive interaction ($k_F a \to 0_-$). In the 1950s Bardeen, Cooper and Schrieffer showed [Bar57] that such a system is unstable towards the formation of so-called Cooper-pairs. These pairs consist of two particles of opposite momentum and spin. The pairing mechanism, which occurs in momentum space, leads to an energy gap in the excitation spectrum at the Fermi surface of the following form[13]

$$\Delta_0 \approx \left(\frac{2}{e}\right)^{7/3} E_F \exp\left\{-\frac{\pi}{2k_F|a|}\right\}. \tag{2.65}$$

This quantity is the so-called zero temperature gap [Gio08] and the gapped excitation spectrum leads to superfluid behavior. This theory named after Bardeen, Cooper and Schrieffer (BCS) was originally derived to explain superconductivity in metals. In these systems, a two-component electron gas attractively interacts through the mediated phonon interaction which leads to the formation of Cooper-pairs and superfluid behavior. It was shown in [Gio08], that the critical temperature for superfluidity of Cooper pairs T_c for an ultracold Fermi system with finite temperature is given by

$$k_B T_c = \frac{e^\gamma}{\pi}\,\Delta_0 \approx 0.28\,E_F \exp\left\{-\frac{\pi}{2k_F|a|}\right\}, \tag{2.66}$$

where $e^\gamma \approx 1.78$ with γ the Euler constant. A more careful analysis shows that the critical temperature for Cooper-pair formation T^* and the onset of superfluidity T_c coincide at infinitely weak attractive interaction.

One should note that for the just discussed systems the pairing mechanism fundamentally differs from the one in the BEC limit. While in the BEC limit the pairing is a simple two-body phenomenon, it is more complicated in the BCS regime. Here,

---

[13] One should note that the result obtained by standard BCS theory is different by a numerical factor of about ~ 2 since it does not include screening effects in the medium. The correct prefactor which is given here, was first derived by [Gor61].

one usually calls the Cooper pairs many-body pairs since the filled Fermi sea below the Fermi surface is necessary for these pairs to form. It is therefore not the attraction to the other particle of opposite spin and momentum that generates the pair but rather the collective interaction with all particles around the Fermi surface. A hand-waving explanation for the existence of such a bound state induced by the many-body system is to consider the two-dimensional Fermi surface as the place where the two constituents of the Cooper pair exist [Ket08]. In a two-dimensional system there is always a bound state even if the attractive interaction is infinitesimally weak[14]. This argument shows that a filled Fermi sphere is necessary for these Cooper pairs to exist.

The Crossover and the Unitary Fermi Gas

These two seemingly independent limits of superfluid systems are connected through a unitary interacting two-component Fermi gas. The theoretical description of this crossover was pioneered by the works of Eagles [Eag69] and Leggett [Leg80] and experimentally investigated shortly after the first realization of molecular BECs (e.g. [Bar04, Chi04, Zwi05, Gre05]).

In the unitary limit, which is reached close to the Feshbach resonance for $k_F|a| \gg 1$, the scattering length is larger than the interparticle spacing and we obtain a system which is at the same time dilute and strongly interacting. This raises the question whether the system is stable or if it collapses due to strong attraction[15]. Since there is no analytic solution to the many-body system in this regime, one uses approximative or numerical solutions to describe such systems. The most regularly used description extends the standard BCS theory to the unitary regime and the obtained results are not exact but the qualitative description they provide are mostly correct. These theoretical consideration and the experiments both find that the system is indeed stable (at least for a two-component Fermi gas) and that below a critical temperature a superfluid is formed (see figure 2.7 and [Gio08]). We know from scattering theory that when a diverges, the two-particle cross section reaches the unitary limit and becomes independent of the scattering length (see equation 2.59). Since the scattering length is no longer a reasonable length scale of the system, it drops out of the description and the interparticle spacing $\sim 1/k_F$ remains the only relevant length scale. Therefore, all thermodynamic quantities only depend on the Fermi energy E_F and the degeneracy T/T_F. From this, one can derive the energy of a Fermi gas at unitarity E_u for $T \to 0$ to be

$$E_u = \mu_u(T=0) = \xi \, E_{F,\text{non-int.}} = (1+\beta) \, E_{F,\text{non-int.}}, \tag{2.67}$$

where β is a universal parameter and $\xi = 1 + \beta$ is the so-called Bertsch parameter (see e.g. [Gio08]). This numerical factor is expected to be universal for all unitary Fermi gases (see section 2.4.3) and was recently experimentally determined to be $\xi =$

---

[14] This is not the case for a three-dimensional system, where the interparticle potential is required to have a certain minimal depth in order to support a bound state for attractive interactions.

[15] This collapse occurs for bosonic systems if the attractive interaction becomes too large.

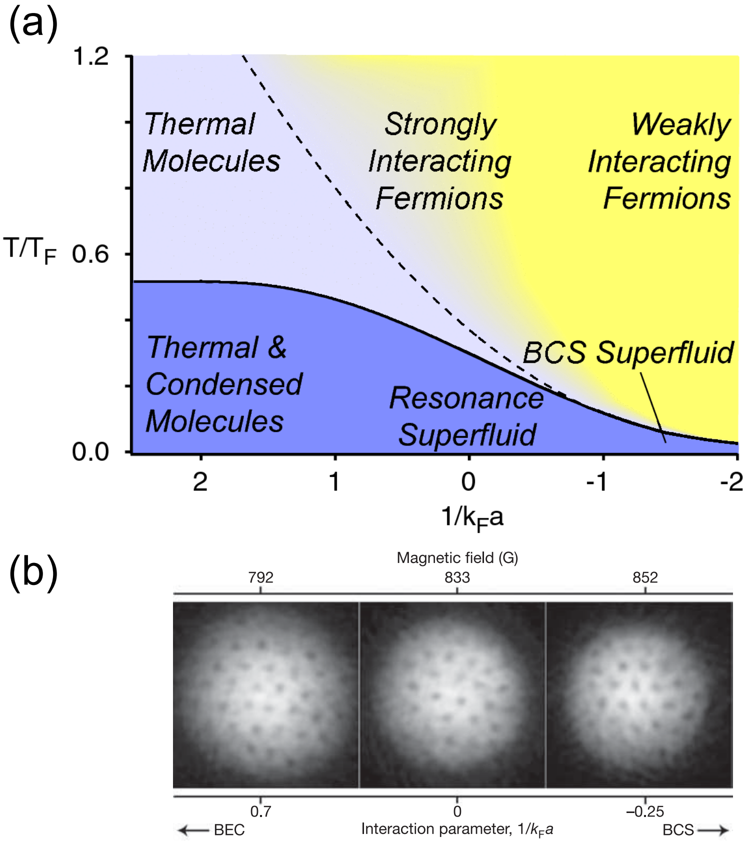

Figure 2.7: (a) Phase diagram of a strongly interacting two-component Fermi gas in the BEC-BCS crossover. The dashed line indicates the pair formation temperature T^* and the solid line indicates the critical temperature T_c for the formation of a superfluid. Taken from [Ket08]. (b) The observation of vortex lattices for rotated strongly interacting Fermi gases across the Feshbach resonance indicates the occurrence of superfluidity in the whole crossover region. It therefore also shows that a unitary Fermi gas realizes a strongly interacting superfluid. Taken from [Zwi05].

0.370(5)(8) [Ku12, Zür13a]. In this measurement of the equation-of-state of a unitary interacting Fermi gas, the critical temperature for superfluidity could also be extracted and the obtained value is $T_c = 0.167(13)\,T_F$.

To obtain a more tangible idea of the crossover, it makes sense to examine the pairs of two fermions across the crossover region. We know that in the BEC limit the pairs are deeply bound diatomic molecules with a size that is smaller than the interparticle spacing. In the BCS limit, the Cooper pairs are significantly larger than the interparticle spacing and pair two fermions on opposite side of the Fermi sphere. A reasonable extrapolation between these two limits is to assume that the size and character of the pair continuously connects these two limiting cases. This assumption was backed by early theoretical considerations and was later confirmed in experiments which measured the size of the pairs in the crossover region [Sch08b]. This crossover from tightly bound diatomic molecules on the BEC side to many-body induced Cooper pairs in the BCS limit is illustrated in figure 2.8. It shows that the two limits are connected by strongly correlated pairs of the size of the interparticle spacing at unitarity. These measurements give further evidence for the validity of an earlier developed projection technique [Reg04, Zwi04, Per05]. This technique uses a quick non-adiabatic magnetic field ramp to the BEC regime which thus projects the strongly correlated pairs onto tightly bound molecules. Then one can obtain an estimate for the condensed and hence superfluid fraction from a bimodal fit to the data after the quick ramp. In this way, one can easily obtain an estimate for the superfluid fraction for the complete crossover region.

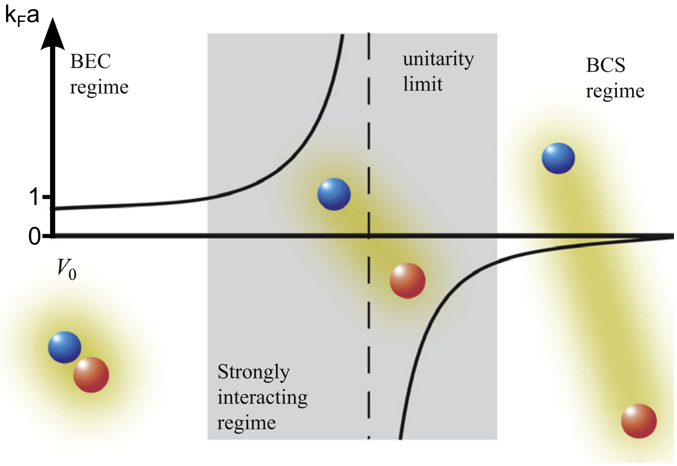

Figure 2.8: The continuous evolution between diatomic molecules and Cooper pairs across the BEC-BCS crossover. In the unitary regime ($k_F a \geq 1$) the strongly correlated two-fermion pairs are of the size of the interparticle spacing. Taken from [Gub13].

While experiments can observe superfluid behavior close to the Feshbach resonance (for large $k_F a \geq 1$), it is in most cases not possible to reach the weakly interacting BEC and BCS limit ($k_F a \to 0$). This is due to the fact that on the BEC side the diatomic molecules become collisionally unstable for small interaction strengths ($k_F a \approx 0$) which inhibits reaching the weakly interacting BEC limit. On the BCS side, the critical temperature T_c depends exponentially on the scattering length (see equation 2.66 and figure 2.7 (a)) and therefore the system is usually too warm [16] to observe a superfluid for weak attractive interactions. This illustrates one of the reasons for the interest in these strongly interacting superfluids: One expects new insight in the understanding

---

[16] When we say "too warm" we mean the relative degeneracy temperature T/T_F. Although the systems studied here are a lot colder than most condensed matter systems the critical temperature T_c in terms of the Fermi temperature is still among the highest ever observed.

and description of high-T_c superconductors (for example cuprates or iron pnictides). These systems are also expected to be strongly correlated and due to universality, there is hope to be able to transfer observations and concepts from cold gases to these interesting condensed matter systems.

2.6 The Influence of Dimensionality

Another characteristic property of high-temperature superconductors that is expected to strongly influence their physical behavior is their anisotropy. It is suggested that, additionally to the strong correlations between the pairs, another reason for their relatively high T_c/T_F is their reduced dimensionality in the direction perpendicular to the superconductive layers (see e.g. [Sch91]). This example shows that the dimensionality of a systems strongly influences its physical properties.

Using particularly shaped optical dipole traps[17], created for example by the interference of several beams, allows to explore different dimensionalities with ultracold gases. The quasi-2D or quasi-1D regime is usually achieved by separating the scales of confinement in different directions. Let us consider an elongated cigar-shaped potential with large aspect ratio $\eta = \omega_r/\omega_z$, where ω_r is the radial and ω_z is the axial trapping frequency. In such a system, one reaches the quasi-1D regime when all energy scales E, which includes the chemical potential μ, the thermal, the interaction and kinetic energy, are significantly smaller than the first excitation in the radial direction ($\hbar\omega_r$). Then there is only negligible influence of the radial excitations and thus the system can be well-described by one-dimensional theory. To reach the quasi two-dimensional regime, only one trapping frequency (e.g. ω_z) is large enough for all energy scales of the system to fulfill $E \ll \hbar\omega_z$.

In the course of this thesis we will work with fermionic and bosonic systems in various geometries. For example the finite Fermi systems investigated in chapter 4 are most of the times quasi one-dimensional, the bosonic ^{87}Rb systems described in chapter 5 are quasi two-dimensional with respect to the spin degree of freedom and finally the composite bosonic dimers of ^{6}Li investigated in chapter 6 are trapped in a quasi two-dimensional geometry. Therefore we will give a brief comparison and overview on the implications of different dimensionalities on ultracold systems.

2.6.1 Effects of the Dimensionality on the Two-Body Parameters

We will now show how the dimensionality affects important physical quantities and characteristics of ultracold gases. First, we note that the Hamiltonian defined in equation 2.13 basically remains unchanged besides the fact that the coordinate and momentum vectors have a lower dimensionality. Second, one has to examine what happens to an ultracold scattering event in quasi one and quasi two-dimensional systems. It

---

[17] One can also use magnetic traps to confine ultracold samples with reduced dimensionality. Since these are, however, not utilized in this thesis we will not further discuss them here.

was shown that then the definition of the scattering length a, given in equation 2.56, is altered. Following [Bus98], the definition of the scattering lengths (a_{3D}, a_{2D} and a_{1D}) is done such that three facts remain unchanged for 3D, 2D and 1D systems

1. $\cot(\theta)$ increases for increasing scattering length a (see table 2.2),
2. the two-body bound state occurs for $a > 0$,
3. the binding energy of that bound state is $E_B = \frac{\hbar^2}{ma^2}$.

Similar to the case of three dimensions, we will still use a zero-range delta function pseudo potential for the description of the interactions in lower dimensional systems and hence $V_{\text{int}} = g\,\delta(\mathbf{r})$ [18]. It is shown in table 2.2, that we obtain a different dependence of the coupling strength g on the scattering length a for different dimensionalities: $g_{3D} \propto a_{3D}$ (see section 2.61), $g_{1D} \propto -1/a_{1D}$ [Ast04, Ols98] and $g_{2D} \propto -1/\ln(k\,a_{2D})$ [Frö12, Blo75]. One can see that the two-dimensional case has a peculiar property since, unlike in the $1D$ and $3D$ case, the scattering process does not become independent of the wave vector k. This means that even in the low-energy limit, the interaction strength still depends on the scattering energy.

The dependence between the coupling strength and the scattering length also has implications on the existence of the two-body bound state since its binding energy is defined by the respective scattering length. In three and one-dimensional systems, the bound state only occurs for either a repulsive ($g_{3D} > 0$) or attractive ($g_{1D} > 0$) mean-field interaction (see table 2.2). For two-dimensional systems, however, there is always a bound state.

We can now also generalize the dimensionless coupling strength γ defined in section 2.4.2. Since we will use this parameter mostly for the description of two-component degenerate Fermi gases, we replace the general wave vector k by the Fermi wave vector k_F. For the three dimensional case it makes sense to define $\gamma_{3D} = k_F\,a_{3D}$ as the scale of the interaction strength. For $\gamma_{3D} \gg 1$ the system is considered strongly interacting. In one-dimensional systems, this definition is slightly altered because the scattering length is inversely proportional to the coupling strength and one usually uses $\gamma_{1D} = \frac{g_{1D}}{k_F} \sim \frac{1}{k_F\,a_{1D}}$. In the literature this quantity is often referred to as the Lieb-Liniger parameter [Ols03]. For two-dimensional systems, one uses $\gamma_{2D} = \frac{1}{\ln(k_F\,a_{2D})} \sim g_{2D}$ as the dimensionless interaction parameter since it is proportional to the coupling strength.

2.6.2 Implications for Many-Body Physics

The changes in the two-body observables like the scattering length, the coupling strength and the two-body bound state also have strong impact on the many-body physics of lower dimensional systems. For example, it leads to the occurrence of a different type of quantum degenerate phase, which is not a BEC, for a two-dimensional system of

---

[18] Note that in the three-dimensional case one should use the regularized delta function in order to avoid unwanted divergences (see section 2.4.1).

	3D	**1D**	**2D**
phase shift	$\cot(\theta) \propto -(ka_{3D})^{-1}$	$\cot(\theta) \propto (ka_{1D})$	$\cot(\theta) \propto \frac{2}{\pi}\ln(ka_{2D})$
$\mathbf{g_{iD}(a_{iD})}$	$g_{3D} = \frac{4\pi\hbar^2\, a_{3D}}{m}$	$g_{1D} = \frac{-2\hbar^2}{m\, a_{1D}}$	$g_{2D} = \frac{-2\pi\hbar^2}{m\, \ln(k\, a_{2D})}$
bound state occurrence	repulsive mean-field int. $g_{3D} > 0$	attractive mean-field int. $g_{1D} < 0$	always all g_{2D}
$\boldsymbol{\gamma}$	$\gamma_{3D} = k_F a_{3D} \sim k_F g_{3D}$	$\gamma_{1D} = \frac{1}{k_F a_{1D}} \sim \frac{g_{1D}}{k_F}$	$\gamma_{2D} = \frac{1}{\ln(k_F\, a_{2D})} \sim g_{2D}$

Table 2.2: Dependence of the scattering phase shift θ, the coupling strength g, the occurrence of the two-body bound state and the dimensionless interaction parameter γ for a two-component degenerate Fermi gas for different dimensionalities.

bosons. This phase is called the Berezinsky–Kosterlitz–Thouless or BKT phase. In this case the "condensate" does not have a constant phase over the whole cloud but the phase coherence decays algebraically as a function of the distance. Consequences like these can be rather complex and we will discuss them when necessary in the respective chapters.

3 Experimental Setups and Techniques

In this chapter we will provide a brief overview of the experimental setups we use to create and investigate ultracold atoms. The measurements performed and described in this thesis were done using the following three different experimental setups:

The few-fermion machine, also called "old" experiment was the first apparatus that was set up in our group in Heidelberg starting in 2007 at the Max-Planck-Institute for Nuclear Physics. This setup was designed for experiments with few fermionic ^{6}Li atoms and the measurements performed with this setup are described in chapter 4. After the completion of the optical dipole trap, however, we performed experiments on universal few-body physics with a three-component Fermi gas of ^{6}Li [Ott08, Wen09, Lom10a, Lom10b]. Since we wanted to proceed towards our goal to deterministically prepare few-fermion samples, we felt that it made sense to build a new experimental setup dedicated to further pursue the measurements with three-component Fermi gases particularly in an optical lattice.

The fermionic-lattice machine, also called "new" experiment was therefore planned and set up in Heidelberg starting in fall 2009. It also uses ^{6}Li atoms and its structure and design very closely follows the few-fermion machine with only minor changes to the vacuum chamber and the initial stages of the experiments. This setup is used for the investigations of quasi two-dimensional Fermi gases that are presented in chapter 6.

The Spinor-BEC machine, where the measurements described in chapter 5 were performed, was built in the group of Prof D.M. Stamper-Kurn at UC Berkeley. It uses bosonic ^{87}Rb atoms and was the update on an existing Spinor machine that was decommissioned in the beginning of 2009 soon before I joined their research group for one year and 3 months as a visiting scholar.

Since the structure and the idea behind all three machines is very similar, this chapter will start with the description of a generic sequence to obtain cold atoms and the design goals of the cold gases machines. Afterwards, we will describe the cooling and trapping techniques, the ways we manipulate the cold atomic clouds with static or oscillatory fields and finally we will briefly introduce the different imaging techniques.

The unique features of each of these machines is then presented and discussed in detail in the respective chapters.

3.1 Design Goals and Structure

When planning cold atom experiments, the aim is to build a machine that fulfills several simple design goals. These kind of experiments normally operate in a sequential process of loading, cooling, manipulating and measuring cold atomic or molecular clouds. Therefore, the setup should be stable over long periods of time and reproducible from shot to shot. To allow the preparation and guarantee sufficient lifetimes of the ultracold samples, the samples have to be very well-isolated from the environment. The stability is generally further improved by having short experimental cycle times. This additionally allows for better adjustments and it minimizes the time needed to measure a large range of different parameters. All of the above mentioned goals should be met while keeping the setup as simple as possible since this facilitates trouble shooting, debugging and maintaining. Furthermore, this shortens the time needed to set up the experiment.

In general, there are a few essential steps and requirements to prepare a sample of ultracold atoms. These steps are very similar for almost all ultracold atom experiments including the three different setups used in this thesis:

- **Vacuum chamber:** In order to isolate the cold samples from the environment one needs an ultra-high vacuum chamber. Usually, the pressures are in the range of 10^{-11} mbar in the main chamber where the experiments are performed.

- **Oven:** To cool and trap atoms inside the UHV chamber, atomic vapor needs to be brought to the main chamber. This is achieved for example by an oven loaded with the desired atomic species, which are most of the time alkali or alkaline earth elements. Another possibility is to use dispensers or desorption to obtain the atomic vapor source inside the UHV chamber.

- **Dissipative precooling stage:** In this stage, the hot atomic vapor coming from the oven is laser cooled in a Zeeman slower or in a 2D magneto-optical trap. Subsequently, these decelerated atoms are then trapped and further cooled in a magneto-optical trap (MOT). The minimal temperature that can be reached in this stage depends on the exact setup, the wavelength of the transition and the polarization of the light. It is however fundamentally limited by the photon recoil energy. In the experiments discussed in this thesis, the lowest temperatures reached in the MOT are about $400\,\mu$K for the lithium machines and about $150-200\,\mu$K in the rubidium machine. The achievable phase-space density in these MOTs is about 10^{-6}, which is far too low to reach the quantum degenerate regime where the phase-space density is on the order of 1.

- **Evaporative cooling in conservative potential:** In order to further increase the phase-space density, the atoms are then usually transferred into a conservative trapping potential provided by an optical dipole trap or by magnetic traps. Here, the atomic clouds are further cooled by forced evaporative cooling and one can reach the quantum degenerate regime.

- **Manipulation of the ultracold sample:** In the magnetic and optical traps of variable geometries, the actual measurements are then performed. The atoms can for example be manipulated using radio-frequency (RF) or microwave (MW) pulses or by applying magnetic fields.

- **Detection:** After the manipulation we have to detect the atoms using one of several available imaging techniques. One can for example count the number of fluorescent photons emitted by the ultracold sample. Another possibility is to record the shadow cast onto a CCD camera while shining a resonant laser beam onto the atomic sample. It is also possible to obtain information about the atomic density without destroying the sample for example by measuring the change in the phase of a non-resonant laser beam that passes through the ultracold cloud.

- **Computer control:** All of the just mentioned steps need to be reproducibly repeated over and over again with sub-millisecond time resolution in order to obtain reliable results. Therefore, a computer control is necessary that sequentially processes such a timing sequence by controlling all needed devices like lasers, power supplies and switches using digital and analog channels.

In the remainder of this chapter we will now give a few details on how some of these steps are realized in the setups used for measurements in this thesis.

3.2 Creation of a Cloud of Ultracold Atoms

To illustrate the details of an ultracold atoms setup, we will now go through the production sequence of a degenerate quantum gas in the fermion lattice experiment. The details of this procedure are already described in various diploma and master theses [Rie10, Sim10, Boh12, Nei13] and therefore we will limit ourselves to a brief summary of the main steps.

3.2.1 Vacuum Chamber

All experiments take place inside a UHV chamber to ensure sufficient lifetimes of the ultracold samples. This is necessary because a collision with a room temperature particle results in a large momentum transfer onto an ultracold atom which is thus kicked out of the trap. The UHV chamber is shown in figure 3.1 and it consists of two main parts: the main chamber and the oven section. In the oven section the vacuum

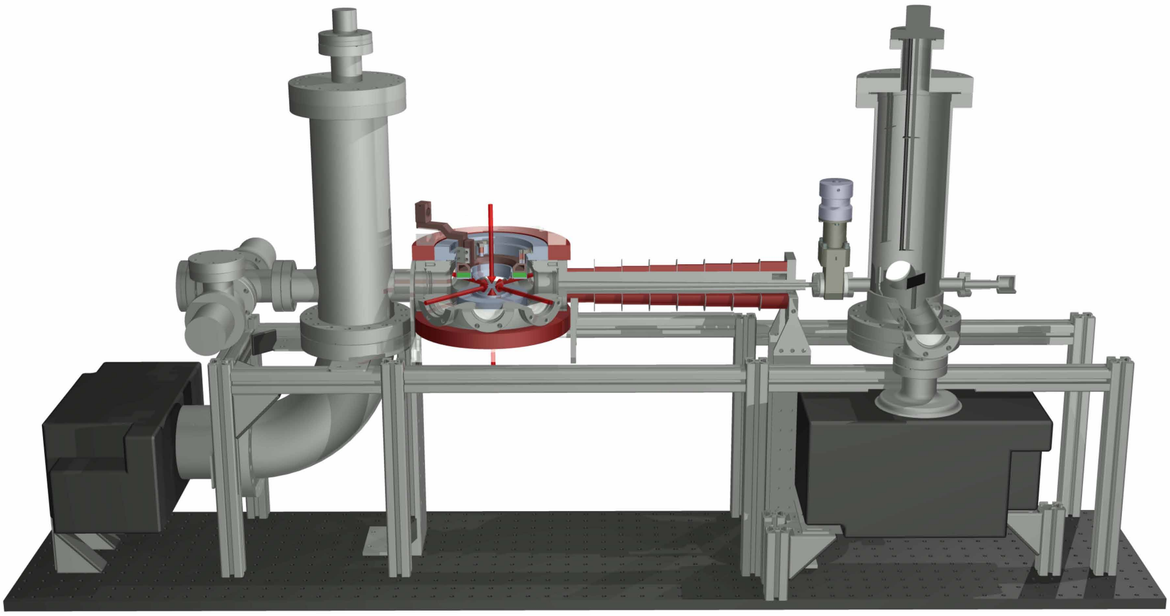

Figure 3.1: The vacuum chamber of the ”new experiment”. After leaving the oven section (right part) the atoms are trapped and cooled in the main chamber. The Zeeman slower and MOT coils are shown in red, the Feshbach coils in green and the red arrows depict the six MOT beams.

is about 3×10^{-11} mbar due to the outgassing of the heated oven. Since we want lower pressures in the main chamber we separate it from the oven section by a differential pumping stage. Additionally, the walls of the octagon, which is the heart of the main chamber, are coated with a non-evaporable getter coating that is activated during the bake out [NEG] and further improves the vacuum. Using an ion pump (Varian StarCell 75 or 45) and a titanium sublimation pump in each section, we reach pressures lower than 10^{-11} mbar in the main chamber. This is sufficient to not limit the envisioned experiments by the collisions of ultracold atoms with the background gas particles.

3.2.2 Oven

As an atom source we use a simple heated stainless steal cup which acts as an oven and evaporates ^{6}Li atoms. The oven is heated to 350 °C to obtain sufficient flux in the atomic beam which is collimated at an aperture before entering the Zeeman slower drift tube. More details on the oven and its characteristics are given in [Ser07].

3.2.3 Zeeman Slower

When the evaporated atoms leave the oven they travel at an average speed of about $1500\,\frac{\text{m}}{\text{s}}$. In order to catch a significant fraction of the atoms in the main chamber, the atoms need to be slowed down. This is achieved with a Zeeman slower where a combination of a counterpropagating laser beam and a spatially varying magnetic field decelerates the atoms. Such Zeeman slowers are very commonly used in cold atom experiments and a detailed description can be found in standard atom physics literature [Met99]. Their working principle is to use the momentum transfer of counterpropagating photons to slow down the atoms. Due to the motion of the atoms, the atomic transition is Doppler shifted and one applies a magnetic field to compensate for this shift. After scattering some photons from the laser beam, the atoms slow down and therefore their Doppler shift decreases. In order to be able to continue the deceleration of the atoms, the magnetic field that compensates the Doppler shift with the Zeeman effect needs to be readjusted. One can calculate that the position-dependent magnetic field should scale with the square root of the position [Met99, Sim10].

In our experiments we use a decreasing field slower where the final part of the magnetic field for the Zeeman slower is provided by the MOT coils. This allows a compact setup and leads to a very small distance between the end of the Zeeman slower and the capture range of the MOT. This is beneficial for a high loading rate of the MOT because then few atoms, that are slowed in the Zeeman slower, are not caught in the MOT. After the Zeeman slower, the decelerated atoms have a velocity of about $50\,\frac{\mathrm{m}}{\mathrm{s}}$ and we expect a flux of about 10^{10} atoms/s. A detailed characterization of this Zeeman slower can be found in [Sim10].

3.2.4 Magneto-Optical Trap (MOT)

After leaving the Zeeman slower the atoms are trapped in a magneto-optical trap which consists of a magnetic quadrupole field and six intersecting laser beams from all directions (see e.g. [Met99]). In the MOT, the spontaneous light force is used to trap the atoms and the slightly red-detuned laser beams dissipatively cool the atoms to about $400\,\mu$K.

In our MOT, we obtain loading rates of about $3 \times 10^8\,\frac{\text{atoms}}{\text{s}}$ when the oven is heated to $T_{\text{oven}} = 350\,^{\circ}$C [Rie10]. The maximum number of atoms we can trap in the MOT at this oven temperature is about 1.2×10^9. In a typical cycle we need to load about $3 - 5 \times 10^8$ atoms to proceed with the preparation of an ultracold gas without being limited by the number of atoms in the MOT. Therefore, the MOT loading is usually performed for about 2 seconds when the oven is run at $T_{\text{oven}} = 350\,^{\circ}$C. This rather low oven temperature should result in a long oven lifetime of about $20,000$ hours. We measured the one-body loss rate of atoms from the MOT, which is caused by collisions with the background gas and obtain a vacuum lifetime of about 23 minutes in the MOT. This indicates a very low background pressure and thus will not limit future experiments. The details of the MOT and the just mentioned measurements are described in [Rie10].

The achievable phase-space density in such a MOT is about 10^{-6}. This is still six orders of magnitude away from quantum degeneracy. Even with subdoppler cooling techniques, which are challenging to implement with ^{6}Li, we are still not able to get anywhere near the quantum degenerate regime. Therefore, we need to transfer the atoms into a conservative potential where they can be cooled further using forced evaporative cooling.

3.2.5 Dipole Trap and Evaporative Cooling

After cooling the atoms in the MOT they are transferred to the optical dipole trap (ODT) created by the intersection of two elliptical laser beams with a wavelength of 1064 nm [Boh12]. An ODT uses the dipole force caused by a far-detuned laser beam. It is a second order process where the oscillating electric field of the trapping beam induces an atomic dipole moment which in turn interacts with the light field via a dipole potential. Similar to a magnetic dipole in an inhomogeneous magnetic field the induced electric dipole of the atoms feels a force towards higher fields for a red-detuned trapping beam (towards lower fields for blue-detuned laser light). Because this is a second order process, the depth of the optical dipole potential is proportional to the square of the electric field, hence the intensity of the trapping beam. In order to minimize non-resonant scattering of atoms from the trapping photons we choose a large detuning of $\Delta_{\mathrm{ODT}} = 1064\,\mathrm{nm} - 671\,\mathrm{nm} = 393\,\mathrm{nm}$. This comes at the price that we need very high laser powers in order to trap the atoms directly from the MOT because the depth of an ODT scales $\propto I/\Delta_{\mathrm{ODT}}$. We therefore use a 200 W continuous-wave fiber laser from IPG photonics (YLR-200-LP-WC) to provide the necessary intensities at a reasonable trap volume.

We transfer about 10^6 atoms from the MOT into the ODT. Due to the way we ramp down the intensities of the MOT beams the atoms in the ODT are in the two lowest Zeeman sublevels of the hyperfine state $|F = 1/2\rangle$ of the electronic ground state. As defined in section 2.5.2 these states are labeled $|1\rangle$ and $|2\rangle$. After the transfer to the ODT, we continue to cool the atomic sample using forced evaporation. Here one decreases the depth of the trap to let the hottest atoms escape. Due to elastic scattering between the remaining atoms the sample rethermalizes and its temperature is decreased. If one has sufficiently high scattering rates the rethermalization process is so quick that one can continuously decrease the trap depth and therefore cool the atomic cloud. In such a way we can quickly cool the atoms from several hundred μK to the nK temperature regime at the price that we lose a large fraction of the atoms.

Elastic collisions are essential for this method to work and therefore for reaching low temperatures and high phase-space densities. Identical fermions have a vanishing cross section at ultracold temperatures therefore a one-component Fermi gas can not rethermalize during the evaporation. Since we already load a mixture of two distinguishable fermions ($|1\rangle$ and $|2\rangle$) into the ODT this does not limit our experiments. Furthermore, we can make use of the broad Feshbach resonance between these two states at 832 G: Close to the resonance the scattering length is very large and therefore thermalization occurs quickly which enables us to perform efficient evaporative cooling. If the evaporation is done at large positive scattering length (e.g. 795 G) we will form diatomic molecules and these will eventually condense into a molecular BEC (mBEC) if we continue to cool further. When the evaporation is done at negative scattering length there is no molecular state accessible and we produce a degenerate Fermi gas

(DFG). The details of the optical setup, the parameters of the ODT, the loading and the evaporation procedure can be found in [Boh12].

These degenerate samples normally contain about $50,000$ to $100,000$ atoms in each spin state and their temperature is on the order of 100 nK. Such systems represent the starting point for the experiments described in this thesis.

3.2.6 Computer Control and the Sequence

In order to precisely time and control all necessary equipment and parameters we use a real-time computer control system (ADwin Pro II). It can control 64 digital channels with a minimal time step of $1\,\mu$s. Additionally, it has 16 analog outputs and 8 analog inputs which can be updated every $10\,\mu$s. These analog channels are used to set and control parameters like the laser power in the optical traps or the magnetic offset fields. A digital PID-feedback loop is implemented in the real-time computer system. This feedback has a bandwidth of up to 100 kHz and is commonly used in our experiments to stabilize optical trap depths and magnetic fields to a high accuracy. It has the great advantage that one can change the PID parameters and switch between open and closed loop control with very little effort even during one experimental run [Zür09]. The timing tables for this system is generated by a LabView code written in our group by T. Lompe [Lom08].

In order to illustrate how a quantum degenerate ^{6}Li sample is created, we show a simplified sketch of a timing graph of the most important analog and digital channels for a typical experimental sequence in figure 3.2.

3.3 Manipulation Tools

After explaining how we prepare an ultracold sample, we can now start the experiments by manipulating the internal or external degrees of freedom of the system.

3.3.1 Homogeneous Magnetic Offset Fields and Feshbach Coils

As explained in chapter 2, we can use magnetic Feshbach resonances to change the strength and the sign of the interaction between the particles (see section 2.5.2). Depending on the magnetic offset field during the evaporation, we can decide if we want to create diatomic bosonic molecules or keep fermionic atoms. As we will later see, this is of fundamental importance for almost all performed measurements.

The magnetic offset field necessary to reach the Feshbach resonance is generated by a pair of magnetic field coils, which we call Feshbach coils. A few properties were important to us when we designed these coils. First, we want to be able to quickly change the magnetic field. Furthermore, we need to reach fields up to about 1400 G in order to tune the scattering length over the full range. Additionally, we wanted to drive the coils with a reasonably priced and available power supply. As a consequence,

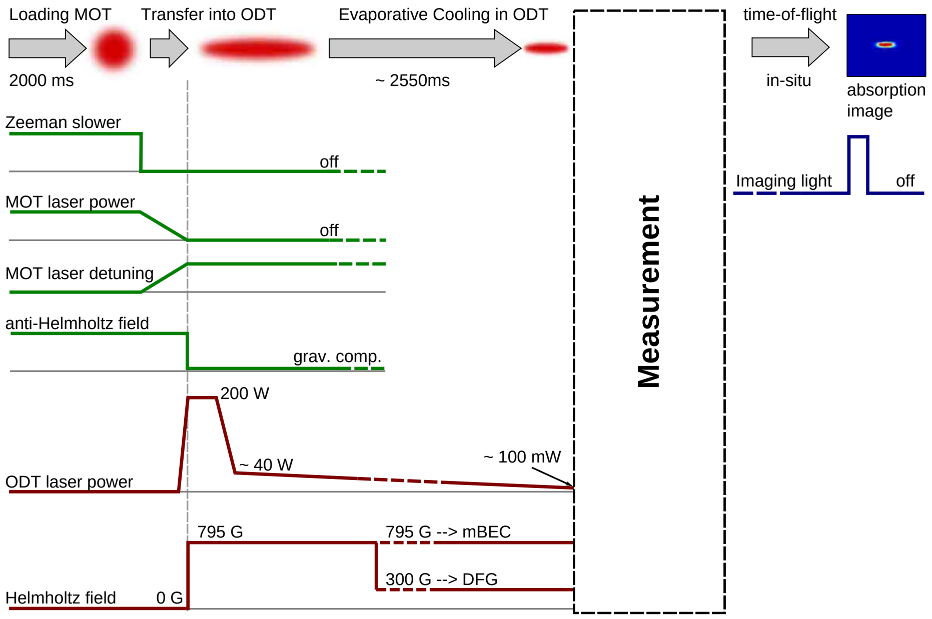

Figure 3.2: Illustration of the sequence to produce an ultracold gas. Shown is a timing graph of a selection of analog and digital channels. Taken from [Nei13].

we planned and built relatively small coils that are located close to the atoms. Using 30 windings of 7 mm×0.6 mm Kapton-insulated copper wire, we need about 200 A to reach 1400 G. We can therefore use an off-the-shelf 3.3 kW power supply from Delta Electronika (SM 30-200). Since the inductance of these Feshbach coils is rather small and because of the comparatively small field volume and energy, we are able to quickly change the magnetic offset fields. While being controlled by the digital PID loop we can change the field by about 300 G in 1 ms. Without feedback we can ramp about 200 G in 100 μs. On long timescales of several days our magnetic offset field is stable to less than 5 mG. Comparing this to the offset field of about 800 G one obtains a relative stability of 6×10^{-6}. On short timescales, we obtain field stabilities of about 1 mG which correspond to a relative stability of 1×10^{-6}.

The used Feshbach coil design has some drawbacks: To get the coils close enough to the atoms, they are recessed around the upper and lower high numerical aperture window (coils are depicted in green, the reentrant viewport in light blue in figure 3.3). Due to the limited space we could not use copper wire with an internal cooling water channel but we rather had to glue the whole coil onto a suitable heat sink that does not diminish the optical access (copper part in figure 3.3). The main challenge was that the amount of heat produced by the coils is very large. Therefore, it is crucial to provide good thermal contact between the coils and the heat sink. This was achieved by lathing the top of the coil in order to get it sufficiently even and then gluing the bare copper of the coil onto the bare copper of the heat sink with good thermal conductivity

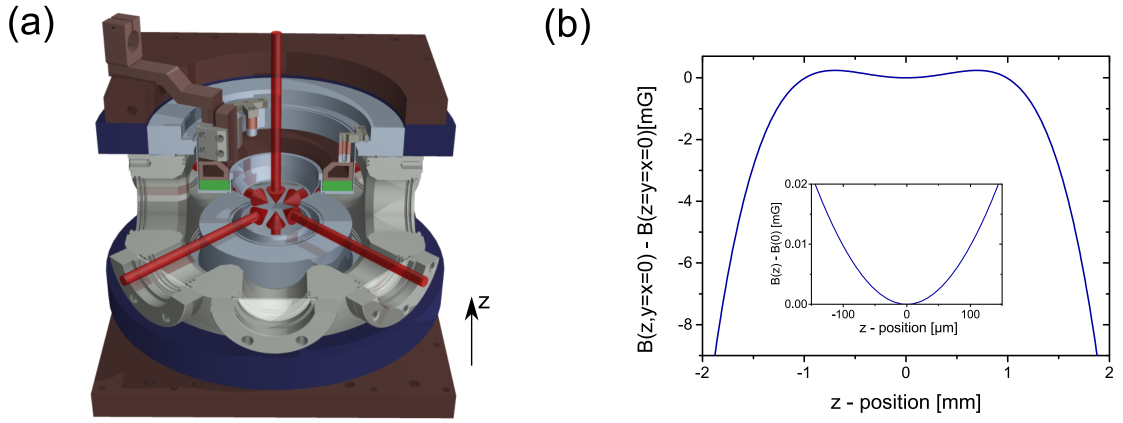

Figure 3.3: (a) Main chamber with octagon (gray), reentrant viewport (light blue), MOT coils and their heat sink (dark blue and copper), Feshbach coils and their heat sink (green and copper) and MOT beams (red arrows). (b) Simulated magnetic offset field $B_{z,y=0,x=0}(z)$ created by the Feshbach coils with 30 windings at a current of 200 A.

but without any electrical contact. For this we used a special diamond filled epoxy and an involved production procedure. An old version of this procedure can be found in [Zür09], it has however been further modified and revised since then.

The coils are mounted onto the outer part of the reentrant viewport. The mounts are constructed such that one can adjust and lock the vertical position of each coil using a set of screws and nuts. In order to obtain a field that is as homogeneous as possible the position and the distance of the coils were optimized by measuring the magnetic fields acting on an atomic cloud. In order to provide the atomic cloud with a small magnetic confinement in the horizontal plane where the optical confinement is weakest, the coils are placed a bit further apart than Helmholtz configuration. This leads to a weak antitrapping in the vertical and a small trapping potential in the horizontal direction. A simulation of the magnetic field in the vertical direction as a function of the vertical position is shown in figure 3.3 (b). In order to make the field in the horizontal direction as spherically symmetric and homogeneous as possible, we furthermore placed small pieces of ferrite steel onto the heat sink of the coils. These steel pieces locally increase the field with their permeability. By adjusting their size and position we minimize or cancel magnetic field inhomogeneities and anisotropies at the position of the atoms. We will later see that this cancellation of residual magnetic field gradients and curvatures is very important because these inhomogeneities lead to dephasing and decoherence of the cloud when radio-frequency (RF) or microwave (MW) pulses are applied. This broadens the transition and therefore leads to a larger uncertainty in spectroscopic measurements.

The Feshbach coil setup used in the few-fermion experiments is very similar to the one just described. The only difference is that in this setup the used copper wire had a cross section of 5mm×1mm and therefore the coils only have 15 windings. This approximately doubles the current and halves the voltage necessary to reach similar field strengths.

3.3.2 Magnetic Quadrupole Fields and Gradients

For some measurements it is necessary to not only apply a homogeneous magnetic offset field but also a magnetic field gradient. In our case these are applied by a set of coils in Anti-Helmholtz configuration. Due to the magnetic moment of the atoms, a linear gradient leads to linear potential hence a constant force onto the atoms. We use such a gradient in both setups in Heidelberg to compensate for the effect of gravity by applying a gradient in the upward direction.

As we will later see, such a linear field gradient is also essential in the deterministic preparation of few-fermion samples (see chapter 4) and for the preparation of quasi two-dimensional systems in the lattice setup (see chapter 6). In both cases the gradient is used to deform the optical trapping potential such that the number of atoms is controlled by the number of remaining states in the trapping potential that is a combination of the optical trap and the magnetic field gradient. Furthermore, a linear gradient is used in the tomographic measurements to resolve the single sheets of the quasi two-dimensional traps used in chapter 6. In most cases these magnetic field gradients are provided by the MOT coils, sometimes we also invert the current through one of the Feshbach coils and thus use these to apply a magnetic field gradient.

For the experiments performed in Berkeley, magnetic field gradients are an unwanted effect since in our experiments with spinor gases we need the field to be as homogeneous as possible. We therefore invested a lot of time to cancel the existing gradients by using various compensation coils. More details on this can be found in chapter 5.

3.3.3 Radio-Frequency and Microwave Pulses

Another common tool for preparing, manipulating and measuring ultracold samples is the application of oscillating radio-frequency (RF) or microwave (MW) fields to change the internal state of the atoms. The transition between Zeeman sublevels is well described by a two-level system and we can thus drive Rabi oscillations between the states. The linewidth of these transition is very narrow and therefore this technique is well suited for precise calibrations and energy measurements (see for example [Gup03, Chi05, Zür13a]).

We already introduced the different Zeeman sublevels and hyperfine states of ^{6}Li (see section 2.5.2). Most of the time we drive RF transitions between two adjacent states of the three lowest Zeeman sublevels ($|1\rangle$, $|2\rangle$ and $|3\rangle$). These transitions occur at a frequency of about 80 MHz for magnetic fields above about 100 G. Figure 3.4 (a) shows the loss of atoms from state $|2\rangle$ when the atoms are transferred to state $|3\rangle$ with a radio-frequency pulse. From such a measurement we can deduce the transition frequency with a relative accuracy of $11\,\mathrm{Hz}/84.614732\,\mathrm{MHz} = 1.30 \times 10^{-7}$. At this

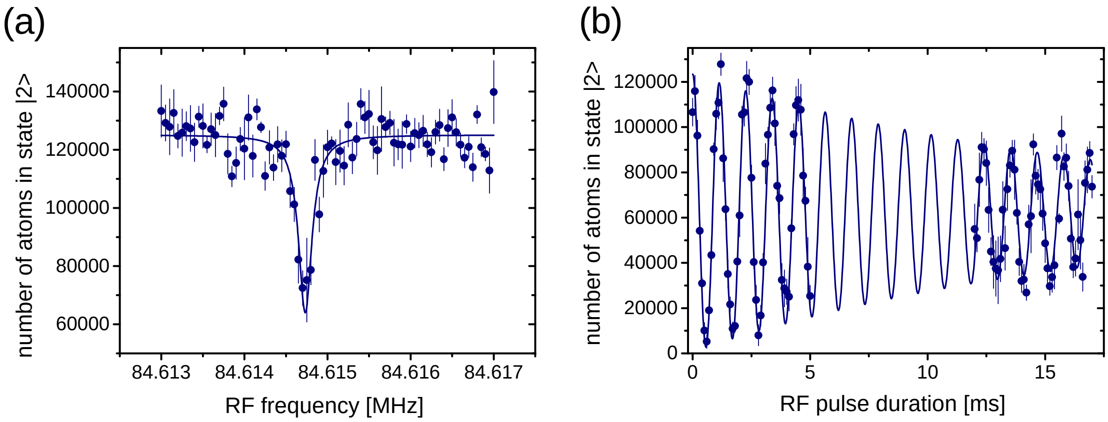

Figure 3.4: (a) Determination of the $|2\rangle$-$|3\rangle$ transition frequency. From a Lorentzian fit we can determine the transition frequency to be $84.61473\,\mathrm{MHz} \pm 11\,\mathrm{Hz}$ with a FWHM of 195 Hz. According to the Breit-Rabi formula this corresponds to a magnetic field of 526.692 G. (b) Rabi oscillations between state $|2\rangle$ and $|3\rangle$. We observe Rabi oscillations with a Rabi frequency of $\Omega = 2\pi\, 875\mathrm{Hz}$ and a coherence time $\tau = 17.7 \pm 1.9\,\mathrm{ms}$. Taken and adapted from [Nei13].

frequency, we can measure the population in state $|2\rangle$ as a function of the duration of the RF pulse (see 3.4 (b)) and observe clear Rabi oscillations. These oscillations have a coherence time of almost 20 ms which is most likely limited by the dephasing through magnetic field inhomogeneities. By adjusting the length of such a RF pulse one can transfer population from one state to another using e.g. π or $\pi/2$ pulses. A different way to transfer atoms between states is to do adiabatic Landau-Zener passages. Here, the applied frequency is slowly ramped over the atomic transition and the atoms are adiabatically transferred into the other state. The advantage of this technique is that small drifts in the magnetic offset fields do not influence the transition probability and therefore they are more stable than π-pulses [Wen08].

The antennas that are used to apply these pulses consist of a single copper wire loop and a small matching circuit. This circuit consists of a few capacitors which resonantly enhance the antenna at the desired frequency and match the impedance of the antenna to the driving amplifier (see figure 3.5 (b) and (c)). One particular feature of the "new" setup is that the RF antenna is placed inside the vacuum chamber. Therefore, the distance between the atoms and the antenna is very short and thus the signal is not attenuated by the stainless steal vacuum chamber. We hoped that this would significantly increase the achievable Rabi frequencies. It turned out that the way the antenna has to be mounted through the vacuum feedthrough makes it more difficult to resonantly enhance and match the impedance of the antenna. This in turn leads to less current through the copper wire which limits the maximal Rabi frequencies. In the end, the Rabi frequencies with the internal antenna are extrapolated to be about $\Omega_{23} = 2\pi\, 8.85\,\mathrm{kHz}$ at 100 W RF power in the "new" setup [Boh12]. They are slightly

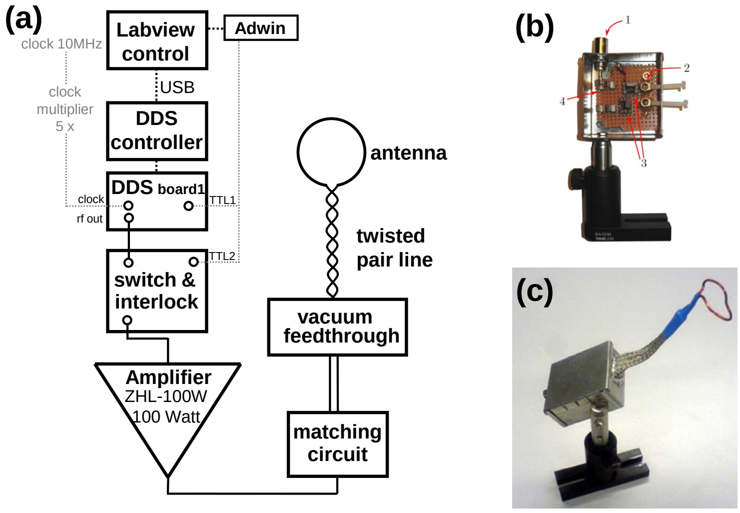

Figure 3.5: (a) Schematic of the RF setup. (b) Picture of the impedance and frequency matching box used for the antenna inside the vacuum chamber (taken from [Heu11]). (c) Antenna used in the "old" setup outside of the vacuum chamber. Its matching circuit is inside the metal box and to minimize stray fields the twisted pair line is enclosed by a metal mesh (from [Lom11]).

larger but of the same magnitude to the ones reached in the old experiment with an antenna outside of the vacuum chamber ($\Omega_{23} = 2\pi\,7\,\mathrm{kHz}$ [Lom11]). More details on the RF setup in the "new" experiment can be found in [Heu11] and on the "old" setup in [Lom11].

In our setups the RF and MW fields are generated by a waveform generator (either a DDS from Analog Devices (AD9854) or an Agilent (E4421B)). To protect the antenna and the feedthrough from overheating the signal passes through an interlock box which turns the signal off if the generated heat in the antenna is too high [Heu11]. Subsequently, the RF signal is amplified, passes the matching circuit and is then applied to the atoms by the antenna (see figure 3.5 (a) and (b)).

For some measurements we want to drive MW transitions from one of the lower three states to the states $|4\rangle$, $|5\rangle$ or $|6\rangle$[1]. The frequency for such a transition is on the order of 1 GHz.

3.4 Imaging Techniques

The final step of each experimental cycle is to image the atom cloud to obtain information about the properties of the cloud. In this way one can distinguish the state the samples are in, determine the number of atoms, their temperature and their

---

[1] Such a transition flips the electron spin. Therefore, the coupling is stronger compared to a RF transition where the nuclear spin of the ^{6}Li atoms is flipped.

density. There are several standard imaging techniques used in cold gases (see e.g. [Hig05b, Ser11a, Ser11b, Guz12]) and we will introduce the ones that we will use in this thesis.

3.4.1 Absorption Imaging

The idea behind absorption imaging is simple[2]. One shines a resonant laser beam onto the atoms and records the shadow that is created by the ultracold cloud with a CCD or CMOS camera. We take three consecutive images: one with the atoms (I_{abs}) and the imaging light, a second one without the atoms but with the imaging beam (I_{ref}) and the final picture without atoms and without imaging light (I_{bg}). From these images, one obtains the two-dimensional optical density of the sample

$$\rho_{\mathrm{od}}(x,y) = -\ln T(x,y) = -\ln \frac{I_{\mathrm{abs}}(x,y) - I_{\mathrm{bg}}(x,y)}{I_{\mathrm{ref}}(x,y) - I_{\mathrm{bg}}(x,y)}, \tag{3.1}$$

where $T(x,y)$ is the relative transmission. Here, we assume that the imaging beam propagates along the z-axis and is resonant with the atomic transition (detuning $\Delta = 0$). By dividing the first image by the reference image, we suppress the inhomogeneities on the imaging beam like for example interference fringes. By subtracting the dark image from both the actual image and the reference image we eliminate the effects of the dark signal from the camera.

If the intensity of the imaging light is much smaller than the saturation intensity of the imaging transition the scattering cross-section between the light and the atoms becomes constant. In the case that we image on a closed transition with σ-polarized light the cross-section along the magnetic field axis is given by $\sigma_0 = \frac{3\lambda^2}{2\pi}$. For different polarizations or imaging along the axis perpendicular to the magnetic field axis the cross-section is reduced by a numerical factor because we have to consider the particular Clebsch-Gordon coefficient.

The transmission of light through the sample in the low intensity regime ($I \ll I_{\mathrm{sat}}$) is given by Lambert-Beer's law

$$I(x,y) = I_0(x,y) \int e^{-\sigma_0\, n(x,y,z)} \mathrm{dz}, \tag{3.2}$$

where $n(x,y,z)$ is the three-dimensional density of the atomic cloud. Using equation 3.2 and $T(x,y) = I(x,y)/I_0(x,y)$, we obtain the two-dimensional column density

$$n(x,y) = \int n(x,y,z)\, \mathrm{dz} = \frac{\rho_{\mathrm{od}}(x,y)}{\sigma_0}. \tag{3.3}$$

Knowing the magnification M of the imaging system and the area A of one camera

---

[2] More details on absorption imaging, the derivation of the optical density and other relevant quantities can be found in [Ott10].

pixel, we can determine the number of atoms imaged onto one pixel

$$N_{\mathrm{pix}}(x,y) = \frac{A}{M^2\,\sigma_0}\,\rho_{\mathrm{od}}(x,y). \tag{3.4}$$

This means that by using absorption imaging we cannot only extract the atom number but also spatial information about the cloud if our imaging resolution is sufficiently good. During each experimental cycle we integrate the two-dimensional optical density along the x or the y-direction and obtain the doubly integrated optical densities. These are fitted with a Gaussian distribution and we obtain the number of atoms and the temperature of the gas[3].

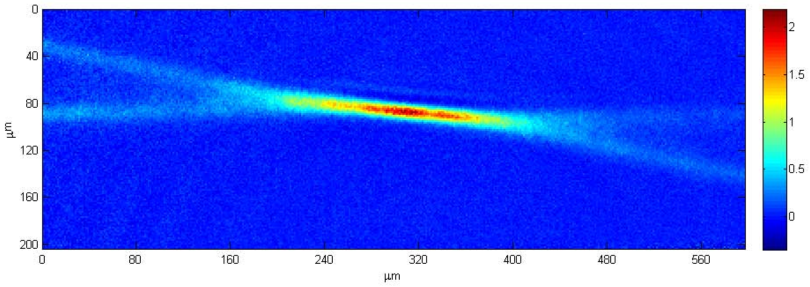

Figure 3.6: Absorption image of a ultracold cloud of ^{6}Li atoms in the crossed beam optical dipole trap.

Due to the absorption of photons from the imaging beam the atomic cloud heats up very quickly which destroys the ultracold sample. As a result, we have to prepare a new ultracold atom cloud after each imaging cycle. The images are usually taken either while the atoms are trapped in an optical dipole or magnetic trap or after switching off the trap and letting them escape for a time-of-flight (tof).

There are several things that we need to be careful about when we want to extract information from absorption imaging. First, the frequency of the imaging light needs to be resonant with the atomic transition. Second, we have to adjust the intensity and duration of the imaging pulse. If the duration of the imaging pulse is too long the atoms start moving during the image due to the photon recoil. This alters the measured density distribution. We usually use pulse durations of $\leq 10\,\mu$s in which the motion of the atoms is in most cases negligible. The intensity has to be chosen such that it is well below the saturation intensity and that the optical density of the atomic cloud is on the order of one. If the optical density is too high or too low, the signal to noise ratio is poor and it becomes difficult to extract meaningful information.

---

[3] Note that the obtained results are only reliable if the sample is thermal since the density distributions of a DFG or a mBEC differ from Gaussian distribution. In these cases, a more detailed analysis is necessary to determine the number of atoms, the temperature and the influence of the interaction between the atoms.

We will later see in chapter 6 that one underestimates the number of atoms if one images at intensities which are not small compared to the saturation intensity. A more detailed description and evaluation of these limitations can be found in [Ott10]. To guarantee that the imaging beam is resonant with the atomic transition, we have to precisely control the frequency of the imaging laser. The $S_{1/2}$-$P_{3/2}$ transition that we use for laser cooling and imaging has a natural linewidth Γ of about 5.8 MHz and a wavelength of about 671 nm (4.47×10^{14} Hz) [Geh03]. Thus the laser frequency needs to be controlled with a relative precision of better than 10^{-8}. We achieve this by actively stabilizing a tunable external diode laser (Toptica DL 100) using Doppler-free saturation spectroscopy (see e.g. in [Peh13]). All cooling and imaging lasers of both experimental setups in Heidelberg are locked to this so-called spectroscopy laser using beat offset locks [Sch99]. The obtained linewidth of the locked lasers are $\lesssim 1$ MHz and thus well below the natural linewidth. A typical absorption image of an ultracold cloud can be seen in figure 3.6.

3.4.2 Fluorescence Imaging

In fluorescence imaging the photons scattered from the atoms are collected with a lens and projected onto a camera. Since the photons are scattered uniformly into the full solid angle, the signal obtained by collecting fluorescent photons with an imaging system depends on its numerical aperture. If the intensity of the beam that excites the atoms is significantly larger than the saturation intensity, the scattering rate between atoms and photons becomes half the natural linewidth $\gamma/2 = \pi\,\Gamma = 18.45$ MHz. Additionally to the fraction of scattered photons reaching the detector due to the finite solid angle, we also have to take the transfer efficiency of the camera into account. This calibration number κ can be measured by shining a laser beam of well-defined intensity and the correct wavelength onto the camera and recording the number of obtained counts. Given a certain exposure time we can now deduce the number of atoms in a atomic cloud from the number of counts obtained by a camera that records the cloud's fluorescence. By choosing a longer exposure time, the number of collected photons increases and therefore the signal-to-noise ratio becomes larger. This fact makes fluorescence imaging very powerful for the detection of small atomic samples where the signal-to-noise ratio of absorption imaging inhibits reliable results. We therefore use fluorescence imaging to determine the number of atoms in the few-fermion samples produced in the ”old” experiment.

To be able to use long exposure times we need to make sure that the atoms are not lost from the sample while scattering photons. We therefore load the sample back into the MOT. There the atoms can scatter a large number of photons without being lost. This however leads to a loss of the spatial distribution the atoms had before. With MOT lifetimes of up to 250 s we are able to use exposure times of up to 500 ms without significantly lowering the efficiency of the detection. We decrease the amount of stray light that reaches the camera by making the MOT beams smaller and by compressing the MOT with a large magnetic field gradient of about 250 G/cm. Then

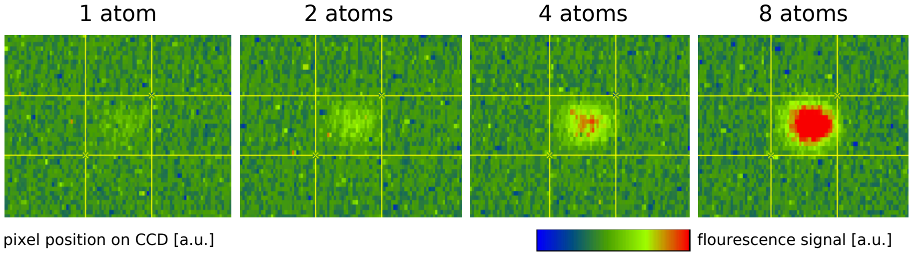

Figure 3.7: Fluorescence signal of few fermions in the microMOT. By integrating the signal inside the region of interest which is indicated by the yellow lines, one can clearly count single atoms. Taken from [Zür12a].

we can count single atoms with very high fidelity in this so-called microMOT [Ser11b]. As an example, fluorescence signals for 1 to 8 atoms recorded with the few-fermion experiment can be seen in figure 3.7. A more detailed analysis, the exact calibration factors and the estimated uncertainties can be found in [Ser11b, Ser11a].

3.4.3 Phase-Contrast Imaging

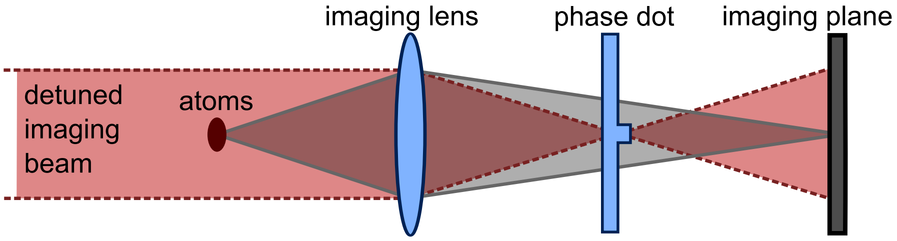

Figure 3.8: Schematic setup of phase-contrast imaging. The light that is scattered from the atoms (gray) obtains a small phase shift while passing through the cloud and is then imaged in the imaging plane. There it interferes with the unscattered light from the detuned imaging beam (red) which obtained a phase shift of about $\pi/2$ from the phase dot in the Fourier plane.

Another technique to extract information from an ultracold sample is called phase-contrast imaging. Opposed to the imaging techniques explained earlier, it is a non-destructive imaging method since it does not rely on absorption and scattering but on the phase imprinted on the imaging beam by the sample. The signal is obtained by interfering a beam which obtained a small phase shift ϕ_{atoms} while passing through the atoms with a beam that passed through a known dielectric medium. This idea is rather old and was originally developed by F. Zernike in the 1940s [Zer42]. In figure 3.8, the schematic idea of an imaging system for phase-contrast imaging of cold atomic samples is shown. The imaging beam used to illuminate the sample is significantly larger than the sample. Therefore, one can separate the incident imaging light into a part that is scattered from the atoms (gray) and a part that is not scattered (red). Due to the spatially varying refractive index of the sample the scattered light spreads and therefore the two parts of the beam have different opening angles. By adding an imaging lens, this difference in opening angle is translated in different focal positions. The focus of the unscattered imaging beam that was collimated before the imaging lens is in the Fourier plane. If we now add a dielectric medium of the correct thickness and refractive index, the phase of the unscattered beam is shifted by $\pi/2$ with negligible effect on the scattered beam. The interference of both parts of the beam can then be imaged on a camera in the imaging plane. Under the assumption that the phase shift from the phase dot is $\phi_{\mathrm{PD}} = \pi/2$ and that the atoms only lead to a small phase shift of the probe light ($\phi_{\mathrm{atoms}} \ll 1$), one can easily show (see e.g. [Guz12]) that the phase-contrast signal obtained on the camera is given by

$$|E_{\mathrm{final}}|^2 \,/\, |E_{\mathrm{in}}|^2 \simeq 1 + 2\,\phi_{\mathrm{atoms}}. \tag{3.5}$$

This means that by adding the phase dot to the setup we obtain a phase-contrast signal which is linearly proportional to the phase imprinted on the beam by the atoms. This is ideal to measure the properties of cold gases.

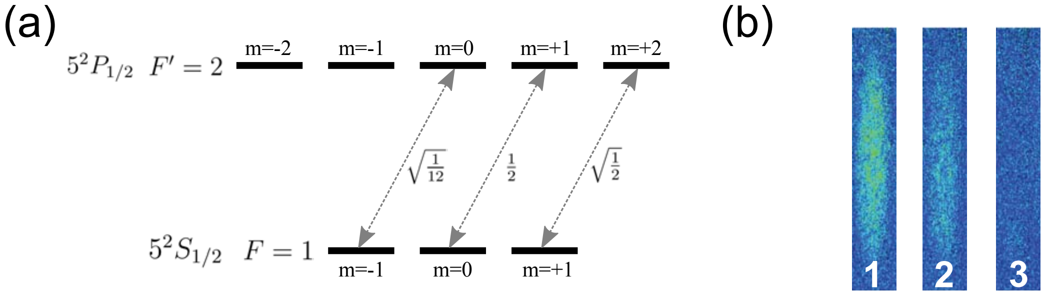

Figure 3.9: Magnetization sensitive phase-contrast imaging. (a) Level scheme of the relevant ^{87}Rb levels and their relative strength for σ^+-polarized light. (b) Phase-contrast images of the same ^{87}Rb BEC with all spins of the cloud pointing antiparallel (1), perpendicular (2) and parallel (3) to the imaging beam.

One can show [Hig05b] that ϕ_{atoms} and therefore the phase-contrast signal depends on the density of the sample and the magnetization of the atoms if one uses polarized imaging light. In the experiments described in chapter 5 we usually used σ^+-polarized light blue detuned ($\delta = -400\,\mathrm{MHz}$) from the $F = 1 \rightarrow F' = 2$ transition. As can be seen in figure 3.9 the coupling between the circularly polarized light and the atoms in $F = 1$ strongly depends on which substate the atoms are in. For atoms in the spin state antiparallel to the probe light ($m = +1$) the interaction strength is a factor of six larger than for atoms in the spin state parallel to the probe light ($m = -1$). As can be seen in figure 3.9 (b) one can measure the projection of the magnetization along the imaging axis of a Spinor gas using phase-contrast imaging. We will later show how we can use several of these projection measurements to determine the three-dimensional vector magnetization using Larmor precession or spin-echo imaging (see chapter 5).

Using phase-contrast imaging also has some drawbacks. The biggest issue is that the signal strength is not as pronounced as it is in absorption imaging. This is usually due to several problems. The density needed to obtain a good phase-contrast signal is rather high, furthermore one needs to be very careful to align the 250 μm size phase dot to the correct position. Therefore, we later implemented polarization-contrast imaging which does not rely on the use of a phase dot. In this imaging technique the signal is generated by the rotation of the polarization of the probe light. This is achieved by illuminating the sample with linearly polarized light. The linearly polarized light can be decomposed into a σ^+ and a σ^--component which acquire different phase shifts when passing through the atoms. One can then measure the rotation of the probe light by placing a polarizer rotated by 45° compared to the polarization of the incident probe beam. The obtained signal is then only dependent on the spin of the sample. Opposed to phase-contrast imaging there is no spin independent term in polarization-contrast imaging.

4 From Few to Many: Experiments with Finite Fermi Systems

> ”These few grains of sand do not constitute a heap, and the addition of a single grain never makes what is not yet a heap into a heap: so no matter how many single grains one adds it never becomes a heap”
>
> According to Eubulides of Miletus,
> *the sorites paradox* [sor13]

Yet we know that heaps of sand exist and they consist of an accumulation of single grains. This paradox illustrates the difficulties in finding the point where the description of a system through its individual constituents can be replaced by a description of an effective entity. In this case, the individual constituents are the grains of sand and the effective entity is the heap. One can also put it in simpler terms and ask, ”How many are many?”

A related question arises when investigating the theoretical description of physical systems. This is due to the fact that for physical systems a similar transition from the description of the single microscopic constituents to an effective description using macroscopic quantities is usually made. This is particularly interesting because in both limiting cases, the few and the many-particle limit, the theoretical treatment can be greatly simplified. In the few-body limit, the complete equations of motion that govern the behavior of each individual particle can be written down *and* solved. In the opposing limit, the many-body regime which is reached for a large number of particles, the approach of describing each single particle usually fails due to its growing complexity. Then a transition from a discrete to a continuous description of the system can be made. This significantly simplifies the theoretical considerations and many examples prove that such many-body approaches are extremely successful in the description of the macroscopic properties of large systems. The question that is related to the initially posed paradox and that even today still remains largely unanswered is: ”How large does a system have to be in order to be well described by the many-body solution?” One key reason why the answer to this question remains so elusive is that in most cases the few-body approach becomes prohibitively complex to solve before its results approach the many-body limit.

Using Helium droplets or in the context of nuclear physics this crossover from few to many-body physics has been experimentally investigated by measuring the emergence of superfluidity for an increasing number of particles [Mig59, Gre98]. Our approach to study this crossover is to use ultracold few-atom systems with tunable interactions and with control over the particle number N on the single particle level [Ser11b]. The idea behind our measurements is to investigate the influence of a growing number of identical fermions onto a single impurity particle. Hence, the impurity acts as a test particle that probes the influence of the majority particles. In our experiments, the impurity and the majority component are two distinguishable spin states of ultracold fermionic ^{6}Li atoms. Therefore, the many-body limit ($N \to \infty$) constitutes the fermionic quantum impurity problem, where one single fermionic atom in state $|\downarrow\rangle$ interacts with a Fermi sea of majority atoms in state $|\uparrow\rangle$ (see figure 4.1(c)).

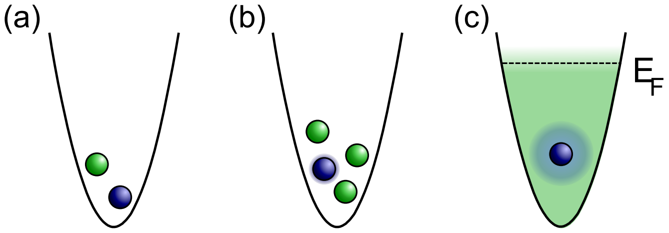

Figure 4.1: From few to many. A single impurity (blue) interacting with one, few and many fermions (green) in a harmonic trapping potential. In the many-body case, the majority component can be described as a Fermi sea with a Fermi energy $\mathrm{E_F}$. Figure and caption taken from [Wen13].

In this chapter, we will present that we can deterministically prepare few-fermion systems that consist of a single atom in one state and a growing number $N_\uparrow$ of majority atoms in state $|\uparrow\rangle$. Starting from the two-particle system ($N = 2$) that consists of one majority ($N_\uparrow = 1$) and one impurity atom ($N_\downarrow = 1$, see figure 4.1(a)), we investigate systems of up to 5 majority particles. We use RF spectroscopy to measure the influence of the repulsive interaction between the single impurity and the majority component as a function of the number of majority atoms.

Due to the low energy scales and the elongated shape of our trapping potential, our systems can be well-described using a one-dimensional framework [Ber03, Idz06]. For one-dimensional systems, there are analytical predictions both for the two-particle case [Bus98] of a single majority atom and for the many-particle limit of an infinite number of majority atoms [McG65]. We can thus compare the measured interaction energies to these theories. We start with a system of one majority atom and then increase the number of majority particles one by one. In this way, we study the convergence towards the many-body prediction of McGuire [McG65]. This means we can observe the formation of a Fermi sea atom by atom. These measurements in the crossover between few and many-body physics for a finite one-dimensional fermionic impurity system are published in [Wen13].

Outline

All the experiments described in this chapter were performed in the few-fermion machine (”old” experimental setup) in Heidelberg. We will start this chapter with an introduction to the theoretical background of one-dimensional systems in section 4.1. In particular, we present the theoretical predictions for one-dimensional two, few and many-particle systems and relate the obtained results to polaronic physics. In section 4.2, we describe how we deterministically prepare and observe few-fermion samples [Ser11b]. After introducing the measurement techniques, we present our studies of various few-fermion systems [Zür12b, Zür13a, Zür13b]. In section 4.5, we then demonstrate how we use RF spectroscopy in the resolved sideband regime to study the crossover from few to many-body physics with a finite fermionic impurity system [Wen13]. Some techniques and results presented in this chapter were already published and described elsewhere [Ser11b, Ser11a, Zür12b, Zür12a, Zür13a, Zür13b, Sal13b, Wen13]. We will still summarize and outline these results and follow the previous notation and arguments wherever it is helpful to comprehend the line of reasoning.

4.1 Theoretical Description of Few-Particle Systems

In this section, we will introduce the theoretical framework to describe fermionic few-particle systems. In our measurements we will investigate systems with $N = 1$ to 10 fermionic atoms in two distinguishable spin states. We will label these states $|\uparrow\rangle$ and $|\downarrow\rangle$ and the number of atoms in each state will be denoted by $N_\uparrow$ or $N_\downarrow$. This means the total number of atoms is given by $N = N_\uparrow + N_\downarrow$. In our experiments, these spin states are given by any two of the three lowest Zeeman sublevels $|1\rangle$, $|2\rangle$ and $|3\rangle$ of the electronic ground state of ^{6}Li (see figure 2.5). While fermionic atoms in the same state are identical and thus non-interacting, atoms in different states are distinguishable and can thus interact.

The just introduced systems are usually described by the following stationary many-particle Schrödinger equation [Arm11]

$$\left(\hat{K} + \hat{V}_{\text{trap}} + \hat{V}_{\text{int}}\right) \Psi(x_1, \ldots, x_N) = E\, \Psi(x_1, \ldots, x_N), \tag{4.1}$$

where $\Psi(x_1, \ldots, x_N)$ is the N-particle wave function, $\hat{K} = \sum_i \left(-\frac{\hbar^2}{2m} \nabla_i^2\right)$ is the kinetic energy operator, $\hat{V}_{\text{trap}}$ describes the trapping potential and $\hat{V}_{\text{int}}$ is the operator that describes the interaction between the particles. This Hamiltonian is very similar to the ones derived in chapter 2. However, in this chapter we will not use the second quantization framework.

As explained in detail in section 2.4.1, we will again approximate the van der Waals interaction potential by a δ function pseudo potential which reproduces the correct scattering phase shift. This approximation will not limit any of the performed measurements because the corrections due to the finite range of the interaction (r_{vdW}) are usually negligible. Most of the time, we will approximate the trapping potential by a harmonic potential. In this case, the Hamiltonian decouples into a center-of-mass term and a term that only depends on the relative distances between the particles. Because the interaction potential only depends on this relative distance, one can easily solve the center-of-mass term which is not affected by the interparticle interaction. This decoupling simplifies the solution of equations like the one given above (equation 4.1), especially for the case of two particles. The harmonic approximation of our trapping potential is usually very good but for some measurements we have to consider the small anharmonicities of our trap. As shown in [Sal13b], this anharmonicity can lead to a coupling between the center-of-mass and the relative motion.

In section 4.2, we will show that our trap is cigar-shaped and well-described by a harmonic potential. We label the harmonic trapping frequencies ω_r for the radial direction and ω_z for the axial direction[1]. Often we will also need the harmonic oscillator lengths $a_i = \sqrt{\hbar/(m\omega_i)}$, which can be obtained from the trapping frequencies ω_r and ω_z. The aspect ratio η of our trap is about 10 : 1 ($\eta = \omega_r/\omega_z \approx 10$). Due to this

---

[1] In some calculations we will use ω_{ax} or $\omega_\parallel$ instead of ω_z. For the radial direction we will also use $\omega_\perp$ instead of ω_r

large aspect ratio, we can actually use the one-dimensional framework to describe our few-particle systems if all energy scales (potential, kinetic and interaction energies) are small compared to $\hbar\omega_r$. For our systems, this is usually fulfilled because we only occupy the lowest axial states in the trap and the interaction energy is generally on the order of $\lesssim \hbar\omega_z$.

We will now introduce the one-dimensional description of ultracold atoms and deduce the one-dimensional coupling strength g_{1D}. Then we will investigate the interacting two-particle system which consists of one spin up ($|\uparrow\rangle$) and one spin down particle ($|\downarrow\rangle$). Afterwards, we will try to describe systems with more than two particles and finally investigate the case of an infinite number of spin up particles that interact with a single impurity particle ($|\downarrow\rangle$). At the end of this section, we will then relate and compare the obtained results to polaronic physics in two and three-dimensional systems.

4.1.1 From 3D to 1D Interaction

The few-particle systems we produce and investigate in this chapter are quasi one-dimensional. This influences the scattering processes between atoms and hence the interactions in these systems. We will therefore follow the reasoning laid out in [Ols98, Ber03, Idz06] and derive the one-dimensional coupling strength for a quasi one-dimensional system from the three-dimensional scattering length a_{3D}[2].

For a zero-range interaction potential and for a harmonic trap, it was shown in [Ols98, Ber03] that the one-dimensional coupling strength can be written as

$$g_{1D} = \frac{2\hbar^2\, a_{3D}}{m_r a_r^2}\, \frac{1}{1 - C\, a_{3D}/a_r}, \tag{4.2}$$

where $C = -\zeta(1/2) = 1.46\ldots$, $\zeta(x)$ is the Riemann zeta function, a_{3D} is the three-dimensional scattering length, $a_r = \sqrt{\hbar/(m_r\omega_r)}$ is the harmonic oscillator length and $m_r = m_{(^6\mathrm{Li})}/2$ is the reduced mass. From equation 4.2, it is easy to see that g_{1D} diverges for $a_r = C\, a_{3D}$. This scattering resonance is usually referred to as a confinement-induced resonance (CIR) and occurs when the scattering length a_{3D} is of the order of the harmonic oscillator length a_r in the tightly-confined radial direction.

For ^{6}Li atoms and the parameters of our confining potential, the CIRs occur between 660 G and 780 G dependent of the states involved. The behavior of the one-dimensional coupling strength as a function of the magnetic field for all scattering channels is shown in figure 4.2. Similar to the three-dimensional case, the scattering resonances allow us to freely tune the interaction strength of the system to almost arbitrary values by applying a magnetic offset field. Such confinement-induced resonances have already been studied using ultracold gases. Most of the time these measurements were performed with bosonic systems [Kin04, Hal09, Hal10a, Hal10b], but there were also some investigations using fermions [Mor05, Lia10]. We usually prepare non-interacting few-fermion

---

[2] In order to avoid confusion, we will explicitly state if we are considering the one or three-dimensional quantities.

systems in the motional ground state of the trap at the zero crossings of the coupling strength which occur between about 500 G and 600 G. The repulsive interactions are then introduced by increasing the magnetic field towards the CIRs.

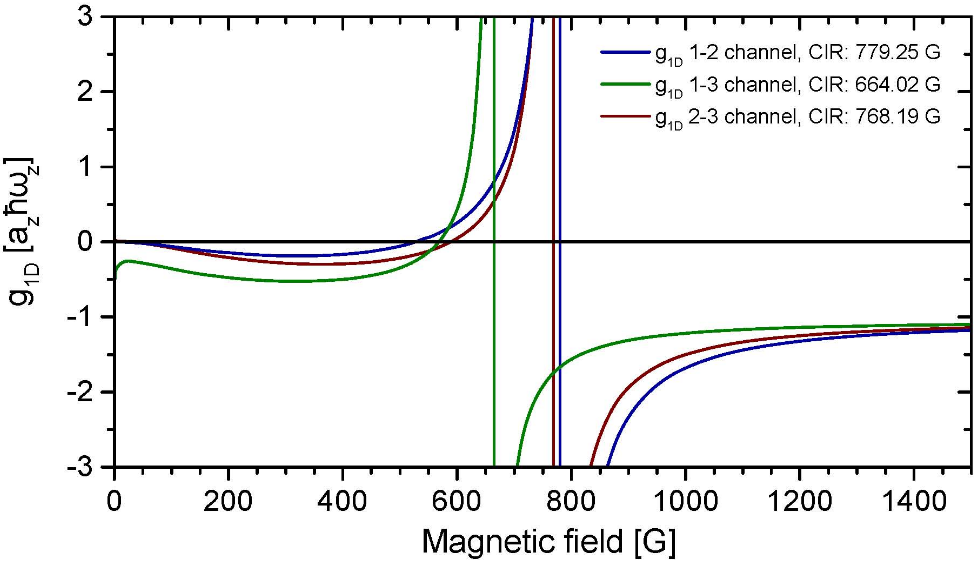

Figure 4.2: Magnetic field dependence of the one-dimensional coupling strength for a quasi one-dimensional system of ^{6}Li atoms in our trapping potential. All possible scattering channels ($|1\rangle$-$|2\rangle$,$|1\rangle$-$|3\rangle$ and $|2\rangle$-$|3\rangle$) exhibit a broad confinement-induced resonance (CIR). The resonance positions are given in the graph. To obtain g_{1D} we used equation 4.2 with $a_r = 0.49\,\mu$m and the scattering lengths as given in [Sca].

It is very instructive to analyze a one-dimensional system of two distinguishable particles ($N_\uparrow = N_\downarrow = 1$, see figure 4.3) in a harmonic trap across a CIR when the atoms are in the motional ground state. This kind of system can be solved analytically and one can calculate the wave function and the energy for arbitrary interaction strengths g_{1D} [Bus98, Idz06]. As we will later see, this relatively simple system qualitatively shows most of the relevant effects and phenomena necessary to gain a deep understanding of one-dimensional few and many-body systems.

4.1.2 The Two-Particle System

Let us consider a one-dimensional system consisting of two distinguishable particles ($N_\uparrow = N_\downarrow = 1$, see figure 4.3) interacting through a δ-function contact interaction in a harmonic trap. Following the notation of [Idz06], the Hamilton operator for such a system has the following form

$$\hat{H} = -\frac{\hbar^2}{2m}\left(\frac{\partial^2}{\partial z_1^2} + \frac{\partial^2}{\partial z_2^2}\right) + \frac{1}{2}m\omega_z^2\left(z_1^2 + z_2^2\right) + g_{1D}\,\delta(z_1 - z_2), \tag{4.3}$$

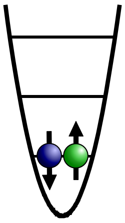

Figure 4.3: Two-particle system consisting of one particle in state $|\uparrow\rangle$ and one particle in state $|\downarrow\rangle$ without interaction.

where z_1 (z_2) is the position of the first (second) particle. The first term describes the kinetic energy, the second one describes the potential energy in the harmonic trap and the last term denotes the zero-range contact interaction with the coupling strength g_{1D}. Because the interaction term only depends on the relative distance between the two particles we can separate the Hamiltonian into a center-of-mass (COM) and a relative motion term. The COM coordinate is given by $R = (z_1 + z_2)/2$ and the relative coordinate by $z = z_1 - z_2$. The COM part of the Hamiltonian looks like a single non-interacting particle of mass $M = 2m$ in a harmonic potential and can therefore be solved easily. If we prepare non-interacting particles in the ground state of the trap, then the COM wave function will be described by a Gaussian. Even if we introduce interparticle interactions, this part will not be affected. This means that in the following we only have to consider the part of the Hamiltonian which depends on the relative distance between the particles. This part is given by

$$\hat{H}_{\text{rel}} = -\frac{\hbar^2}{2m_r}\frac{\partial^2}{\partial z^2} + \frac{1}{2}m_r\omega_z^2 z^2 + g_{1D}\,\delta(z), \tag{4.4}$$

where $m_r = m/2$ is the reduced mass.

It is useful to continue the calculations in dimensionless variables and therefore we write all energies in terms of $\hbar\omega_z$ and all lengths in terms of $a_z = \sqrt{\hbar/(m_r\omega_z)}$. By expanding the wave function into a complete set of orthogonal harmonic oscillator functions (see [Bus98, Idz06]), one can find an implicit relation for the relative energy $\mathcal{E}$ of the eigenstates of the system

$$-\frac{1}{g_{1D}} = \frac{m_r}{2\hbar}\frac{\Gamma(-\mathcal{E}/2)}{\Gamma(-\mathcal{E}/2+1/2)}, \tag{4.5}$$

with $\mathcal{E} \equiv \Delta E = E - E_0$, where E is the total energy of the relative motion, E_0 is the energy of the zero-point motion and $\Gamma(x)$ is the Euler gamma function.

Figure 4.4 shows the resulting energies of the lowest eigenstates as a function of the one-dimensional coupling strength g_{1D} (solid blue lines). For $g_{1D} > 0$ the ground state is given by the repulsive branch and for $g_{1D} < 0$ by the attractive branch. The CIR is located at $1/g_{1D} = 0$. The binding energy of the two-body bound state for $g_{1D} < 0$ (attractive branch) increases for more attraction and diverges at the CIR. It

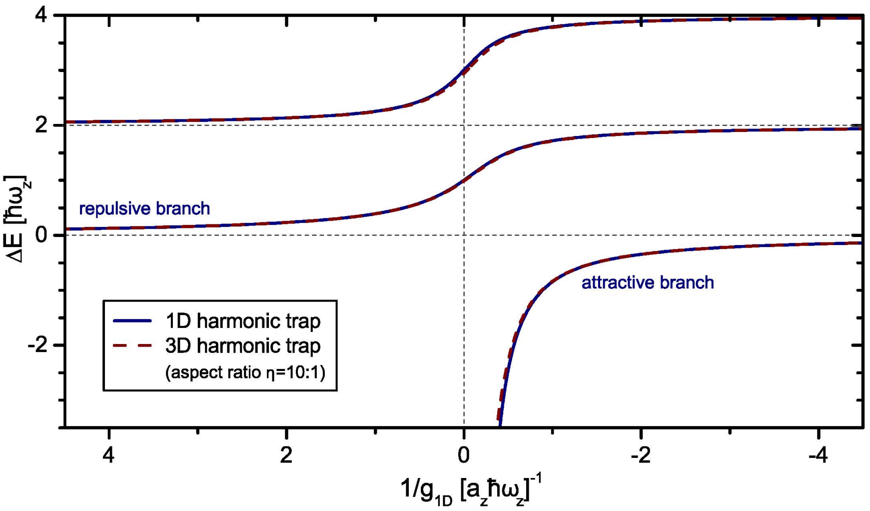

Figure 4.4: Relative energy $\Delta E = \mathcal{E}$ of the eigenstates of the two-particle system in a harmonic trapping potential. For a true one-dimensional system (solid blue line), the energy of the eigenstates is calculated according to equation 4.5 [Bus98]. The relative eigenstate energy for a three-dimensional system with an aspect ratio $\eta = 10$ is calculated according to [Idz06] and is shown as a dashed red line.

is important to note that in the true one-dimensional case this molecular state never crosses the CIR and is only defined for $g_{1D} < 0$ (see also section 2.6.1). We are going to perform most of our experiments on the repulsive branch and in the following we will therefore investigate it in more detail. First however, we are going to compare the results we just obtained using the 1D framework with a quasi 1D calculation of a three-dimensional harmonic trapping potential with an aspect ratio of $\eta = 10$.

Two Interacting Particles: 1D vs. 3D

It is also possible to calculate the eigenenergies of a three-dimensional system[3] trapped in a harmonic oscillator potential with an aspect ratio $\eta = 10$. This calculation is explained and performed in [Idz05, Idz06, Zür12a]. Using the relation between the three-dimensional scattering length and the one-dimensional coupling strength given in equation 4.2, we can also obtain the relative energy as a function of g_{1D}. The resulting eigenenergies for this anisotropic 3D system are shown in figure 4.4 as red dashed lines.

One observes that the difference between the 1D theory and the anisotropic 3D description is relatively small. The attractive branch of the 3D theory is only well described by the 1D calculation if the binding energy is small, i.e. smaller than $\hbar\omega_z$.

---

[3] For the 3D case, the δ function in the interaction term needs to be regularized in order to avoid divergences (see section 2.4.1).

For large attractive interactions $g_{1D} \to -\infty$, the molecular state is very deeply bound and the influence of the tight confinement in the radial direction decreases. In the limit of very large binding energies, one recovers the isotropic 3D solution and thus the one-dimensional theory is not a good approximation anymore. For the repulsive branch, the 1D theory agrees very well with the 3D model and the relative difference between both theories is below 1%[4]. This means that for experiments involving the repulsive branch we can simply describe our experimentally realized systems by the 1D theory. We will now present the predictions made by the one-dimensional framework and later we will use these results to describe and interpret our experimental data.

The Repulsive Branch of a 1D Two-Particle System and Fermionization

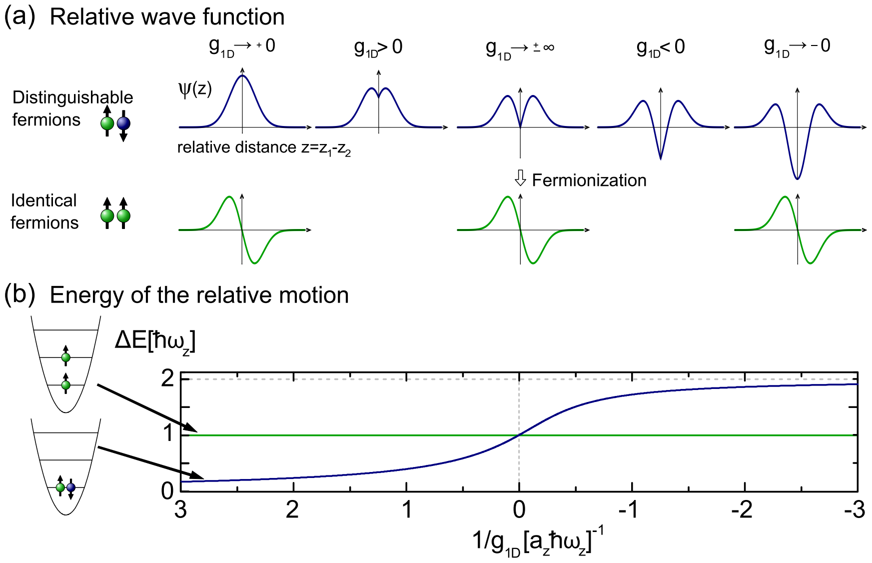

Figure 4.5: (a) Relative wave function of two interacting fermions (blue) and two identical fermions (green) in a 1D harmonic potential. For diverging coupling strength ($g_{1D} \to \infty$), the probability to find the two distinguishable fermions at the same position vanishes. In this case, the square modulus of the spatial wave function of two distinguishable fermions becomes the same as for two identical fermions. (b) The blue line shows the energy of the lowest repulsive branch of two interacting fermions in state $|\uparrow\downarrow\rangle$ as a function of the coupling strength g_{1D}. The green line shows the energy of two identical fermions in state $|\uparrow\uparrow\rangle$ and it crosses the energy for two interacting particles at the CIR. Figure and caption taken and adapted from [Zür12b].

For increasing repulsive interaction, the energy of the repulsive branch increases and for diverging coupling strength $1/g_{1D} \to 0^+$, the gain in relative energy is exactly $\hbar\omega_z$

---

[4] For higher excited states, the agreement decreases and the largest deviations are observed right at the CIR.

(see figure 4.5(b)). This means that at this point the energy of the two distinguishable interacting particles (in our case $|\uparrow\downarrow\rangle$) is equal to the energy of a system that consists of two identical fermions ($|\uparrow\uparrow\rangle$, see figure 4.5). This limit is called fermionization and was introduced several decades ago by Girardeau [Gir60] for the description of one-dimensional strongly repulsive bosons. Girardeau found that for 1D systems one can map a strongly interacting gas of bosons onto a system of non-interacting identical fermions[5]. For two distinguishable fermions, this mapping is not only correct for the energy of the system but is also true for the modulus square of the wave function (see figure 4.5). The wave function of the relative motion for this interacting two-particle system can be analytically calculated. Following [Gir10], one obtains

$$\psi_{rel}(z) = D_{\mathcal{E}}(z), \tag{4.6}$$

where ψ_{rel} is the wave function of the relative motion, $\mathcal{E}$ is the relative energy used in equation 4.5 and $D_{\mathcal{E}}$ are the parabolic cylinder functions. The relative wave function for a non-interacting system of distinguishable fermions is simply given by the lowest harmonic oscillator eigenstate. If we introduce a repulsive interaction ($g_{1D} > 0$), the particles start to repel each other. As a consequence, the probability of finding both particles at the same location ($z = 0$) decreases. This can be seen by the cusp that develops in the relative wave function shown in figure 4.5(a) as a blue line for $g_{1D} > 0$. At the CIR, the probability to find both particles at the same position vanishes ($\psi_{rel}(z = 0) = 0$) and the modulus square of the wave function becomes identical to the one for two identical fermions (green line in figure 4.5(a)).

The repulsive branch does not end at the CIR but crosses it and becomes an excited state of the system. This regime above CIR is called the super-Tonks regime [Hal09] and the interaction is often referred to as super-repulsive since the state is a continuation of the repulsive branch but is located on the attractive side of the CIR. As can be seen in figure 4.5(b), the system gains $2\hbar\omega_z$ of interaction energy if one follows the repulsive branch deep into the super-Tonks regime $g_{1D} \to 0^-$. There, the wave function of the relative motion becomes identical to the second excited harmonic oscillator wave function (see figure 4.5(a)). In this regime, the energy of this super-repulsively interacting system is twice as large as the energy of a system of identical fermions ($|\uparrow\uparrow\rangle$).

4.1.3 Few-Particle Systems

We will now consider few-fermion systems with more than two particles. The systems we investigate are still harmonically trapped, quasi one-dimensional and the interactions between atoms in different spin states are well-described by a zero-range pseudo potential. For $N > 2$, more than one atom will be in the same spin state and the

---

[5] In principle, this mapping between bosons and fermions for one-dimensional systems also works for intermediate coupling strengths. There however, the mapping does not significantly simplify the description of the system.

non-interacting ground state of the system is formed considering the Pauli exclusion principle for the identical fermions. This means that, for vanishing interactions, identical fermions will be located on different harmonic oscillator levels (see for example figure 4.6). Using the one-dimensional description, these kind of N-particle systems are described by the following Hamilton operator

$$\hat{H} = -\frac{\hbar^2}{2m}\sum_{i=1}^{N}\frac{\partial^2}{\partial z_i^2} + \frac{1}{2}m\omega_z^2\sum_{i=1}^{N} z_i^2 + g_{1D}\sum_{i<j}^{N}\delta(z_i - z_j), \tag{4.7}$$

where z_i are the spatial coordinates of the particles. For more than two particles there is no analytic solution for this Hamiltonian for arbitrary interaction strength g_{1D}. However, in recent years a strong effort was made to theoretically investigate these few-fermion systems using a vast amount of different approaches, like exact diagonalization or basis set expansion approaches [Mor04, Kes07, Gha12, Gha13, Sow13, Vol13, D'A13, Deu13, Cui13], Quantum Monte-Carlo techniques (QMC) [Bug13, Ast13], multiconfigurational time-dependent Hartree methods (MCTDH) for fermions [Bro13], analytical approximations and semi-analytical methods [Gir10, Ron12, Bro12, Bro13, Lin13]. These studies focused on various different subjects: the repulsive branch, fermionization of distinguishable fermions for more than 2 particles, spin correlations in the super-repulsive regime, differences between 1D and anisotropic 3D models, comparisons between numerical and analytical models, tunneling dynamics of few-fermion systems and attractively interacting systems.

The Three-Particle System

We will now start the description of few-fermion systems with $N > 2$ by considering the simplest non-trivial of these systems: the three-particle system with $N_\uparrow = 2$ and $N_\downarrow = 1$.

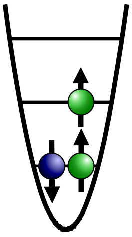

Figure 4.6: Three-particle system consisting of two identical fermions in state $|\uparrow\rangle$ and one atom in state $|\downarrow\rangle$ without interaction.

This particular system, which is sketched in figure 4.6, has already been thoroughly investigated by theorists (see for example [Mor04, Kes07, Gha12, Bro13, Gha13, Bug13, Lin13, Vol13, D'A13]). The eigenenergies calculated using various different approaches as a function of the one-dimensional coupling strength g_{1D} between the distinguishable particles[6] are shown in figure 4.7.

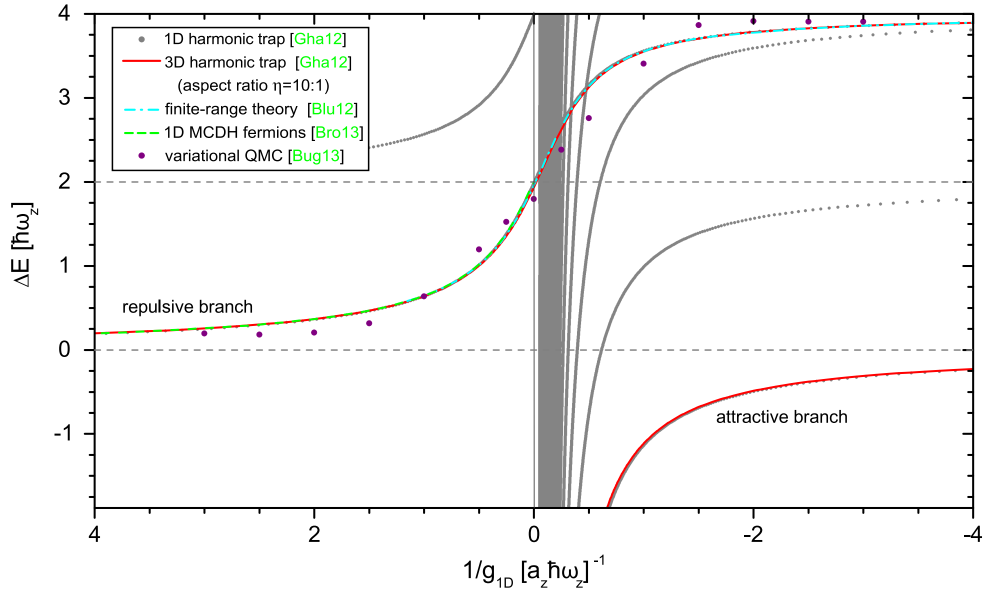

Figure 4.7: Comparison of the eigenenergies of the three-particle system calculated with various methods ([Gha12, Blu12, Bro13, Bug13]). For three particles the gain in energy when going from the non-interacting system to diverging coupling strength on the repulsive branch is $2\hbar\omega_z$. In the super-Tonks regime, the repulsive branch maximally reaches $4\hbar\omega_z$ for $g_{1D} \to 0^-$. The agreement between 1D and anisotropic 3D theory is again very good. One should note the large number of states, which include a two-body bound state, whose binding energies diverge for $1/g_{1D} \to 0^-$. These states cross the repulsive branch slightly above the CIR.

Due to our preparation scheme we are interested in the state with minimum energy for $g_{1D} \to 0^+$. The gray data points in figure 4.7 are the eigenenergies of the systems with odd parity and they were calculated using a basis set expansion approach [Gha12]. The structure of the eigenenergy spectrum is qualitatively similar to the two-particle case. There is a repulsive branch with energy $\Delta E = 0$ for $g_{1D} = 0$. The energy of this state increases for increasing repulsive interaction. At the CIR the energy of this state reaches $2\hbar\omega_z$ and thus the energy of the system is equal to the energy of a systems of three identical fermions (all in state $|\uparrow\rangle$) for a true one-dimensional system. This means that for $N > 2$ the concept of fermionization persists at least with respect to the energy of the system. The repulsive branch, calculated with the 1D theory (gray points), is again in very good agreement with the calculations for an anisotropic 3D system with an aspect ratio of $\eta = 10$ (red line in 4.7). The relative deviations between both

---

[6] The identical particles only obey the Fermi-Dirac statistic and do not interact at ultralow temperatures.

approaches is $\lesssim 2\%$. The finite-range theory developed by D. Blume [Blu12] (shown as the light blue dash-dotted line) and the MCTDH calculation [Bro13] (dashed green line) are also in good agreement with the 1D theory. The eigenenergies calculated with the variational quantum Monte Carlo approach (vQMC) qualitatively follow the same behavior but these calculations show some deviations from the other models.

Similar to the two-particle case, there is also an attractive branch. For small attractive interaction, the agreement between 1D theory (gray points) and anisotropic 3D model is again reasonable. Additionally, there is a multitude of states which include a two-particle bound state. In [Gha13], these states are referred to as " 'diving states,' reflecting the fact that the 1D δ function potential with negative g_{1D} supports a two-body bound state." It is important to note that for the anisotropic 3D theory and thus also for our experimental systems these states are not restricted to attractive interactions but also extend onto the other side of the CIR, where $g_{1D} > 0$. These states, which accumulate in the vicinity of the CIR, open inelastic loss channels because the particles can access lower-lying bound states by three-body recombination. This process releases so much kinetic energy that the atoms leave the trap. These inelastic three-body events were not possible in a two-particle system. In our experimental studies, we notice that, in agreement with this theoretical few-particle prediction, the inelastic loss probability close to the CIR increases strongly for increasing N.

There is also another type of states that has no equivalent in the two-particle system. The eigenenergies of these states have a similar dependence on the coupling strength g_{1D} as the repulsive branch. However, for $g_{1D} \to 0^+$ their energy ΔE does not approach 0. For more than two particles, there are different ways to adjust the symmetry between the different particles. For the two-particle system, there is only the totally antisymmetric or the totally symmetric spatial wave function. For $N > 2$, there are also states with mixed spatial symmetry. These states influence the wave function of the system at the CIR because at this point all states, no matter which exact symmetry they have, are degenerate in energy. Therefore, the state which is reached when adiabatically increasing the interaction strength and following the repulsive branch all the way to the CIR is not the fully "fermionized" one[7], which was predicted in [Gir10]. It is actually a combination of the different orthogonal states that are degenerate for $g_{1D} \to \infty$ [Gha13, Vol13]. This also explains why the fermionized wave function is indeed an eigenstate of the problem at the CIR. It is however not the wave function that is reached when gradually increasing the interaction strength on the repulsive branch [Gha13]. The energy of all these systems, independent of their symmetry, is still fermionized, i.e. it becomes equal to the energy of a state consisting of N identical fermions. The reason why the fermionized wave function works for the two-particle system is that for only two particles all states have either a totally symmetric or a totally antisymmetric spatial wave function.

---

[7] More details about this and the definition of the fermionized wave function can be found in [Gha13].

More Than Three Particles

There are different classes of few-fermion systems with more than three particles. These different types are shown in figure 4.8 and depending on the total number of particles and the number in each spin state, one can obtain impurity, balanced or imbalanced systems.

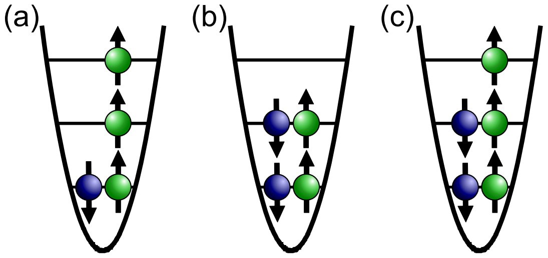

Figure 4.8: Few-particle system with $N \geq 3$. There are different types of few-fermion systems for $N > 3$. (a) Impurity system: For $N_\downarrow = 1$ the systems consist of a single impurity particle in state $|\downarrow\rangle$ and $N - 1$ majority particles in state $|\uparrow\rangle$. (b) Balanced system: For an even number of particles the system can have the same number of atoms in both states $N_\uparrow = N_\downarrow = N/2$. (c) Other imbalanced systems: For $N_\downarrow > 1$ and $N_\uparrow \neq N_\downarrow$, the system is neither an impurity system nor a balanced system.

Some of these configurations have already been theoretically investigated (for example in [Bro12, Gha13, Bro13, Bug13, Vol13, Lin13, Sow13]). The obtained eigenenergies of these systems exhibit a structure which is qualitatively similar to the one of the three-particle system. There is again an attractive branch and an even larger amount of states which include a bound state whose binding energy diverges close to the CIR. Therefore, the stability of the experimental realization of these systems is expected to become even smaller for growing N. There is also a repulsive branch and for $g_{1D} \to \infty$ the energy of this state again fermionizes to the energy of N identical fermions. For $N > 3$, there are even more states that become degenerate at the CIR and which have different symmetries [Gha13, Vol13].

For the measurements presented in this thesis, we are most interested in the repulsively interacting impurity systems (see figure 4.8(a)) and later we will compare our experimentally observed data to the calculated eigenenergies of these systems.

4.1.4 The Many-Body System

We will now consider the many-body limit, where a single impurity atom ($N_\downarrow = 1$) interacts with an infinite number of majority atoms ($N_\uparrow \to \infty$). We will slightly adjust our notation and define $N = N_\uparrow$. This means the total number of atoms in our system will now be $(N + 1)$. This is done in order to be able to use the same notation as in [Ast13, Wen13]. For a one-dimensional system in a harmonic trap, this system is described by the following Hamiltonian

$$H = \sum_{i=0}^{N} \left(-\frac{\hbar^2}{2m} \frac{\partial^2}{\partial z_i^2} + \frac{1}{2} m \omega_z^2 \, z_i^2 \right) + g_{1\mathrm{D}} \sum_{i=1}^{N} \delta(z_i - z_0), \tag{4.8}$$

where z_0 is the position of the single impurity atom, z_1 to z_N are the spatial coordinates of the N majority atoms, ω_z is the harmonic trapping frequency and g_{1D} is the one-dimensional interaction strength.

The Homogeneous Case

This problem can be analytically solved for a one-dimensional homogeneous system, i.e. $\omega_z \to 0$. Using the Bethe ansatz, J. McGuire was able to obtain an analytical solution for repulsive and attractive interactions in his seminal publications in the 1960s [McG64, McG65, McG66][8].

Using the line density $\rho = k_F/\pi$, where k_F is the Fermi wave vector of the majority component, we can define a dimensionless interaction parameter[9]

$$\gamma = \frac{m}{\hbar^2} \frac{g_{1D}}{\rho} = \frac{\pi m}{\hbar^2} \frac{g_{1D}}{k_F}. \tag{4.9}$$

Following the derivations of [McG65] and rewriting his results using γ, we obtain the following analytical form for the rescaled interaction energy of the $(N+1)$-particle system

$$\mathcal{E}_\infty = \Delta E/E_F = \frac{\gamma}{\pi^2} \left[1 - \frac{\gamma}{4} + \left(\frac{\gamma}{2\pi} + \frac{2\pi}{\gamma} \right) \arctan\left(\frac{\gamma}{2\pi} \right) \right], \tag{4.10}$$

where $E_F = \hbar^2 k_F^2/(2m)$ is the Fermi energy of the majority component.

This equation is valid both for attractive ($\gamma < 0$) and for repulsive ($\gamma > 0$) interactions and the resulting normalized interaction energy $\Delta E/E_F$ is shown in figure 4.9 as a function of γ. One again obtains a repulsive (orange line) and an attractive branch (green line) similar to the few-body cases. The attractive branch tends to $-\infty$ for large attractive interactions ($1/\gamma \to 0^-$). The repulsive branch again increases in energy for increasing repulsions between the atoms. For diverging coupling strength ($1/\gamma \to 0^+$), the energy reaches the Fermi energy of the majority component, which means that the energy of the system is the same as for a system of $(N+1)$ identical fermions. This means that even in the many-body limit for an infinite number of majority particles the concept of fermionization for the energy still persists. This was already understood by McGuire, who notes in [McG65]: "This result would be anticipated from the work of Girardeau [Gir60], who showed that particles interacting with infinite strength delta

---

[8] We will now, however, not use the notation used in [McG65], but follow the notation and definitions used in [Ast13, Wen13].

[9] This quantity is often called Lieb-Liniger parameter.

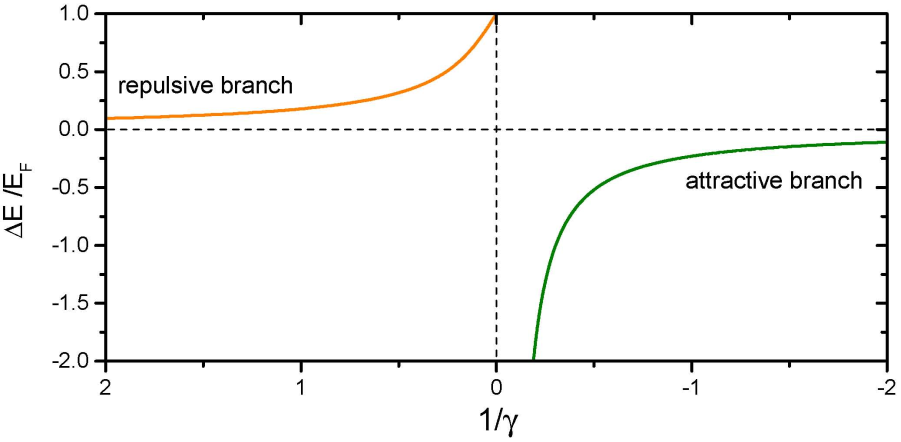

Figure 4.9: Normalized interaction energy as a function of the interaction parameter γ as predicted by McGuire [McG65].

function potentials in one dimension have a Fermi-like ground state independent of statistics."

The expression for the interaction energy, derived by McGuire and given in equation 4.10 only describes the ground state of the system. Therefore, it does not provide us directly with a solution of the repulsive branch in the super-Tonks regime. In [McG65], he does, however, also derive the effective mass m^* of the impurity particle and with our definition of γ his result can be written as

$$\frac{m^*}{m} = \frac{2}{\pi}\left[\arctan\left(\frac{2\pi}{\gamma}\right)\right]^2 * \left[\arctan\left(\frac{2\pi}{\gamma}\right) - \frac{2\pi}{\gamma}\Big/\left(1+\frac{4\pi^2}{\gamma^2}\right)\right]^{-1}. \tag{4.11}$$

The effective mass m^* describes the fact that due to the interaction with the medium the impurity becomes dressed with excitations of the surrounding particles. Thus, the impurity and its interactions can be described as an effective free particle of mass m^*. The effective mass divided by the bare mass of one fermion as a function of the repulsive interaction strength γ is shown in figure 4.10. As expected, the effective mass m^* is equal to the bare mass m for weak interactions. For increasing repulsion, the effective mass grows and diverges for diverging coupling strength $\gamma \to +\infty$.

There are also other calculations that reproduce the analytic results of McGuire using different methods. In [Gir09], they use an "approximate method developed in the three-dimensional case, where the Hilbert space for the excited states of the N fermions is restricted to have at most two particle-hole pairs" and recover the predictions by McGuire. The calculations of [Gir09] were performed to investigate the validity of their approximative method for the three-dimensional case. In three dimensions, the system consisting of one impurity immersed in a sea of fermions is generally treated in the quasiparticle picture of a Fermi polaron. Although one does not expect a well-defined quasiparticle operator for a one-dimensional system [Gua13], it is

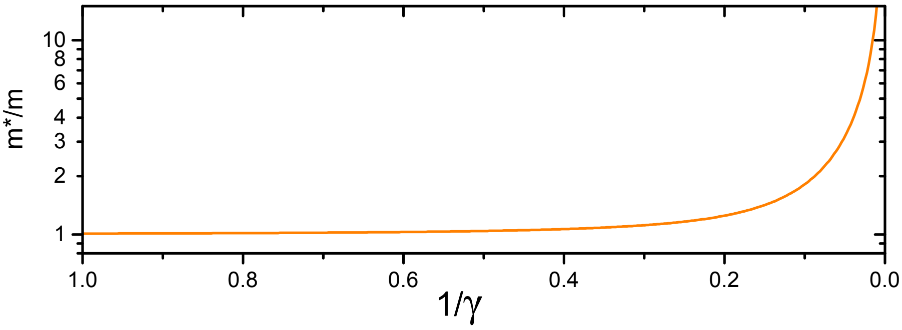

Figure 4.10: Effective mass m^* divided by the bare mass m as a function of the dimensionless interaction parameter γ as given in equation 4.11.

still interesting and instructive to relate the one-dimensional Fermi impurity problem [McG65, McG66] to the polaronic physics in two and three-dimensional systems (for example [Pro08a, Pro08b, Sch12a, Mas13]). This is particularly relevant since only recently Fermi polarons (both attractive and repulsive) were experimentally observed in two and three-dimensional systems [Sch09, Koh12, Kos12]. In the next section, we will therefore investigate this relationship and try to work out the similarities and the differences between one and higher-dimensional systems.

4.1.5 Connections to Polaronic Physics and Higher Dimensions

In the many-body case, where a single impurity is immersed in a Fermi sea of majority atoms we have only considered the one-dimensional theory so far. Due to the integrability of this one-dimensional problem, an analytical solution can be found [McG65]. For two and three-dimensional systems, such an analytical solution does not exist. Still, these fermionic impurity systems are of high interest in several fields of physics since the scattering on impurities and imperfections can strongly influence the behavior of solid state and condensed matter systems. Landau [Lan33] and Pekar [Pek46] already proposed that quasiparticles called polarons could be used to explain the properties of electrons inside a dielectric medium [Mas13]. Such a polaron can be thought of as an impurity which is dressed by the collective excitations of the surrounding medium. The description of impurity systems with polaronic quasiparticles was later extended to the fermionic quantum gases [Pro08a, Pro08b]. Since the first observation of Fermi polaron-like behavior in highly-imbalanced Fermi gases [Sch09], a large amount of both theoretical [Mas11, Sch12a, Mas13] and experimental work [Kos12, Koh12] has been dedicated to investigate such fermionic quantum impurity systems in two and three dimensions.

As shown in figure 4.11, the polaronic quasiparticles exist for both attractive and repulsive interactions. The energy of the repulsive polaron increases for increasing interaction strength. This repulsive polaron (shown in figure 4.12(a) as a red band and in (b) as a solid red line) is the higher dimensional equivalent of the repulsive branch

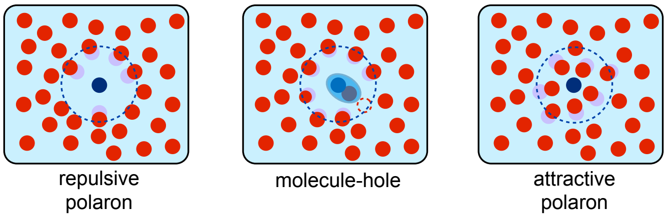

Figure 4.11: Possible states in a two or three-dimensional system of an impurity immersed in a Fermi gas. Figure and caption taken and adapted from [Mas13].

that we discussed earlier for one-dimensional systems. In the attractive case, one observes an attractive polaron up to a critical strength of the interparticle interaction. Then the impurity chooses to form a molecule with one of the majority particles. As shown in figure 4.12, a system which includes such a molecule and holes in the Fermi sea is located between the repulsive and attractive branch. This molecule-hole continuum leads to a finite lifetime of the repulsive polaron. Besides the interaction energy and the lifetime, there are also other characteristic quantities of the polaron, like the effective mass and the quasiparticle residue. The polaronic quasiparticle behaves like a free particle with mass m^*. According to [Sch10], the quasiparticle residue is related to the effective mass and quantifies the fraction of the bare impurity which is contained in the quasiparticle at momentum k .

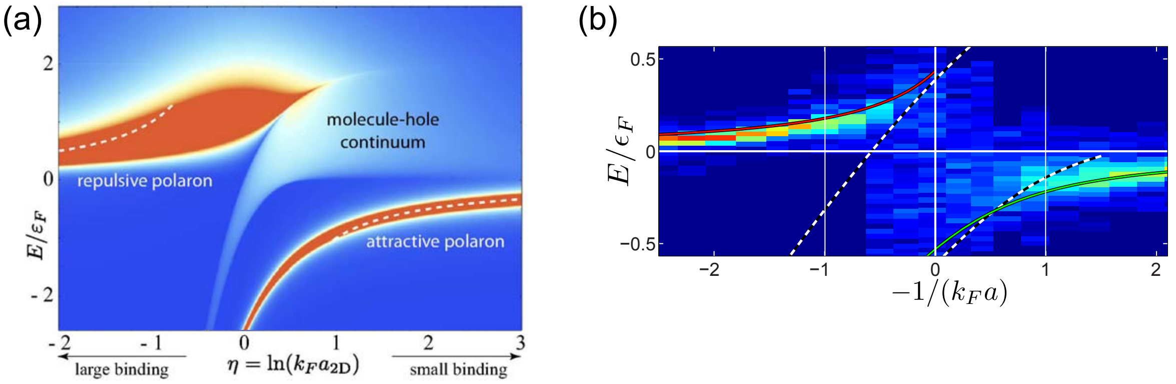

Figure 4.12: (a) Spectral function versus the interaction strength for a two-dimensional Fermi impurity system. Taken from [Sch12a]. (b) Excitation spectrum of a three-dimensional system of fermionic ^{40}K impurities in a bath of ^{6}Li atoms. Taken from [Mas13].

There is however a significant difference between the just described two and three-dimensional polaronic systems and the quantum impurity system in one dimension. While, for both 2D and 3D, these systems are described using Landau's Fermi liquid theory, this description breaks down for a one-dimensional system [Voi95]. Therefore, there is no well-defined quasiparticle operator [Gua13, Mas13] for a homogeneous one-dimensional system. Still, for weak attractive and repulsive interactions even in the 1D case, the dispersion relation of the interacting impurity particle can be described by a free particle with an effective mass m^* (see figure 4.10). This shows that at least some polaron-like behavior persists even in one-dimensional systems.

4.2 Deterministic Preparation of Few-Fermion Systems

In this section we will present our ability to deterministically prepare samples consisting of few fermionic ^{6}Li atoms with full control over their motional quantum state.

As illustrated in figure 4.13 (a), the idea behind our preparation scheme is to control the number of atoms by controlling the number of states present in a small volume optical dipole trap which we call the microtrap. This is possible because according to the Pauli exclusion principle only one fermionic atom per spin state can occupy each level of the microtrap.

Following [Ser11b, Ser11a, Zür12b, Zür12a], we will now go through the individual steps and introduce the techniques we use to prepare few-fermion samples with a very high reproducibility. To measure the success of our preparation technique, we define the preparation fidelity f as the number of realizations with the planned outcome N_p divided by the total number of prepared systems N_t. The goal is to obtain a fidelity $f = \frac{N_p}{N_t}$ as close to unity as possible.

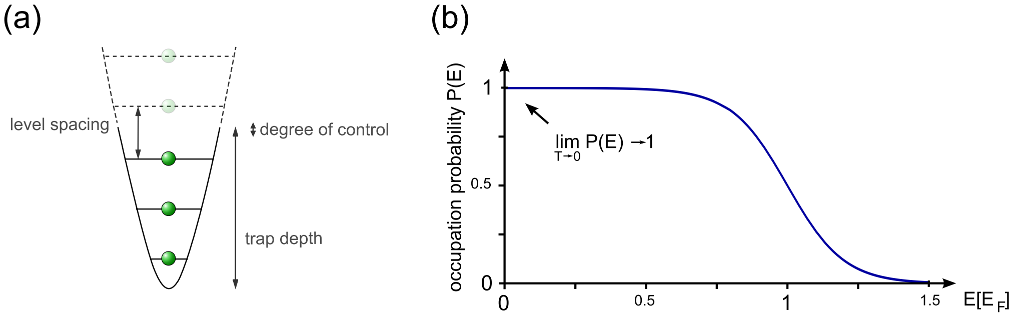

Figure 4.13: (a) In our preparation scheme, we control the number of particles by controlling the number of bound states in our microtrap. (b) In order to have no unoccupied states in the lower levels of the microtrap, the energy E of the fermionic systems must be significantly smaller than the Fermi energy E_F. This is achieved by using a highly degenerate Fermi gas where the occupation probability of the low-energy region tends to unity for $T/T_F \to 0$. Taken from [Zür12a].

4.2.1 The Cold Atoms Reservoir Trap

In order to load atoms into the microtrap we need a reservoir of cold atoms. These fermionic atoms obey the Fermi-Dirac statistics. Hence, the occupation probability $P(E)$ of the trap levels both in the reservoir and in the microtrap is given by the corresponding distribution function for fermions (see figure 4.13 (b) and equation 2.19). For a state with $E \ll E_F$ the Fermi-Dirac distribution function and thus the occupation probability approaches 1 for $T \ll T_F$. We do not want unoccupied trap levels far below the Fermi energy for our final sample inside the microtrap because this would limit the fidelity f for the preparation of few-fermion systems. Therefore, the reservoir has to be sufficiently cold in order not to be limited by these thermal excitations. We will later show that for this, it is sufficient for the reservoir to have a degeneracy of about $T/T_F \approx 0.5$. Furthermore, the sample should be large enough so that it is not significantly disturbed by the presence of the small volume microtrap. We achieve these requirements by using a large volume optical dipole trap created by the intersection of two focused laser beams red-detuned from the atomic transition.

In chapter 3, we explained how we produce an ultracold sample in such a crossed-beam optical dipole trap and the reservoir used to fill the microtrap is created in a very similar fashion[10]. The waist of the trapping beams is $40\,\mu$m, they intersect at a crossing angle of about 15°, the trapping laser has a wavelength of 1070 nm and therefore the final trap is cigar-shaped and the long axis lies in the horizontal plane. Using a sequence similar to the one shown in figure 3.2 with the final optical evaporation at 300 G, we obtain a two-component degenerate Fermi gas consisting of atoms in state $|1\rangle$ and $|2\rangle$ with about 20 000 atoms per spin state. At the final trap depth the trapping frequencies are $\omega_r = 2\pi\,370\,\text{Hz}$ and $\omega_z = 2\pi\,34\,\text{Hz}$ in radial and axial direction, respectively. The temperature of the atoms in the reservoir is $T \lesssim 250\,\text{nK}$ which corresponds to $T/T_F \approx 0.5$.

4.2.2 The Microtrap

The next step in the preparation of a few-fermion system is the transfer of a small fraction of atoms from the reservoir trap to the microtrap.

Design Criteria

In order for our preparation scheme (see figure 4.13(a)) to work, it is necessary to control the depth of the microtrap with significantly higher precision than the level spacing in the microtrap. The precision with which we can control the trap depth is given by the relative intensity stability of the microtrap beam. Using a well adjusted PID loop [Ser11a, Zür12a], we can reach relative intensity stabilities of about 10^{-3}. A

---

[10] The main difference is that the reservoir is created by the intersection of two round laser beams and not by elliptical ones as described in chapter 3. More details on the initial cooling and trapping stages used in the "old" experiment can be found in [Ser11a, Ser11b, Zür12a].

deterministic preparation therefore only becomes possible when the level spacing of the microtrap is sufficiently large. Therefore, we need to understand how the level spacing changes with the size of the focus. For a single beam optical dipole trap like ours, the confinement in radial (axial) direction is set by the focal waist w_0 (the Rayleigh range $z_R = \frac{\pi w_0^2}{\lambda}$) of the trapping beam. According to [Gri00, Zür12a], such an optical trap can be harmonically approximated and the obtained radial and axial trapping frequencies are given by

$$\omega_r = \sqrt{\frac{4V}{m w_0^2}} \quad \text{and} \quad \omega_z = \sqrt{\frac{4V}{m z_R^2}}, \tag{4.12}$$

where V is the trap depth and m is the mass of a ^{6}Li atom. It is now easy to see that the level spacing $\hbar\omega$ increases for smaller waists w_0. This means that it is beneficial for the preparation fidelity to have a focal waist which is as small as possible.

The Microtrap Setup

When designing an optical setup one has to bear in mind that a smaller focus requires a more elaborate design, a more precise manufacturing procedure and a more careful alignment of the focusing objective. Therefore, we chose a setup which is able to create a focus with a waist $w_0 \approx 1.8\,\mu$m and this represents a reasonable compromise between price, effort and achievable spot size. Figure 4.14 shows the objective with a numerical aperture (NA) of about 0.36 which created the microtrap that was used to record the data described in this thesis[11]. A detailed description of the design, construction and characterization of this objective can be found in [Ser11a]. It consists of an aspheric lens ($f = 40$ mm from Thorlabs) and a meniscus lens ($f = 800$ mm from JML Optical), which compensates for the fused silica vacuum window with a thickness of about 6 mm.

As illustrated in figure 4.14, the long axis of the microtrap is in vertical direction since we use the high NA reentrant viewport on the upper side of the main chamber. Therefore, the microtrap is perpendicular to the large volume reservoir trap whose long axis lies in the horizontal plane.

Loading of the Microtrap

We adiabatically ramp on the microtrap potential to transfer the atoms from the reservoir trap to the microtrap. To minimize the induced heating by the change of the potential shape we use a quadratic increase of the microtrap depth as a function of time. The timescale for this ramp τ is chosen such that it is significantly longer than the inverse trapping frequency ($\tau \gg 1/\omega$) and usually the complete ramp to full power takes about 120 ms. More information about and a quantitative analysis of the adiabaticity criterion can be found in [Ser11a]. During this intensity ramp the magnetic

---

[11] After the data presented in this thesis had been taken, the setup moved into the new labs at the University of Heidelberg and subsequently we implemented a new microtrap setup with an even smaller spot size [Ber13].

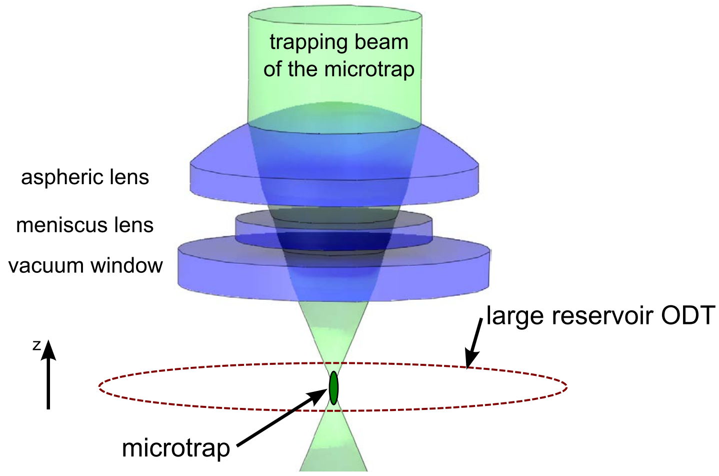

Figure 4.14: Schematic setup of the microtrap which is created by the focus of a single infrared laser beam using an objective with a numerical aperture NA≈ 0.36. Both the reservoir trap (dark red dashed line) and the microtrap (solid dark green ellipse) have an aspect ratio $\eta = \omega_r/\omega_z \approx 10$. Their orientation is indicated in the picture, the sizes and aspect ratios shown are not to scale. Adapted from [Ser11b].

offset field is held at 300 G where the scattering length in the $|1\rangle$-$|2\rangle$ channel is about $-290\,a_0$. This leads to thermalization in the combined potential through elastic scattering events. Additionally, we hold the cloud for another 20 ms at this magnetic field to be sure that the sample has completely thermalized.

The degeneracy T/T_F of the system in the combined trapping potential of the reservoir trap and the microtrap is significantly lowered due to the increase of the Fermi energy at nearly constant temperature which occurs when we turn on the microtrap. This effect is often called the dimple trick (see for example [Sta98b, Ser11a]). When we assume that the temperature of the atoms is not increased during the transfer then the gas in the combined trap is still at $T \lesssim 250\,\mathrm{nK}$. Before the transfer, the Fermi energy of the gas was determined by the depth of the reservoir trap V_{res}, in the combined trap however it is almost completely determined by the depth of the microtrap V_{MT} (see figure 4.15(a)). The gain in Fermi energy can thus be estimated to be $V_{\mathrm{MT}}/V_{\mathrm{res}} = 3.3\,\mu\mathrm{K}/0.5\,\mu\mathrm{K}= 6.6$. This means that we obtain $T/T_F \approx 0.08$ in the microtrap when we start with a degeneracy of $T/T_F \approx 0.5$ in the reservoir. Therefore, the calculated occupation probability of the lowest state in the microtrap is 0.9999 [Ser11b, Ser11a] and hence the unoccupied states due to the finite temperature should not constrain our preparation fidelity.

After the additional 20 ms of equilibration time, the magnetic offset field is ramped to 523 G which is close to the zero crossing of the scattering length. Then the interaction between the atoms is negligible[12] and we can turn off the reservoir trap without affecting

---

[12] For this magnetic field value, the scattering length is $a = -14\,a_0$.

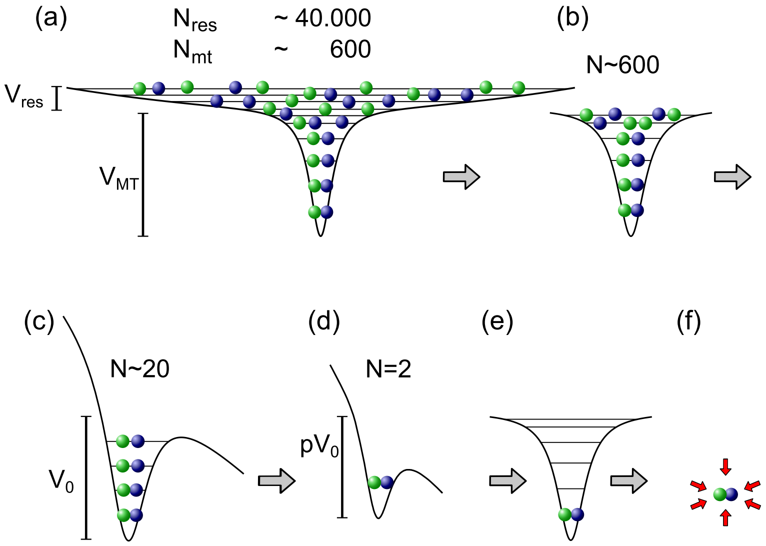

Figure 4.15: Illustration of the different stages of the deterministic preparation of few-fermion samples. After loading the microtrap from the reservoir (a),(b) we use a magnetic field gradient to deform the trapping potential (c) such that only about 20 atoms are left in the microtrap. We then change the depth of the microtrap potential to deterministically prepare few atom samples (d),(e) which are then counted by recording the fluorescence of the atoms in a MOT (f). Taken and adapted from [Zür12a].

the atoms in the microtrap. We are then left with about 600 non-interacting atoms in two different spin states ($|1\rangle$ and $|2\rangle$) in the microtrap (see figure 4.15(b)).

The Microtrap Potential

We noted earlier that the confinement in the radial direction is determined by the focal waist of the trapping beam w_0 and the axial confinement is determined by the Rayleigh length z_R. Close to the maximum of the intensity we can approximate[13] the optical potential of the microtrap by the following form

$$V_{\mathrm{MT,opt}}(x,y,z) \approx V_r(x) + V_r(y) + V_z(z), \tag{4.13}$$

where the radial part (V_r) and axial part (V_z) of the potential are given by

$$V_r(x_i) = V_{0r}\left(1 - e^{-\frac{2x_i^2}{w_{0s}^2}}\right) \quad \text{and} \quad V_z(z) = V_0\left(1 - \frac{1}{1+(z/z_R)^2}\right). \tag{4.14}$$

---

[13] In principle, the optical potential can not be written as a sum of independent parts, but since we will later mostly only consider the axial direction, the error we make is on the order of the anharmonicity correction which is on the percent level.

Using precise measurements of the level spacings and WKB calculations (more details in [Ser11a, Zür12a] and in section 4.3.1) we obtain that our optical potential is well described by $w_{0s} \approx 1.6\,\mu$m, $z_R = \frac{\pi w_0^2}{\lambda}$ and $w_0 \approx 1.838\,\mu$m. Using a harmonic approximation, we obtain an aspect ratio of the trapping frequencies of $\eta = \omega_r/\omega_z \approx 10$. This means that the energetically lowest ten states are in the radial ground state and we only need to consider radial excitations above these levels. This will later become an important fact since it will allow us to describe all systems which never populate radially excited states in a quasi one-dimensional framework (see section 2.6).

4.2.3 The Spilling Process

To further decrease the number of atoms in the microtrap in a controlled way, we apply a linear magnetic field gradient in the z-direction (along the long axis of the microtrap). This is done by generating a magnetic quadrupole field using the MOT coils. Due to their high inductance, it takes about 150 ms until the current through these coils reaches its final value and the final field strength is measured to be 18.9(2) G/cm [Ser11b]. The linear gradient, which is acting on the almost non-interacting two-component Fermi gas at 523 G, deforms the trapping potential as shown in figure 4.15(c). After the gradient has reached its final value we wait for another 20 ms to ensure that all now untrapped atoms have enough time to leave the region of the microtrap. At the end of this procedure only the lowest 10 states are still bound in the trapping potential and the number of atoms is about 20. The reason why we perform this spilling with a non-interacting sample is that we want to avoid interaction effects like correlated tunneling. After the magnetic field gradient has reached its final value, the combined potential of the optical microtrap and the magnetic field gradient has the following form[14]

$$V_{\mathrm{MT}}(z) = V_{\mathrm{ax}}(z) + V_{\mathrm{mag}} = p\, V_0 \left(1 - \frac{1}{1 + (z/z_R)^2}\right) - \mu B'\, z, \qquad (4.15)$$

where $V_0/k_B \approx 3\,\mu$K is the depth of the optical potential, p is the fraction of the total depth, $z_R = \frac{\pi w_0^2}{\lambda}$ is the Rayleigh length with $w_0 \approx 1.838\,\mu$m, μ is the magnetic moment of the atoms and $B' = 18.9(2)$G/cm is the magnetic field gradient.

The second step in the spilling process, which fine tunes the atom number, is performed by lowering the fraction of the total power p of the optical microtrap potential. In this way, we can create samples where only the lowest state of the trap is still occupied (see figure 4.15(d)). The optical power is linearly ramped down from the initial value of $p = 1$, which corresponds to 291(5) μW, to about 65% to 85% of the original depth ($p \approx$ 0.65-0.85). This ramp takes 8 ms and after reaching the final trap depth we wait for another 25 ms to make sure that the unwanted atoms escape. Afterwards, we increase the power back to its initial value ($p = 1$) within 8 ms in a second linear

---

[14] Since all atoms left in the trap are only in the radial ground state we will from now on only consider the potential in the axial direction and neglect the radial part of the potential.

ramp. Now we have created a few-fermion sample and to deduce the fidelity of this preparation scheme, we need a reliable way to measure very small atom numbers. This single atom detection uses the fluorescence imaging technique introduced in chapter 3 and we will now present it in more detail.

4.2.4 High-Fidelity Single Atom Detection

In order to analyze the prepared few-fermion systems we need a very efficient and reliable way to measure the small number of atoms in the microtrap. We achieve this by catching the atoms in a magneto-optical trap (MOT) and recording their fluorescence signal (see section 3.4.2 and [Hu94, Ser11b]) after releasing them from the microtrap potential (see figure 4.15(f)). The fluorescence signal is recorded on a CCD camera and given sufficiently long exposure times we can distinguish the number of particles with single particle precision.

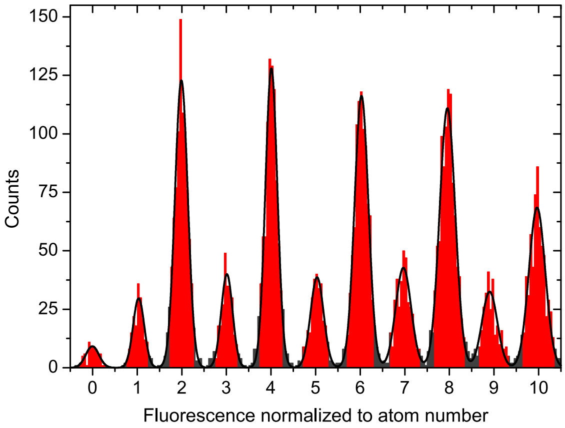

Figure 4.16: Histogram of the rescaled fluorescence signal obtained in the experimental run shown in figure 4.17, where we record the number of atoms as a function of the final optical trap depth p. The distinct peaks correspond to integer atom numbers and they can be fitted by Gaussians (black lines). The peaks are separated by about 6σ and all data within the 2σ region of a peak is binned to the corresponding integer number (red). All counts outside this region (dark gray) are rejected. From this kind of measurement one can deduce a detection fidelity of at least 98(1)%. Taken and adapted from [Ser11b].

There are several important issues that one has to consider for this scheme to work properly. First, in order to be able to use long exposure times, the lifetime of the sample in the MOT needs to be large compared to the exposure time. For our MOT, we have lifetimes of about 250 s and thus we are limited to an exposure time of $t_{exp} \leq 500\,\text{ms}$ in order to achieve a lifetime limited detection fidelity larger than 99%. We also need to increase the MOT light scattering rate to record sufficient photons to be able to distinguish the fluorescence signal of single atoms. This is achieved by operating the MOT at high intensities close to the saturation intensity and additionally the detuning of the MOT light from the atomic resonance is chosen to be comparatively small. A second issue is stray light that reaches the camera and thus inhibits a reliable determination of the atom number. Therefore, the amount of stray light that reaches the camera needs to be minimized. This is achieved by decreasing the size of the MOT beams (diameter $\approx 4\,\mathrm{mm}$) and applying a relatively large quadrupol field ($250\,\mathrm{G/cm}$). This decreases the volume of the MOT and therefore lowers the accumulated stray light at the position of the atoms on the camera. Finally, the intensity and the detuning of the MOT beams slowly vary on a few percent level over the timescale of several minutes. This effect would lead to a slow change in the normalization from fluorescence counts to number of atoms and would thus make it difficult to compare data taken over long periods of time. This drift is compensated by using a running average over an adequate number of previous and following experimental realizations[15]. More details on the precise parameters and techniques and a more quantitative analysis of the properties of the detection MOT are given in [Ser11a] or in the supporting material of [Ser11b].

For a given series of measurements, we can bin the obtained fluorescence signals into a histogram like the one shown in figure 4.16. For this particular run, we recorded the fluorescence signal as a function of the fraction of the optical trap depth p. One clearly observes distinct peaks which correspond to integer atom numbers and these can be fitted by Gaussians. The separation between the peaks is about 6σ and we bin the values within 2σ of an integer peak to the respective atom number. The remaining realizations which account for roughly 5% (gray bars in figure 4.16) are rejected. Because the preparation and the detection are independent, this does not affect the final outcome of the experiments. The reason why even atom numbers occur more often in the histogram is related to the fact that the measured trap depths where not equally spaced and we measured more values that led to even numbers in the trap. Additionally, each trap level is occupied by two atoms (one in each spin state) and this further increases the probability to measure even atom numbers more often.

The overall detection fidelity we obtain using the just described technique is 98(1)% per particle. We will now use this technique to determine the fidelity with which we can prepare the desired few-fermion systems using the spilling scheme described before.

4.2.5 The Preparation Fidelity

As illustrated in figure 4.15(c)-(f), the number of particles that remain trapped in the microtrap after the spilling process depends on the fraction p of the optical trap depth. We can now utilize the just introduced single atom detection method and measure the mean number of atoms as a function of the trap depth p. The result of such a measurement is shown in figure 4.17. For each trap depth p, we averaged

---

[15] In almost all cases, the running average over 10 previous and 10 following measurements seems to be sufficient.

about 190 measurements and the variance of these measurements is shown as green squares in figure 4.17. One observes that the mean atom number decreases for smaller trap depths p. Furthermore, one notes that there are plateaus for even atom numbers which are caused by the double occupancy of each trap level. At these trap depths the variance and thus the atom number fluctuation is strongly suppressed. A comparison to a system obeying Poissonian statistics shows that we measure a suppression of the number fluctuation of 18 dB of variance over mean [Ser11b].

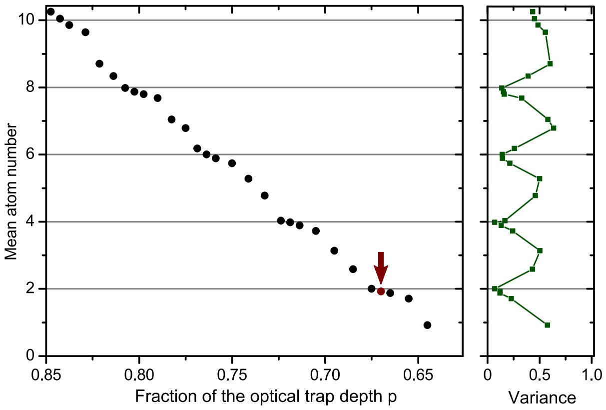

Figure 4.17: Dependence of the mean number of atoms on the fractional trap depth p. Each point is the average of 190 measurements. For even atom numbers we observe a strong decrease of the number fluctuation which is shown by the suppression of the variance at these trap depths. Taken and adapted from [Ser11b].

We can now also bin the observed fluorescence signals for a fixed p into a histogram. For the fractional trap depth which produces mostly two atoms in the ground state of the trap (indicated by the red arrow in figure 4.17) this histogram is shown in figure 4.18(a). It shows that the preparation fidelity f for such a system is almost unity (96%) and only in 2% of the measurements we prepare either 1 or 3 atoms. If we choose a fractional trap depth of about $p = 0.8$ which mostly leaves 8 atoms in the trap, we still observe a preparation fidelity of 87% (see figure 4.18(b)). By combining a second spilling process and a combinatorial model we can deduce that the probability of producing the two (eight) atom system in the ground state is 93(2)% (84(2)%) [Ser11b]. If we delay the second spilling process by a variable hold time, we can also show that the $1/e$-lifetime of the two atoms in the ground state of the trap is about 60 s.

4.2.6 Imbalanced Samples

So far we have shown that we are able to prepare an even number of fermions with a very high fidelity in the ground state. By using the magnetic field dependence of the magnetic moment μ for the fermionic atoms we can also prepare imbalanced samples. Figure 4.19(a) shows that the difference in magnetic moments for atoms in state $|1\rangle$ and

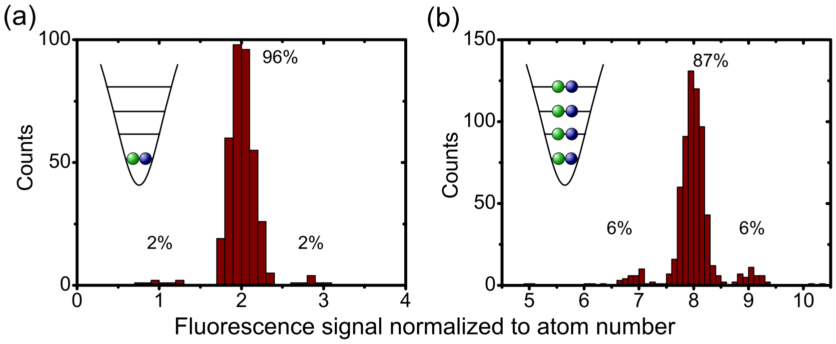

Figure 4.18: Histogram for the determination of the fidelity for a two (a) and eight (b) atom system. Taken and adapted from [Ser11b].

$|2\rangle$ is less than one per cent for magnetic fields larger than about 550 G. In the low-field regime however the magnetic moments differ significantly. The magnetic moment of atoms in state $|2\rangle$ vanishes for a magnetic offset field of about 27 G (vertical green line in figure 4.19(a)). Hence, at this magnetic field value the atoms in that state do not feel a force due to the magnetic field gradient. If we now perform an additional spilling process close to this magnetic field, only the atoms in state $|1\rangle$ are spilled from the trap and the ones in state $|2\rangle$ remain unaffected (see figure 4.19(b)). Using Landau-Zener sweeps or π-pulses after the spin selective spilling process, we can invert the population imbalance or transfer one of the spin populations to a different hyperfine state.

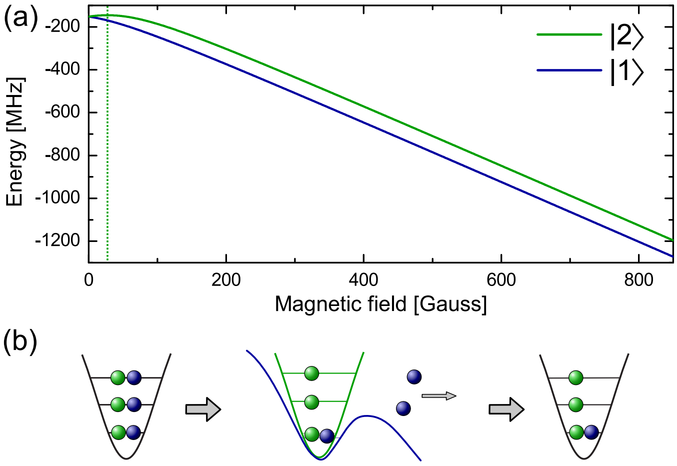

Figure 4.19: (a) Magnetic field dependence of the Zeeman energy for state $|1\rangle$ and $|2\rangle$. At about 27 G the magnetic moment μ of atoms in state $|2\rangle$ vanishes (indicated by dashed green line). (b) We can produce imbalanced few-fermion systems when the spilling process is performed close to this magnetic field value. There, the atoms in state $|2\rangle$ do not feel the force due to the magnetic field gradient and only the atoms in state $|1\rangle$ are spilled. Taken and adapted from [Ser11b, Zür12a].

Such a spin selective spilling process can further be used to perform state selective detection. We obtain the number of atoms in state $|2\rangle$ by counting the number of atoms left after removing all atoms in state $|1\rangle$ with a state selective spilling process. By comparing this result to the total number of atoms without the additional spin selective spilling process we can also determine the number of atoms that initially were in state $|1\rangle$. This scheme can again be generalized to all three Zeeman states by performing appropriate Landau-Zener sweeps or radio-frequency π-pulses.

4.3 Measuring the Energy of Few-Fermion Systems

In the next step, we are going to characterize the potential of the microtrap by measuring the single particle trap levels for non-interacting systems using sinusoidal modulations of the trap depth and trap position. The parameters we obtain from these measurements are essential for the determination of the interaction strength and thus the interaction energy of our systems. Afterwards, we will show that we can use the tunneling through a well-defined potential barrier to determine the interaction energy of few-fermion systems. For distinguishable fermions with repulsive interactions, we reach the fermionization limit and can even enter the Super-Tonks regime. The results presented in this section were published in [Zür12b, Sal13b, Zür12a].

4.3.1 Trap Modulation Spectroscopy

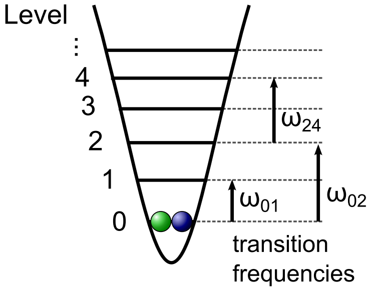

Figure 4.20: Definition of the trap levels and the transition frequencies between them in the slightly anharmonic microtrap.

The microtrap is created by the focus of a Gaussian beam. Therefore, the optical part of the microtrap potential is not perfectly harmonic. This means that the trap levels are not equally spaced as in a perfectly harmonic potential but their energy difference becomes smaller for higher energies (See figure 4.20). This effect is further enhanced by the addition of the magnetic field gradient. Consequently, the energy difference $\hbar\omega_{z,02}$ between the axial levels 0 and 2 is larger than the energy difference $\hbar\omega_{z,24}$ between the axial levels 2 and 4. The difference between these two transitions is on the order of 3%. Hence, this effect is too large to be ignored for some of the experiments we want to perform. We therefore experimentally measure the spacing between certain trap levels and combine the obtained information with theoretical considerations to precisely determine the shape of the potential. In order to obtain the unperturbed single particle trap levels these measurements are either performed with non-interacting systems or with systems that only consist of a single atom.

transition	transition frequency ω [kHz]	uncertainty (FWHM) [Hz]
$\omega_{z,01}$	$2\pi\,1.486$	11
$\omega_{z,02}$	$2\pi\,2.985$	10
$\omega_{z,24}$	$2\pi\,2.897$	20
$\omega_{r,01,x}$	$2\pi\,13.96$	80
$\omega_{r,01,y}$	$2\pi\,14.82$	90
$\omega_{r,02,x}$	$2\pi\,26.43$	-
$\omega_{r,02,y}$	$2\pi\,28.26$	250

Table 4.1: Transition frequencies between different trap levels for a fractional trap depth of $p = 1$. The transition frequency between the axial levels i and f is denoted $\omega_{z,if}$. Due to the imperfect radial symmetry there are two orthogonal radial directions x and y. The radial transition frequencies $\omega_{r,ij}$ in these two directions are slightly different. This is caused by a small anisotropy of the trap.

The transition frequency between states of equal parity can be measured using trap depth modulation spectroscopy. In this technique one couples states, for example level 0 and level 2, by sinusoidally varying the optical trap depth. We can coherently drive these kind of transitions and thus precisely determine $\omega_{z,02}$ and $\omega_{z,24}$ using for example Ramsey-type experiments. The coherence time for this kind of coupling is larger than 50 ms [Ser11a]. To measure the excitation frequency between states of opposite parity (e.g. $\omega_{z,01}$), we sinusoidally translate the position of the microtrap in space. This is achieved by slightly moving the microtrap beam before it enters the objective. Both methods can also be used to determine the transition frequencies in the radial direction $\omega_{r,if}$. More details on these techniques and the measurements are given in [Ser11a, Zür12a]. The measured values for the transition frequencies in axial ($\omega_{z,if}$) and radial ($\omega_{r,if}$) direction can be found in table 4.1.

We can now optimize the axial trap parameters of the theoretical model for the potential (trap depth V_0, focal waist w_0, magnetic field gradient strength B') such that we reproduce the experimentally determined transition frequencies. This is done by using the WKB method[16] and the obtained trap parameters are

$$\begin{aligned} V_0 &= k_B \times 3.326\,\mu\mathrm{K}, && (4.16)\\ w_0 &= 1.838\,\mu\mathrm{m}\ \text{and} && (4.17)\\ B' &= 18.92\,\mathrm{G/cm}. && (4.18) \end{aligned}$$

We can furthermore combine all axial measurements and deduce a more precise value for the axial trapping frequency and obtain $\omega_z = 2\pi\,(1.488 \pm 0.014)\,\mathrm{kHz}$. Similar considerations can be done for the radial trap parameters which can be found in [Zür12a]. For the experiments described in this thesis, the only radial parameter which we need is the effective radial trap frequency $\omega_r = 2\pi\,(14.22 \pm 0.35)\,\mathrm{kHz}$. This parameter is especially important since it determines the position of the resonance in the coupling strength of the quasi one-dimensional system.

In principle this technique of driving transitions between different trap levels can also be used to precisely control the motional state of a few-fermion sample. Due to the coherent nature of the trap depth modulation technique, we can even create coherent superpositions of different motional states. We have so far only used this technique for non-interacting samples (or systems only consisting of single atoms) but it can also be used for interacting systems. We determined the interaction energy of two repulsively interacting atoms using this method [Zür12a]. However, the analysis of the observed spectra for interacting systems, especially for systems with more than two particles, can become quite challenging. This is due to the large amount of possible excitations and due to the anharmonicity of the trap. Therefore, the precision with which one can deduce the interaction energy is limited. In the following, we will show that there are other methods that are easier to interpret and lead to more precise results.

4.3.2 Tunneling Measurements and Fermionization

Another method we use to determine the energy of few-fermion systems is related to the spilling technique we introduced earlier for the preparation. The idea behind this technique is shown in figure 4.21. It relies on the fact that atoms can tunnel out of the microtrap potential when the magnetic field gradient and the optical trap depth are chosen appropriately. When the tunneling barrier remains unchanged the tunneling time constant then depends exponentially on the energy of the particle in the trap. We use this method to determine the interaction energy of two distinguishable fermions which interact repulsively (see figure 4.21).

We choose the tunneling barrier such that, for the system of identical fermions (see figure 4.21(a)), the atom with higher energy (on level 1 in figure 4.20) tunnels out on a timescale of about 70 ms. As shown in chapter 2 identical fermions do not scatter at ultracold temperatures, hence the system consisting of identical fermions is non-interacting. The tunneling dynamics for such a system is shown in figure 4.22 as green

---

[16] The detailed description of the method and the calculations are given in [Ser11a, Zür12a].

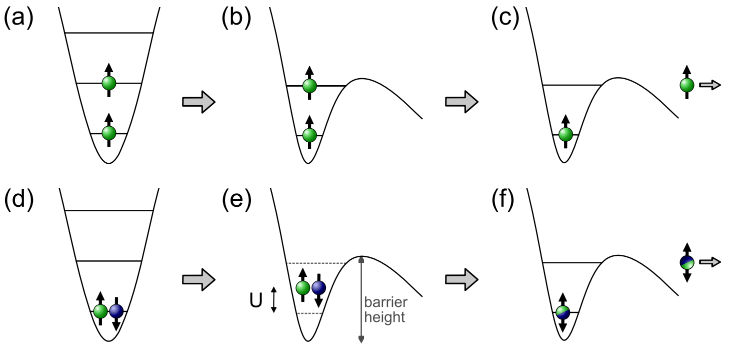

Figure 4.21: We prepare a system of two identical (a) or two distinguishable fermions (d) in the ground state without interaction. We then increase the energy of the distinguishable fermions by introducing a repulsive interaction between the atoms. This energy can be measured by investigating the tunneling dynamics through the barrier (e) and we can directly compare it to the system of identical fermions (b). For a suitable barrier height it is very likely that after a certain time, one particle left the trap (c,f) while the probability of the other particle to leave the trap is negligible.

points. The mean number of atoms N_{mean} in the trap at a given time t is very well described by an exponential decay

$$N_{\mathrm{mean}}(t) = N_{\mathrm{tunnel}} e^{-t/\tau} + N_{\mathrm{remain}}, \tag{4.19}$$

where N_{tunnel} is the mean number of tunneled atoms, N_{remain} is the mean number of remaining atoms and τ is the tunneling time constant. In principle, one expects $N_{\mathrm{remain}} \approx N_{\mathrm{tunnel}} \approx 1$, but due to the finite preparation fidelity both obtained values are slightly smaller than 1. We fit the observed tunneling process with this model (e.g. green line) and obtain the tunneling time constant for the non-interacting system. We then repeat the same measurement for two distinguishable atoms. By tuning the magnetic field to the vicinity of the confinement induced resonance (CIR) we can record the decrease of the mean atom number due to tunneling through the barrier as a function of the interaction energy. We observe that the tunneling time constant τ is significantly larger for small interaction energies ($U < \hbar\omega$) than for the two identical particles (see figure 4.22 and 4.23(a)). For large interaction energies ($U > \hbar\omega$) the observed tunneling process happens a lot faster than for the identical non-interacting particles. In the region where $U \approx \hbar\omega$ we observe very similar tunneling time constants for both systems. This happens at magnetic fields of about 782 G.

In figure 4.23(a) we show the tunneling time constants τ for the interacting distinguishable particles (blue) and for the non-interacting identical particles (green) as a function of the magnetic field. We can furthermore use the radial trapping frequency

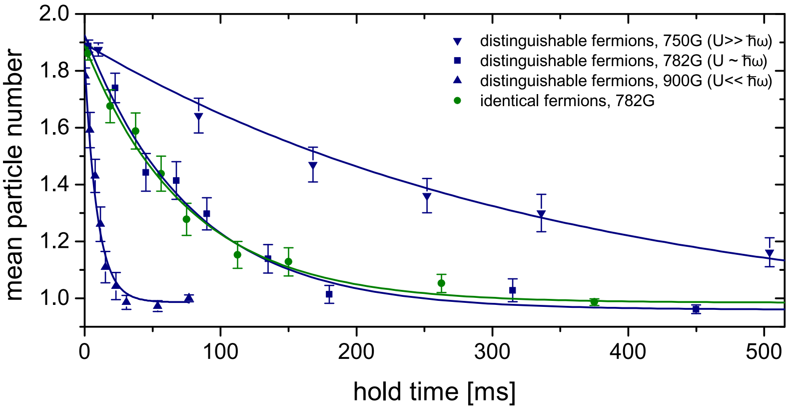

Figure 4.22: The mean number of particles remaining in the trap is exponentially decreased by the tunneling process as a function of the hold time. Depending on the magnetic field and thus the interaction energy the tunneling time constant varies from a couple of 100 ms to about 10 ms. The solid lines are exponential fits to the observed decay. Taken and adapted from [Zür12b].

determined by the trap modulation spectroscopy and the 3D scattering length a_{3D} to determine the one-dimensional coupling strength g_{1D} [Ols98]. The result of this calculation as a function of the magnetic field is shown in 4.23(b). The position of the CIR for the tilted trap used for the tunneling measurement is 783.1 ± 0.5 G. Within our experimental uncertainties, this value coincides with the crossing point between the tunneling time constants for the non-interacting identical and the interacting distinguishable particles. Using a WKB method, we can determine the energy of the system from the tunneling time constants. The result of this calculation is shown in 4.23(c). Since the tunneling times are equal at diverging coupling strength the energies also coincide. For our one-dimensional two-particle system, there is a unique solution for the square modulus of the wave function $|\psi(z_1, z_2)|^2$ for a given energy. Therefore, systems with the same energy also have an identical square modulus of the wave function. This means that one can map a system of resonantly interacting distinguishable particles onto a system of non-interacting identical fermions (see section 4.1.2). This concept of fermionization was initially developed by Girardeau [Gir60] for bosonic systems and later adapted to a system of distinguishable fermions [Gir10].

A one-dimensional system of two particles which interact via a delta function potential in a harmonic trap is one of the few quantum mechanical systems that can be solved analytically for arbitrary interaction (see section 4.1.2 and [Bus98]). This analytic prediction is shown in figure 4.23(c) as a blue solid line[17]. Below and at the CIR this prediction agrees well with the experimentally determined interaction energy. Above the CIR one enters the so-called super-Tonks regime where the system is in a highly correlated metastable state. Here the theoretical prediction is systematically

---

[17] For this calculation, we used the level spacing of the two lowest single particle levels in the tilted trap as the harmonic oscillator frequency.

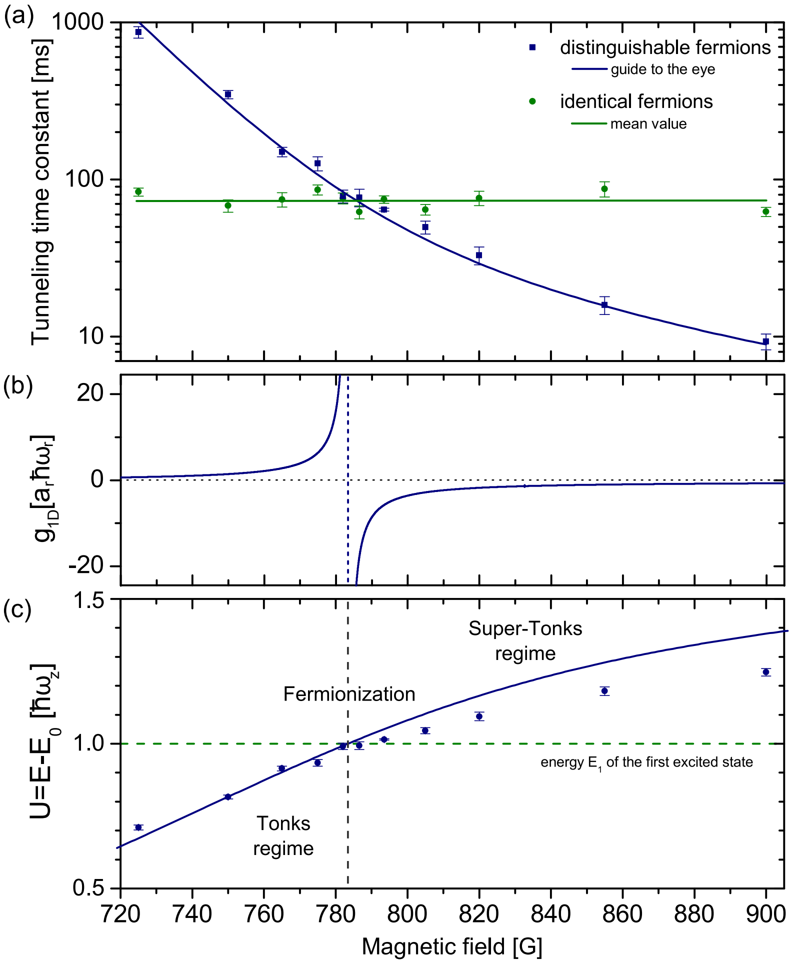

Figure 4.23: Tunneling time constant τ, coupling strength g_{1D} and the interaction energy U as a function of the magnetic field. At the CIR (783.4 ± 0.4 G) where the coupling strength diverges (b) we observe that the tunneling times (a) and hence the energy of the two systems (c) coincide. This is the point of fermionization where a resonantly interacting system of distinguishable particles can be mapped onto non-interacting identical fermions [Gir10]. Taken and adapted from [Zür12b].

higher than the measurements. This discrepancy can be explained by the strong anharmonicity of our tilted trap. A more elaborate calculation using a quasiparticle wave function approach and perturbation theory, which does take the anharmonicity into account, was performed in [Ron12]. This calculation also agrees well with the measured data in the region above the CIR.

Tunneling for Systems with N>2

We also investigated the tunneling dynamics of repulsively interacting systems consisting of more than two particles. For these systems one expects that for diverging coupling strength $g_{1D} \to \infty$ the energy becomes equal to the energy of a system of identical non-interacting fermions [Gir10, Bro12, Blu10]. This means that the energy of the interacting system reaches the Fermi energy of a system of identical fermions. This fermionization of the energy persists for any combination of spin up and spin down particles. The many-body wave function on the other hand which was originally derived by [Gir10] using the Bose-Fermi mapping does not seem to be the complete solution of the many-particle problem at the CIR. Recent calculations [Gha13, Vol13] suggest that the many-particle wave function close to the CIR becomes more complicated than initially predicted by [Gir10] (see also section 4.1).

For these systems with more than two particles, the super-Tonks regime is especially interesting. In this regime the interaction energy of the system exceeds the Fermi energy and thus one expects that ferromagnetic spin correlations lower the total energy. It is however not straightforward to determine the spin correlations of the investigated systems from tunneling measurements and therefore this data is still being analyzed. Nevertheless, there have however been quite a few theoretical publications that investigate this regime [Bug13, Gha13, Vol13, Cui13, Deu13] and hopefully we will soon be able to use this knowledge to extract meaningful results from our data.

Tunneling Spectroscopy for Attractively Interacting Systems

In [Zür13b], we used tunneling spectroscopy to also measure the interaction energy of attractively interacting systems. In this case, the lifetime of the atoms in the tilted trap is enhanced by the attractive interactions since these lower the energy of the trapped atoms.

The main results of these measurements are shown in figure 4.24. We observe that the attraction between particles, that occupy the same trap level at vanishing interaction strength, is stronger than for particles that start out in different trap levels before the interaction strength is increased. This effect is related to the intershell versus intrashell pairing and thus it is connected to the odd-even effect known from nuclear physics [Bri05].We observe a strong difference in single-particle separation energies between balanced systems ($N_\uparrow = N_\downarrow$) and systems where there is one additional atom in one of the spin states ($N_\uparrow = N_\downarrow + 1$).

The last method we regularly use to determine the energy of ultracold few-fermion systems is radio-frequency spectroscopy. This method allows us to obtain very precise values of the interaction or binding energy of a system. It also works with high precision for systems with larger particle numbers. Since we will extensively use this technique in different regimes, we will present it in more detail both theoretically and experimentally in the following section.

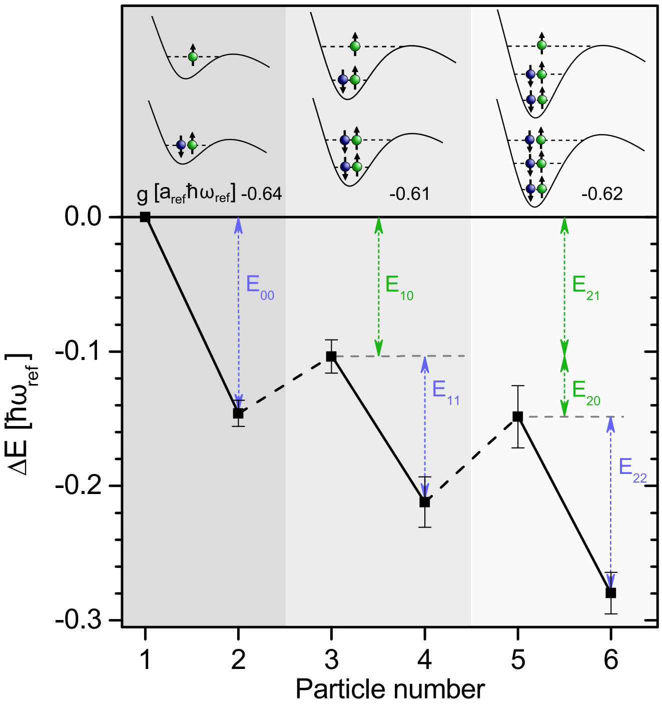

Figure 4.24: Single particle separation energies deduced from tunneling measurements for systems with up to 6 particles at a interaction strength $g_{1D} \approx -0.6\, a_{\text{ref}}\, \hbar\omega_{\text{ref}}$. The arrows indicate the contributions to the interaction energy from intrashell and intershell interaction. E_{ij} denotes the interaction energy between a particle in level i interacting with a particle of opposite spin in level j. Taken and adapted from [Zür13b].

4.4 RF Spectroscopy in Finite Systems

In this section, we will introduce a commonly used technique to determine the interaction energy of ultracold atoms. We showed in section 3.3.3 that one can use radio frequency pulses to change the Zeeman sublevel of ultracold atoms. For a non-interacting system, this RF transition occurs at a frequency which is determined by the Breit-Rabi formula and thus solely depends on the magnetic offset field (see figure 4.25(a)). Such a transition is often called a bare or a free-free transition. If the atom we want to transfer to another hyperfine state is however bound in a molecule or interacting with other atoms, the transition frequency is shifted. In this case, the RF photon also has to supply the energy difference between the initial $|i\rangle$ and final state $|f\rangle$ of the transition. By comparing the transition frequency between the interacting and the free-free transition, one can therefore determine the energy difference between the initial and the final state. If for example the final state is non-interacting then the transition frequency is given by

$$\nu_{RF} = \nu_{ff} + E_{int}/h \; (+E_{kin}/h) \, , \tag{4.20}$$

where ν_{ff} is the free-free transition frequency, E_{int} is the interacting energy in the initial state and E_{kin} is a possible difference in the kinetic energy between the initial and final state[18].

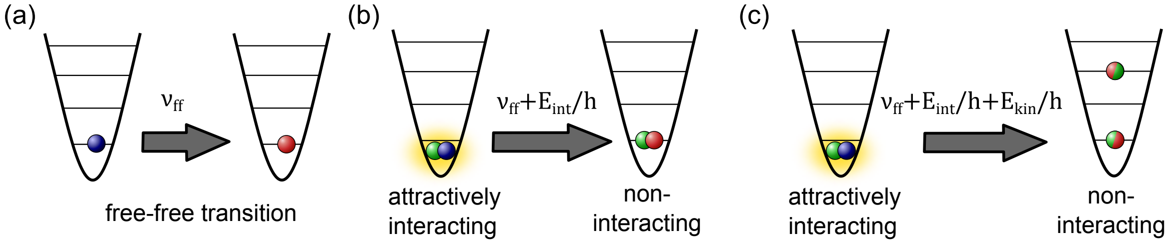

Figure 4.25: Illustration of radio-frequency transitions between different Zeeman sublevels of ^{6}Li in a trapping potential. The colors indicate the states defined in figure 2.5. (a) For a non-interacting system, the transfer occurs at the bare free-free transition frequency ν_{ff}. (b) For an attractively interacting system, the RF photon also has to supply the interaction or binding energy E_{int}. (c) There are also other transitions which involve a change in kinetic energy E_{kin}. In the case of a trapped system, this means that the final state is then an excited state of the relative motion.

RF spectroscopy has been successfully used for example to determine the binding energy of weakly bound dimers [Reg03, Bar05]. These measurements can be used to precisely calculate the ultracold collision parameters like the s-wave scattering

---

[18] This term is not always relevant but we will later see that it will have consequences especially for small systems in the microtrap.

length. Furthermore, RF spectroscopy was used to investigate the BEC-BCS crossover [Chi04, Sch08a, Sch08b], the influence of lower dimensionalities [Frö11, Fel11, Som12], imbalanced Fermi systems or polaronic physics [Sch09, Kos12, Koh12] and Efimov trimers [Lom10b, Nak11].

We will now briefly present the theoretical framework to describe RF transitions and spectroscopy. For this, we will follow the reasoning and notation of [Chi05], which describes RF transitions for ultracold systems in detail. This knowledge is then used to investigate how the RF spectrum evolves when the system size changes from large and continuous systems to small systems with discrete levels. The discreteness of our system allows us to perform RF spectroscopy with an increased accuracy. Therefore, we are able to measure the binding energy of the weakly bound dimer state with unprecedented precision and hence the accuracy of the ultracold scattering parameters is significantly increased.

4.4.1 Basic Principles of RF spectroscopy

Experimentally, RF transitions are driven by applying an oscillatory magnetic field to the atoms. This field couples to the magnetic moment of the atoms and drives a magnetic dipole transition between an initial state $|\Psi_i\rangle$ and a final state $|\Psi_f\rangle$. The frequency of the RF photon must satisfy equation 4.20 and thus supply the difference in energy (hyperfine energy, interaction energy and kinetic energy) between the initial and final state. Following [Chi05] we obtain the transition rate of a RF transition from Fermi's golden rule

$$\Gamma_{if} = \frac{2\pi}{\hbar} \left| \left\langle \Psi_f \middle| \hat{M}_{RF} \middle| \Psi_i \right\rangle \right|^2 , \tag{4.21}$$

where Γ_{if} is the transition rate and $\hat{M}_{RF} = \frac{\hbar\hat{\Omega}}{2}$ is the operator that describes the RF interaction with a Rabi frequency Ω. The total wave function $|\Psi_j\rangle$ can be written as a direct product of an external and an internal degree of freedom. The external degree of freedom is given by the spatial wave function $|\psi_j\rangle$ and the hyperfine or spin wave function $|\mathrm{hf}_j\rangle$ constitutes the internal degree of freedom of the atom. The energy of the RF photon is in the MHz regime and therefore the momentum transfer of the photon on the atoms is negligible. This means that the RF transition matrix element does not change the spatial wave function. We can thus write the resonant Rabi frequency in the following way

$$\Omega_{if} \propto \left\langle \Psi_f \middle| \hat{M}_{RF} \middle| \Psi_i \right\rangle = \langle \mathrm{hf}_f | \hat{M}_{RF} | \mathrm{hf}_i \rangle \, \langle \psi_f | \psi_i \rangle . \tag{4.22}$$

This shows that, for a particular transition, for example between the Zeeman sublevels $|1\rangle$ and $|2\rangle$ (as defined in figure 2.5), the relative strength is determined by the Franck-Condon overlap of the initial and final spatial wave functions.

Bound-Free Transitions

We will later use RF spectroscopy to determine the binding energy of weakly-bound diatomic molecules which can be obtained by dissociating the dimers into free particles. To derive the transition rate we will consider a bound-free transition of a stationary dimer into free atoms[19] [Chi05]. In this case the initial wave function is given by the universal wave function of a weakly-bound dimer

$$|\psi_i\rangle = |\psi_m(r)\rangle = \sqrt{\frac{2}{a}}\, e^{-r/a}, \tag{4.23}$$

where a is the 3D scattering length. The final state of free particles is described by a plane wave with energy $K = \hbar^2 k^2/(2m_r)$

$$|\psi_f\rangle = |\psi_K(r)\rangle \propto \frac{1}{\sqrt{k}} \sin(kr). \tag{4.24}$$

Since the final state is continuous in energy K, the transition rate will also be a function of the total energy. As a result, the observed spectrum will consist of a sharp rise at low RF frequencies which occurs as soon as the energy of the RF photon is sufficient to change the hyperfine state of the atoms and dissociate the dimer. For higher frequencies the transition rate has a tail which is due to the transfer of kinetic energy to the free atoms. A sketch of such an asymmetric spectral line shape can be found in figure 4.26(a). These kinds of molecule dissociation spectra were experimentally observed in various measurements [Chi04, Bar05, Sch08b].

Bound-Bound Transitions

When the initial and final states are bound molecular states, both states of the transition have a discrete energy. This means that the kinetic energy of the final state K is fixed and is given by the binding energy of the final molecular state E'_B [Chi05]. Consequently, the transition is only possible when the RF photon fulfills

$$\nu_{RF} = \nu_{ff} + E_B/h - E'_B/h, \tag{4.25}$$

where $E_B(E'_B)$ is the binding of the initial (final) molecular state. Due to the extremely long lifetimes of the hyperfine states, which significantly exceed the experimental timescales, the bound-bound transitions are expected to be very narrow. The width is in our case limited by the finite stability of the magnetic offset field. Thus, the expected line shape and width are similar to the free-free transition: a very narrow symmetric line shape which is described by a Lorentzian or Gaussian. Since our magnetic field stability is about 1 mG, the minimal full width at half maximum (FWHM)

---

[19] Since there is no momentum transfer with RF photons, there is no center-of-mass motion of the free atoms after their dissociation. Consequently, we only need to consider changes in the relative motion between the particles.

we are usually able to observe is on the order of 100-200 Hz for these bound-bound transitions.

4.4.2 From Continuous to Discrete Systems

In cold atom experiments, the atoms are usually trapped in harmonic traps. Therefore, all states in this trapping potential have a discrete energy. In most measurements that involved RF spectroscopy in the past, the level spacing $\hbar\omega_{\mathrm{trap}} = h\nu_{\mathrm{trap}}$ of the trap was small compared to the resolution of the RF spectroscopy ν_{res} which can for example be defined by the FWHM of the free-free transition. The resolution is usually determined by the stability of the magnetic offset field, the length of the RF pulse, the temperature and the anharmonicity of the trap. For $\nu_{\mathrm{res}} > \nu_{\mathrm{trap}}$ one cannot resolve the single trap levels and thus the trapped system can be well approximated by a system with continuous energies. As a consequence, one observes the asymmetric line shape introduced earlier and shown in figure 4.26(a) when one dissociates a weakly-bound molecule into free atoms (see for example [Bar05, Chi04]).

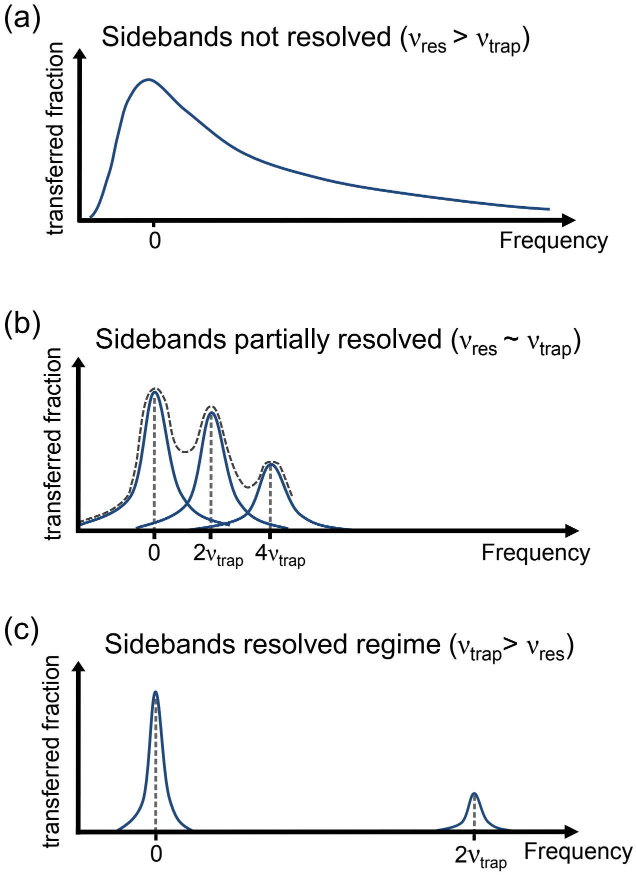

Figure 4.26: Different regimes of the RF spectroscopy of weakly bound dimers in a trapped system. Taken and adapted from [Wen13].

When the resolution of the RF spectroscopy is better than the level spacing ($\nu_{\text{res}} < \nu_{\text{trap}}$), then each RF transition occurs between two states of discrete energy. Thus, one expects a spectrum that consists of several symmetric sharp peaks which can be associated to certain final motional states with discrete energies (see figure 4.26(c)). These lines are called trap sidebands and therefore this regime is often referred to as the resolved trap sideband regime. If the initial state is again a weakly bound dimer state and the final state is a non-interacting harmonic oscillator state $\Phi_i(r)$, then due to the symmetry of the wave function the lowest accessible trap sideband is the second excited state. This state is separated by $2\nu_{\text{trap}}$ from the transition which leaves the motional state of the system unchanged. The relative height between the sidebands is given by the Franck-Condon overlap of the initial and final spatial wave function.

In the intermediate regime where the RF resolution is on the order of the trapping frequency ($\nu_{\text{res}} \sim \nu_{\text{trap}}$), the trap sidebands are only partially resolved. As illustrated in figure 4.26(b) the measured spectrum can then become rather complicated and is obtained by the sum of the overlapping symmetric spectral lines broadened by the RF resolution.

Influence of the Driving Power and Pulse Duration

For the molecule dissociation spectroscopy, the binding energy of the molecular state can be obtained from the frequency necessary to dissociate the weakly-bound dimers. As indicated in figure 4.26, this frequency is given by the sharp rise in the spectral function in the continuously described regime. Due to its asymmetry the precise peak shape depends on saturation effects and thus on the driving power and pulse duration. Therefore, the experimentally determined dissociation frequency can also be affected by these effects and thus one has to be careful when analyzing such spectra. In the resolved sideband regime, the transitions are symmetric and thus saturation effects usually only influence the width and shape of the peak without affecting its center position. As a result, it is much simpler to precisely determine the dissociation frequency from measurements with resolved sidebands.

We will now show how we could significantly improve the precision of the ultracold ^{6}Li scattering parameters by performing RF spectroscopy in the partially resolved trap sideband regime.

4.4.3 Precise Determination of the Lithium-6 Scattering Parameters

The most common method to determine the position of a Feshbach resonance is to perform RF dissociation spectroscopy on the weakly bound dimer states that are associated to the respective Feshbach resonance [Reg03, Bar05]. For large 3D scattering lengths a, the binding energy of these dimers is given by $E_B = \hbar^2/(ma^2)$ and thus these universal dimers become unbound exactly at the Feshbach resonance. From the measured binding energy of the molecule, one can thus obtain the resonance position and, with more elaborate theoretical considerations, the complete dependence of the scattering length on the magnetic field $a(B)$.

We are going to measure the binding energy of molecules in the $|1\rangle$-$|2\rangle$ channel of ^{6}Li-atoms close to the Feshbach resonance at about 830 G. This extremely broad resonance with a width on the order of 200-300 G has been extensively used e.g. to investigate the BEC-BCS crossover or unitary Fermi gases [O'H02, Bar04, Zwi05]. The previous determination of this resonance position had an uncertainty of 1.5 G and was performed in the group of R. Grimm [Bar05]. We will now present how we can improve the precision of this resonance position to an uncertainty of only about 80 mG. This is achieved by performing the spectroscopic measurement in the partially resolved trap sideband regime which is made possible by using low density samples of only about 30 weakly-bound molecules in a large volume optical dipole trap. These measurements, the results and the calculated magnetic field dependence of the scattering length that we will present in the following are published in [Zür13a].

Preparation of the Low Density Samples

To obtain a sample of ultracold $|1\rangle$-$|2\rangle$ molecules in our reservoir, we evaporate a mixture of atoms in state $|1\rangle$ and $|2\rangle$ in the large volume optical dipole trap as explained in chapter 3. To form molecules the evaporation is performed at 760 G which is on the repulsive side of the Feshbach resonance. At the end of the evaporation process, we obtain about 10^5 molecules and about 1 000 of the molecules are then transferred into the microtrap. Using the spilling technique, we decrease the number of molecules to about 30. The shot-to-shot fluctuation of the number of molecules is ±2. Due to a technical problem at the time of this measurement[20], the calibration of the absolute number of molecules had a large uncertainty of about ±15 molecules. The relative shot-to-shot fluctuations are however not affected by this overall calibration factor. To create a non-degenerate gas of molecules and to lower the density of the system, we transfer the molecules from the microtrap back into the large volume ODT. This transfer is performed by suddenly switching off the microtrap and due to this non-adiabatic change in the trapping potential, the molecules obtain a mean kinetic energy of $\geq 0.4\,\mu$K per molecule. This ensures that the sample in the large volume ODT is non-degenerate and the peak density of the molecular cloud obtained in such a way is $n_0 \leq 10^9 \frac{1}{cm^3}$. The trap frequencies of the large volume ODT are $\nu_r = \omega_r/2\pi = 349(3)$ Hz in radial direction and $\nu_z = \omega_z/2\pi = 35(1)$ Hz in axial direction [Zür13a]. This means the aspect ratio of the trap is about $\eta = \nu_r/\nu_z = 10$.

The RF Spectroscopy Measurement

To measure the binding energy at different magnetic fields and thus different scattering lengths, we linearly ramp from the preparation field (760 G) to the magnetic field of interest in 10 ms. The spectroscopic measurement is performed at 721 G, 781 G,

---

[20] The oven shutter was not functional at the time.

801 G and 811 G. After ramping to one of these fields, we wait for another 5 ms. Then the magnetic field has stabilized to an uncertainty of about 1 mG. Subsequently, we apply the RF pulse for a duration of 10 ms to transfer the particles to a different hyperfine state. We perform a reference measurement of the free-free transition, i.e. without interaction, once before and once after each of the actual molecule dissociation measurement. Figure 4.27 shows one of these measurements at 811 G as red points. Using the Breit-Rabi formula, we can determine the magnetic offset field with very high precision[21]. Between the two reference measurements we measure the dissociation spectrum of $|1\rangle$-$|2\rangle$ molecules into a free atom in state $|1\rangle$ and a free atom in state $|3\rangle$ and obtain a spectrum as shown in figure 4.27 in blue. When driving these transitions we usually adjust the RF power such that we do not transfer more than half of the atoms because we want to limit the effects of saturation on the shape of the transition.

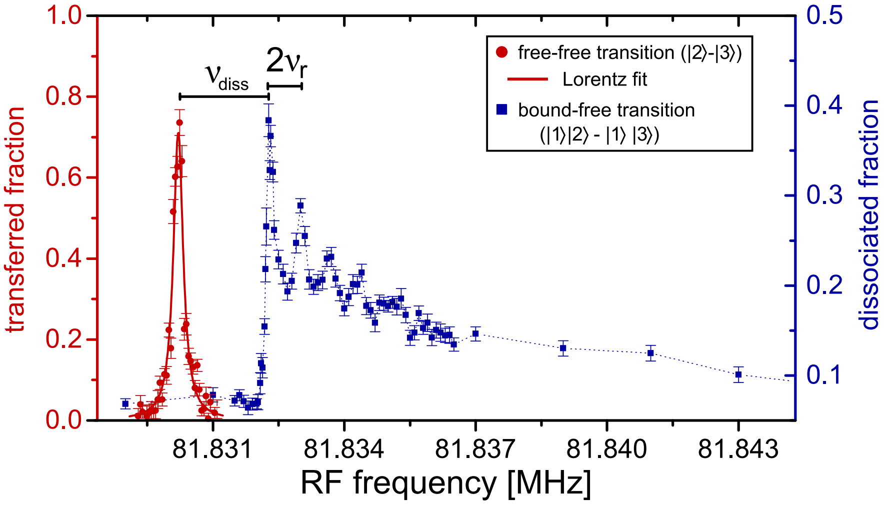

Figure 4.27: Free-free (red) and bound-free (blue) spectrum at a magnetic offset field of 811 G. The free-free transition can be fitted by a Lorentzian (red line). In the bound-free spectrum one clearly observes a peak structure which can be attributed to the radial trap sidebands. Taken and adapted from [Zür13a].

In figure 4.27, one can clearly see several distinct peaks in the bound-free spectrum. A more careful analysis shows that they are exactly spaced by twice the radial trapping frequency $2\nu_r = 2 \times 349 Hz \approx 700$ Hz. As illustrated in figure 4.28(a), the ODT is cigar-shaped and has an aspect ratio of about $\eta = \nu_r/\nu_z \approx 10$. This means that the axial sidebands are only spaced by about 70 Hz and we do not resolve them. This however is not surprising since the resolution of our RF spectroscopy is about $\nu_{\text{res}} \approx 120$ Hz. Figure 4.28(b) shows that the total line shape of the bound-free transition can be obtained by the sum over all radial (blue) and axial (gray) transitions which are weighted by the

---

[21] The reference measurements are performed with a spin polarized Fermi gas in state $|2\rangle$ which is transferred to state $|3\rangle$ by the RF pulse.

Franck-Condon overlap between the initial molecular state and the final state of free atoms in a harmonic trap.

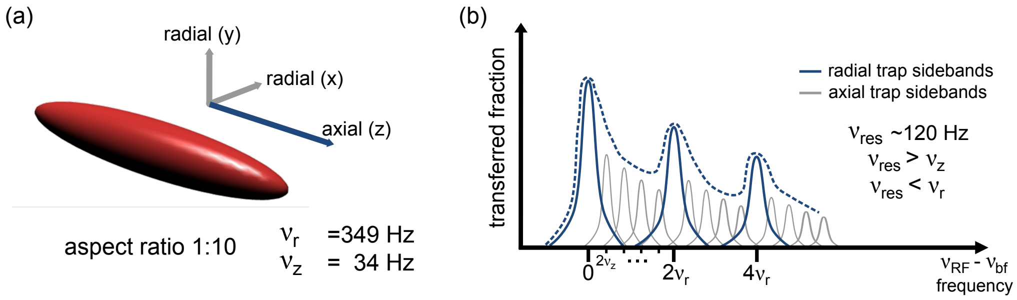

Figure 4.28: (a) Illustration of the cigar shaped ODT with an aspect ratio of $\eta \approx 10$. (b) The bound-free transition spectrum can be obtained from the sum over all accessible trap sidebands in radial and axial direction. The width of the sidebands is determined by the uncertainty of the magnetic offset field and their weight can be obtained by the Franck-Condon overlap between the initial and final state wave functions.

Theoretical Model

We will now develop a simple theoretical model that allows us to extract the molecule dissociation frequency $\nu_{\text{diss}} = \nu_{bf} - \nu_{ff}$, where ν_{bf} is the bound-free transition frequency and ν_{ff} is the free-free transition frequency. We fit the free-free transition spectra with Lorentzians and obtain ν_{ff} from the weighted mean of these two reference measurements[22]. In order to determine ν_{bf}, we will numerically calculate the transition rates to all accessible trap sidebands and fit the measured spectra with the sum over all trap sidebands. The initial state is well described by the universal wave function of a weakly-bound Feshbach molecule (see equation 4.23) and thus we can write

$$|\psi_i(a, r)\rangle = \sqrt{\frac{2}{a}}\, e^{-r/a}, \tag{4.26}$$

where a is the 3D scattering length and r is the relative distance between the atoms. One expects that this wave function is slightly altered by the confinement especially for large interparticle distances r. Due to its small relative weight, this part of the molecular wave function is not relevant for the determination of the overlap. For the sake of simplicity we will therefore neglect this effect. The large volume ODT is well approximated by a harmonic potential. Therefore, the final state of two free atoms $|\psi_f(r)\rangle$ can be approximated by the product of harmonic oscillator wave functions for each coordinate $|\phi_{n_x}(x)\,\phi_{n_y}(y)\,\phi_{n_z}(z)\rangle$. Each one of these harmonic oscillator states

---

[22] The errors are determined by the weighted addition of the errors of the two measurements. The determination of these errors can be found in the supplementary material of [Zür13a].

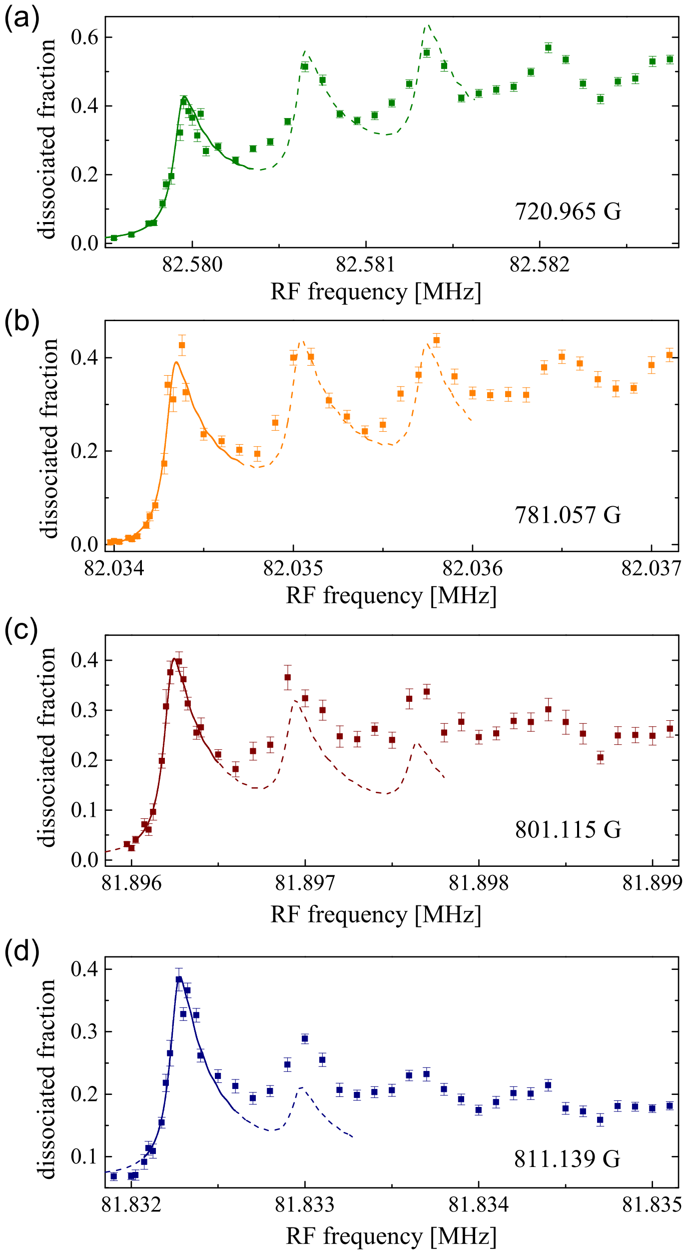

Figure 4.29: Bound-free dissociation spectra for different magnetic offset fields. Due to the magnetic field dependence of the 3D scattering length a, the width of molecular wave function changes for different offset fields. This leads to an altered overlap to the final state and thus for smaller (larger) fields we observe an overall rising (falling) shape of the total spectrum. The line shows the fit using the theoretical model described in the text. The solid part of the lines indicate the data included in the fit. Taken from [Zür13a].

is given by the well-known Hermite polynomials. Since the initial molecular state is symmetric, the overlap to all antisymmetric trap states vanishes and we only have to consider symmetric harmonic oscillator states for the final state. We calculate the Franck-Condon factor for a given 3D scattering length a as

$$C_{a,n_x,n_y,n_z} = |\langle\psi_i(a,r)|\psi_f(r)\rangle|^2 = \left|\int_{-\infty}^{\infty} \psi_i^*(a,r)\phi_{n_x}(x)\,\phi_{n_y}(y)\,\phi_{n_z}(z)\,dx\,dy\,dz\right|^2, \quad (4.27)$$

where n_x, n_y and n_z are the quantum numbers of the trap states in the respective directions and these quantum numbers assume all possible combinations of non-negative even integers. The difference in motional energy state between the initial state and each final state is given by $E_f(n_x, n_y, n_z) = h\,((n_x + n_y)\,\nu_r + n_z\,\nu_z)$. This determines the frequency at which a particular sideband can be driven. In the calculation, we assume all sideband transitions to be infinitesimally narrow and the weight of each δ function is given by the overlap. In order to be able to compare the model to the experimentally obtained spectra, we need to include the finite resolution of the RF spectroscopy. We thus convolute each transition, weighted by its Franck-Condon overlap C_{a,n_x,n_y,n_z}, with a Lorentzian of a FWHM of 122 Hz. By summing all weighted Lorentzian trap sidebands with an energy smaller than $E_f \approx 2.5 \times h\,\nu_r$, i.e. $n_z \leq 25$, $n_{x,y} < 3$, we obtain the low-energy part of the spectrum which can be used as a fit function for the measured bound-free spectra. The free parameters of the fit are the bound-free transition frequency ν_{bf}, the overall amplitude and a small offset in the number of dissociated atoms due to collisional dissociation of molecules [Zür13a]. To determine ν_{bf}, we fit the obtained model to the data in the region of the lowest radial trap sideband. The fitting region is indicated by the solid line in figure 4.29 and is in good agreement with the experimental data in the fitted region. For higher trap sidebands, the agreement between the model (dashed line) and the data decreases but the qualitative behavior is still reasonably described. A possible explanation for the observed discrepancies are saturation effects which have a particularly strong influence on trap sidebands with completely different weights. This would explain why the agreement between theory and measurement for lower magnetic fields (720.965 G and 781.057 G) is better than for higher magnetic fields (801.115 G and 811.139 G). Other possible reasons for the difference between the model and the experiment are a small anisotropy of the trap ($\nu_{r,x} \neq \nu_{r,y}$), the anharmonicity of the trap and small changes to the initial and final state wave functions due to the confinement. The measured free-free and bound-free transition frequencies, the determined magnetic fields and the dissociation frequencies are listed in table 4.2.

Obtaining the Binding Energy and the Scattering Parameters

In order to determine the binding energy of the $|1\rangle$-$|2\rangle$ molecules from the dissociation frequency we still have to take some corrections into account. We want to determine the scattering parameters for an untrapped, hence homogeneous system and thus we need to correct for the effects of the confinement. The largest contribution to this

Magnetic field B (stat.) [G]	Free-free transition ν_{ff} (stat.) [MHz]	Bound-free transition ν_{bf} (stat.)(sys.) [MHz]	Dissociation frequency $\nu_{\mathrm{bf}} - \nu_{\mathrm{ff}}$ (stat.)(sys.) [kHz]
811.139 (1)	81.830 115 (3)	81.832 271 (7)(8)	2.156 (8)(16)
801.115 (5)	81.891 539 (33)	81.896 236 (3)(8)	4.697 (33)(16)
781.057 (1)	82.019 823 (1)	82.034 336 (6)(8)	14.513 (6)(16)
720.965 (1)	82.452 482 (2)	82.579 943 (13)(8)	127.461 (13)(16)

Table 4.2: Measured free-free and bound-free transition frequencies and the obtained dissociation frequencies at different magnetic fields. The dissociation frequency ν_{diss} is given by the difference $\nu_{\mathrm{bf}} - \nu_{\mathrm{ff}}$. A detailed discussion of the statistical and systematic errors can be found in the Supplemental Material of [Zür13a].

correction is the zero-point energy of the relative motion of the dissociated particles in the ODT which is given by $E_0 = h\nu_0 = h(\frac{1}{2}\nu_r + \frac{1}{2}\nu_r + \frac{1}{2}\nu_z) = h\,367(4)\,\mathrm{Hz}$. Additionally, we must also consider the effect of the trapping potential on the energy of the two particles in the trap. This correction ν_i can be calculated using the formulas derived in [Idz06]. By combining both terms, we obtain the corrections due to the trapping potential which is given by ν_{cs}. The binding energy of the molecules for a homogeneous system is then given by $E_B = h(\nu_{\mathrm{diss}} - \nu_{\mathrm{cs}})$ and the obtained values are shown in table 4.3. More details on their derivation and the performed calculations can be found in [Zür12a, Zür13a].

Magnetic field B (stat.) [G]	Confinement shift $\nu_{\mathrm{cs}} = \nu_0(\mathrm{sys.}) + \nu_{\mathrm{i}}(\mathrm{sys.})$ [kHz]	Binding energy$/h$ $\nu_{E_{\mathrm{B}}}$ (stat.)(sys.) [kHz]
811.139 (1)	0.367(3) – 0.014(1)	1.803 (8)(17)
801.115 (5)	0.367(3) – 0.011(1)	4.341 (33)(17)
781.057 (1)	0.367(3) – 0.011(1)	14.157 (7)(17)
720.965 (1)	0.367(3) – 0.021(1)	127.115 (14)(17)

Table 4.3: We obtain the binding energy $E_B = h\nu_B$ of the molecule for a homogeneous system from the dissociation frequency ν_{diss} and the correction due to the confining potential ν_{cs}. Values taken from [Zür13a].

These results can now be used as input parameters for coupled-channel calculations. Using the methods described in [Zür13a], J. Hudson and P. Julienne performed these calculations using the binding energies shown in table 4.3. They obtain the magnetic field dependence of the 3D scattering length a for the relevant scattering channels ($|1\rangle$-$|2\rangle$, $|1\rangle$-$|3\rangle$, $|2\rangle$-$|3\rangle$) of ultracold ^{6}Li (a table for $a(B)$ can be found online [Sca]). Due to the increased experimental resolution, the positions of the Feshbach resonances are also

Scattering channel	Pole [G]	Δ [G]	a_{bg} $[a_0]$
$\lvert 1\rangle$-$\lvert 2\rangle$	832.18(8)	$-262.3(3)$	$-1582(1)$
$\lvert 1\rangle$-$\lvert 3\rangle$	689.68(8)	$-166.6(3)$	$-1770(5)$
$\lvert 2\rangle$-$\lvert 3\rangle$	809.76(5)	$-200.2(5)$	$-1642(5)$

Table 4.4: Position of the Feshbach resonance, width of the resonance Δ and background scattering length a_{bg} for the different scattering channels obtained from coupled-channel calculations [Zür13a].

determined with improved accuracy (see table 4.4). The former value for the resonance position in the $\lvert 1\rangle$-$\lvert 2\rangle$ channel was 834.15±1.5 G [Bar05]. This means that the resonance position changed by almost 2 G. Furthermore, the uncertainty in the position decreased by almost a factor of 20. This large improvement became possible due to several facts. First, by resolving the trap sidebands we are able to determine the bound-free transition frequency with a significantly improved accuracy. Second, in order to avoid systematic errors one has to perform the spectroscopy in a regime where the interparticle spacing is a lot larger than the scattering length, hence $n^{1/3}a \ll 1$. Due to the extremely low densities in our experiments of only $n_0 \leq 10^9 \frac{1}{cm^3}$, we can measure the binding energy for larger scattering lengths without being limited by density dependent shifts. In the previous measurements, the densities were on the order of $n \approx 10^{13} \frac{1}{cm^3}$ and thus only binding energies larger than $E_B \approx h \times 100\,\text{kHz}$ could be measured. With our decreased density, we can measure binding energies down to about $E_B \approx h \times 2\,\text{kHz}$ which therefore constitutes an approximatively 50-fold improvement compared to [Bar05].

Implications for Many-Body Physics

In recent year, two-component Fermi gases of ultracold ^{6}Li atoms have become very commonly used for the investigation of unitary Fermi gases. Recently, the equation of state of these unitary Fermi gas could be determined with such a high accuracy [Ku12, Nas10] that the uncertainty of the resonance position is one of the leading sources of error. One of the main findings presented in this publication is the precise determination of the Bertsch parameter ξ [Bak01] which relates all extensive quantities of a unitary Fermi gas to a non-interacting Fermi gas rescaled by this universal numerical number ξ. In [Ku12], they obtain $\xi = 0.376 \pm 0.004$ for the Bertsch parameter. However, their measurement was still performed at the resonance position (834.15 G) determined in [Bar05]. Comparing this to the actual position of the Feshbach resonance (832.18 G) shows that Ku et al.[Ku12] did in fact not measure at diverging scattering length but rather at a large and negative value. Using our new measurements one obtains $a(834.15\,\text{G}) = -2.124(80) \times 10^5\,a_0$. We can now use the universal Tan contact $C(a)$ [Tan08, Ku12] to relate the measurement performed at finite scattering length to a resonantly interacting system. From these considerations we obtain a corrected value for the Bertsch parameter which is $\xi = 0.370(5)_{\text{stat}}(8)_{\text{sys}}$ [Ku13, Zür13a].

This measurement and its implications on the behavior of unitary Fermi gases beautifully illustrate how a deep and precise understanding of few-particle physics is necessary to make good predictions of many-body observables like the Bertsch parameter.

4.4.4 The Resolved Sideband Regime

In the previous section, we showed how resolving the trap sidebands in RF spectroscopy with small samples can significantly increase the precision of the RF measurement. Although we used the microtrap for the preparation of the molecular samples, the measurements were performed in the large volume ODT. We will now go back to measurements in the microtrap and show that in the microtrap potential we can actually reach the resolved trap sideband regime. We will later see that this fact will allow us to perform very precise RF spectroscopy measurements in the microtrap.

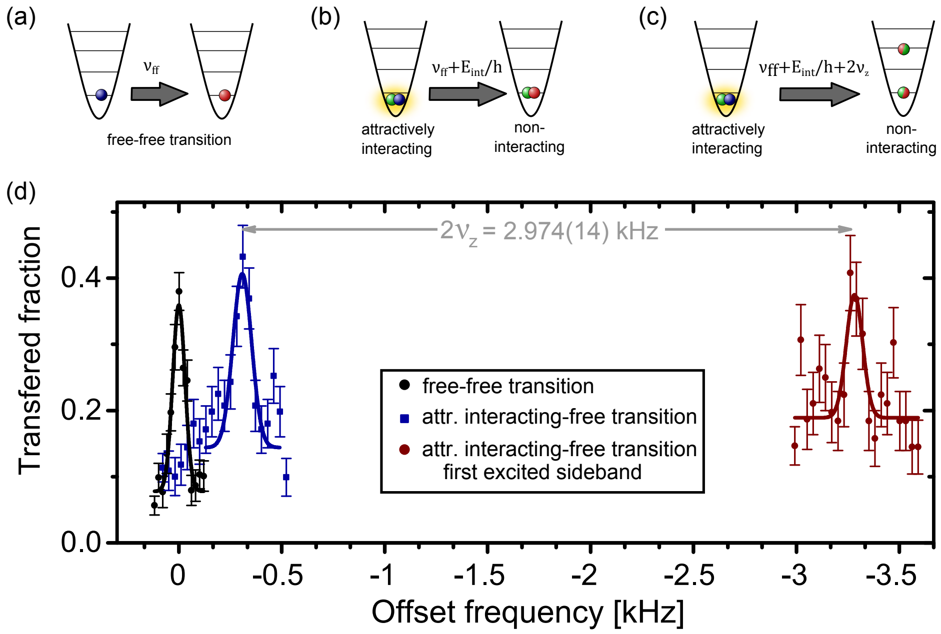

Figure 4.30: RF transitions in the resolved sideband regime in the microtrap. We can use a single non-interacting atom and measure the free-free transition as illustrated in (a) and shown as black points in (d). For the attractively interacting system ($g_{1D,|1\rangle-|3\rangle} = -0.27\,a_z\hbar\omega_z$), we can either drive a transition without adding kinetic energy, i.e. a trap sideband (b and blue squares in d), or we can transfer to the lowest possible excited trap state (b and red points in d). Taken and adapted from [Wen13].

To show that we can reach the resolved sideband regime as depicted in figure 4.26(c) we will now present a spectroscopic RF measurement performed with two attractively interacting atoms prepared in the ground state of the trap. We initially prepare a two atom sample consisting of one atom in state $|1\rangle$ and one in state $|3\rangle$ in the ground state of the trap. The spilling is in this case performed at 568 G where the 1D coupling strength[23] in the $|1\rangle$-$|3\rangle$ channel vanishes ($g_{1D,|1\rangle-|3\rangle} = 0$). We then ramp to 527 G where the atoms attractively interact with $g_{1D,|1\rangle-|3\rangle} = -0.27\, a_z \hbar\omega_z$. At this field we apply a RF pulse and transfer the atom in state $|3\rangle$ to state $|2\rangle$. We therefore end up with one atom in state $|2\rangle$ and one in state $|1\rangle$. This system is non-interacting since $g_{1D,|1\rangle-|2\rangle} = 0$ at 527 G. As a result, we dissociate the attractively interacting system into a non-interacting system as shown in figure 4.30(b,c). Depending on the frequency of the RF pulse we can now either drive a transition to a final state on the same trap level (figure 4.30(b) and blue squares in (d)) or access the first excited trap sideband (figure 4.30(c) and red points in (d)) by increasing the frequency of the RF pulse by twice the axial trap frequency ($2\nu_z$). In order to observe this higher sideband we need to significantly increase the Rabi frequency of the transition which is achieved by increasing the power of the RF pulse by 16 dB and by extending the duration of the RF pulse by a factor of 10. We fit the obtained spectra with Gaussians and the obtained distance between the peak positions of the two sidebands is 2973.8 ± 13.7 Hz. Within the uncertainties, this agrees with the value of $2\nu_z = \frac{2\omega_z}{2\pi} = 2985 \pm 10$ Hz (see table 4.1) determined by trap modulation spectroscopy and WKB optimization. Furthermore, as evident in figure 4.30(d), the sidebands are clearly separated because the widths of the single peaks are significantly smaller (FWHM$\sim 70 - 110$ Hz) than the spacing between the trap sidebands which is on the order of about 3000 Hz.

RF spectroscopy measurements in the resolved sideband regime also work for repulsively interacting systems. The only difference is that the RF photon needs to provide less instead of more energy as in the case of attractively interacting systems.

---

[23] Since we are performing our experiments in the lowest states of the microtrap, we have to go back to a description in the quasi one-dimensional framework.

4.5 From Few to Many: Experiments with a Single Impurity Atom

We will now use RF spectroscopy in the resolved trap sideband regime to investigate the interaction between a single impurity atom and a growing number of atoms in a different state. In this measurement, the impurity atom, which we will also refer to as the atom with spin down ($|\downarrow\rangle$), can be considered to be a test particle which measures the influence of a growing number of majority atoms (also referred to as spin up $|\uparrow\rangle$). The systems we are going to investigate are repulsively interacting, i.e. $g_{1D} \geq 0$, and consist of a single impurity and up to five majority particles.

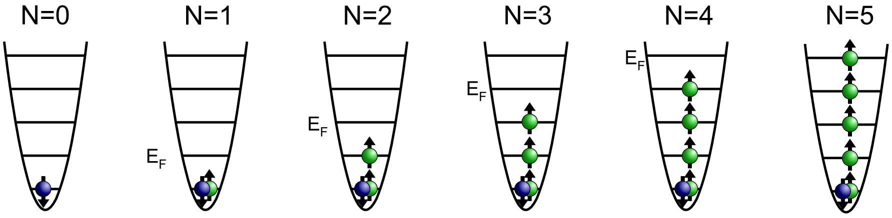

Figure 4.31: Initially prepared non-interacting $(N + 1)$-particle systems used as the starting point for the RF measurements. These samples are prepared according to the methods presented in section 4.2. Taken and adapted from [Wen13].

As a starting point, we prepare non-interacting $(N+1)$-particle systems with N majority atoms[24] and one single impurity atom in the non-interacting many-body ground state (see figure 4.31). The minority atom is located on the lowest trap level and the majority atoms fill the trap with one particle per state up to the Fermi energy E_F. We then introduce a repulsive interaction between the impurity and the majority atoms[25] and perform a RF spectroscopy measurement on the impurity particle. The RF spectroscopy is performed as a function of the number of majority atoms and measured for systems with weak ($g_{1D} = 0.36\, a_z\hbar\omega_z$), intermediate ($g_{1D} = 1.14\, a_z\hbar\omega_z$) and strong ($g_{1D} = 2.80\, a_z\hbar\omega_z$) interactions. The one-dimensional coupling strength g_{1D} will in this section always be given in units of $a_z\hbar\omega_z$, where $a_z = \sqrt{\hbar/(m\omega_z)}$ is the harmonic oscillator length in the axial z-direction of the microtrap[26]. Therefore, we will from now on refrain from writing these units.

---

[24] Note that we use the definition introduced in section 4.1.4 in order to have a notation which is consistent with [Wen13].

[25] There is no interaction between the majority atoms because they are identical fermions.

[26] In the previous sections of this chapter, we used the reduced mass for the definition of the harmonic oscillator length. Thus, all numerical values of g_{1D} given in units of $a_z\, \hbar\omega_z$ in this section become larger by a factor of $\sqrt{2}$.

4.5.1 Preparation of the (N+1)-Particle Samples

In the present section, we will explain the preparation procedure and estimate the preparation fidelity for the (N+1)-particle systems. This is done following the reasoning laid out in the supporting material of [Wen13].

We prepare balanced systems with an even total number of atoms ranging from 2 to 10 according to the scheme presented in section 4.2. These samples have the same number of atoms in state $|1\rangle$ and state $|2\rangle$ and are prepared with a fidelity of $f \gtrsim 88\%$. We then perform a second spilling process at low magnetic field ($\sim 40\,\mathrm{G}$) which only affects the atoms in state $|1\rangle$ (see section 4.2.6). For this spilling process we choose the barrier height such that all but one atom in state $|1\rangle$ are removed from the trap. This means we end up with systems consisting of N particles in the state $|2\rangle$ and a single impurity in state $|1\rangle$ (see figure 4.31). In most of the measurements that we will describe in the following, we want the impurity atom to be in state $|1\rangle$ and the majority component to consist of atoms in state $|3\rangle$. Therefore, we perform a Landau-Zener passage and transfer the N majority atoms from state $|2\rangle$ to state $|3\rangle$. This passage has an efficiency of 95% per atom. Thus, we obtain a fidelity of $\gtrsim 68\%$ for the preparation of these non-interacting $|1\rangle$-$|3\rangle$ systems with 5 majority particles.

In the next step we introduce a repulsive interaction by ramping to a magnetic field with $g_{1D} > 0$. Due to relaxation to states with lower energy we observe atom loss which is largest for strong interactions and large particle numbers. We obtain an upper bound of 29% on the probability for atom loss by investigating a system with $N = 6$ for the strongest interaction strength investigated here. Combining the fidelities of the different stages of the preparation yields a lower bound on the preparation fidelity of interacting $(N{+}1)$-particle systems of $\gtrsim 48\%$. As shown in [Wen13], the finite preparation fidelities for systems with $N \leq 5$ still allows us to extract reliable and meaningful results from the spectroscopic measurement. This is due to the fact that our RF spectroscopy is performed in the resolved sideband regime. Thus, most of the incorrectly prepared systems are either clearly separated from the relevant RF transition or just lead to a constant background which does not influence the measurement of the interaction energy. For even larger systems ($N > 5$), the fidelity quickly drops as a function of growing N. Hence, obtaining precise results for the RF spectroscopy measurement becomes challenging[27]. More details on the preparation fidelities and their influence on the obtained results can be found in the supplementary material of [Wen13].

4.5.2 The RF Spectroscopy Method

To probe the interacting $(N + 1)$-particle systems we change the state of the minority atom from the initial state $|\downarrow_i\rangle$ to a final state $|\downarrow_f\rangle$. When the final system is non-interacting, the interaction energy can be obtained by the frequency shift from the free-

---

[27] Furthermore, we do not want to populate more than 5 trap levels because in this case the influence of the first excited radial levels becomes significant and thus the system would leave the quasi one-dimensional regime.

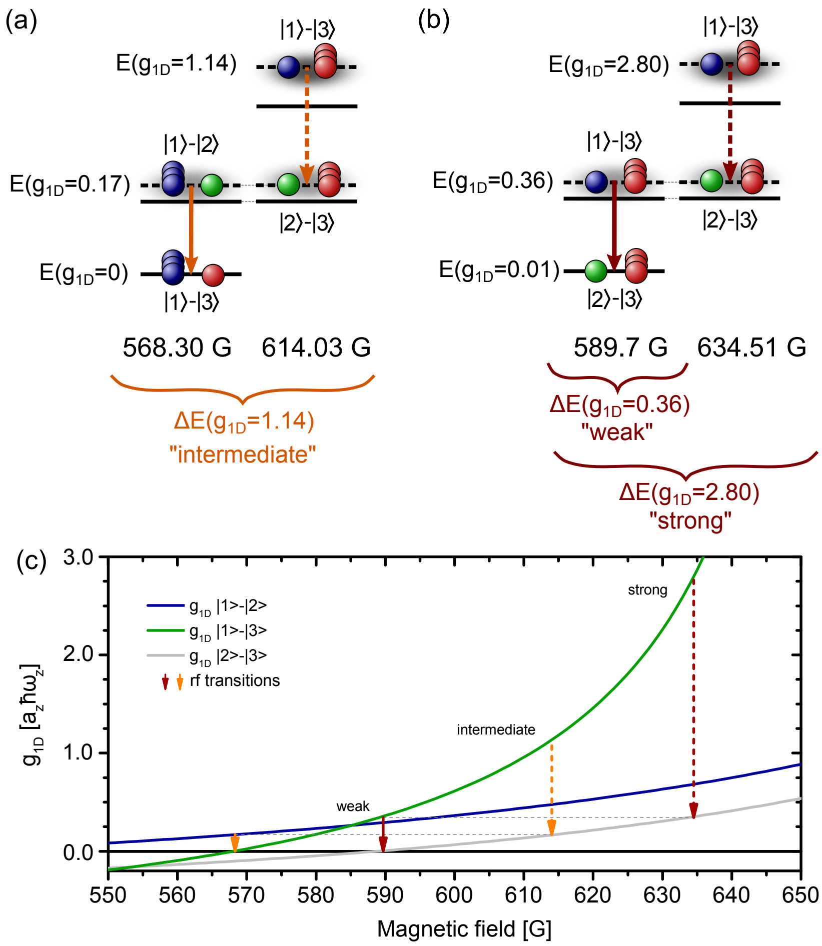

Figure 4.32: (a,b) Illustrations of the two-step process to determine the interaction energy of repulsively interacting few-particle systems. To reach a non-interacting final state we use an intermediate step for the measurement at strong ($g_{1D} = 2.80$) and intermediate ($g_{1D} = 1.14$) interaction strength. The majority component is indicated by the state with several atoms. (c) Magnetic field dependence of the one-dimensional coupling strength g_{1D} for all used hyperfine combinations. The vertical lines indicate the RF transitions used for the determination of the interaction energies. Taken and adapted from [Wen13].

free transition which is obtained for systems with no majority atoms (N=0). For weak interactions ($g_{1D} = 0.36$), we perform this measurement at 589.69 G where the final state, which consists of a $|2\rangle$-$|3\rangle$ mixture, is non-interacting. For strong ($g_{1D} = 2.80$) and medium ($g_{1D} = 1.14$) interaction strengths, there is no magnetic field where the final state is non-interacting. Therefore, we use a two step process which is illustrated in figure 4.32. This technique relies on the fact that the RF measurement determines the interaction energy difference between the initial and the final system. We can now use a second measurement (most of the time with a different spin mixture) and independently measure the interaction energy of the final system. By adding the two contributions one obtains the total interaction energy of the strongly interacting initial state. The magnetic field values, the initial and final states and their interaction strengths are summarized in table 4.5.

	B [G]	$g_{1\mathrm{D},i}$	$g_{1\mathrm{D},f}$	$\lvert\uparrow\rangle$	$\lvert\downarrow_i\rangle$	$\lvert\downarrow_f\rangle$
weak	589.69	0.36	0.01	$\lvert 3\rangle$	$\lvert 1\rangle$	$\lvert 2\rangle$
intermed. first	568.30	0.17	0.00	$\lvert 1\rangle$	$\lvert 2\rangle$	$\lvert 3\rangle$
intermed. second	614.03	1.14	0.17	$\lvert 3\rangle$	$\lvert 1\rangle$	$\lvert 2\rangle$
strong first	589.69	0.36	0.01	$\lvert 3\rangle$	$\lvert 1\rangle$	$\lvert 2\rangle$
strong second	634.51	2.80	0.36	$\lvert 3\rangle$	$\lvert 1\rangle$	$\lvert 2\rangle$

Table 4.5: List of all used RF transitions. Given are the magnetic field values, coupling strengths in the initial and final system as well as the hyperfine states of the atoms in the initial and final system. Table and caption taken and adapted from [Wen13].

4.5.3 The RF Spectra and the Interaction Energies

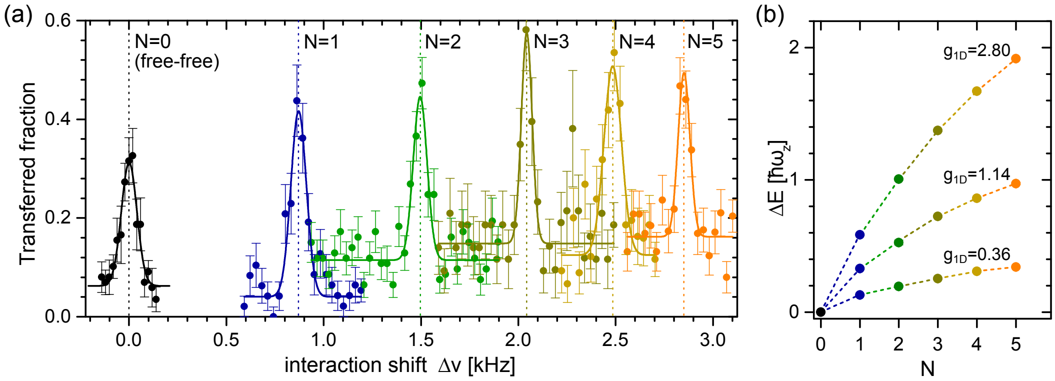

Figure 4.33: (a) Measured RF spectrum of the strongly interacting system ($g_{1D} = 2.80$) for one impurity atom and N majority atoms. For $N = 0$, there is no majority atom present and we therefore obtain the free-free transition frequency. (b) Interaction energies for all three interaction strengths as a function of the number of majority particles. They are obtained by Gaussian fits (solid lines) to the measured RF spectra. Taken and adapted from [Wen13].

Using the just described method we obtain RF spectra for all three interaction strengths as a function of the number of majority atoms N. Figure 4.33(a) shows the spectrum for strong interactions ($g_{1D} = 2.80$). As previously explained, we are in the resolved sideband regime and therefore we observe symmetric line shapes. We fit the peaks for different numbers of majority atoms with Gaussians. From the peak position we obtain the interaction energy ΔE as a function of the number of majority atoms. This quantity is shown in figure 4.33(b) for all three measured interaction strengths. The errors in the interaction energies are obtained by the uncertainty in the fits of the spectral peaks.

The number of atoms, with which the impurity can interact, increases when we add more majority atoms. It is therefore not surprising that the interaction energy increases with growing N. The absolute gain in interaction energy per additional majority particle however decreases in size if there are already more majority particles present. This behavior can be observed by the decrease of the slope of $\Delta E(N)$ for growing N. For weak interactions, it was shown in [Ast13] that the interaction energy should increase proportional to $\sqrt{N}$.

4.5.4 Natural Scales and Corrections due to Anharmonicity and the Finite Aspect Ratio

For a growing number of majority particles, the interaction energy shift ΔE is expected to diverge for $N \to \infty$. In order to compare the measurements for different N and to avoid this divergence, we rescale the interaction energy by the natural energy scale of the system, the Fermi energy E_F. We thus obtain a dimensionless interaction energy $\mathcal{E} = \Delta E/F_F$. In a trapped system, the Fermi energy is given by the lowest trap level that is not occupied by a majority atom. Since we are only interested in the gain of interaction energy, we set the energy offset[28] such that in a harmonic trap the Fermi energy is given by $E_{F,\mathrm{harm}} = N\hbar\omega_z$. Due to the anharmonicity of our microtrap (see section 4.3.1), the Fermi energy in our trap $E_{F,\mathrm{trap}}$ is slightly lower. From trap modulation measurements and WKB calculations we can precisely calculate the energy of the trap levels and hence derive the Fermi energy for our system. The corrections to the harmonic case are smaller than 2.5% and the obtained Fermi energies as a function of N are given in table 4.6.

The addition of majority particles changes the density of the investigated system. Therefore, it is useful to rescale the interaction strength g_{1D} with the line density of the majority component $\rho(z)$. We approximate the spatially varying density by its peak value[29] $\rho = k_{F,\mathrm{trap}}/\pi$ which is given by the Fermi wave vector $k_{F,\mathrm{trap}} = \sqrt{2mE_{F,\mathrm{trap}}}/\hbar$. With this rescaling of the interaction strength, we obtain the dimensionless interaction parameter[30]

$$\gamma = \frac{\pi m}{\hbar^2}\frac{g_{1D}}{k_F}. \tag{4.28}$$

---

[28] This means that we define our energy offset such that there is no zero-point motion of $\frac{1}{2}\hbar\omega_z$.

[29] This peak density approximation was shown to be very accurate for our system [Ast13].

[30] In a harmonic system where $E_F = N\hbar\omega_z$, the Fermi wave vector is proportional to $\sqrt{N}$ and thus $\gamma = \frac{\pi}{\sqrt{2}}\frac{g_{1D}}{\sqrt{N}}$.

N	1	2	3	4	5
$E_{F,\mathrm{harm}}[\hbar\omega_z]$	1	2	3	4	5
$E_{F,\mathrm{trap}}[\hbar\omega_z]$	1.01	2	2.97	3.93	4.88

Table 4.6: Comparison between the Fermi energies in a harmonic trap $E_{F,\mathrm{harm}}$ and in our slightly anharmonic trap $E_{F,\mathrm{trap}}$ for different numbers of majority atoms. We use the measured level spacing between the ground state and the second excited state of the trap as the reference for our harmonic approximation, since this is the most precisely determined level spacing of our trap [Zür12b]. Table and caption taken from [Wen13].

This quantity is often referred to as the Lieb-Liniger parameter (see section 2.6.1). We can therefore compare our data to the predictions made for a homogeneous system.

Because we want to compare our experimental results to theories calculated for a true one-dimensional system [Bus98, McG65], we also have to consider the effects resulting from the finite aspect ratio of the microtrap ($\eta = 10$). They are largest for strong interactions and for large particle numbers. The largest correction is on the order of 2% and we estimate it from the comparison between true one-dimensional [Bus98, Gha12, McG65] and quasi one-dimensional calculations [Idz05, Gha12, Blu12]. For the data taken at weak interactions ($g_{1D} = 0.36$), the relative correction is on the order of 2×10^{-3} which is smaller than the resolution of our measurement. Thus we neglect this contribution. For intermediate and strong interactions however the corrections need to be considered. The correction factors which rescale the interaction energies of a quasi 1D system onto those for a true 1D system are given in table 4.7. For strong interactions ($g_{1D} = 2.80$), we have theoretical predictions both for the true and quasi one-dimensional case for up to $N = 3$ majority particles. We can therefore calculate the correction factor by the ratio between these two values. For $N \geq 4$, we approximate the correction factor by the value for $N = 3$. For intermediate interaction strength ($g_{1D} = 1.14$), we only have calculations up to $N = 2$ and approximate the correction for $N \geq 3$ with the factor calculated for $N = 2$.

4.5.5 Comparison to Theoretical Predictions

With these corrections we can now compare our experimental data to theoretical predictions made for a true one-dimensional, homogeneous system. In section 4.1, we introduced the analytically determined interaction energies for the two-particle system ($N = 1$) [Bus98] and the many-particle system ($N \to \infty$) [McG65] with repulsive interactions. The interaction energies for these two cases are shown in figure 4.34(a) as solid lines. The many-body prediction for the interaction energy $\mathcal{E}_\infty$, as determined in [McG65], in orange and the two-particle solution ($\mathcal{E}_2$) in blue. Both predictions coincide for the two limiting cases of the dimensionless interaction parameter γ. For vanishing interaction strength $\gamma = 0$, the systems are non-interacting and

N	1 [Bus98, Idz05]	2 [Gha12]	3 [Blu12]	4	5
$g_{1\mathrm{D}} = 0.36$	1	1	1	1	1
$g_{1\mathrm{D}} = 1.14$	1.0051	1.0072	1.0072	1.0072	1.0072
$g_{1\mathrm{D}} = 2.80$	1.0106	1.0176	1.0206	1.0206	1.0206

Table 4.7: Correction factor for the finite aspect ratio of our trap. By multiplying our experimentally determined interaction energies for a quasi one-dimensional system with this number we can compare them to the theory derived for a true one-dimensional system [Bus98, Gha12, McG65]. The correction for the data at weak interaction is smaller than the resolution of our RF measurement and we thus neglect it. For intermediate and strong interactions we do not have precise theoretical predictions for large majority numbers ($N \geq 3$). We approximate these correction factors by the values obtained for the largest number of majority atoms available for this interaction strength. Table taken from [Wen13].

thus the interaction energy vanishes. Fermionization is reached in the opposed limit of diverging interaction strength $\gamma \to \infty$. There, the interaction energy of a system consisting of one impurity atom and N atoms in the majority component becomes equal to the energy of a system of $N + 1$ identical fermions. We already discussed the concept of fermionization for the two-particle system (see section 4.3.2). It was shown that, at least for the energy, this prediction still persists even for a larger number of particles[31] [Gir60, McG65, Gir10, Bro12, Gha12, Vol13, Ast13]. Lately, it was shown that the initially predicted "fermionized" wave function [Gir60, Gir10] is not the complete solution for the many-body wave function for diverging coupling strength [Gha12, Gha13, Vol13]. In between the limits of fermionization and vanishing interaction strength both theories have a similar functional form and only differ by a couple of percent. We can now add our experimental data[32] (colored points in figure 4.34) and compare them to the theoretical predictions. Due to the small difference between the two and many-particle solution it is useful to subtract the interaction energy of the two-particle system $\mathcal{E}_2$ from all interaction energies. In this way, one can see the differences between systems with different number of majority particles in more detail (see figure 4.34(b)).

The data for the two particle system ($N = 1$, blue dots) agrees well with the theoretical prediction (blue line) from [Bus98]. For $N = 2$, i.e. two majority atoms and the impurity atom, there is no analytic prediction but several state-of-the-art numerical calculations [Gha12, Bro12, Bug13, D'A13]. We compare our data for this system (green points) to the predictions made in [Gha12] and also obtain good agreement. For larger numbers of majority atoms one observes a quick convergence of the measured

---

[31] This statement is true for the balanced case ($N_\uparrow = N_\downarrow$) and for all imbalanced cases ($N_\uparrow \neq N_\downarrow$).

[32] This is the data after correction for the anharmonicity, the finite aspect ratio of the microtrap and using the peak density approximation.

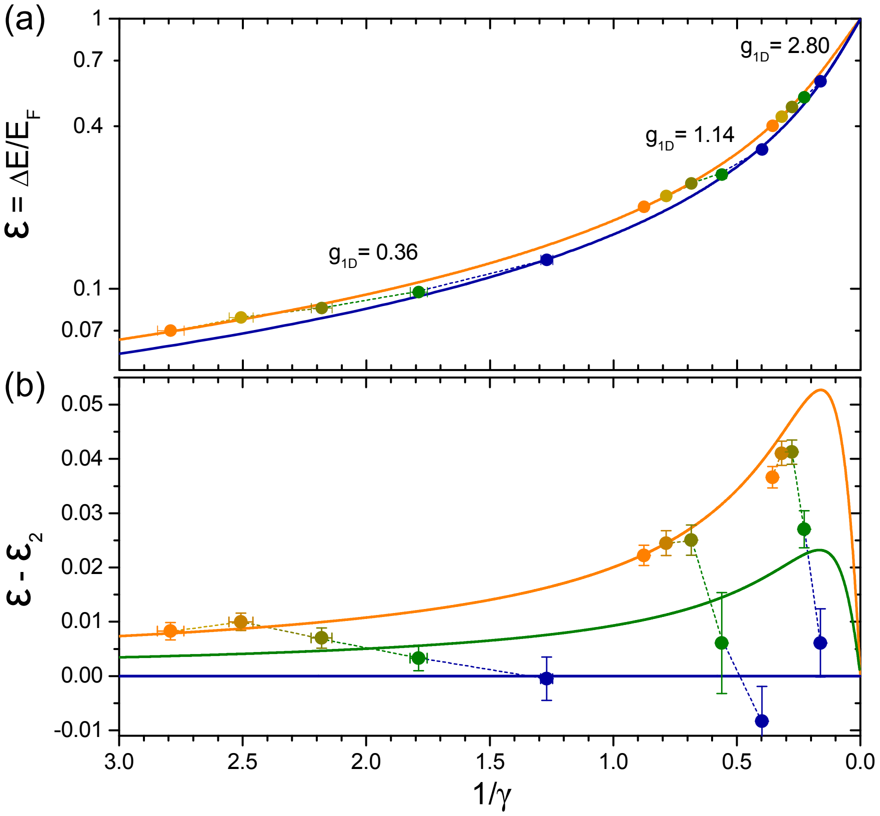

Figure 4.34: (a)Comparison between theoretical predictions for the normalized interaction energy for the two-particle system [Bus98] (blue line), the many-particle system [McG65] (orange line) and the experimental data (colored points). The colors of the data points indicate the number of majority atoms from $N = 1 \dots 5$ (blue to orange). (b) Difference between the normalized interaction energies and the theoretical prediction for the two-particle system ($N = 1$). The numerical prediction for the normalized interaction energy for $N = 2$ [Gha12] is shown as a green line. One observes that the measured interaction energies for the two-particle system agree well with the theoretical prediction. For $N \geq 4$ the normalized interaction energy converges towards the many-body limit which is indicated by the orange line. Taken from [Wen13].

interaction energy towards the analytic many-body prediction given in equation 4.10 [McG65]. For strong interaction strengths, the data follows the shape of the theoretical model but lies slightly below the prediction. This small deviation might be due to the peak density approximation or uncertainties in the corrections for anharmonicity and finite aspect ratio of the trap. For weak and intermediate interaction, already four majority particles seem to be sufficient to reach a system which is well-described by the theory for $N \to \infty$. This shows that one of the most important properties of the investigated systems, namely the interaction energy, is already well-described by the many-particle theory for as few as 4 majority particles.

4.6 Conclusion and Outlook

The amount of theoretical predictions with different state-of-the-art numerical and analytical approaches for the description these kind of few-fermion systems is steadily increasing (e.g. [Gir60, McG64, McG65, McG66, Bus98, Mor04, Kes07, Gir09, Gir10, Liu10, Bro12, Gha12, Ron12, Ast13, Bro13, Bug13, Cui13, D'A13, Deu13, Gha13, Gua13, Lin13, Sow13, Vol13]). This shows the importance of experimental studies with these mesoscopic systems as a benchmark for the evaluation of various different techniques and models.

It is truly remarkable that only about four majority atoms are necessary for the energy of the impurity system to be well-described by the many-body prediction [McG65]. Additionally, this quick convergence of the interaction energy raises several intriguing questions for future theoretical and experimental studies. For example, one wonders how quickly the few-particle wave function converges towards the infinite particle limit. Additionally, one could also measure the effective mass of the system as a function of the number of majority atoms and compare it to the predictions by McGuire (see equation 4.11 and figure 4.10). This could be achieved by measuring the excited trap sidebands as shown in figure 4.30. In this way, one would obtain the excitation spectrum and thus the effective mass of the system. Measuring the excitation spectrum as a function of the number of majority atoms would also lead to further insights to the polaron-like disperson relation that persists for weak interactions even for a one-dimensional system (see section 4.1.5). We already mentioned that the quasiparticle operator becomes ill-defined for a homogeneous one-dimensional system [Gua13, Mas13]. In our experiments, we are only quasi one-dimensional and trapped in a harmonic potential. How the impurity system behaves in this case is so far not clear and would be an interesting topic for future research. One could then investigate the emergence of polaronic properties when the system leaves the quasi one-dimensional regime and radial excitations become allowed. Studying this behavior as a function of the number of majority particles could help to gain a deeper understanding of the fermionic quantum impurity problem.

Another interesting question when expanding such an impurity system to higher dimensions would be to investigate the point of diverging coupling strength. Although the lifetime of a strongly interacting repulsive fermionic quantum impurity system is expected to be very short, the repulsive polaron state itself is still well-defined. For the one-dimensional case we know that $\Delta E/E_F \to 1$ for $g_{1D} \to +\infty$. For the three-dimensional system one expects that the Fermi energy E_F remains the only energy scale of the system if the interaction strengths diverges. Hence, any universal energy in the unitary regime should be described by a numerical universal constant ζ times the Fermi energy E_F. In this case, one would obtain the following limit for the repulsive polaron branch: $\Delta E_{3D}/E_F \to \zeta$ for $k_F a \to +\infty$. This 3D fermionization parameter ζ can be thought of as a quantity which is similar to the Bertsch parameter ξ, just for a repulsive system with a single impurity.

An entirely different topic that can also be investigated, especially in one-dimensional systems, is the emergence of ferromagnetic correlations between the particles in the super-Tonks regime. We already performed some investigations in this regime but up to now they are not fully understood. There are however several theoretical publications [Liu10, Gha13, Vol13, Bug13, Deu13, Cui13] that consider the question whether ferromagnetic correlations are obtained for these super-repulsive systems.

All these considerations and future research opportunities show that there is still a lot to learn about the system where one impurity atom interacts with a larger number of other fermions. The control over the number of particles and the interaction strength as well as the possibilities to change the trapping geometry and hence the dimensionality of a system make ultracold few-particle systems a perfect candidate to further explore these kinds of questions.

5 Long Timescale Dynamics of a Spinor BEC of Rb-87

In this chapter we discuss experiments on the equilibration of F=1 spinor BECs of ^{87}Rb performed during my stay (May 2009 to July 2010) at the University of California, Berkeley in the group of Prof. D. M. Stamper-Kurn. A spinor BEC is a condensate that, due to its additional spin degree of freedom, is no longer described by a scalar field but instead by a three-dimensional spinor [Ho98]. This property significantly influences the phase diagram of such systems since the vector magnetization plays a crucial role in the determination of the ground state structure and the dynamics of such systems.

By combining phase or polarization-contrast imaging with spin-echo techniques we observe the evolution of the vector magnetization for such a spinor system. We investigate the spin dynamics of different initial spin mixtures and observe that small spin textures ($\sim 10\mu$m) coarsen to larger ferromagnetic domains for long evolution times of up to 4 seconds. The system therefore approaches the expected mean-field phase. The system, however, only reaches a steady state for small quadratic Zeeman shifts ($|q| \lesssim q_0$). Furthermore, we observe the emergence of a spin space anisotropy with predominantly easy-axis or easy-plane magnetization depending on the sign of the quadratic shift. The main findings and techniques presented in this chapter are published in [Guz11] and further details are described in [Guz12]. We will thus in most cases follow their notation and line of reasoning.

To illustrate and understand the performed measurements, this chapter starts with a brief introduction on Bose-Einstein condensation and spinor BECs. We will then discuss the properties and techniques used in this particular experiment setup. After a basic introduction into the theoretical description of spinor gases we will introduce the utilized imaging techniques before finally presenting the actual measurements and results.

5.1 Introduction and Motivation

The possibility to trap BECs in optical dipole traps [Sta98a] enabled trapping of several spin states at the same time with negligible differences in the trapping potential for the different states. Consequently, researchers could then investigate systems with an additional spin degree of freedom. The theoretical framework to describe such ”spinor” or multi-component Bose condensates was established in 1998 [Ho98, Ohm98]. This name was chosen because contrary to a single-component BEC, where the order parameter $\psi(\mathbf{r})$ is a scalar, the order parameter in a BEC with a spin degree of freedom is a vector quantity and transforms like a vector under spin space rotations. Soon afterwards the formation of spin domains in a BEC could be observed. This was achieved with a spinor BEC of ^{23}Na in the $F = 1$ manifold which consists of the three states with $m_F = +1, 0, -1$ [Ste98].

A wide range of new quantum phenomena are predicted for these spinor Bose-Einstein condensates. Due to the vector character of the magnetization, one expects: a change in structure of the ground state [Sad06b], the emergence of spin textures [Ven08], topological and energetic instabilities, the occurrence of special modes of spin waves, a change in spin dynamics through coherent spin changing collisions and the existence of skyrmions [Kha01, Cho12a, Cho12b] to just name a few. Studying these phenomena opens up a new playground for research with ultracold atoms. In this chapter, our contribution towards the ongoing effort to understand such systems is described. We will focus on our investigations on the dynamics of initially unmagnetized spinor systems. After condensing, these systems show small scale (order of a few microns) spin textures that slowly grow in size and evolve towards the expected ferromagnetic ground state.

5.2 Experimental Setup

The structure of the vacuum chamber of the Berkeley setup is very similar to the chambers used in Heidelberg and most of its parts and their properties were already discussed in chapter 3. Therefore, these standard parts and techniques are only briefly presented, whereas the particular features of this setup which allow the studies of spinor BECs are described in more detail. For a more extensive description of this experimental setup we will refer to [Guz12].

5.2.1 Preparation of a BEC and the Vacuum Chamber

A drawing of the vacuum chamber of the spinor machine can be found in figure 5.1. The setup consists of three major parts: the oven chamber, the MOT chamber and the science chamber. We will now present the different steps for the preparation of a Bose-Einstein condensate with this particular experimental setup.

The Oven Chamber

The purpose and the idea behind the design is to provide an atomic beam of sufficient flux while maintaining a low vacuum pressure in the MOT and science chamber. However, the higher vapor pressure of rubidium at room temperature leads to some design differences compared to the lithium oven presented in chapter 3. This has several implications. First, the oven does not have to be heated that much. Therefore, the oven in Berkeley was usually only heated to 115°C [1]. A second consequence is that

---

[1] In the case of lithium the oven is usually operated at 350°C to 400°C.

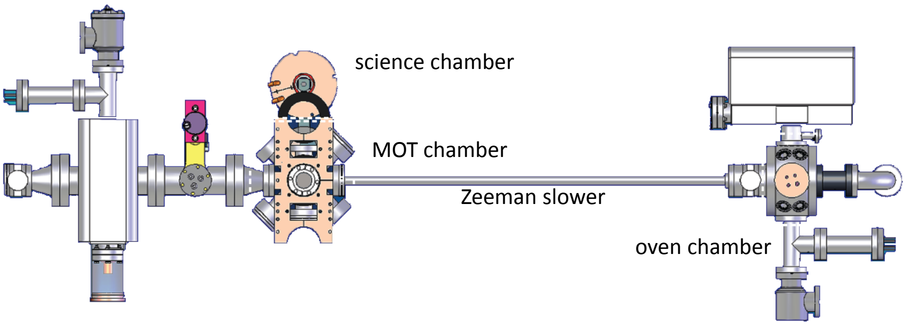

Figure 5.1: Vacuum chamber of the ^{87}Rb spinor BEC machine. The chamber consists of three main parts. The oven chamber where the rubidium is vaporized, the MOT chamber where the atoms are caught in a MOT and precooled in a magnetic quadrupole trap and the science chamber where the optical dipole trap is located and where the actual experiments take place. Taken and adapted from [Guz12].

even at room temperature the vapor pressure of rubidium is non negligible. Thus, one has to be more careful where the atoms end up that are not cooled and trapped in the Zeeman slower and the MOT. For this reason, the oven chamber has an additional copper piece with a small aperture in the direction of the Zeeman slower tube which is called cold catcher. Using a thermo-electric cooler (TEC), the cold catcher is cooled to temperatures of about −15°C to −10°C which means that the majority of rubidium atoms that do not travel directly towards the slower are caught by it. In order to save rubidium in the oven reservoir, we use a special exit nozzle which creates a large flux of atoms in the direction of the Zeeman slower with a low transverse momentum spread. Since this nozzle is constantly heated to 200°C, the atoms that cannot travel through it are recirculated back into the reservoir. To further reduce the pressure in the MOT and science chamber, there is an atomic beam shutter that dumps the beam inside the cold catcher when necessary. In order to allow for easy maintenance of the oven chamber, e.g. for refilling the reservoir, a gate valve is placed between the oven section and the Zeeman slower tube.

The MOT and the Magnetic Transport

After leaving the oven chamber the atomic beam is decelerated in the Zeeman slower, which is built in an increasing field configuration and is described in detail in [Mar10a]. When the atoms reach the MOT they are already decelerated to about 20 m/s after initially leaving the oven with about 300 m/s. In the MOT the atoms are further cooled and trapped using cooling light that is red detuned by about 18 MHz from the $D2$ F=2 to F'=3 transition (see figure 5.2). The six MOT beams have a diameter of about 38 mm and the total power in all beams is about $130 - 150$ mW. Additionally, we use repump light which is resonant to the $D2$ F=1 to F'=2 transition with a total power of about 2.5 mW. With these parameters it takes about 4 s to load approximately

8×10^9 atoms into the MOT and they have a temperature of about $150 - 200\,\mu$K.

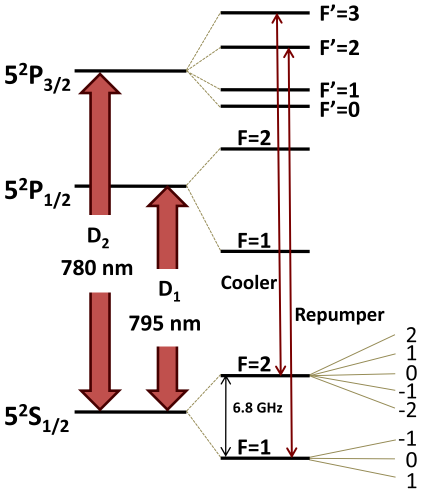

Figure 5.2: Level scheme of ^{87}Rb. Laser cooling and absorption imaging is usually performed using the $D2$ transition (see cooler and repumper). For phase-contrast imaging we use a laser with a wavelength of about 795 nm which is blue detuned from the $D1$ line.

Before transferring the atoms into the magnetic quadrupole trap, the MOT is compressed by increasing the magnetic quadrupole field of the MOT while decreasing the intensity of the MOT beams. Afterwards all MOT beams and magnetic fields are turned off for about 2 ms for optical pumping, before the atoms are trapped in the magnetic quadrupole trap. From there, the cloud is magnetically transported to the science chamber with three additional sets of overlapping quadrupole coils. During this 6 s long transport, the atoms are heated to about $600 - 900\,\mu$K. More details on the transport parameters and optimization are given in [Guz12]. The reason for magnetically transporting the atoms into the glass cell is that the vacuum limited lifetime in the science chamber is significantly better than in the MOT chamber. Additionally, the glass cell offers more optical access which is important for the high-resolution imaging system and for the planned optical lattice setup. Furthermore, using a glass cell also increases the amplitude of RF and MW fields that can reach the trapped atoms since a metal chamber usually absorbs and reflects parts of the fields.

Evaporation in the Science Chamber

The science chamber consists of a glass cell that is connected to the MOT chamber (see figure 5.3). The dimensions of the glass cell are about 25 mm×25 mm×75 mm and the walls have a thickness of about 2.5 mm. The last of the three magnetic transport coils is independently mounted and cooled (black part in figure 5.3) and was initially designed to produce homogeneous offset fields to be able to access magnetic Feshbach resonances at fields up to about 1000 G. For all the experiments described here, however, we only

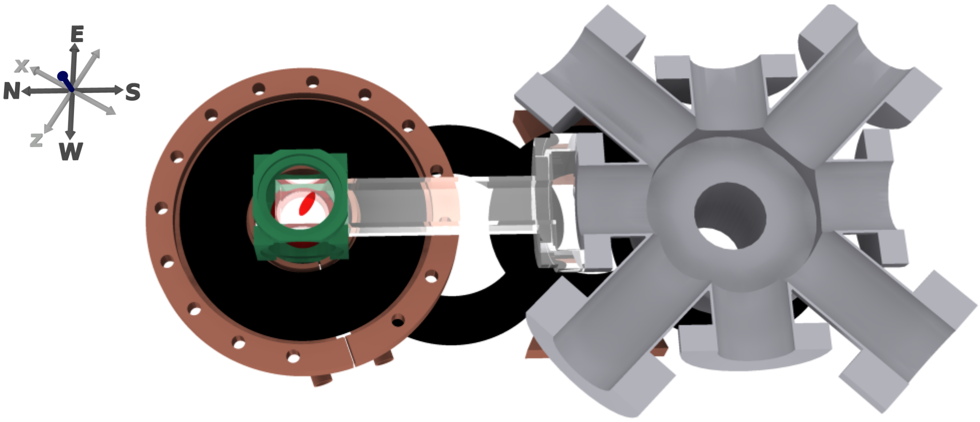

Figure 5.3: Cut through the main part of the vacuum setup with the MOT chamber (gray), the glass cell (clear) and the used coordinate system (left). The atoms are moved into the glass cell using the magnetic transport coils (black). After MW evaporation they are transferred into the optical dipole trap which is aligned in the z-direction. Here the atomic cloud (bright red) is further evaporated into degeneracy. The magnetic field cage (green) is used to apply and compensate magnetic fields and gradients in various directions.

used it as the final magnetic quadrupole trap where the atoms are further cooled by MW evaporation. This evaporation starts with about 2×10^9 atoms in the magnetically trappable state F=1, $m_F = -1$ ($|1, -1\rangle$). By applying a circularly polarized microwave field slightly detuned from the $|1, -1\rangle$ to $|2, -2\rangle$ transition, the trapped atoms with the highest temperature and energy are transferred to state $|2, -2\rangle$. Atoms in this state are not trapped and thus lost from the trap. By sweeping the MW frequency closer to resonance the atomic sample is evaporatively cooled and after 10 s of this MW knife evaporation we obtain samples with about 1×10^8 atoms at a temperature of about 30 μK. Already during the last stages of this MW evaporation the ODT is turned on and after finishing the MW evaporation about 1×10^7 atoms are transferred into the optical trap. By exponentially lowering the intensity of the ODT beam over 2.4 s we further evaporate until we reach the critical temperature for Bose-Einstein condensation. At the critical temperature T_c the sample consists of about 3.5×10^6 atoms. After further evaporation we can obtain BECs consisting of about 2×10^6 atoms with negligible thermal fraction. Table 5.4 summarizes the temperature, the atom number and the phase space density of the atomic cloud in the different stages of the experiment.

5.2.2 The Optical Dipole Trap

The laser light for the single beam ODT is provided by a fiber laser (IPG Photonics) at a wavelength of 1064 nm and a maximum power of 20 W. Thus the light of the dipole trap is red detuned from the atomic transitions of ^{87}Rb at 780 nm and 795 nm. Due to

Stage	Temperature	Number	Phase-space Density
Oven	475 K ($\sim$ 300 m/s)		
Zeeman Slower	4 K ($\sim$ 20 m/s)		
MOT	$\sim 150 - 200\,\mu$K	8×10^9	$\sim 10^{-6}$
		(2×10^9 s^{-1})	(4 s loading)
Magnetic Trap (TP0)	$\sim 150 - 200\,\mu$K	2×10^9	$\sim 10^{-6}$
Glass Cell, no evap.	$\sim 600 - 900\,\mu$K	2×10^9	$\sim 10^{-7}$
End of μ-Evaporation	$\sim 30\,\mu$K	100×10^6	$\sim 5 \times 10^{-4}$
End of Optical Trap Evap.	$\sim$ 100 nK	2.5×10^6	$\gg 1$

Figure 5.4: Number of atoms, their temperature and phase-space density during the different stages of the experiment. Taken from [Guz12].

this large detuning, the photon scattering rate is negligible and therefore does not limit the lifetime of atoms in the sample. For the active intensity stabilization the ODT beam passes through an acousto-optical modulator before it is magnified in two perpendicular cylindrical telescopes. These generate an elliptical beam where the vertical size is about 10 times larger than the horizontal one. This beam is then focused into the glass cell along the z-direction (see figure 5.3) and leads to a "surfboard" shaped trap with an aspect ratio of $\omega_y \approx 10\,\omega_x \approx 50\,\omega_z$. This means that the tightest confinement is in the vertical y-direction and the weakest in the z-direction. During the transfer from the magnetic trap the power of the ODT beam is about 4.5 W which corresponds to a trap depth of about 0.3 mK which is sufficiently larger than the temperature of the atoms at that stage ($30\,\mu$K). After the evaporation, the final trap depth is about $1\,\mu$K which corresponds to about 30 mW of power in the ODT beam. The Thomas-Fermi radii of the finally achieved BEC are about $r_z \approx 80\,\mu$m, $r_x \approx 20\,\mu$m and $r_y \approx 2\,\mu$m. The reason we choose such a trap geometry is that in our system the spin healing length ξ_{spin} is similar in size to the condensate in vertical direction. Therefore, the condensate is quasi two-dimensional with respect to the spin degree of freedom [Ven08]. This will make it easier to image the spin in-situ since the change of the spin along the imaging direction is then negligible[2].

5.2.3 Static Magnetic Fields

It is obvious that applying static magnetic fields is a very important tool when working with the spin of a system. Through the Zeeman effect the energy and the structure of the system is determined by magnetic fields. It makes sense to distinguish between different field configurations: static offset fields, static magnetic field gradients and oscillatory fields. In our setup both types of static fields are provided by different sets of coils mounted in a cage made of plastic (Delrin, see green part in figure 5.7(a)). Additionally, two pairs of coils along the long axis of the optical dipole trap (z-direction) were added later.

---

[2] This is not true for the healing length ξ, therefore the sample is a 3D BEC with respect to the density but quasi 2D with respect to spin.

Magnetic Offset Fields

The offset fields are provided using pairs of coils that are approximately in Helmholtz configuration which is done to achieve as homogeneous fields as possible. In order to be able to provide an offset field along any necessary direction we use three different sets of coils which are named according to the orientation: the up-down coils, the north-south coils and the z coils. Two sets of coils (up-down and north-south) are mounted inside the magnetic field cage. The z coils were added later and are attached to the outside of the heat sink of the magnetic quadrupole trap coils. This was necessary since the east-west coil pair in the Delrin mount was found to be electrically shorted to the main chamber and the optical table.

Using RF transitions from state $|\mathrm{F}{=}1{,}m_F{=}{-}1\rangle$ to the states $|\mathrm{F}{=}1{,}m_F{=}0 \text{ or } 1\rangle$ the offset fields created by each pair of coils were calibrated. A small program was then created to calculates the control voltages for each coil given a desired field strength and direction. This program significantly simplified the field calibration procedure because the field coils are neither perpendicular to each other nor necessarily along the axis of the condensates. This means that one usually needs a combination of current through several sets of coils to produce an offset field in a certain direction.

The magnetic offset field value we usually use during the experiments is $0.267\,\mathrm{G}$ which corresponds to an RF transition frequency of about $187\,\mathrm{kHz}$. In most cases the field is directed along the intermediate axis of the cloud which is also called the x-direction (for a definition of the directions, see figure 5.3).

Magnetic Field Gradients

In order to minimize the inhomogeneities of the magnetic fields we use magnetic gradient coils to actively cancel existing gradients. To create these gradients we use sets of coils in anti-Helmholtz configuration. This leads to a vanishing offset field in the center of the two coils. The magnetic field on the center axis of the coil pair depends linearly on the distance from the center.

Due to the small extent of the condensate in the up-down or y-direction ($r_{TF,y} = 2\,\mu\mathrm{m}$), magnetic field gradients along this direction can be neglected. The gradients we therefore need to cancel are along the long (z-direction) and intermediate axes (x-direction) of the condensate, namely dB_z/dz, $dB_z/dx = dB_x/dz$ and dB_x/dx. At an offset field of $267\,\mathrm{mG}$ the uncorrected field gradients were about $20 - 40\,\mathrm{kHz/cm}$ depending on the particular direction. To minimize these gradients we use three sets of coils. They are named according to their orientation: the z-gradient coils, the up-down gradient coils and the north-shim gradient coils. We use Larmor precession imaging to measure the gradient that is applied to the atoms by observing the local phase of the precession of transversely magnetized clouds (see section 5.4.2). Then the current through each of the three coils is adjusted to minimize the size of the magnetic field gradients. By gradually increasing the evolution time after which we measure the gradient, we can increase the sensitivity of our gradient measurement. Precession could be observed up to 3 s of evolution time and in the end the measurement was limited by the lifetime of the condensate. We can deduce that for this configuration, the inhomogeneities of the magnetic fields are less than 1 μG over the size of the condensate. This corresponds to an absolute field inhomogeneity of about 6 μG/mm. Compared to the offset field of 267 mG this leads to an inhomogeneity of about 2×10^{-5} over one mm. More details and images of the cloud with and without a gradient can be found in section 5.4.2.

5.2.4 RF and MW Pulses and Magnetic Field Stability

As introduced in chapter 3, the populations of different hyperfine states and their Zeeman sublevels can be manipulated using radio-frequency (RF) or microwave (MW) pulses. Here, this technique is employed to prepare the desired spin mixture and later to probe the spinor samples. As previously explained, we also use these transitions to calibrate our magnetic fields since the transition frequency between the states depends on the applied magnetic offset field through the Breit-Rabi formula.

Radio-Frequency Fields and Magnetic Field Stability

The RF fields necessary for driving the transition between the states of the $F = 1$ manifold are on the order of several hundred kHz. In our setup these fields are generated with a function generator (Stanford Research System DS345) which can provide RF signals of up to 30 MHz. After the generator, the signal passes a RF switch before it is amplified and applied to the atoms using a RF antenna, which consists of a single copper winding placed right above the glass cell.

While calibrating the magnetic offset fields, we observed a transfer of atoms into different states for smaller magnetic fields, even when the RF signal is turned off. This effect can be attributed to RF noise from different sources in the lab, for example switching power supplies, DC/DC converters or other noise on the power line. A more careful investigation reveals a broad noise background up to about 100 kHz and several noise peaks in the region up to 130 kHz. This limits the magnetic offset fields available for our studies of the spinor condensates because the noise would strongly affect our measurements. For this reason, we choose a field of 267 mG which corresponds to an RF transition frequency of 187 kHz which is in a region without measurable RF noise.

In addition to this RF noise we also noticed that the resonance frequency of the RF transitions fluctuate by about 10 kHz over the course of a day. This rather large effect makes it difficult to drive several RF π or RF $\pi/2$-pulses which are necessary for some of our measurements and imaging techniques. Therefore, we decided to monitor the magnetic field in our laboratory. For this we used a magnetometer (Honeywell HMC2003), which can precisely measure magnetic fields in a range from 40 μG to 2 G in three orthogonal directions. The signal from this sensor was then measured using highly precise voltmeters (Agilent 34410 Digital Multimeter). Using a self-written Labview code, we were able to log the magnetic field in our laboratory over a couple of

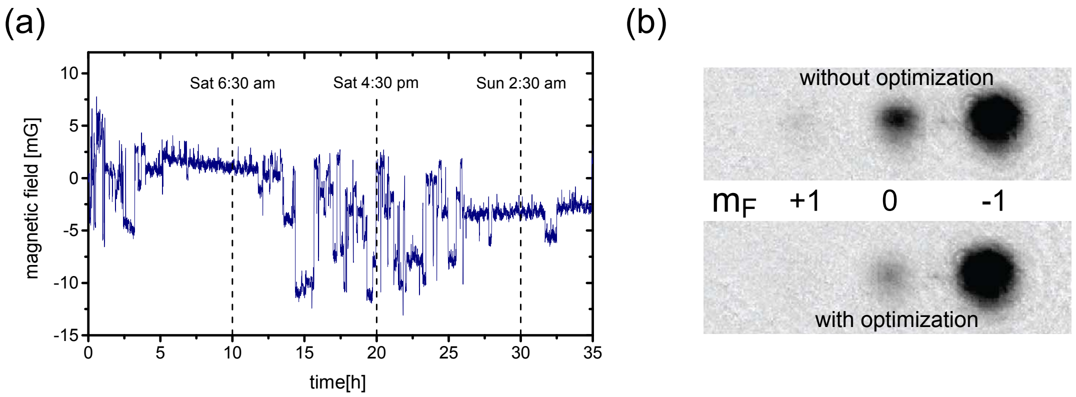

Figure 5.5: (a) Magnetic field in the laboratory measured with the three-axis magnetometer. The field fluctuations are caused by the elevator across the hall from the laboratory. One can clearly see at which times the elevator was used and in which floor it was at a given time. (b) Populations after 4 sequential π-pulses in the different hyperfine states of the F=1 manifold with and without careful optimization of the RF pulse amplitude. The images were taken using Stern-Gerlach time-of-flight absorption imaging. Figure adapted from [Guz12].

days. The result of such a measurement can be found in figure 5.5(a). We observed a correlation between the activity of the elevator and the measured fields and therefore concluded that these strong magnetic field fluctuations are caused by the elevator with its large iron counterweight.

There are several possible ways to circumvent this problem of changing magnetic fields due to the elevator. They range from simpler solutions of deactivating the elevator for the course of important measurements to more sophisticated solutions like implementing a feed forward on the magnetic field or frequency of the RF pulse. We opted for a simple method of shortening the pulse duration, so that the frequency width of the RF pulses are increased. In order to still transfer all of the atoms one has to increase the amplitude of the RF field at the same time. In this way, we increased the Rabi frequency to about 25 kHz which is sufficient to not be limited by the shot-to-shot fluctuations of the magnetic field anymore.

For the spin-echo imaging technique it is crucial to be able to drive several sequential RF π-pulses with high fidelity. We therefore determine the transition frequency which is not extremely critical due to the large frequency width of the applied pulse (see above). Then we optimize the applied amplitude by checking the optimal transfer of atoms between the different hyperfine states after several π-pulses. Figure 5.5 (b) shows that by optimizing the signal after 4 sequential RF π-pulses we can significantly improve the fidelity of RF π-pulses.

Microwave Fields for Evaporation and for Quadratic Zeeman Shift

The spinor experiment has two different setups to generate and apply MW pulses. The first one is used for the MW evaporation in the magnetic trap and was already briefly described earlier. We will therefore focus on the second MW setup which is of more interest for the performed experiments. It is used to tune the quadratic Zeeman energy of the sample. We will later see that this quadratic Zeeman energy plays a crucial role in the determination of the ground state of the ^{87}Rb spinor system in the $F = 1$ manifold.

We apply a MW field which is detuned from the $|1,0\rangle$ to $|2,0\rangle$ transition by $\delta = \pm 2\pi\, 40\,\mathrm{kHz}$. This changes the energy of the $|1,0\rangle$ state with respect to the $|1,\pm1\rangle$ states. We will later see that this is the quadratic Zeeman energy and that it scales proportionally to the square of the resonant Rabi frequency and inversely proportional to the detuning δ [Les08]. Therefore, we can modify the quadratic Zeeman shift provided by the MW fields q_{MW} by changing the power of the microwaves at a fixed detuning. We choose the detuning large enough so that the population transfer into the $|2,0\rangle$ state is negligible but not so large that the states $|1,\pm1\rangle$ are significantly shifted.

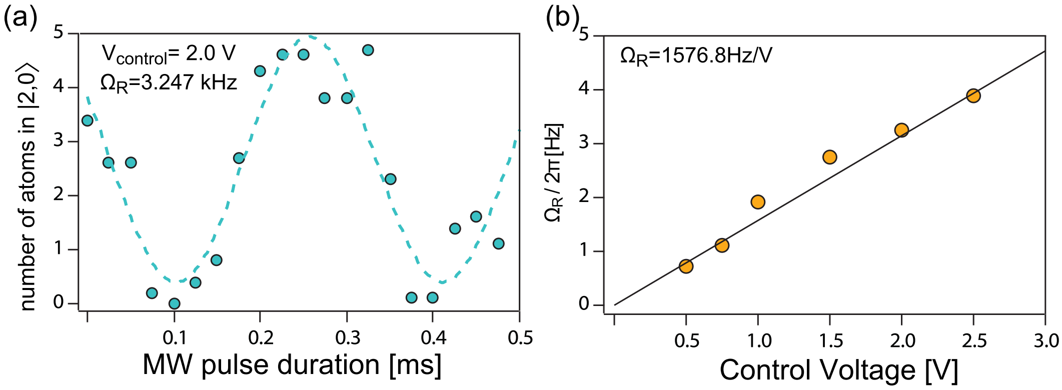

Figure 5.6: (a) Rabi oscillations between the states $|1,0\rangle$ and $|2,0\rangle$ at a control voltage of 2 V at the modulation input of the SRS waveform generator. (b) Calibration between Rabi oscillations and the control voltage. Figures adapted from [Guz12].

The setup consists of a MW source which provides a signal at 3.4 GHz. This signal is then frequency-doubled and mixed together with a signal at a frequency of about 20 MHz created by a SRS DS340 waveform generator. After an amplifier (20 W) the signal is impedance-matched with a stub tuner (Maury Microwave 1819D) to a linear MW waveguide which applies the linearly polarized MW field to the atoms. By scanning the frequency of the SRS sideband, we can find the resonance frequency of the $|1,0\rangle$-$|2,0\rangle$ transition and then measure the Rabi oscillation between these two states as a function of the applied RF power in the sideband (see figure 5.6(a)). With this calibration we know the Rabi frequency as a function of the amplitude of the SRS (figure 5.6(b)) and therefore we can calculate the applied quadratic shift using this Rabi frequency and the detuning of $\delta = 2\pi\,40\,\text{kHz}$. With these parameters, we are able to reach quadratic Zeeman energies of up to $q_{MW} \approx h \times 500\,\text{Hz}$, both positive and negative depending on the sign of the detuning. This is significantly larger than the quadratic Zeeman energy provided by the offset field of 267 mG which is on the order of $q_B = h \times 5\,\text{Hz}$. Hence, we can access all relevant regimes in the $F = 1$ spinor phase diagram.

5.2.5 The High-Resolution Imaging Setup

In our experiments we are interested in small scale structures of the size of the spin healing length ξ_{spin}, which in our system is on the order of $\approx 1.5\,\mu\text{m}$ [Guz12]. Therefore, we need an imaging system that has at least a resolution of the same order of magnitude. Since it is too complicated to place flexible imaging optics inside the vacuum, we have to image our sample through the glass cell. In order to obtain the information we are interested in, the high-resolution objective is used in the vertical (y-direction) and mounted in the center of the cooling body for the magnetic quadrupole field coils (see figure 5.7). Due to the size of the glass cell, the working distance of the objective has to be $\geq 13\,\text{mm}$ and the field of view should be large so that the whole cloud can be imaged without strong aberrations.

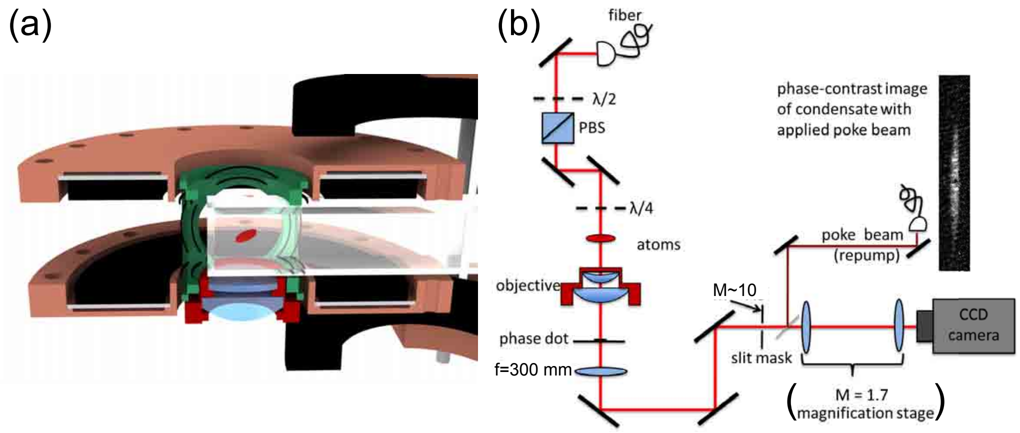

Figure 5.7: (a) Vertical cut through the science chamber. The high-resolution objective (dark red) consisting of an asphere (lower light blue) and a meniscus (upper light blue) is placed inside the bottom part of the magnetic field cage (green). The field cage houses several sets of coils in various directions which provide magnetic gradient and compensation fields (narrow black circles). (b) Schematic of the complete phase-contrast imaging setup.

Designing the Objective

The idea during the design phase the objective was to use one large aspheric lens (Thorlabs AL3026-B, focal length $f = 26.0\,\mathrm{mm}$, NA$= 0.52$, working distance $\sim 20\,\mathrm{mm}$) which is diffraction-limited when used without a glass cell. Furthermore, we planned to use a second meniscus lens that compensates for the effects of the 2.5 mm thick glass cell. The optical design software OSLO was used to find the parameters of a suitable meniscus lens by optimizing the obtained spot size and wave front error function. The resulting requirements were met by a BK7 meniscus lens from JML optical (CMN11258) with a focal length of $f = 1000\,\mathrm{mm}$. A vertical cut through the objective assembly consisting of the two lenses (light blue) inside their custom-built mount (dark red) can be found in figure 5.7(a).

The High-Resolution Imaging Setup

We want to use the high-resolution setup to take in-situ phase or polarization-contrast images of our spinor condensates. As explained before we use a laser that is blue-detuned from the $D1$ line by about 400-500 MHz for phase-contrast imaging. The laser light for this is provided by a Vortex II laser from New Focus which is locked to the D1 line of a ^{87}Rb vapor cell using a Doppler free FM-spectroscopy lock. The light is then frequency shifted by passing twice through a 250 MHz acousto-optical modulator (IntraAction) before it is coupled into a polarization maintaining single mode optical fiber. In this fiber, the light is then delivered to the experiment table. Figure 5.7(b) shows the schematic setup of the imaging path from the fiber to the CCD camera used to image the atoms with phase-contrast imaging. After cleaning the polarization and adjusting the intensity of the beam using a combination of a half-wave plate and a polarizing beam splitter, the light passes through a quarter-wave plate to obtain a σ^+- polarization which is necessary for magnetization sensitive phase-contrast imaging (see section 3.4.3). After passing through the atoms, the light is collected by the objective which has an effective focal length of about 30 mm. The collimated image is then focused using a $f = 300\,\mathrm{mm}$ lens which creates an intermediate focal plane that is magnified by a factor of about 10. The phase dot is placed in the beam at the position where the imaging beam has a focus and it is mounted in a 3 axis translation stage to facilitate its alignment. In the intermediate imaging plane, where the image of the atoms is again in focus, we place a mask that crops the image so that only a slice, which is slightly broader than the atomic cloud, reaches the camera. After the mask the image is again magnified[3] by a factor of 2 before it is imaged using a CCD camera (Princeton Instruments Max with a pixel size of $12.9\,\mu\mathrm{m}\times 12.9\,\mu\mathrm{m}$). The mask is necessary to only illuminate the CCD chip where the atomic cloud is located. Then we can use the frame transfer mode of the camera which allows us to take up to 20 images of the same cloud with a time delay of only about $100\,\mu\mathrm{s}$ between the images.

---

[3] This secondary magnification stage can actually be replaced by a system with less magnification which is beneficial for imaging larger clouds.

This time is needed to shift about 100 already exposed pixels into the masked region. We will later see that taking several images of the same cloud is necessary to be able to extract the vector magnetization for example using Larmor precession imaging [Hig05b] or spin-echo imaging (see section 5.4.5).

External Resolution Tests

In order to determine whether all parts of the imaging system work as planned and expected, we built a test setup to measure the achievable resolution of the imaging system outside of the actual experimental setup. More details on the exact procedures can be found in [Guz12].

In a first test we used a 1951 USAF resolution test pattern that consists of groups of lines of different sizes and spacings. By illuminating the test pattern and imaging it onto a CCD camera, one can extract the modulation transfer function (MTF) of the objective. This is done by fitting each group of lines to a two-dimensional sine wave and recording its contrast. The MTF measures the response of an imaging system to a sinusiodally varying signal as a function of the wavelength of the signal. The MTF is measured for three different setups in order to check each piece of the imaging objective. With only the aspheric lens (without the glass cell), we obtain a NA of about 0.5 which is in agreement with the specifications of the lens. When the lens was placed in the custom built mount the obtained NA was only about 0.43. This is due to the retaining ring which holds the lens in place and limits the NA by reducing the aperture of the lens. When we add the glass cell and the meniscus lens we again obtain a NA of about 0.43 which shows that the meniscus nicely compensates the effect of the glass cell. When we compare the results for the vertical and horizontal lines we obtain very similar contrasts and therefore we conclude that the astigmatism of the imaging system is negligible.

The test pattern limits the minimal size of objects with which we can test the objective to the smallest available line spacing. In order to obtain further information about the imaging objective we thus perform a second test by imaging a pinhole using the objective. If the pinhole is significantly smaller than the imaging resolution one obtains the point-spread function (PSF) from such a measurement. The image can then be fitted using an airy disc. From such a measurement one can extract the diffraction limited resolution. The used pinhole from Data Optics, however, was more than two times larger than specified and STM images show that it was also not completely round [Guz12]. A fit to a simulated signal for such an asymmetric object yields a diffraction limited resolution of about $1.33\,\mu$m which corresponds to a NA of about ≈ 0.37. Due to the approximations made, this is a reasonable agreement to the determination of the MTF performed with the test pattern. By moving the pinhole with respect to the imaging objective we can observe how the size of the out-of-focus object increases. By comparing the obtained sizes for the horizontal and vertical direction, one can extract information about a possible astigmatism. As with the test pattern, the signals are similar within the experimental uncertainties.

In-Situ Resolution Tests

The tests performed on the bench gave us a good indication of the quality and the criticality of the alignment of the objective. However, to really show the resolution of the complete imaging setup we have to measure the resolution in the actual experimental setup using the atoms.

After aligning the entire imaging path as shown in figure 5.7 (b) we used repump light to create a beam that is fed into the imaging path in opposite direction using a pellicle beamsplitter which has a focus in the intermediate imaging plane. This focus is imaged onto the atoms through the objective. The repumped atoms are then in the F=2 manifold and hence they are not visible using phase-contrast imaging on the $D1$ line. Therefore, we observe a small hole in the imaged condensates. This beam can be used to check whether all lenses and mirrors are correctly aligned. Furthermore, by scanning the focus of this ”poke” beam against the position of the imaging objective, one can try to minimize the observed hole to precisely find the minimal focus. A picture of a condensate with a hole taken in such a way is shown in figure 5.7 (b) as an insert. The stability of this method, however, was not very good and probably due to movements of the pellicle or other parts of the poke beam setup, the ”poke” beam would significantly move (sometimes more than the horizontal size of the cloud) from shot to shot. This inhibited a reliable measurement of the size of the created hole and therefore we had to find a better method to characterize the imaging setup in-situ.

The method that turned out to be ideally suited for the task of measuring the MTF, and therefore the resolution of our imaging system, was using helical spin textures. In this method, we create spin helices by applying a magnetic field gradient to a transversely magnetized condensate. Depending on the duration of this gradient pulse, the wavelength of the spin structure decreases. This generates a sinusoidal test pattern from which one can easily extract the contrast and therefore the MTF. By applying the offset field in different directions we are furthermore able to create this test pattern in arbitrary directions which is a suitable test for the astigmatism of the imaging system. So far we have neither introduced the details of the preparation nor described how we image the magnetization. Thus we will present the results of this in-situ test of the resolution in section 5.4.4. For the sake of this section’s completeness, however, we will still present the results obtained with this in-situ technique. Using this sinusoidal atomic test pattern method we can test lengths scales from about $50\,\mu$m, limited by the size of the cloud, to about $4\,\mu$m. We obtain an experimentally determined value for the NA of the imaging setup by fitting the data with a diffraction limited theory. From such a fit, we obtain a NA of ≈ 0.31. This is significantly smaller than the values obtained for the resolution tests on the bench. We believe that the reason for this discrepancy can be found in the orientation of the glass cell. Since the glass cell is attached to a non rotatable flange the glass cell is tilted by about $10°$ with respect to the vertical direction. We try to compensate this by aligning the objective parallel to the surface of the glass cell. But due to the limited space inside the heat sink of the quadrupole coils, we are not able to completely compensate this and a residual angle of about 1° to 3° remains between the glass cell and the objective.

5.3 Basics of a F=1 Spinor Condensate

In this section, we will give a short introduction to the theoretical description of spinor condensates. We will follow the reasoning and notations of several prior publications [Ho98, Hig05a, Guz12, Sad06a] and use the Hamiltonian derived for weakly interacting Bose gases in section 2.3.

5.3.1 The Hamiltonian

The description of multi-component BECs is significantly simplified when we write the bosonic field operator $\hat{\psi}$ (see section 2.1.3) as a multi-component vector. Each component of this so-called spinor describes one of the magnetic m_F Zeeman sublevels. The field operator then takes the following form

$$\hat{\Psi}(\mathbf{r}) = \begin{pmatrix} \hat{\psi}_1(\mathbf{r}) \\ \hat{\psi}_0(\mathbf{r}) \\ \hat{\psi}_{-1}(\mathbf{r}) \end{pmatrix}, \tag{5.1}$$

where $\mathbf{r}$ is the position in real space and the subscript index stands for the m_F quantum number. With this definition, the non-interacting part of the Hamiltonian can be written as

$$H_0 = \int d\mathbf{r}\, \hat{\Psi}^\dagger(\mathbf{r}) \left(-\frac{\hbar^2}{2\,m} \nabla^2 + V(\mathbf{r}) \right) \hat{\Psi}(\mathbf{r}), \tag{5.2}$$

where m is the atomic mass and $V(\mathbf{r})$ is the optical trapping potential. To describe the systems we want to study, we need to add the ultracold atom s-wave interaction term to this non-interacting Hamiltonian. When we consider two $F = 1$ atoms colliding with each other, we notice that there are only two possibilities for the total angular momentum F_{tot} of the colliding bosons. Either the spins of the particles are parallel, which leads to $F_{\text{tot}} = 2$, or they are antiparallel, which leads to $F_{\text{tot}} = 0$. With this knowledge at hand, we can adopt a clever notation for the interaction part of the Hamiltonian introduced by [Ho98] and we obtain

$$H_{\text{int}} = \frac{c_0}{2} \int d\mathbf{r}\, \left(\hat{\Psi}^\dagger(\mathbf{r}) \cdot \hat{\Psi}(\mathbf{r}) \right)^2 + \frac{c_2}{2} \int d\mathbf{r}\, \left(\hat{\Psi}^\dagger(\mathbf{r})\, \mathbf{F}\, \hat{\Psi}(\mathbf{r}) \right)^2, \tag{5.3}$$

where $\mathbf{F}$ are the 3×3 spin-1 matrices and c_0 (c_2) are the interaction coefficients for the spin independent (spin dependent) part of the contact interaction. These interaction coefficients can be derived from the $F_{\text{tot}} = 0$ and $F_{\text{tot}} = 2$ scattering lengths a_0 and a_2

in the following way

$$c_0 = \frac{4\pi\hbar^2}{3m}\,(a_0 + 2a_2)\,, \qquad c_2 = \frac{4\pi\hbar^2}{3m}\,(a_2 - a_0)\,. \tag{5.4}$$

From [Kem02] we know that for the case of ^{87}Rb

$$a_0 = 101.8\,a_{\mathrm{B}} \quad \text{and} \quad a_2 = 100.4\,a_{\mathrm{B}}, \tag{5.5}$$

where a_{B} is Bohr's radius. This means that for ^{87}Rb the spin dependent part of the contact interaction is negative $c_2 < 0$ because $a_0 > a_2$. Furthermore, this shows that for ^{87}Rb, the spin-dependent contact interaction energy is more than 100 times smaller than the spin-independent contact interaction energy.

5.3.2 Mean-Field Theory and the Ground State

In order to derive the structure of the ground state of the system, it is useful to use the Bogoliubov approximation (see section 2.3.2 and [Bog47, Ho98]) and to replace the field operators by complex valued functions. This means that the above defined spinor takes the following form

$$\hat{\Psi}(\mathbf{r}) \mapsto \Psi(\mathbf{r}) = \sqrt{n(\mathbf{r})}\,\psi(\mathbf{r}) = \sqrt{n(\mathbf{r})}\begin{pmatrix} \psi_1(\mathbf{r}) \\ \psi_0(\mathbf{r}) \\ \psi_{-1}(\mathbf{r}) \end{pmatrix}, \tag{5.6}$$

where $n(\mathbf{r})$ is the density of the sample and $\psi(\mathbf{r})$ is a three dimensional complex valued function with the normalization $\psi(\mathbf{r})^\dagger\,\psi(\mathbf{r}) = 1$.

Following [Ho98], we need to minimize the energy at a fixed particle number in order to find the ground state of the system. Using the above mentioned approximation we obtain the following energy functional

$$E\left[\Psi(\mathbf{r})\right] = \int d\mathbf{r}\,\left(\frac{\hbar^2}{2\,m}\,|\nabla\Psi|^2 - [\mu - V(\mathbf{r})]\,n(\mathbf{r}) + \frac{n(\mathbf{r})^2}{2}\left[c_0 + c_2\langle\mathbf{F}\rangle^2\right]\right), \tag{5.7}$$

where μ is the chemical potential, $\langle\mathbf{F}\rangle \equiv \psi(\mathbf{r})^\dagger\,\tilde{\mathbf{F}}\,\psi(\mathbf{r})$ is the local vector magnetization and $\tilde{\mathbf{F}}_i$ are the 3×3 spin-1 Pauli matrices.

Since the ground state is determined by the minimization of $E\left[\Psi(\mathbf{r})\right]$, the sign of c_2 becomes important for the structure of the ground state since it is the only spin dependent part of the Hamiltonian. We can now distinguish two cases:

The Polar State ($c_2 > 0$) If $c_2 > 0$ the energy of the system is minimized by $\langle\mathbf{F}\rangle = 0$. There is a whole class of vector magnetizations that fulfill this requirement. They are all related to each other by a gauge transformation ($e^{i\theta}$) and a spin rotation $\mathcal{U}(\alpha, \beta, \gamma)$

with the Euler angles α, β, γ and have thus the following structure

$$\psi_{\text{polar}} = e^{i\theta}\,\mathcal{U}\begin{pmatrix} 0 \\ 1 \\ 0 \end{pmatrix} = e^{i\theta}\begin{pmatrix} -\frac{e^{-i\alpha}}{\sqrt{2}}\sin\beta \\ \cos\beta \\ \frac{e^{i\alpha}}{\sqrt{2}}\sin\beta \end{pmatrix}. \tag{5.8}$$

Such a state is for example realized with an $F = 1$ ^{23}Na spinor BEC as for this system c_2 is positive [Ho98].

The Ferromagnetic State ($c_2 < 0$) In this case the energy functional given in equation (5.7) is minimized by $\langle \mathbf{F} \rangle^2 = 1$. The spinor for such a ferromagnetic state is given by

$$\psi_{\text{ferro}} = e^{i\theta}\,\mathcal{U}\begin{pmatrix} 1 \\ 0 \\ 0 \end{pmatrix} = e^{i(\theta-\gamma)}\begin{pmatrix} e^{-i\alpha}\cos^2(\beta/2) \\ \sqrt{2}\cos(\beta/2)\sin(\beta/2) \\ e^{i\alpha}\sin^2(\beta/2) \end{pmatrix}. \tag{5.9}$$

Such a ferromagnetic state is for example realized with a $F = 1$ spinor BEC of ^{87}Rb because here $c_2 < 0$ [Kem02].

5.3.3 Adding Magnetic Fields and Spin Mixing Dynamics

In the last paragraph, we have shown that we expect a ferromagnetic state for our $F = 1$ rubidium condensate. One important aspect of the experiments that has been neglected up to this point is the presence of magnetic fields. This is incorporated by extending the Hamiltonian $H_{\text{total}} = H_0 + H_{\text{int}}$ by an additional term which describes the interaction of the system with external magnetic fields. It is clear that the addition of such fields will significantly alter the behavior of the spins. Already for a field of about $10\,\mu$G, the Zeeman energy of a system like ours becomes comparable to the energy related to the spin dependent part of the contact interaction [Sad06a]. This shows that the zero-field regime is extremely difficult to reach with magnetic shielding. We will therefore now derive the energies associated with presence of a magnetic field along the z-direction.

Spin Mixing We said earlier that due to the symmetry of the system only collisions with $F_{\text{tot}} = 0$ or 2 are allowed. Additionally, the conservation of angular momentum will lead to the fact that only collisions of the following form are allowed

$$|1,0\rangle + |1,0\rangle \rightleftarrows |1,-1\rangle + |1,+1\rangle. \tag{5.10}$$

In these spin mixing collisions, two atoms in state $m_F = 0$ collide and change into one atom in a state with $m_F = -1$ and the other one in $m_F = +1$. This process is reversible and was shown to be coherent [Cha05]. For our experimental investigations, this means that the only way the spin configuration can change is through these spin changing collisions.

Zeeman Shifts There are several contributions to the energy of the systems due to the Zeeman effect. A magnetic field gradient leads to the addition of a space dependent energy shift $E_{\text{grad}} = g_F \mu_B B' \, z \langle F_z \rangle$, where g_F is the Landé g-factor, μ_B is the Bohr magneton and B' is the strength of the magnetic field gradient. Such an inhomogeneity will strongly influence our experiments since it will cause a spatial separation of the different spin components. This effect would reduce the spatial overlap between the spin components thus inhibiting spin changing collisions. Therefore, we must minimize the strength of such gradients (B') in order to not be limited by this effect (see section 5.4.3). The linear Zeeman shift is given by $E_{\text{lin}} = g_F \mu_B B_0 \langle F_z \rangle$ but we do not need to consider this effect due to the conservation of angular momentum[Les08].

Quadratic Zeeman Shift The next term we need to consider is the quadratic Zeeman shift. Its energy is given by $E_q = q \, \langle F_z^2 \rangle$, with $q = (72 \, h \, B^2) \, \mathrm{Hz/G^2}$. We will later see that such a quadratic shift is not only created by a magnetic field but can also be created using MW fields. Therefore, we define the quadratic shift in a more general way as the difference between the mean energy of the $|1,+1\rangle$ and $|1,-1\rangle$ states compared to the energy of the $|1,0\rangle$ state. Using the definition of the Zeeman energy as shown in figure 5.8, we obtain

$$q = \frac{E_{+1} + E_{-1}}{2} - E_0 \tag{5.11}$$

for the quadratic Zeeman energy q. If such a shift is generated by a magnetic field, we will label it q_B and in this case $q_B \propto B^2$. For ^{87}Rb, the quadratic Zeeman shift generated by a magnetic field q_B is positive and about $q_B \approx h \times 5\,\mathrm{Hz}$ for an offset field of 267 mG.

5.3.4 Mean Field Phase Diagram

To obtain the phase diagram for a system like ours, we need to examine the spin-dependent part of the energy functional given in equation 5.7 including the just derived term for the quadratic Zeeman shift. We obtain

$$E_{\text{spin}}\left[\Psi(\mathbf{r})\right] = \int d\mathbf{r} \, n(\mathbf{r}) \left(\frac{n(\mathbf{r}) \, c_2}{2} \langle \mathbf{F} \rangle^2 + q \langle F_z^2 \rangle \right), \tag{5.12}$$

where q is the total quadratic Zeeman shift. From this equation it becomes obvious that the term due to the quadratic shift competes with the term due to the spin-dependent contact interaction. This competition drives and determines the spin mixing dynamics and the ground state of the system.

Earlier we noted that $c_2 < 0$ for ^{87}Rb. Therefore, the system tends towards a ferromagnetic state for vanishing magnetic fields. For non-zero fields we can again distinguish several regimes. For a negative quadratic shift $q < 0$, the complete energy functional is still minimized by $\langle \mathbf{F} \rangle^2 = 1$ and the system tends towards a ferromagnetic state. If we analyze figure 5.8 more closely, we can find a handwaving argument for this: A negative quadratic shift leads to an increase of the energy of the $m_F = 0$ state with respect to the $m_F = \pm 1$ states. Therefore, the spin mixing dynamics tends towards the accumulation of more atoms in the $m_F = \pm 1$ states and hence a magnetized system. For very large positive quadratic shifts $q \gg n(\mathbf{r})\,|c_2|$ the same consideration shows that the energy of the $m_F = 0$ state is significantly lower than the average energy of the $m_F = \pm 1$ states. Therefore, the system tends towards a polar state. It was shown in [Sad06b, Muk07, Lam07], that these regimes are separated by a second-order quantum phase transition, which occurs at a critical value of the quadratic shift of $q_0 = 2|c_2|n$. At this point, the system changes from an unmagnetized polar state to a magnetized state. A more careful theoretical analysis [Muk07] shows that the state for $0 < q < q_0$ is a linear combination of the polar state and a ferromagnetic state with transverse magnetization $F_\perp(\mathbf{r}) \equiv F_x(\mathbf{r}) + iF_y(\mathbf{r})$ with $F_i \equiv \psi(\mathbf{r})^\dagger \, \tilde{\mathbf{F}}_i \, \psi(\mathbf{r})$. For negative quadratic shift $q < 0$, the system is thought to have a magnetization along the field direction $F_\parallel = F_z$ which is sometimes also referred to as an easy axis magnet [Muk07, Kjä09, Guz11].

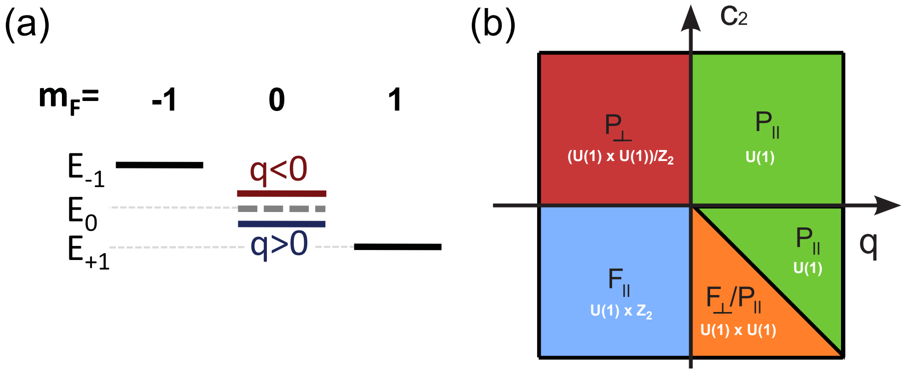

Figure 5.8: (a) Energy levels of the $F = 1$ manifold, including the linear Zeeman shift and the quadratic Zeeman shift q. (b) Mean-field phase diagram for the ground state of a $F = 1$ spinor condensate. The lower half ($c < 0$) applies for the just discussed case of ^{87}Rb. In the phase diagram $\mathbf{F}$ stands for a ferromagnetic and $\mathbf{P}$ stands for a polar phase. Adapted from [Muk07, Kjä09]

5.3.5 Observing the Phase Transition

In first experiments, researchers measured the time evolution of the populations in the different m_F states after quenching into the expected ferromagnetic phase with all atoms of the condensate only in the $m_F = 0$ state [Sad06a]. After long evolution times the system would reach a steady state where the populations in the $m_F = \pm 1$

state would be $\rho_{+1} = \rho_{-1} = 1/2$ and in the $m_F = 0$ state $\rho_0 = 1/\sqrt{2}$. Unfortunately, there are several spinors which could lead to this population distribution both with ferromagnetic and polar wave functions. This tells us that it is not sufficient to measure the populations in the m_F states. Additionally, to determine in which state the system is in, we also need information about the vector magnetization **F**. This is achieved by using magnetization sensitive phase or polarization-contrast imaging. With this imaging technique it was then possible to observe the quench through the polar-to-ferromagnetic quantum phase transition discussed above [Sad06b]. Figure 5.9 shows how ferromagnetic domains are formed in the condensate after a quench of the quadratic shift from values larger than q_0 to values smaller than q_0.

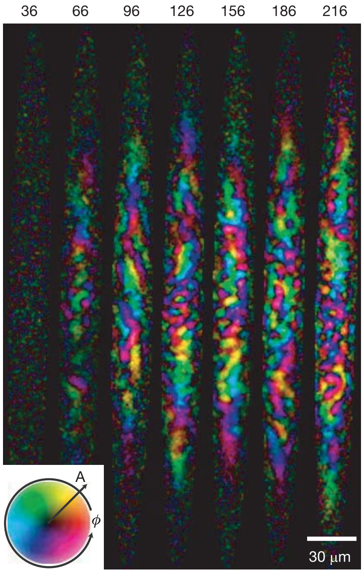

Figure 5.9: In-situ images of the transverse magnetization using phase-contrast Larmor precession imaging. With this imaging technique one can observe the growth of magnetization (clouds become brighter for longer evolution times). The color indicates the local phase of the transverse magnetization and one can clearly observe small spin domains. Taken from [Sad06b].

5.4 Imaging the Magnetization of a Spinor BEC

We will now discuss the different techniques that are available to obtain information about spinor condensates and then show how we can use these methods to determine magnetic field gradients and the resolution of the imaging system. These techniques were already extensively explained and discussed in several other publications [Hig05b, Sad06b, Guz11] and theses [Hig05a, Sad06a, Les08, Guz12] from the Berkeley group. Therefore, I will only outline the most important facts that are necessary to understand their concept and further explain these methods using a specific examples.

5.4.1 Stern-Gerlach Time-of-Flight Measurements

The simplest method to extract information from a spinor BEC is to make use of the magnetic moments of the populations in the different Zeeman substates. It uses regular time-of-flight absorption imaging with the addition that, shortly (about $6-10$ ms) after letting the atoms freely expand, a magnetic field gradient (about 20 G/cm) is turned on for about 10 ms. This leads to a spatial separation of the atoms in the three Zeeman substates as shown in figure 5.10. By counting the populations we gain insight into the spin mixing dynamics and the possible equilibration of the sample. Without knowing the magnetization of the sample, however, this is not enough to be able to decide if a sample is ferromagnetic or polar.

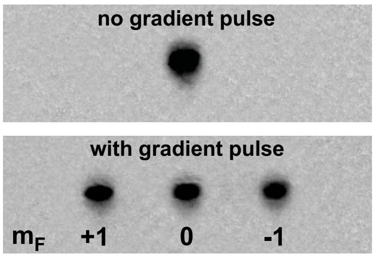

Figure 5.10: Absorption images of a BEC with small thermal fraction after time-of-flight without (upper) and with (lower) applied gradient pulse. The magnetic field gradient acts along the horizontal axis of the image and separates the atoms in different Zeeman sublevels. Using this technique, we can determine the number of atoms in each state N_i.

5.4.2 Larmor Precession Imaging

In order to measure the vector magnetization of a sample we need an imaging technique that does not only measure the populations of the levels but the full three-dimensional magnetization vector. We will not be able to extract a three-dimensional quantity from a single two-dimensional image. Therefore, in order to properly reconstruct the magnetization vector $\mathbf{F}$, we have to take several shots of the same sample. One technique that is capable of doing this is Larmor precession imaging. It relies on the fact that the transverse magnetization (in the plane perpendicular to the magnetic field direction) precesses around the direction of the magnetic field with the Larmor frequency $\omega_L = g_f \mu_B B/\hbar$. This leads to a sinusoidal oscillation of the local phase-contrast signal. The amplitude of this signal is proportional to the magnitude of the transverse magnetization. The phase of the oscillation contains information about the local orientation of the transverse magnetization. Therefore, one can reconstruct the local transverse magnetization $F_\perp(\mathbf{r})$ of a sample by fitting a sine function to the Larmor precession of a series of phase-contrast images of the same sample. To measure the longitudinal magnetization $F_\parallel$ one applies a RF $\pi/2$-pulse after about half of the phase-contrast shots. In the following images the projection of the longitudinal magnetization will then create an oscillating phase-contrast signal along the imaging axis. From these two series of images one can reconstruct the magnetization vector $\mathbf{F}$.

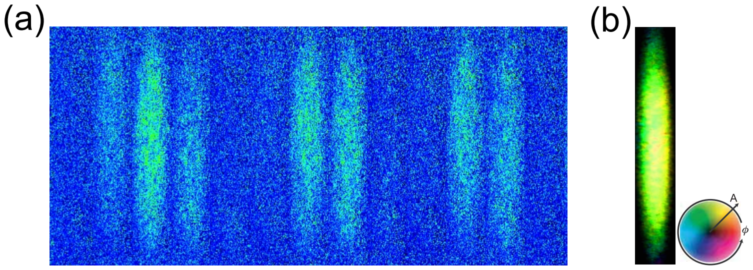

Figure 5.11: (a) Series of Larmor precession images of a uniform transversely magnetized condensate. (b) Phase and amplitude map for a uniformly magnetized condensate like the one shown in (a). Taken and adapted from [Ven08].

In our experimental setup, the magnetic offset field is usually applied along the x-direction which is the intermediate axis of the condensate (see figure 5.3). The imaging is done along the y-direction. Therefore, the transverse magnetization is in the z-y-plane. To better understand this technique we investigate a completely transversely magnetized sample which is precessing around the magnetic field direction. For this we prepare a condensate, where all spins are aligned along the magnetic field direction. This is achieved by preparing a BEC of atoms in $m_F = -1$ with the field in x-direction. We then apply a RF $\pi/2$-pulse which leads to a precession of the magnetization of the whole cloud in the z-y-plane. As a result, the sequentially taken shots of the cloud oscillate between fully bright (all atoms antiparallel to the imaging axis) and fully dark (all atoms parallel to the y-axis). The phase-contrast images of a precessing spatially homogeneous condensate can be found in figure 5.11 (a). From such a series of pictures we are able to extract the amplitude and the phase of the local transverse magnetization. The resulting phase and amplitude map for a uniform magnetization can be found in figure 5.11(b). In these pictures, the brightness represents the amplitude of the magnetization and the local phase of the magnetization is given by the hue.

Several known issues of Larmor precession imaging exist. At a magnetic field of 267 mG the precession frequency is $\omega_L = 2\pi\,187\,\mathrm{kHz}$. This is about a factor of 10 larger than the possible sampling rate of the camera which is about 20 kHz. Therefore, we cannot observe the precession directly but we have to measure at an alias frequency. As a result, this imaging technique is extremely vulnerable to changes of the magnetic offset field. It is then possible that one always samples all spins pointing up. This makes the sinusoidal fits to the precession difficult, numerically unstable and the results obtained from such a measurement are therefore unreliable. Furthermore, the numerical analysis of the Larmor precession images is complex and time consuming due to the sinusoidal fit for each pixel over a set of pictures. In the raw images, it is often challenging to see if the alias frequency was in a regime where meaningful results for the magnetization can be deduced. To avoid these problems, we developed a new imaging technique called spin-echo imaging that does not suffer from the just mentioned problems. More details about spin-echo imaging can be found in section 5.4.5.

5.4.3 Gradient Cancellation

We noted earlier that it is essential for our measurements to have very homogeneous magnetic fields. We therefore actively cancel the magnetic field gradients using special gradient coils. Hence, the field gradients have to be precisely measured. We accomplish this by using Larmor precession imaging. The magnetic field gradient leads to a spatially varying magnetic field and hence the Larmor precession frequency changes if the sample is evolving in such an inhomogeneous field. It can be easily understood that a linear gradient leads to a linear phase change of the transverse magnetization and this results in a helical spin texture of the sample. The pitch of this helix is proportional to the magnitude and the duration of the applied gradient. An example for an initially uniform sample that was exposed to a magnetic field gradient can be seen in figure 5.12.

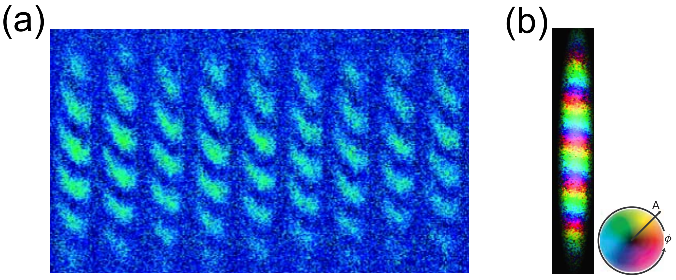

Figure 5.12: (a) Larmor precession images of spin helix produced by exposing a uniformly magnetized condensate to a linear field gradient. (b) Phase and amplitude map for a spin helix (adapted from [Ven08]).

By extending the evolution time of the sample in the gradient, we can increase the sensitivity of our gradient measurement. Thus, we can iteratively cancel the present gradients with increasing precision. In the end, we observe a uniformly precessing clouds, even after about 3 s. From this we can determine that the magnetic field inhomogeneity over the size of the cloud must be smaller than 1 μG.

5.4.4 In-Situ MTF measurement

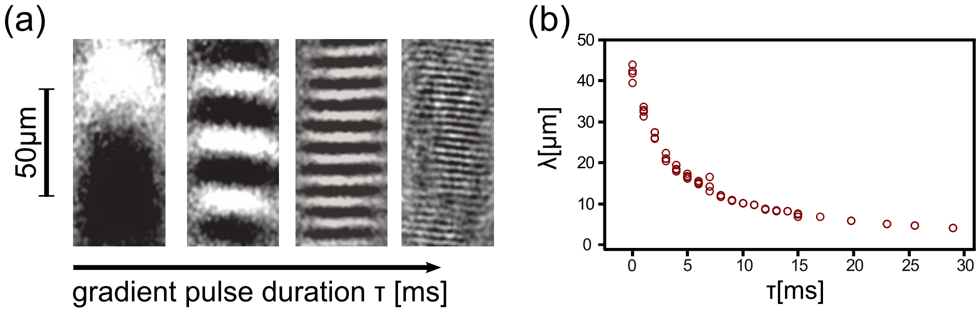

Figure 5.13: (a) Polarization-contrast images of the created spin helices for different gradient pulse durations τ. (b) Wavelength of the obtained sinusoidal signal as a function of τ (adapted from [Guz12]).

The helical spin textures produced by applying a gradient pulse to a condensate are ideally suited to test the resolution of the high-resolution imaging setup. These structures have sinusoidal modulations with tunable wavelengths which are perfect to extract the MTF of the imaging system.

We therefore apply a magnetic offset field and magnetic field gradient along the z-direction. The gradient has a strength of about 140 mG/cm and the duration of the gradient pulse τ varies between 1 ms and 30 ms. This short but strong gradient pulse is used to ensure that the spin helix does not break up into small spin domains as described in [Ven08]. The structures created by the gradient pulse have wavelengths from about 50 μm for the shortest to about 4 μm for the longest gradient pulse durations (see figure 5.13).

To extract the MTF, we integrate the polarization-contrast images along the short axis and obtain a one-dimensional signal which we fit by a sine function multiplied with a Gaussian envelope times an amplitude A. Such a spin helix and its integral including the just described fit can be found in 5.14(a,b). The contrast which is given by the amplitude A can then be plotted as a function of the inverse wavelength $1/\lambda$. We can now compare the obtained data to a theoretical diffraction limited MTF and obtain good agreement using a NA of about 0.31. This is about a factor of 0.3 lower than expected from the measurements on the bench. We attribute this decreased resolution to the already discussed tilt of the glass cell (see 5.2.5). Unfortunately, we are not able to create spin helices with wavelengths smaller than about 4 μm. We are not entirely sure why this is the case. One possible explanation for this is that the spin helices dissolve and form ferromagnetic domains. Such a behavior was previously observed in

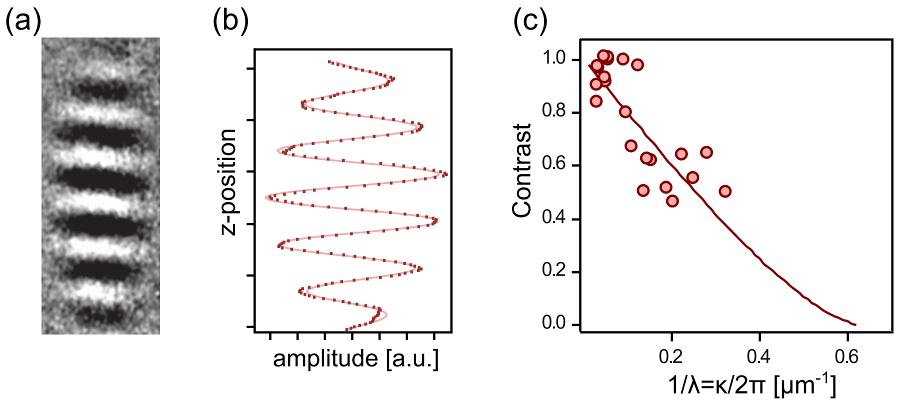

Figure 5.14: (a) Polarization gradient image and its integral along the x-axis (b). The contrast is given by the amplitude of a sine function multiplied with a Gaussian envelope. (c) Obtained MTF for the imaging system by plotting the contrast as a function of the inverse wavelength of the modulation (adapted from [Guz12]).

[Ven08]. Another reason for this could be a slight misalignment of the imaging system which leads to a reduced contrast and thus a smaller NA.

So far we have only explored the resolution along the long axis of the condensate (z-direction) but in order to investigate a possible astigmatism we make use of the fact that we can rotate the magnetic offset field freely in the z-x-plane.

To compare the obtained helices with different symmetry axis, we perform the spatial Fourier transform of the polarization gradient images (see figure 5.15(a)). We can then compare the spectral weights of the magnitude of the Fourier transformation for different orientations of the spin helix and plot the obtained results as a function of the angle. As can be seen in figure 5.15(c), the obtained spectral weights depend very weakly on the orientation which suggests that the existing astigmatism is smaller than our measurement accuracy.

As we will see later, we wanted to test whether the spin domains observed in [Ven10] actually had a crystalline structure or if the structure was only observed due to imaging aberrations. Therefore, we need to know how the ferromagnetic domains appear if the high-resolution objective is not completely in focus. We therefore deliberately moved the objective position away from the optimal focal position. For such a misaligned setup, we then remeasure the MTF in the same way as shown in figure 5.14. Already for a distance of $300\,\mu$m from the optimal focal position, we observe strong deviations from the MTF obtained with a well aligned objective. For the "misplaced" position, the observed contrast for certain wave vectors is significantly reduced while for other wave vectors the contrast is enhanced with respect to the in-focus MTF. Furthermore, we investigated the astigmatism for such a misaligned objective and found significant angular dependence of the observed contrast. These findings raise the question whether the crystalline structure observed in [Ven10] is due to dipolar interactions or just caused

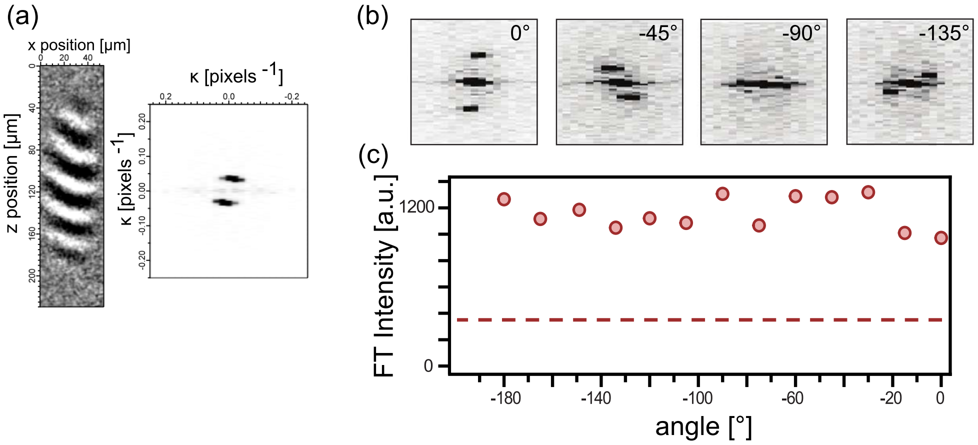

Figure 5.15: (a) Polarization gradient image of a spin helix and the amplitude of its spatial Fourier transform. (b) Fourier power spectra for spin helices with different orientations. (c) The integrated spectral weight of the relevant part of the Fourier transformations as a function of the symmetry angle of the spin helix (adapted from [Guz12]). The weak dependence of the spectral intensity on the angle shows that the astigmatism of the imaging system is negligible.

by imaging aberrations.

5.4.5 Spin-Echo Imaging

Spin-echo imaging is a new imaging technique we adapted for the measurement of the vector magnetization in ultracold gas experiments. With this technique we can extract the vector magnetization in just three shots by using spin-echo pulses between the images to increase the time between images so that the camera is able to image two consecutive images with orthogonal magnetization without severe dephasing of the sample.

The spin-echo sequence starts with the first polarization gradient image. In this frame we measure the projection of the transverse magnetization along the imaging axis. We will call this projected magnetization $\tilde{M}_x$ and it is given by $\tilde{M}_i = g_F \mu_B \tilde{n}\, F_i$, where $\tilde{n}$ is the integrated column density. After a certain time τ_0 we apply a radio-frequency π pulse which leads to a reversal of the Larmor precession. If we now wait for another time $\tau_1 = \tau_0$ after the π pulse, we will obtain another image of $\tilde{M}_x$. By waiting an additional quarter of the Larmor precession time ($\tau_1 = \tau_0 + \tau_L/4$), we will obtain a different projection of the transverse magnetization $\tilde{M}_y$ which is orthogonal to the initial projection $\tilde{M}_x$. Thus, we measured the complete transverse magnetization. We can test this technique by using a spin helix and comparing the relative phases between the first and the second frame as a function of $\Delta\tau = \tau_1 - \tau_0$. Hence, we can optimize $\Delta\tau$ such that the first and second frame yield orthogonal magnetizations.

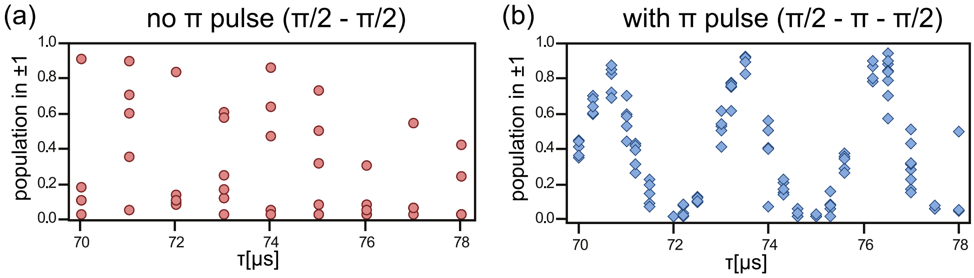

Figure 5.16: Test of the observed coherence in a Ramsey type experiment without (a) and with (b) the spin-echo π pulse. Using a first $\pi/2$ pulse, we create a homogeneously precessing cloud. After an evolution time of τ we apply a second $\pi/2$ pulse either with or without a spin-echo π pulse in between. Finally, we record the population in $m_F = \pm 1$ and only with the spin-echo pulse the system shows the expected Ramsey fringes (adapted from [Guz12]).

In principle, the same sequence can also be done without the spin-echo π pulse. But due to the quick Larmor precession which is significantly shorter than the possible imaging intervals (limited by the shift speed of the camera), the system dephases which will inhibit a reliable extraction of the transverse magnetization. The dephasing is most likely due to magnetic field fluctuations and inhomogeneities. We investigate the coherence of the system by recording the populations in the Zeeman substates $m_F = \pm 1$ after a Ramsey-like experiment performed with a completely transversely magnetized precessing sample. Figure 5.16(a) shows that the obtained population does not show typical Ramsey fringes after evolution times of about $\tau = 70 - 78\,\mu$s. However, if we add a spin-echo π pulse between the two $\pi/2$ pulses, the dephasing is significantly reduced and one can observe clear Ramsey fringes (see 5.16(b)).

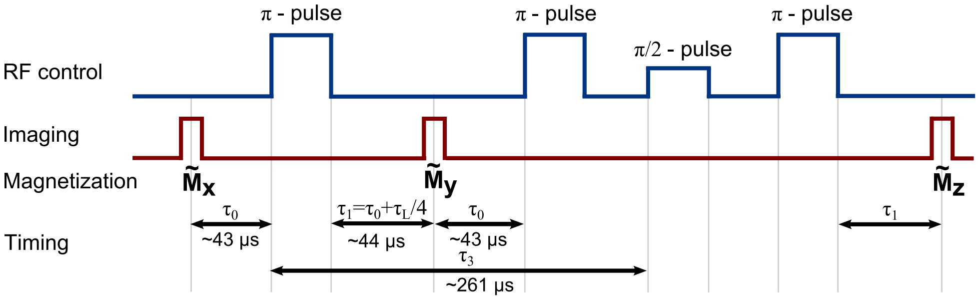

Figure 5.17: Schematic view of the spin-echo sequence described in the text.

We already explained above how one can extract the transverse magnetization ($\tilde{M}_x$ and $\tilde{M}_y$) from recording two imaging frames and a spin-echo π pulse in-between. In order to now also obtain the longitudinal magnetization $\tilde{M}_z$ we have to perform another spin rotation. This is achieved by applying a $\pi/2$ radio-frequency pulse after the two imaging pulses and two spin-echo pulses (see figure 5.17). After this $\pi/2$ pulse, the longitudinal magnetization $\tilde{M}_z$ and one of the initial transverse magnetization then precess around the magnetic offset field. By adjusting the moment of the $\pi/2$ pulse we can choose to exactly image $\tilde{M}_z$. We can again test and optimize this part of the spin-echo sequence by creating a longitudinally magnetized BEC in state $m_F = -1$. The first two images of the transverse magnetization therefore occur perpendicular to the aligned spins. We then scan the time τ_3 of the $\pi/2$ pulse; and after another spin-echo pulse, we record another image. The signal shows sinusoidal oscillations as a function of τ_3 with a minimal signal when we image the component of the former transverse magnetization and a maximal signal when we image $\tilde{M}_z$. Thus, we have recorded all three projections of the vector magnetization. This means we can construct amplitude and phase maps of the transverse and longitudinal magnetization.

Spin-echo imaging has several clear advantages in comparison to the other ways of extracting the vector magnetization. First, it does not rely on aliasing the Larmor precession, which led to the fact that some of the Larmor precession data had to be discarded when one could not fit the precession properly. Additionally, spin-echo imaging only needs three imaging frames to obtain the vector magnetization $\mathbf{F}$. Larmor precession imaging on the other hand needed almost 20 images to do so. This means that using spin-echo imaging we can record the vector magnetization multiple times for a given sample. This allows us to study the time evolution of a single sample in the future. Therefore, we could use this technique to observe how vortices and domain walls evolve in time.

There are however also some drawbacks to spin-echo imaging. Most importantly, this new imaging technique is very vulnerable to interference fringes on the images. These fringes emerge due to a combination of mechanical movement or dirt on the optical components in the imaging path on one side and the coherence of the imaging laser beam on the other side. By using a fringe removal algorithm that uses the spatial Fourier transform of an image, where the atoms are masked, we can significantly reduce the fringes and hence the fringes do not limit the envisioned experiments significantly.

5.5 Long Timescale Dynamics in a F=1 Spinor BEC

We will now describe the measurements we performed to investigate how an unmagnetized ^{87}Rb sample in the F=1 manifold evolves when cooled into degeneracy. This is evaluated for several different initial spin populations and as a function of the quadratic Zeeman shift. For our analysis, we use Stern-Gerlach time-of-flight imaging to examine the spin mixing dynamics and spin-echo polarization contrast imaging to extract the vector magnetization. We published the obtained results in [Guz11] and the arguments presented here will therefore follow the same line of reasoning[4].

---

[4] Further details can also be found in the thesis of J. Guzman [Guz12].

5.5.1 Goal and Motivation

The experiments described here are the continuation of measurements performed in the same group with the previous experimental setup [Ven08, Ven10]. They observed that a spin helix dissolved into a myriad of small ferromagnetic domains after a certain evolution time [Ven08]. Similar patterns emerged when they cooled unmagnetized samples into degeneracy [Ven10].

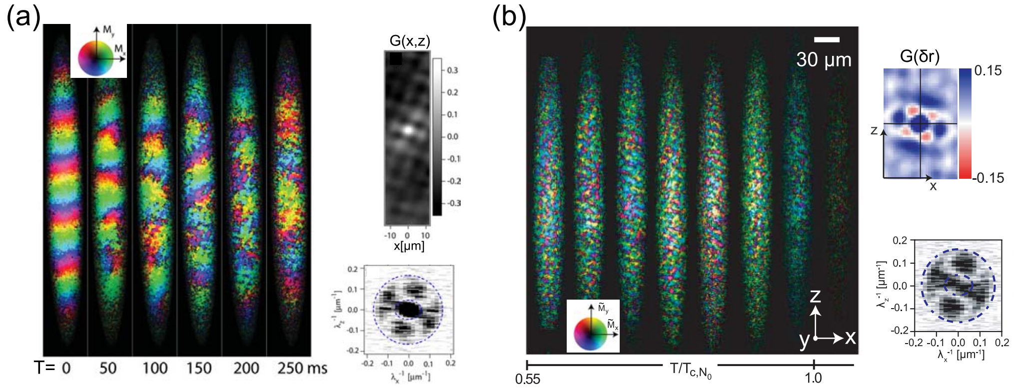

Figure 5.18: (a) Time evolution of a spin helix (from [Ven08]). The helix dissolved into ferromagnetic spin domains after evolution times $T \gtrsim 50\,\mathrm{ms}$. The upper right panel shows the correlation function $G(x, z)$ and the lower right panel shows the power spectrum of the Fourier transform for the samples at $T = 250\,\mathrm{ms}$. (b) Evolution of Spin textures from unmagnetized sample for different temperatures, the obtained correlation function and the power spectrum of the Fourier transformation (from[Ven10]).

The observed ferromagnetic domains seem to arrange in a structure that resembles a checkerboard pattern with fixed orientation. It was proposed that these structures are formed due to dipolar interactions between the atoms. Because of the relatively short lifetimes ($\tau \lesssim 1000\,\mathrm{ms}$) of the ultracold samples in the old version of the spinor setup used in [Ven08, Ven10], it was not possible to investigate the dynamics and evolution for longer times. Additionally, the evolution of samples with different initial spin distributions did not reach a common final state after the accessible observation times. This raised the question whether the small ferromagnetic domains are equilibrated or if the sample is still changing.

To shed light on the evolution for long timescales, we continued their effort to gain more understanding of the dynamics, the equilibration times and the phases relevant for $F = 1$ ^{87}Rb spinor condensates. As already explained before, we took great care in properly focusing the high-resolution objective in order to be sure that no particular structure is enhanced due to imaging aberrations. Furthermore, we examined the evolution of the samples for times up to $4\,s$, which is almost an order of magnitude larger than in the previous experiments. Our goal is therefore to determine whether the previously observed periodic spin textures are the ground state of the system or if the system continues to evolve, for example, towards the mean field phase diagram shown in figure 5.8 or in figure 5.19(a).

5.5.2 Mapping Out the Phase Diagram

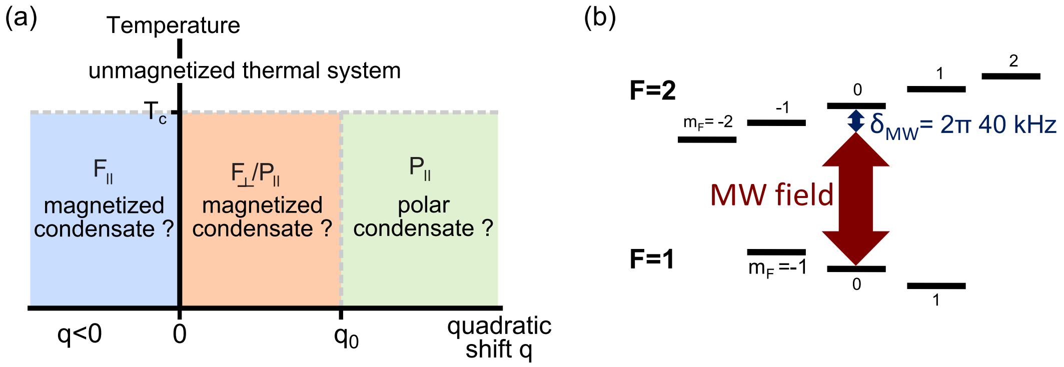

Figure 5.19: (a)Possible mean field phase diagram as suggested by [Muk07, Kjä09]. (b) Illustration of the generation of a quadratic Zeeman shift using detuned microwave fields.

To obtain information about the realized phases and the equilibration timescales, we cool different unmagnetized spin mixtures into degeneracy. The thermal spin mixtures are prepared during the evaporation in the optical trap before we reach the quantum degenerate regime, i.e. before Bose-Einstein condensation. They have zero vector magnetization both in the transverse direction (no coherences between the m_F states) and in the longitudinal direction ($N_{+1} = N_{-1}$). We start from these different spin compositions to test whether all of them reach a common state after a certain equilibration time which should be related to the mean field phase diagram shown in figure 5.19(a). The last stage of evaporative cooling into degeneracy is performed at various different quadratic Zeeman shifts and thus we can map out the complete phase diagram.

In the following, we will define the used spin mixtures and show how the quadratic Zeeman shift is applied.

The Initial Spin Mixtures

In our measurements we study the evolution of three different thermal spin compositions. They are characterized by their fractional population of the Zeeman sublevels $\zeta^{(\mathrm{th})} = (\zeta^{(\mathrm{th})}_{+1}, \zeta^{(\mathrm{th})}_{0}, \zeta^{(\mathrm{th})}_{-1})$, where $\zeta_i \equiv \frac{N_i}{N_{\mathrm{total}}}$, N_i is the number of atoms in the state $m_F = i$ and N_{total} is the total number of atoms. Sometimes we will also label the samples with a parameter η defined as $\eta \equiv \zeta_0 - \zeta_{+1}$. To test the preparation of these different spin compositions, we measure the populations in each state using Stern-Gerlach time-of-flight absorption imaging. We also test the vanishing magnetization using polarization-contrast imaging.

The $\zeta^{(\text{th})} = (1/3,\ 1/3,\ 1/3)$ or $\eta = 0$ mixture. In this case, the initial population in all three states is the same. This is also one of the mixtures investigated in [Ven10]. Figure 5.18 (b) shows how such a mixture behaves as it is cooled into degeneracy. Due to the same populations the condensation occurs in all components at the same time[5]. This system is produced by about 10 radio-frequency $\pi/2$ pulses during which a magnetic field gradient is applied in order to lead to the decoherence of the sample. Due to the large number of RF pulses, the whole Bloch sphere is randomly sampled which leads to the same population in all Zeeman sublevels.

The $\zeta^{(\text{th})} = (1/4,\ 1/2,\ 1/4)$ or $\eta = 1/4$ mixture. In this mixture, the number in the $m_F = 0$ state is twice as large as $N_{\pm 1}$. This spin mixture is created with a single $\pi/2$ pulse. To destroy the coherence of the sample a subsequent magnetic gradient field pulse is applied for about 400 ms. Due to the larger population in the $m_F = 0$ state, this component will condense slightly before the other ones. Therefore, there is a larger initial coherent part of the sample right after condensation and hence we expect the spin mixing dynamics to be quicker than in the $\eta = 0$ case. This is the second mixture that was also studied in [Ven10]. There, at least for temperature closer to T_c, this particular mixture did not show small ferromagnetic (like the ones shown in figure 5.18) domains but larger textures.

The $\zeta^{(\text{th})} = (0,\ 1,\ 0)$ or $\eta = 1$ mixture. Here, all atoms are in the $m_F = 0$ state. We create such a system by a single $\pi/2$ pulse followed by a very strong magnetic field gradient pulse (about 30 G/cm) which pulls the atoms in the $m_F = \pm 1$ states out of the optical trap.

Applying a Quadratic Zeeman Shift

In order to explore the full range of the phase diagram we need to be able to apply various positive and negative total quadratic Zeeman shifts. To change the quadratic shift only with the magnetic offset field is very challenging. First, it is difficult to apply a negative q_B. Additionally, one would have to cancel the magnetic field gradients for each new offset field; and at low fields RF noise inhibits reliable measurements. To avoid these problems, we work at a single magnetic offset field and use detuned MW fields to generate quadratic Zeeman shifts.

In section 5.2.4 we explained how we apply such a shift by shining in a linearly polarized microwave field which is detuned from the $|F{=}1, m_F{=}0\rangle$-$|2, 0\rangle$ transition by 40 kHz (see also figure 5.19(b)). It was shown in [Les08] that in our parameter regime

---

[5] In this case "condense" means that a bimodal distribution appears after time-of-flight. Due to the myriad of ferromagnetic domains, the expected long-range order of a BEC is not realized. Therefore, some people refer to such a state as a quasi-condensate. We will however not make this distinction in the following.

the quadratic Zeeman shift generated by a detuned MW field is given by

$$q_{MW} = -\frac{\hbar\Omega_R^2}{4\,\delta}, \tag{5.13}$$

where Ω_R is the resonant Rabi frequency of the applied MW field and $\delta = 2\,\pi(\nu_{MW} - \nu_0)$ is the detuning between the applied MW frequency ν_{MW} and the $|1,0\rangle$-$|2,0\rangle$ transition frequency ν_0. As already shown in section 5.2.4 this means we can tune q_{MW} by changing the power of the microwave fields at a fixed detuning of 40 kHz after calibrating the resonant Rabi frequency Ω_R.

The total quadratic shift $q = q_B + q_{\mathrm{MW}}$ is the sum of the quadratic shifts generated by the MW fields q_{MW} and the magnetic offset field which is usually on the order of about $q_B \approx h \times 5\,\mathrm{Hz}$ for our field values. By changing the sign of the detuning δ of the MW field, we can access positive and negative quadratic Zeeman shifts since we can reach $|q_{\mathrm{MW}}| \approx 500\,\mathrm{Hz}$ for detunings of $\delta = 40\,\mathrm{kHz}$ with our experimental setup. Even for these large shifts, the detuning is large enough so that the population in the $|2,0\rangle$ state is still below 3%.

By changing the total quadratic Zeeman shift over such a wide range, we can precisely tune the spin dependent part of the spinor BEC Hamiltonian (as given in equation 5.12) and thus access all relevant regions of the phase diagram.

5.5.3 Experimental Parameters and Sequence

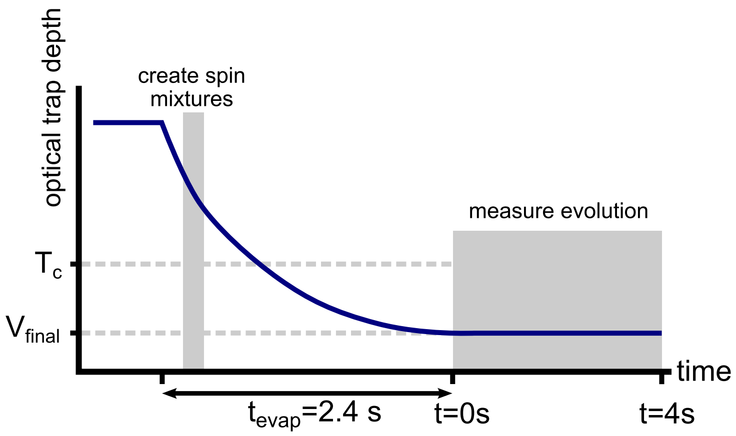

Figure 5.20: Schematic cooling, evolution and measurement sequence used for the experiments.

The atoms are in the $|1,-1\rangle$ state when we transfer them from the magnetic quadrupole trap into the optical dipole trap (ODT). We then begin the optical evaporation while the offset field is pointing in the x-direction at a value of 267 mG. At this field, the gradients are canceled as explained in section 5.4.3, which means that the magnetic field inhomogeneity is smaller than about $1\,\mu\mathrm{G}$ over the size of the cloud. Still during the evaporation in the optical trap and before we reach the critical temperature for Bose-Einstein condensation, we prepare the three different spin mixtures as can be seen in figure 5.20. During the evaporation we already apply the MW fields that lead to different quadratic Zeeman shifts and these fields stay on for the remainder of the experiment. The quadratic shift due to the MW fields can be varied by changing the power and the sign of the detuning. The quadratic shift due to the magnetic offset field is about $q_B = h \times 5\,\mathrm{Hz}$ for our offset field value of 267 mG. We continue the evaporation and hence reach the quantum degenerate regime at the critical temperature T_c. The system then condenses into a BEC which we detect by the emergence of a bimodal distribution after time-of-flight. After a total optical evaporation time of 2.4 s we reach a final optical trap depth V_{final}. We define the moment when we reach the final trap depth as the zero of our evolution time t and then investigate the samples for evolution times up to 4 s. At the final trap depth ($t = 0$) the sample consists of 3×10^6 atoms with a thermal fraction of 30% and the peak density is about $n_0 = 2.6 \times 10^{-14}\,\mathrm{cm}^{-3}$. After 4 s of evolution time 1.2×10^6 atoms are left and the peak density is then $1.8 \times 10^{-14}\,\mathrm{cm}^{-3}$. At the final trap depth, the trapping frequencies of the ODT are $(\omega_x, \omega_y, \omega_z) = 2\pi(25, 380, 7.3)\mathrm{Hz}$. For the initial parameters at an evolution time of $t = 0$, we expect the ferromagnetic to polar phase transition to occur at $q_0 = 2|c_2|n_0 = h \times 10\,\mathrm{Hz}$.

One should note that for these measurements our offset field is aligned in the x-direction and hence the axes for the theoretical predictions made in section 5.3 have to be renamed. In particular, the x-axis now gives the direction of the field and thus of quantization. This means that in the following measurements the transverse magnetization will be in the y-z-plane and the longitudinal magnetization will be along the x-axis.

5.5.4 Time-Of-Flight Measurements

In order to evaluate the possible equilibration of our three different spin mixtures we first use Stern-Gerlach time-of-flight imaging. With this technique we can count the number of condensed atoms $N_i^{(c)}$ in each spin component $m_F = i$. This is done for various quadratic shifts and as a function of the evolution time t for all different mixtures. For these measurements a useful quantity is the temporal evolution of the fraction of atoms in the $m_F = \pm 1$ state, which we define as $\zeta_{\pm 1}^{(c)} = \frac{N_{-1}^{(c)} + N_{+1}^{(c)}}{2\,N_{\mathrm{total}}}$. This quantity is plotted for the (1/3, 1/3, 1/3) or $\eta = 0$ mixture and the (1/4, 1/2, 1/4) or $\eta = 1/4$ mixture as a function of the quadratic Zeeman shift and for different evolution times in figure 5.21 (a) and (b).

For short evolution times ($t \lesssim 200\,\mathrm{ms}$), the spin distribution is still very similar to the initial thermal spin distribution which is indicated by the horizontal dashed lines. These initial values are $\zeta_{\pm 1}^{(c)} \approx 1/3$ for the $\eta = 0$ mixture and $\zeta_{\pm 1}^{(c)} = 1/4$ for the $\eta = 1/4$ mixture. For longer evolution times t, the system changes due to the spin mixing dynamics and shows a behavior that strongly depends on the quadratic shift. The

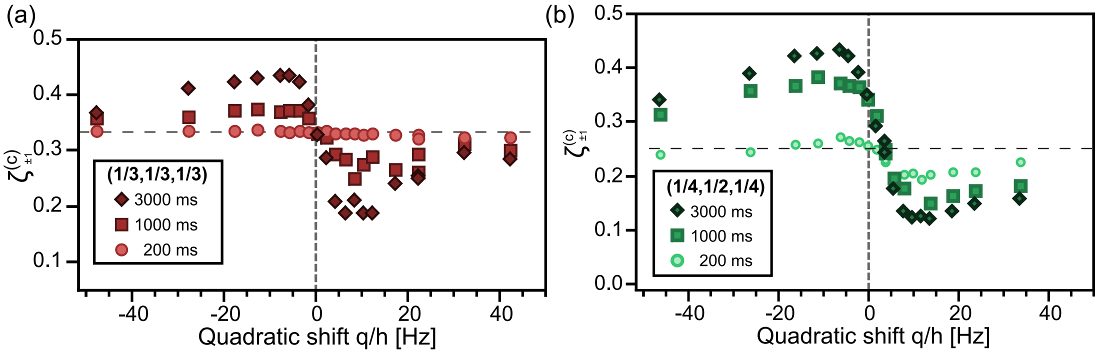

Figure 5.21: Fraction of atoms $\zeta^{(c)}_{\pm 1}$ in the $m_F = \pm 1$ state for a (1/3, 1/3, 1/3) or $\eta = 0$ mixture (a) and a (1/4, 1/2, 1/4) or $\eta = 1/4$ mixture (b) at different quadratic Zeeman shifts q after evolution times $t = 200\,\mathrm{ms}$, $1000\,\mathrm{ms}$ and $3000\,\mathrm{ms}$. A common spin distribution is only reached for a narrow regime of the quadratic shift $q \lesssim h\,10\,\mathrm{Hz}$ after long evolution times of several seconds. Adapted from [Guz11].

thermal energy scale of the system is given by $E_{\mathrm{therm}} \approx k_B\,50\,\mathrm{nK} = h\,1\,\mathrm{kHz}$ [Guz11]. The observed changes of the spin mixing dynamics shown in figure 5.21 happen on a scale of about $q = h\,10\,\mathrm{Hz}$, thus two orders of magnitude lower than the thermal scale. This suggests that the influence of the thermal component on the spin mixing dynamics is very small and spin-mixing collisions occur predominantly in the condensate.

For negative quadratic shifts, the sample seems to evolve towards $\zeta^{(c)}_{\pm 1} = 0.5$. At $q = 0$ we observe $\zeta^{(c)}_{\pm 1} = 1/3$ and for positive q $\zeta^{(c)}_{\pm 1}$ tends towards 0. Comparing the results for the two mixtures, one observes that they seem to reach a common spin distribution only for small absolute values of the quadratic shift $|q|/h \lesssim 10\,\mathrm{Hz}$. For larger absolute values of the quadratic shift $|q|/h \gtrsim 10\,\mathrm{Hz}$ however the spin distribution of the systems barely changes at all. Further evidence for an equilibration of the system only for small absolute values of q is given by investigating the fraction $\zeta^{(c)}_{\pm 1}$ for all three different initial mixture after an evolution time of 2 s (see figure 5.22).

Here one clearly observes that all mixtures (red triangles: $\eta = 0$, green dots $\eta = 1/4$ and blue squares $\eta = 1$) show a similar behavior for small absolute values of the quadratic shift which is indicated by the gray region.

Comparison to the Mean-Field Prediction

We compare the behavior observed in figure 5.22 to the mean field predictions for such a ^{87}Rb F=1 spinor condensate [Ste98, Guz11]. Since in our experiments the spin state populations are only changed by the spin mixing collisions[6] of the form

$$|1,0\rangle + |1,0\rangle \rightleftarrows |1,-1\rangle + |1,+1\rangle, \tag{5.14}$$

---

[6] This is true if one neglects dipolar relaxation.

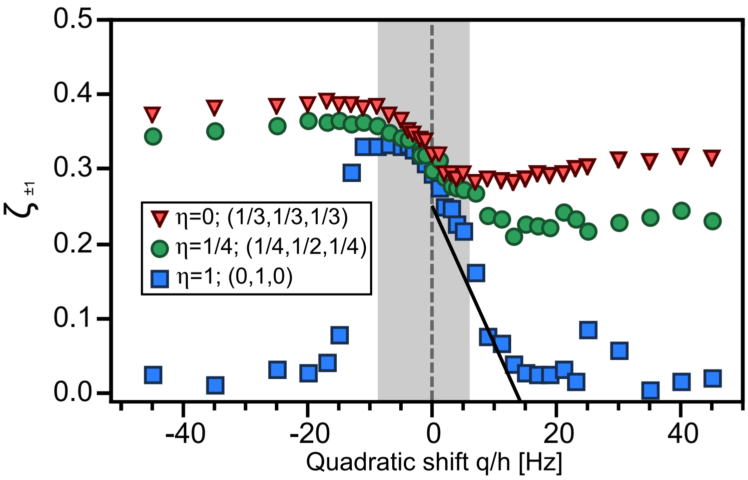

Figure 5.22: Fraction of condensed atoms $\zeta^{(c)}_{\pm 1}$ in the $m_F = \pm 1$ state for all three initial thermal mixtures ($\eta = 0$ red triangles, $\eta = 1/4$ green dots and $\eta = 1$ blue squares) after an evolution time of 2 s as a function of the quadratic Zeeman shift. The gray area depicts the region of small quadratic shifts $|q| \lesssim h \times 10\,\text{Hz}$ where all systems reach a common state spin distribution. The black solid line indicates the mean field solution (further details in the text). Adapted from [Guz11].

the total magnetization in the direction of the magnetic field $\langle F_x \rangle$ is conserved. Therefore, for $q < 0$ one expects the system to consist of domains oriented only along the x or $-x$-direction. This would lead to a fraction $\zeta^{(c)}_{\pm 1} = 0.5$. We see in figure 5.22 that for all three spin states the systems seems to develop towards this limit for $-10\,\text{Hz} \lesssim q/h < 0\,\text{Hz}$. For $q/h < -10\,\text{Hz}$, the dynamic of the system slows down considerably and especially the $\eta = 1$ sample remains close to its initial value of $\zeta^{(c)}_{\pm 1} = 0$. For large quadratic shift $q > q_0 \approx h \times (8 - 10)\,\text{Hz}$, the system should be in a polar state and the $m_F = 0$ state is energetically favored. We again observe a trend towards this state but for $q \gtrsim h \times 20\,\text{Hz}$ all mixtures again remain close to their initial distribution over the different states. The intermediate region is given by $0 < q < q_0 = 2|c_2|\bar{n}_y \approx h \times 8\,\text{Hz}$, where $\bar{n}_y = 1.85 \times 10^{14}\,\text{cm}^{-3}$ is the density averaged in y-direction after an evolution time $t = 2\,\text{s}$. Here one can calculate that $\zeta^{(c)}_{\pm 1}$ should scale linearly from 0.25 at small q to 0 at q_0 (see [Guz11, Guz12]). This is in qualitative agreement with the data for the $\eta = 1$ mixture (black solid line and blue squares in figure 5.22). The other mixtures still seem to be closer to their initial distribution but are developing towards the correct limit. For vanishing quadratic shift $q = 0$ one expects a system of magnetized domains in all spin directions and hence $\zeta^{(c)}_{\pm 1} = 1/3$ which is in good agreement for all three spin mixtures.

The fact that the spin mixing is strongly suppressed for large values of the quadratic shift $|q| > h \times 20\,\text{Hz}$ is consistent with the measurements of the spin mixing dynamics in the single mode regime, which was studied in [Cha05, Kro06]. This effect seems to occur as soon as the energy difference between the average of E_{+1} and E_{-1} and the energy of the $m_F = 0$ state E_0 is larger than the spin mixing interaction energy scale $q_0 = 2|c_2|n$.

One expects a strong influence of the spin domains and domain walls on the dynamics and the local vector magnetization of spinor system and thus on the equilibration of the system. This issue cannot be addressed with these Stern-Gerlach time-of-flight measurements. Therefore, we will now investigate the local magnetization of the system inside the optical trap using the spin-echo polarization-contrast imaging technique.

5.5.5 In-Situ Measurements

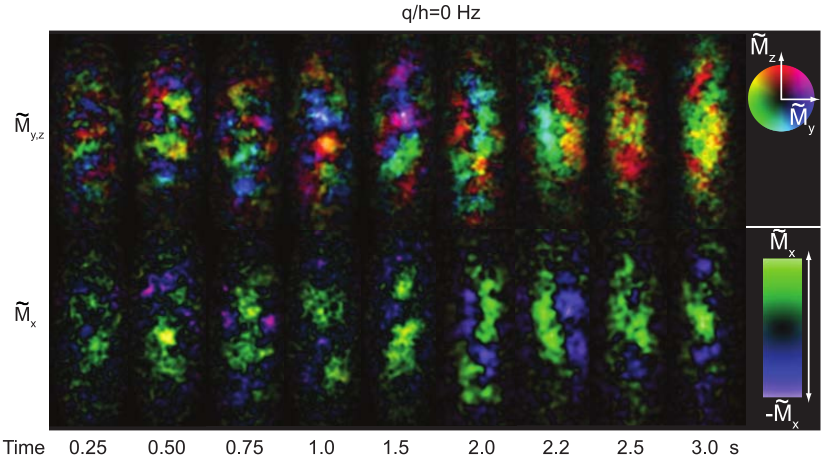

Figure 5.23: Polarization-contrast images of the transverse ($\tilde{M}_{y,z}$, top) and longitudinal ($\tilde{M}_x$, bottom) magnetization density for a $\eta = 0$ mixture as a function of the evolution time at vanishing quadratic Zeeman shift $q/h = 0\,\text{Hz}$. For short evolution times the systems show a corrugated pattern of spin domains which for longer times t develop towards larger and stronger magnetized spin domains. Adapted from [Guz12].

We will now obtain detailed information about the structure of the vector magnetization and the spin domains using the already described in-situ spin-echo technique (see section 5.4.5). From the time-of-flight measurements we know that equilibration happens only for $|q| \lesssim h \times 10\,\text{Hz}$ and we will therefore focus on this region of the quadratic shift.

The spin-echo images are taken using a $200 - 300\,\text{ns}$ long imaging pulse detuned from the F=1 to F'=2 $D1$ transition by $\delta = 400\,\text{MHz}$. Due to these short pulses (shorter than $0.25\,\tau_L$), the Larmor precession of the atoms does not lead to a change of the magnetization during a single imaging pulse. We image along the vertical y-direction, which is the narrow direction of the sample. Since the vertical size of the condensate is on the order of the spin healing length, there is no change in the magnetization in the imaging direction. We apply the precisely timed spin-echo pulse sequence (see figure 5.17) and thus in each shot we obtain a different component of the magnetization density vector $\tilde{\mathbf{M}} = g_F \mu_B \bar{n} \mathbf{F}$ [Guz12, Guz11, Hig05b], where $\bar{n}$ is the integrated column density.

We will first investigate a $\eta = 0$ ($\zeta^{(\mathrm{th})} = (1/3,\, 1/3,\, 1/3)$) mixture at vanishing quadratic Zeeman shift $q = 0$. Figure 5.23 shows typical images of the transverse (upper row) and the longitudinal (lower row) magnetization as a function of time. The magnitude of the magnetization which is shown through the brightness of the signal increases significantly from short to long evolution times. Furthermore, one notices that the number of spin domains decreases (the spin domains are given by regions of same color) while the average size of the domain becomes larger. For relatively short evolution times of $t \lesssim 500\,\mathrm{ms}$, we observe domains with sizes of about $8-10\,\mu\mathrm{m}$ similar to the ones observed in [Ven08, Ven10]. For longer times however the domains continue to grow and merge and the strength of the magnetization continues to increase.

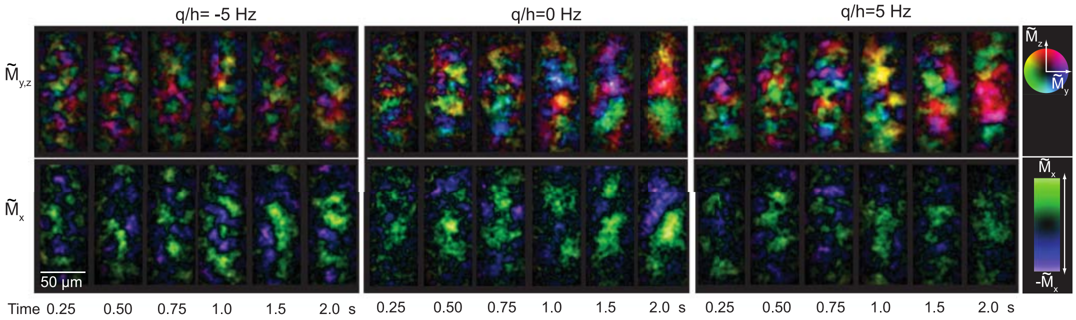

Figure 5.24: Transverse (upper row) and longitudinal (lower row) magnetization for different values of the quadratic shift and as a function of the evolution time. After longer evolution times $t \gtrsim 1\,\mathrm{s}$, one observes that for $q/h = -5\,\mathrm{Hz}$ ($q/h = +5\,\mathrm{Hz}$) the magnetization occurs predominantly in the longitudinal (transverse) direction. At $q/h = 0\,\mathrm{Hz}$ the magnetization seems to be similar for both orientations. Adapted from [Guz11].

We can now also study the evolution of such a $\eta = 0$ mixture for different quadratic shifts. Figure 5.24 shows the magnetization density for $q/h = -5\,\mathrm{Hz}$ and $q/h = +5\,\mathrm{Hz}$ as a function of time. For a better comparison we also show $\tilde{\mathbf{M}}$ for $q/h = 0\,\mathrm{Hz}$. Comparing the brightness, hence the magnitude of the magnetization of the images for the longest evolution times, one clearly observes a spin space anisotropy. For negative quadratic shift ($q/h = -5\,\mathrm{Hz}$), the longitudinal magnetization $\tilde{M}_x$ is brighter, hence more magnetized as the transverse magnetization $\tilde{M}_{y,z}$. This behavior is inverted at $q/h = +5\,\mathrm{Hz}$ where the transverse magnetization is stronger than the longitudinal one. For vanishing quadratic shifts, the magnetization seems to have a similar strength for $\tilde{M}_{y,z}$ and $\tilde{M}_x$. For all quadratic shifts we again observe growing and merging of spin domains of increasing size and the timescale for this coarsening seems to be the same independent of the fact if q is small and positive $q/h = +5\,\mathrm{Hz}$ or small and negative $q/h = -5\,\mathrm{Hz}$. In order to evaluate these changes in more detail and in a more quantitative way, we will now introduce the magnetization correlation function.

The Magnetization Correlation Function

The i-th component of the dimensionless magnetization correlation function vector can be defined as

$$G_i(\delta\mathbf{r}) = \frac{\sum_{\mathbf{r}} \tilde{M}_i(\mathbf{r}) \cdot \tilde{M}_i(\mathbf{r} + \delta\mathbf{r})}{(g_F \mu_B)^2 \sum_{\mathbf{r}} \bar{n}(\mathbf{r}) \cdot \bar{n}(\mathbf{r} + \delta\mathbf{r})}, \tag{5.15}$$

where $\bar{n}(\mathbf{r})$ is again the integrated column density and $\tilde{M}_i(\mathbf{r})$ is the respective component of the magnetization density vector. Using this quantity allows us to quantitatively evaluate the domain coarsening and the observed spin space anisotropy.

The Variance of the Magnetization For $\delta\mathbf{r} = 0$ the correlation function defines the variance of the magnetization. As defined in [Guz11], the variance of the longitudinal magnetization is defined by $G_{\parallel}(0) = G_x(0)$ and the variance of the transverse magnetization by $G_{\perp}(0) = \frac{1}{2}\,(G_y(0) + G_z(0))$. For a completely magnetized sample we expect $\sum_i G_i(0) = G_{\parallel}(0) + 2\,G_{\perp}(0) = 1$. To obtain meaningful results for the variance of the magnetization, there are several issues we have to consider. First, in order to minimize the effect of noise on the results we do not only consider $\delta\mathbf{r} = 0$ but rather evaluate $\delta\mathbf{r}$ over an area of $3.5\,\mu\mathrm{m}\times 3.5\,\mu\mathrm{m}$ centered at $\delta\mathbf{r} = 0$. To minimize the amount of noise resulting from the thermal cloud, we only evaluate the correlation function inside a $35\,\mu\mathrm{m}\times 85\,\mu\mathrm{m}$ area of the condensate. Additionally, we have to take special care to normalize the correlation function. This is done with a combination of experimental and theoretical considerations which are further described in [Guz12]. They include the loss of atoms due to the finite lifetime, the depletion of atoms due to the polarization-contrast pulse and the resulting decline in the polarization-contrast signal.

Figure 5.25 shows how the anisotropy in the spin directions evolves for different values of the quadratic shift for a sample initialized as a $\eta = 0$ mixture. After an initial time where the magnetization variance develops evenly distributed between longitudinal and transversal direction, we observe that $\mathbf{G}(0)$ increases predominantly in longitudinal (transverse) direction for $q/h = -5\,\mathrm{Hz}$ ($q/h = 5\,\mathrm{Hz}$). The spin distribution remains evenly distributed for $q/h = 0\,\mathrm{Hz}$ even after long evolution times. The spin anisotropy can also be observed if we plot the variance of the magnetization after $t = 2\,\mathrm{s}$ as a function of the quadratic shift (see figure 5.26).

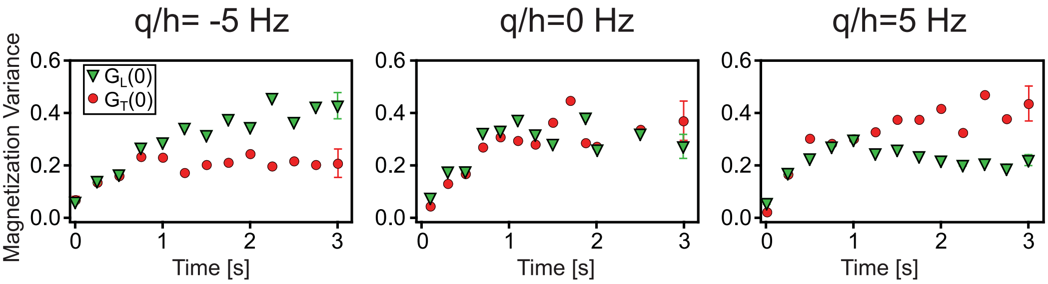

Figure 5.25: Variance of the magnetization for different values of the quadratic shift as a function of time for a sample initialized with $\eta = 0$. After an initial isotropic growth of the magnetization variance a spin space anisotropy emerges. It leads to more magnetization along the longitudinal (transverse) direction for a negative (positive) quadratic Zeeman shift. For $q/h = 0\,\text{Hz}$, the magnetization variance stays isotropic. The data is an average over 6 measurements and the error bars are given by the standard deviation. Figure and caption taken and adapted from [Guz11].

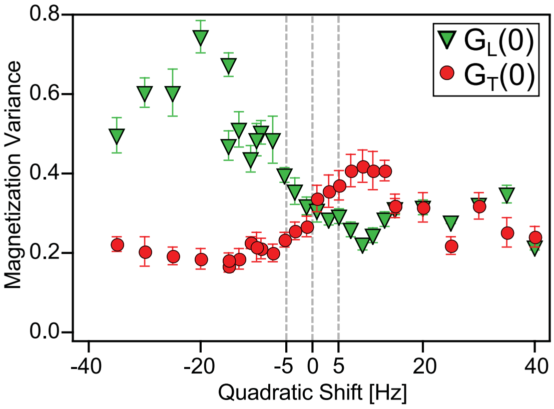

Figure 5.26: Variance of the magnetization after $t = 2\,\text{s}$ evolution time as a function of the quadratic shift. Shown is an average of six experimental realizations and the errors are the standard deviation. One can distinguish three different regimes: For $q < 0$ the variance of the magnetization is predominantly in the longitudinal direction, for $0 < q/h < q_0 \approx h \times 10\,\text{Hz}$ the variance of the magnetization is mostly in the transverse direction and for $q/h > q_0$ the system is in a polar state. The error bars are given by the standard deviation of 6 measurements. Figure and caption taken and adapted from [Guz11].

Domain Coarsening We can also use the correlation function defined in equation 5.15 to extract an average domain size of the observed spin textures. As shown in figure 5.27 we calculate the corresponding correlation map from $\tilde{M}_i(\mathbf{r})$. From this we can obtain the characteristic length of the domains $l = \sqrt{4A/\pi}$, where A is the area of the central region with positive correlation (see white area in the domain map in figure 5.27(a)). Figure 5.27(b) shows the domain length as a function of time at vanishing quadratic shift for a sample that was initially prepared with $\eta = 0$. The length of the domains are at the beginning about $10\,\mu$m and then increase until the domain length seems to saturate at about $40\,\mu$m. The observation of domain coarsening reveals that our system is, at least for short evolution times, not in an equilibrated state. Usually, the dynamics of domain coarsening is described by a self-similar growth of the characteristic length scale of the systems and its temporal evolution is described by a power law behavior: $l(t) \sim t^b$ [Guz11]. The exponent b depends on the order parameter of the system which is in our case given by the magnetization [Muk07].

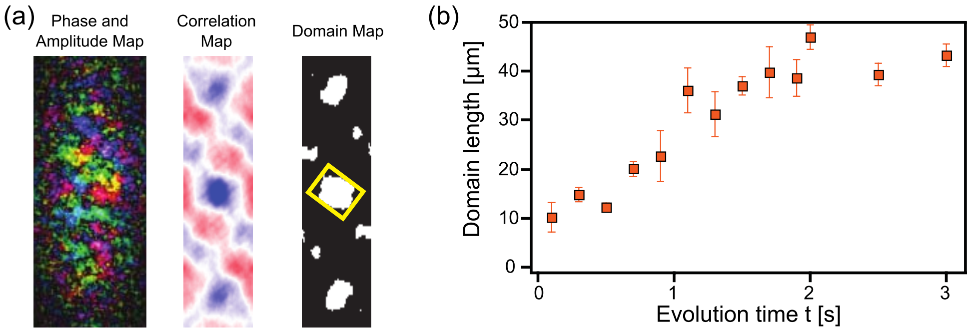

Figure 5.27: (a) Extraction of the domain size from the correlation map. Shown is one realization of a phase and amplitude map for an intermediate evolution time and the respective correlation and domain map. From the correlation map we extract the characteristic domain size by measuring the area of the central region of positive correlation. (b) Temporal evolution of the domain size. Adapted from [Guz11, Guz12].

In principle, we can extract the observed coarsening exponent using a fit to the data shown in figure 5.27(b). To be able to obtain reasonable results for this quantity, finite size effects should be negligible. This means that the domain size should be orders of magnitude smaller than the total size of the sample which is not fulfilled in our case. We still perform such an analysis and the obtained exponent for $q/h = 0\,\text{Hz}$ ($q/h = -5\,\text{Hz}$) is $b = 0.27 \pm 0.02$ ($b = 0.27 \pm 0.03$)[7]. These results are in remarkable agreement with the theoretical predictions for the domain coarsening for such a spinor system which predicts an exponent of 1/4 (1/3) for $q/h = 0\,\text{Hz}$ ($q/h = -5\,\text{Hz}$) [Guz11, Guz12]. The validity of these results is however difficult to estimate due to the finite size of the system.

---

[7] The details of this analysis can be found in [Guz12]

The Power Spectrum of the Fourier Transform

Another way to extract information about the length scales, the correlations and characteristic symmetry axes of the system is to use the power spectrum of the two-dimensional Fourier transformation. It is defined by the absolute modulus square of the two-dimensional Fourier transformation

$$P(k_i, k_j) = \left|\tilde{M}(k_i, k_j)\right|^2 = \left|\mathcal{F}\left(\tilde{M}(i, j)\right)\right|^2, \tag{5.16}$$

where (k_i, k_j) is the wave vector associated to the imaging plane (i, j) (see e.g. [Ven10]). Examples for this quantity were already shown in figure 5.18 where results obtained with the previous experimental setup are summarized. These power spectra were also used in section 5.4.4 to extract the MTF of the imaging setup. Figure 5.28 shows the power spectra of the transverse and longitudinal magnetization averaged over about 6 realizations at a quadratic shift of $q/h = +5\,\text{Hz}$.

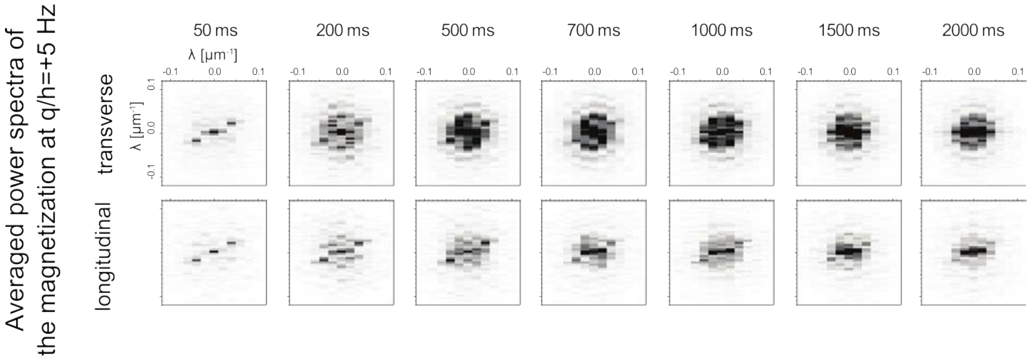

Figure 5.28: Averaged power spectrum of the transverse and longitudinal magnetization at a quadratic shift of $q/h = +5\,\text{Hz}$. The power spectrum increases for longer evolution times. This growth is more pronounced for the transverse magnetization which is due to the already discussed spin space anisotropy. Adapted from [Guz12].

For our analysis, it seemed easier and more stable to extract a characteristic length scale from the correlation function and not from the power spectrum. However, we are still able to obtain some information from the power spectra. One can again observe the spin space anisotropy since the power spectrum of the transverse magnetization seems significantly stronger than for the longitudinal magnetization. This is in agreement with our previous results using the correlation function. Furthermore, we can use these power spectra to compare our results to the ones obtained in [Ven08, Ven10]. Comparing our power spectra to the ones shown in 5.18, one notes that we do not observe one unchanged symmetry axis for different evolution times and we also do not observe the two distinct wave vector modulations.

5.5.6 Conclusion

To conclude, we have studied the time evolution of a $F = 1$ spinor Bose-Einstein condensate of ^{87}Rb. We measured the redistribution of spin populations using Stern-Gerlach time-of-flight imaging which showed that an equilibrated state is only reached for small absolute values of the quadratic Zeeman shift ($|q|/h \lesssim 10\,\mathrm{Hz}$). This process has a timescale of $1-2\,\mathrm{s}$, which is shown by the fact that the system reaches a common spin distribution independent of the initial spin composition. Recently, a measurement with a $F = 1$ spinor BEC of sodium [Jac12] observed similar equilibration timescales on the order of seconds. For large absolute values of the quadratic shift ($|q|/h > 10\,\mathrm{Hz}$), the dynamics of the systems slows down further and even after evolution times of about $4\,\mathrm{s}$ the system never leaves its initial configuration.

Furthermore, we also investigated the vector magnetization of the sample in the trap using a newly developed imaging technique called polarization contrast spin-echo imaging. With this technique, we observe three main features. First, we measure an increasing magnetization after cooling an unmagnetized sample into the quantum degenerate regime. Second, the dominant direction of the magnetization depends on the quadratic Zeeman shift. This spin space anisotropy is in agreement with the mean-field phase diagram [Muk07, Kjä09, Kaw10] since we observe a predominantly longitudinally (transversally) magnetized system for $q/h < 0\,\mathrm{Hz}$ ($0 \leq q < q_0$). The final observation is that the size of the spin domains grow as a function of time and the obtained exponents seem in agreement with theoretical predictions.

Our results for both the time-of-flight and the in-situ observations agree with the mean-field phase diagram. We did not reproduce the two wave vector ”crystalline” magnetization with fixed orientation observed in [Ven08, Ven10]. The analysis of out-of-focus images described in section 5.4.4 or in [Guz12] suggests that they are most likely due to imaging aberrations. Furthermore, we could show that the $8-10\,\mu\mathrm{m}$ spin textures observed before are only an intermediate state which further develops towards a system which is in agreement with the mean field phase diagram. This makes it unlikely that the previously observed corrugated spin textures [Ven08, Ven10] are in equilibrium and caused by dipolar interactions of the atoms. Our experimental observation is further backed by theoretical considerations which predict that dipolar interactions would lead to a long wavelength modulation of the magnetization with a size of $30-40\,\mu\mathrm{m}$ [Kaw10].

5.6 Outlook

There are still various open questions that could be addressed in future studies both experimentally and theoretically. The exact mechanism that sets the seconds long equilibration timescale is still not known. Related to this question is what happens at large quadratic shifts where the system's dynamics slow down even further. One could also use our novel imaging technique to measure the time evolution of one single realization of a spinor BEC to study the dynamics of spin vortices and domain formation.

For now, the experiments in Berkeley have taken a different route since an optical kagome lattice was added to the setup after I left the group in 2010 [Jo12]. This lattice geometry is known for its high degree of frustration due to the particular geometry of the system. The plan is then to study this frustration by accessing the flat s-orbital band of the kagome lattice. This offers particularly interesting physics if one uses fermionic atoms like for example ^{6}Li. According to [Jo12], one expects interesting phenomena like flat-band ferromagnetism [Tas92] or enhanced Cooper pairing [Ima00] for such a system. This is particularly interesting since the vacuum chamber was built such that one can easily add lithium to the setup without having to rebuild the whole machine.

6 An Ultracold Fermi Gas in Two-Dimensions

Changing the dimensionality of an ultracold atom system has strong implications on its expected behavior. As we already laid out in section 2.6, lowering the dimensionality of a system does not only affect the two-particle properties, like the scattering process, of an ultracold Fermi gas. It also strongly influences the many-body physics. In recent years the interest in quasi two-dimensional ultracold fermionic systems has increased strongly. After the observation of the Berezinskii-Kosterlitz-Thouless (BKT) transition from a normal to a superfluid phase with ultracold bosonic atoms in two dimensions [Had06], efforts were made to also investigate two-dimensional fermionic systems [Mar10b, Frö11, Dyk11, Fel11, Frö12, Vog12, Kos12, Som12]. In these studies, the evolution of systems in the crossover from 3D to 2D were investigated [Dyk11, Som12] and spectroscopic methods were adapted to 2D systems (e.g. RF [Frö11] and Arpes spectroscopy [Frö12]). These methods were then used to investigate the pairing [Fel11, Som12], the interactions [Frö12], polaronic physics [Kos12] and the excitations [Vog12] in ultracold two-dimensional Fermi gases. So far however, unlike in the bosonic case [Des12], superfluid behavior and the BKT phase could not be observed with fermionic systems. This regime of fermionic superfluidity for a strongly correlated two-dimensional system is particularly relevant because it is expected to be related to the mechanisms occurring in high-T_c superconductors. Furthermore, these phenomena can possibly influence the understanding of two-dimensional electron gases and quasi two-dimensional thin films of fermionic ^{3}He.

In this chapter, we are going to present our efforts towards realizing a strongly interacting Fermi gas of ^{6}Li in a quasi two-dimensional setting. Our studies investigate the phase fluctuations when loading a mBEC into the 2D confinement. After presenting preliminary results deep in the mBEC regime we extend our studies towards strongly correlated systems where the fermionic nature of the atoms starts to play an important role. All studies presented in this chapter were carried out using the fermionic-lattice machine which is also called "new" experiment in Heidelberg in the group of Prof. Jochim. Since these investigations have not been finalized yet, the preliminary results are presented in chronological order.

We will start with a quick introduction on how we create a standing wave optical dipole trap for the 2D confinement[1]. After the characterization of the resulting stack

---

[1] The interferometer setup and initial tests and measurements where previously discussed in [Boh12, Sta12, Nei13]. In these parts, we will summarize the results and follow their arguments.

of oblate, pancake-shaped optical traps, we show how we can load a mBEC in a single slice of the stack of traps. We will then briefly introduce the theoretical description of ultracold two-dimensional systems. Subsequently, we will investigate phase coherences of a molecular Bose gas in this single pancake-shaped trap. Finally, we show how these measurements could in the future be used to obtain information about the state of the system.

6.1 Creation of a 2D Confining Potential

In chapter 3, we explained how an ultracold degenerate Fermi gas or a molecular Bose-Einstein condensate is prepared in the fermion lattice experiment. We will now explain the production, the setup and the loading of a stack of quasi two-dimensional optical dipole traps.

To reach the quasi two-dimensional regime with fermions it is crucial to have a trap with a very large aspect ratio, hence with strong confinement in the z direction and weak confinement in the radial directions (x and y). Only then it is possible to load a reasonable amount of atoms into the trap without populating the excited states in the z-direction. We achieve this by using a standing wave created by the interference between two coherent laser beams. By choosing an adequate diameter of the trapping beams, we can create an interference pattern where the interference maxima are approximatively round in the horizontal direction. Due to their oblate, pancake-like shape, we will refer to a single maximum of the interference pattern as a pancake or a pancake-shaped optical trap and to the whole standing wave as the stack of pancakes.

One needs to consider several crucial points when planning and building such a setup:

- We want to have a long lifetime in the 2D confinement and heat the atoms as little as possible. Therefore, the wavelength of the trapping light should be very far detuned from the atomic transition and the intensity noise of the trapping light in regime of the trap frequencies must be small.

- The pancake-shaped optical potentials need to be deep enough to trap the relatively light ^{6}Li atoms.

- Because we do not want coupling or tunneling between adjacent pancakes, the distance between them should be sufficiently large.

- To be able to address the atoms in one single pancake, the spacing between adjacent pancakes should be large enough.

- To guarantee that one always loads into the same pancakes, the position of the pancakes should be stable and not change even over the timescale of several days.

6.1.1 Creating the Trapping Light for the Pancake Traps

We use a Mephisto laser from Innolight as a source of laser light for our two-dimensional optical trap. This single frequency laser runs at a wavelength of 1064 nm which is sufficiently far detuned from the atomic transition of ^{6}Li atoms ($\lambda = 671\,\text{nm}$). The intensity noise of this laser is very low and we measured a relative intensity noise (RIN) below $-130\,\text{dBm/Hz}$ [Nei13]. The output power of this laser is only 500 mW and thus not sufficient for the trapping of the atoms. Therefore, we use the Mephisto as a seed for a 50 W, 1064 nm fiber amplifier from Nufern (Sub-1174-22). In our setup, the amplifier generates about 40 W of laser light at a wavelength of 1064 nm. The light from the amplifier is split into several beams, each of which passes an acousto-optical modulator (AOM) for intensity stabilization and is subsequently coupled into a high-power optical fiber[2]. Each of these fibers delivers up to about 8 W of intensity stabilized single-frequency laser light at a wavelength 1064 nm to the experimental table. We also analyzed the intensity noise of the trapping light after the fiber amplifier and observe a significant increase of the RIN due to the amplifier. A more detailed analysis of the intensity noise is described in [Nei13]. It shows that, although the intensity noise is higher after the fiber amplifier, it will still not limit the envisioned experiments. Therefore, the just described setup fulfills the earlier set requirements of providing a low noise, single frequency laser beam of sufficient power.

6.1.2 The Setup

To obtain a standing wave pattern where the positions of the individual pancakes is stable over days and weeks, we choose an integrated design for the interferometer (see figure 6.1(a)). It basically consists of a large piece of aluminum; and all necessary optical components are directly attached to it.

The laser beam enters the interferometer from the bottom right before it is split at a non-polarizing beam splitter cube (light blue). Then both beams are reflected on dielectric mirrors and leave the interferometer such that they intersect in the middle of the main chamber under an angle of 14° (see figure 6.1(c)). This results in an interference pattern in vertical direction. The spacing between the maxima of the standing wave is about $4\,\mu$m. We choose the diameter of the trapping beams to be about 1.3 mm. This leads to pancakes which are approximately round in the horizontal (x-y) plane (see figure 6.1 (b),(c)). For such a system, we calculate an expected aspect ratio between the trap frequencies of $\eta = \omega_z/\omega_{x,y} \approx 300$.

The spacing of $4\,\mu$m is enough to suppress tunneling between adjacent pancakes at the trap depths that we usually operate at. The integrated design makes the setup very robust and stable. One additional reason which leads to a good long-term stability is that both paths of the interferometer have the same length[3]. We will later show

---

[2] The other beams are used for two additional optical lattice beams. A sketch of the optical setup on the so-called "Nufern breadboard" can be found in [Nei13].

[3] One can calculate that for a path length difference of about 20 cm the change of air pressure due

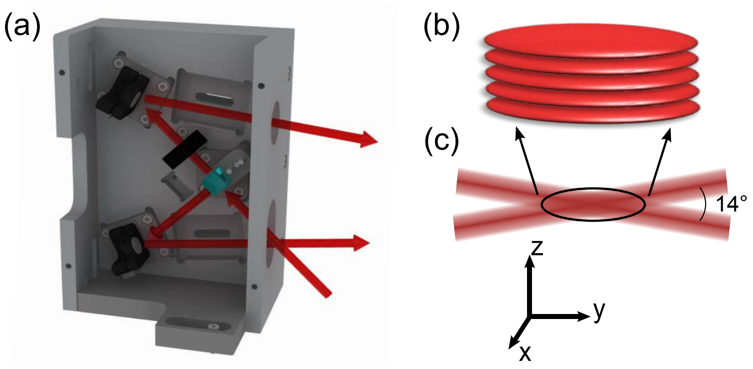

Figure 6.1: (a) Interferometer to create the stack of pancake-shaped traps. (c) The beams leave the interferometer such that they intersect in the center of the main chamber under an angle of 14°. (b) The interference pattern leads to a stack of traps with an aspect ratio of about $\eta = \omega_z/\omega_r \approx 300$. The individual pancakes are spaced by $4\,\mu$m.

that we can investigate the stability of the pancake positions using a tomographic RF spectroscopy method (section 6.2.2). With such a measurement, we were able to show that the position of the pancakes moves by less than $0.5\,\mu$m over the course of a week [Nei13]. This small change of less than an eighth of the pancake spacing will allow us to reproducibly load and address single pancakes.

6.1.3 Transfer into the Pancake Trap

We fill the quasi two-dimensional stack of optical traps by transferring ultracold clouds from the dipole trap into the pancakes. The optical dipole trap (ODT) in the fermionic lattice setup is created by two intersecting laser beams. These have orthogonal polarization and thus they do not interfere. The beams are elliptical (aspect ratio of about 6:1) before they are focused into the main chamber. Thus, the resulting trap is not cigar-shaped but flattened in the vertical direction (”surfboard”-shaped). This geometry helps us to load only few pancakes since it reduces the size of the cloud in the vertical direction.

After the last stage of the optical evaporation, we are usually left with about 1.5×10^5 particles. Depending on the magnetic field value of the final stages of the evaporation we either obtain fermionic atoms or bosonic molecules. We usually only want to transfer a fraction of the cloud into the pancakes. Therefore, we have to further decrease the number of atoms. There are two different methods with which we achieve this. We can either turn on a magnetic field gradient. This leads to a force on the atoms and thus they are spilled from the ODT. This method is similar to the one presented in chapter 4 for the preparation of few-fermion samples. The other method is to slowly decrease the

---

to a sudden change in weather could already be enough to move the interference pattern by half a wavelength. Such a change would inhibit the reproducible loading of a single pancake.

depth of the ODT by lowering the intensity of the trapping light. With both methods[4] we can prepare samples with numbers down to about 10^4. After this additional spilling process, we again increase the depth of the ODT slowly. This leads to an adiabatic compression of the ultracold cloud which reduces the cloud size, particularly in the vertical direction. We then slowly turn on the pancake-shaped trap by increasing the intensity in this particular trapping beam. During this transfer we make sure that there is sufficient scattering between the particles to allow them to thermalize into the stack of pancakes. After an additional thermalization time of about 100-200 ms, we then decrease the depth of the optical dipole trap until it is completely off. Figure 6.2 shows absorption images of the atomic clouds before the transfer, that is in the ODT in the upper row. Images after the transfer, where the atoms are trapped in the stack of pancake-shaped traps, are shown in the lower row.

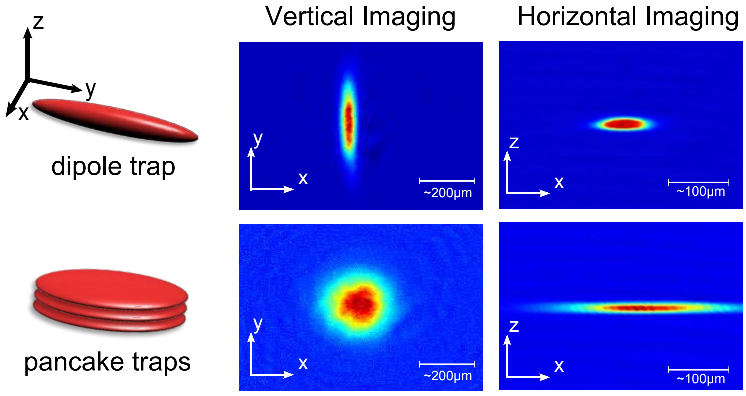

Figure 6.2: Sketch and absorption images of the ultracold clouds before the transfer (upper row) and after the transfer to the stack of quasi-two dimensional traps. In this case the atoms are transferred in about 5 adjacent pancakes. Adapted from [Nei13].

The images in the vertical direction (middle column) clearly indicate that the cloud is transferred from the narrow surfboard-shaped trap into the round stack of pancakes. The picture of atoms in the ODT taken along the horizontal direction (top right panel) shows the anisotropy between the two tighter confined directions (x and z). For these pictures, the vertical size of the cloud in the ODT is $\sim 20\,\mu$m. This is significantly larger than the vertical size of one pancake of $4\,\mu$m. Thus we transfer into about 5 adjacent pancakes. Due to the tight confinement along the vertical (z) direction in the individual pancakes, the cloud is squeezed and thus significantly expands along the x-direction (compare upper right and lower right panel).

---

[4] In this setup, the decrease of the optical trap depth seems to work with a higher accuracy than the spilling with a magnetic field gradient.

6.2 Characterization of the Potential

As we can see in the bottom right panel of figure 6.2, we cannot resolve the individual pancakes when imaging the pancakes from the side, i.e. in the horizontal direction. The main reason that inhibits a direct optical observation of single pancakes is their large size in the horizontal direction. In order to resolve the individual pancakes, we would need an imaging setup with a resolution of about 2 μm. The depth of focus of an imaging setup can be estimated by the Rayleigh range and one obtains $\pi \times (2\mu\mathrm{m})^2/(1064\,\mathrm{nm}) \approx 11.8\,\mu$m. The size of the cloud in a pancake in the horizontal is about 100-200 μm. This is almost an order of magnitude larger than the focal depth. Hence, it is not possible to optically resolve the single pancakes from the side.

There are however other methods that can be employed in order to indirectly make the pancake-shaped traps visible. We will now present the two approaches we use to characterize our trapping potential without having to optically resolve the individual pancakes.

6.2.1 Kapitza-Dirac Scattering

In the first method, we use the diffraction of the atoms from the standing wave to measure the depth and the spacing of the pancakes. This process is regularly used to evaluate periodic potentials. It can be thought of as the analogue of the classical diffraction of light on a grating. Only that in our case, the roles between atoms and light are reversed [Nei13]. The standing wave leads to a discrete momentum transfer onto the atoms in the ultracold cloud. From the distances of the diffraction orders we can determine the spacing between pancakes and the relative number of atoms in the different diffraction orders gives us information about the depth of the standing wave.

In order to observe the diffraction pattern, we produce a mBEC of about 10^4 atoms by evaporation of a two-component Fermi gas ($|1\rangle$-$|2\rangle$ mixture) on the BEC side of the broad Feshbach resonance (see section 2.5.2). At an offset field of 795 G, the scattering length is very large and positive ($a_{3D,12} \approx 9600\,a_0$). This leads to a very fast expansion of the cloud when the ODT is turned off[5]. The fast expansion in the vertical direction would prevent us from observing the different diffraction orders since the momentum transfer due to the standing wave is rather small ($\hbar k_{\mathrm{trap}} = \hbar 2\pi/\lambda_{\mathrm{trap}}$). To limit the expansion of the condensate in the vertical direction, we do not immediately switch off the power in the dipole trap. We rather ramp it down and thus slowly release the atoms from the trap. We further reduce the expansion of the cloud by ramping the magnetic field to about 650 G while we turn off the ODT. Here, the scattering length is only about $800\,a_0$ and thus the interaction energy of the sample is significantly lowered. At this magnetic field and after the optical dipole trap is already switched off, the standing-wave beam is turned on for a short period of time. The duration of that pulse lies between 11 and 101 μs and the length is controlled using the AOM in the standing-

---

[5] Due to the anisotropic trap the expansion occurs predominantly in the vertical direction.

wave beam path. After the pulse, we let the different orders separate and the atoms expand for a time-of-flight (t_{tof}) of about 10 ms and then take an absorption image. For this image, we ramp the magnetic field back to 770 G. This has to be done because at 650 G the molecules are so deeply bound that the signal obtained with absorption imaging is very weak.

Due to the very short pulses of the standing-wave, we cannot actively control the intensity in the beam. Thus, the beam intensity fluctuates by about 20% from shot-to-shot. Since these fluctuations would not allow us to extract meaningful results, we record the integrated pulse area on a photodiode. According to these values, we then bin all pulses into intervals and average all obtained absorption images that fall within one of these intervals. The resulting, averaged images for no pulse of the standing-wave and for a total pulse area that corresponds to 193 mV on the photodiode are shown in figure 6.3(a,b). To analyze the images, we integrate along the horizontal axis and obtain doubly integrated line profiles (black data in (a) and (b)). Several of these graphs for different overall pulse areas are shown in figure 6.3(c).

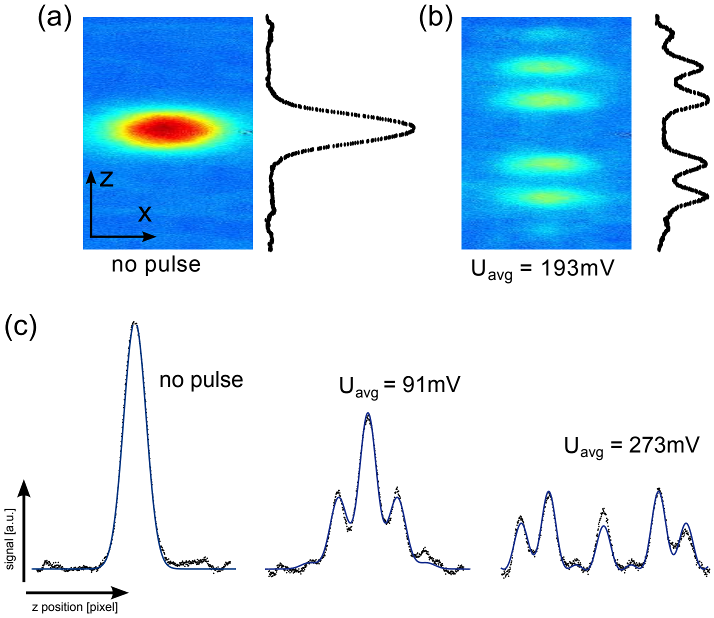

Figure 6.3: (a,b) Averaged absorption images after Kapitza-Dirac diffraction of a mBEC on the standing wave of the pancake traps. (c) By integrating the images in horizontal direction we obtain a one-dimensional column density which is shown in black for different integrated pulse areas. The blue solid lines indicate the fit according to the theoretical model for Kapitza-Dirac diffraction. Adapted from [Nei13].

We can now use a theoretical model [Ovc99, Nei13] to describe the line profiles in the Raman-Nath regime. It basically weights the relative number of atoms in the n-th diffraction order with $J_n(\beta/2)$, where J_n are Bessel functions of the first kind and β

is the total pulse area in units of $\hbar$ (for a more detailed description see [Nei13]). The position of the n-th diffraction order is simply given by $\Delta z_n = n t_{tof} \hbar k_{\text{trap}}/(2m_{Li})$. Fits to the experimental data using this theoretical prediction are shown in figure 6.3(c) as blue lines. The agreement between the theoretical prediction and the data is reasonable. For the spacing between the pancakes we obtain $d_{PC} = (3.6 \pm 0.36)\,\mu\text{m}$ [Nei13]. The error of these measurements is dominated by the uncertainty in the magnification of the imaging setup which we estimate to be 10%. This is in agreement with the calculated spacing of $d_{PC,theo} = 3.9\,\mu\text{m}$. The obtained trap depths are approximately a factor of 2 smaller than the theoretical estimates. They are however consistent with the trap depths obtained from a trap frequency measurement similar to the one presented later in this section. Although the obtained depth does not agree with the theoretical prediction, we can still use the diffraction technique to compare relative depths of the standing wave. In fact, we performed several iterations of this measurement to optimize the overlap between the two interfering beams which create the standing wave.

6.2.2 RF Tomography

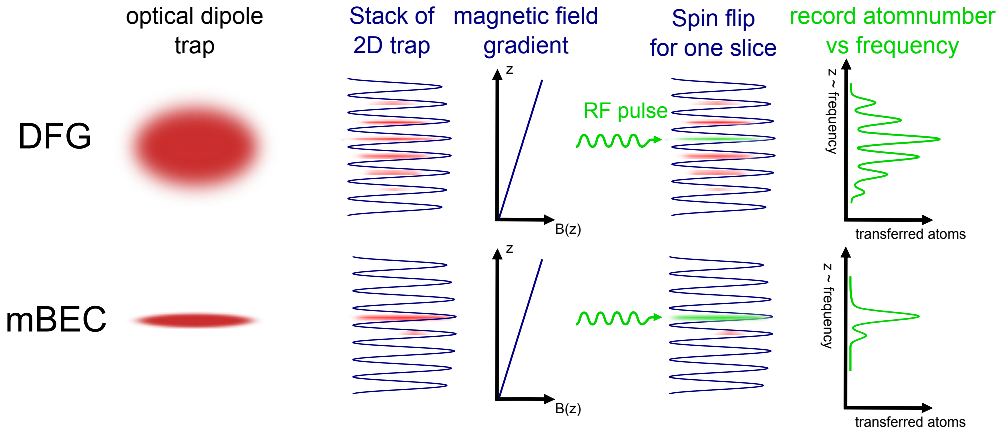

Figure 6.4: RF tomography of a mBEC and a DFG in the pancake-shaped trap. The amount of pancakes that are filled during the transfer from the optical dipole trap depends on the initial size of the sample. With a magnetic field gradient the transition frequency changes as a function of the z-position and thus we can tomographically resolve the populated pancakes.

We will now show how we use tomographic RF spectroscopy to measure the atom distribution in the pancakes and test the long-term stability of the standing-wave trap. The idea of the RF tomography method is simple and is illustrated in figure 6.4. By applying a magnetic field gradient in the vertical direction, the local magnetic field depends linearly on the vertical position. If the difference in magnetic fields between two adjacent pancakes (distance $\sim 4\,\mu\text{m}$) is larger than the width of our RF spectroscopy, then we can resolve the individual pancakes with an RF pulse which transfers atoms from an initial to a final state. By imaging the number of atoms that were transferred into the final state, we obtain the density distribution of atoms over the pancakes convoluted with the width of the RF measurement.

As shown in figure 6.4, the distribution of the atoms over the pancakes strongly depends on the size and position of the atom cloud before the transfer. Due to the Pauli pressure the size of a degenerate Fermi gas is significantly larger than the size of a molecular Bose-Einstein condensate. Therefore one expects to load more pancakes when starting with a DFG.

Although the method is comparatively simple to understand, there are quite a few details that one has to consider when performing such a measurement. Therefore, we will now list the occurring challenges and issues and explain how we will deal with each one of them:

Point 1: The signal of the transferred atoms is very weak since we usually only transfer a couple of hundred to a couple of thousand atoms (see figure 6.5).

Solution: Optimize the initial parameters for fits to the absorption images. Most of the time, we average several images before we extract the number of atoms with a Gaussian fit.

Point 2: The applied magnetic field gradient exerts a force on the atoms. If the gradient is too large, the atoms get spilled from the pancakes.

Solution: By increasing the depth of the pancake traps we can weaken this effect. However, due to the finite power that is available in the trapping beam, this will fundamentally limit the size of the gradient and the maximum number of atoms that are left after applying the gradient.

Point 3: The interactions between particles lead to a broadening and shift of the RF transition.

Solution: Remove all atoms in one of the states (usually $|1\rangle$). The remaining one-component Fermi gas in state $|2\rangle$ is non-interacting. For a Fermi gas this is done with a non-interacting mixture and thus we do not significantly disturb the remaining atoms. If we load a mBEC, the removal of one component is more complicated and leads to substantial heating of the remaining atoms. This however, does not affect in which pancake or in how many pancakes the atoms are trapped.

Problem 4: Due to the large magnetic field gradient, the atoms quickly dephase during the RF pulse.

Solution: This problem cannot be solved because the available RF power is limited. Therefore, we have to accept that we can only drive incoherent pulses. This means we can at most transfer half of the atoms.

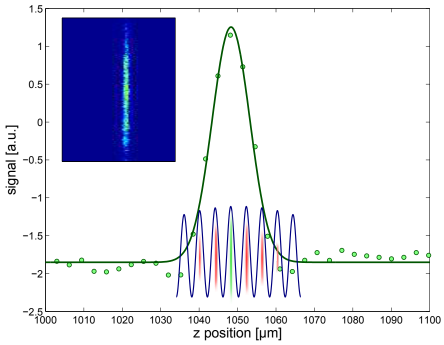

Figure 6.5: Integrated line density from the average of about 50 absorption images taken after transferring atoms in one pancake using a tomographic RF pulse (green points). Due to the low resolution of the imaging systems, we cannot resolve individual pancakes. The center of the Gaussian fit (solid line) to the absorption imaging data can however indicate the position of the transferred pancake. The inset shows the average over 50 absorption images. For better comparison, the size of the pancakes is indicated by the sketch. Adapted from [Nei13].

First Tomographic Measurements with a Fermi gas

We will now explain the RF tomography sequence for an ultracold Fermi gas. The two-component Fermi gas ($|1\rangle$-$|2\rangle$ mixture) is transferred into the pancakes at a magnetic field of about 300 G. The interaction between the components ensures that the atoms thermalize into the pancakes. After we turn off the dipole trap, the magnetic field is increased to 527 G. Here, the two components are non-interacting and we remove all atoms in state $|1\rangle$ with a resonant light pulse of about 10 μs. Afterwards, we ramp to the magnetic field value where we want to perform the tomography measurement. We then use the MOT coils to apply a magnetic field gradient and wait until the gradient has stabilized[6]. While the gradient field increases, we also increase the power in the beam which creates the pancake traps. This limits the number of atoms that are spilled from the trap due to the force exerted by the gradient. Next, we apply the RF pulse which transfers a part of the atoms at a certain position from state $|2\rangle$ to state $|3\rangle$. The RF pulse duration is longer than 12 ms, so the transition is not broadened due to the Fourier limit.

The result of such a tomographic RF measurement is presented in figure 6.6. Plotted are the number of transferred atoms and the center position of the fits as a function of the applied frequency of the pulse. Furthermore, figure 6.6(c) shows a histogram of the occurring fit centers. In figure 6.6(a) one can clearly observe the position of the individual pancakes. Due to the small magnetic field gradient of only about 40 G/cm and due to the finite resolution of the RF transition of about 100 Hz, the pancakes are

---

[6] Due to the large inductance of the MOT coils, this takes several hundred milliseconds.

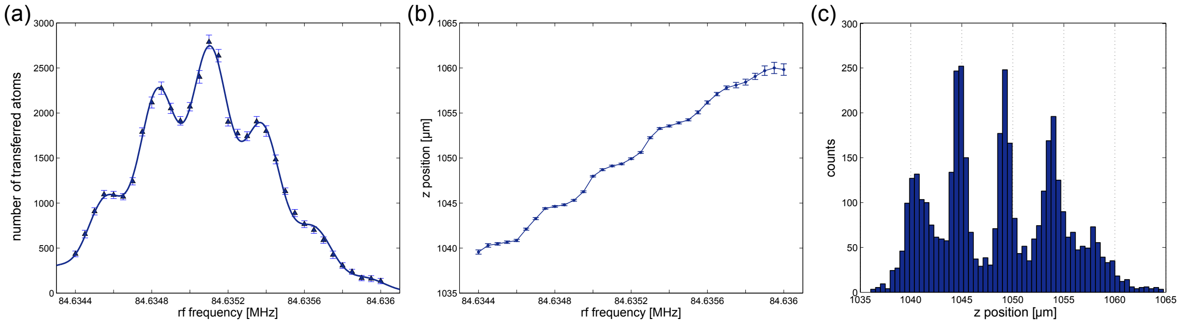

Figure 6.6: RF tomography of a Fermi gas before the optimization. Shown are the number of transferred atoms (a) and the centers of the Gaussian fits (b) as a function of the frequency of the RF pulse. A histogram of all occurring fit centers is shown in (c). Taken and adapted from [Nei13].

however not completely separated[7].

Stability of the Pancake Position

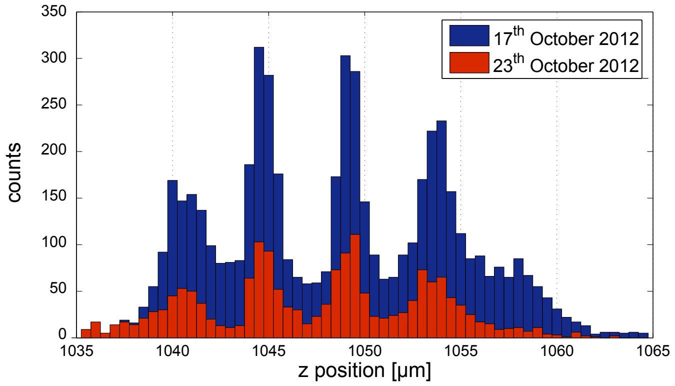

Figure 6.7: Comparison of the fit center histogram for two tomography measurements performed on October 17 and October 23, 2012. A detailed analysis shows a change of less than $\Delta\phi \lesssim \pi/5$ between both measurements. Adapted from [Nei13].

By independently analyzing parts of the just presented RF tomography measurement [Nei13], we can show that the short term stability of the pancake position is very good. The phase change of the standing wave is $\Delta\phi \leq \pi/12$. In an external stability measurement, where we used a microscope objective and a CCD camera to measure the stability of the interference fringes, we obtained a short term stability of $\Delta\phi \lesssim \pi/30$ [Sta12]. These values are more than sufficient to not limit the repeated loading of

---

[7] The resolution of our RF spectroscopy was in this measurement limited by the stability of the magnetic field.

a particular pancake. We mentioned however that we also want a good long-term stability. This was tested by repeating the tomography measurement presented above about a week later. A comparison of the histogram of the centers of the fits is shown in figure 6.7. From the comparison of these two measurements we obtain a long-term stability of $\Delta\phi \leq \pi/8$. This means that over the course of six days, the position of the pancakes changes by less than 500 nm[8]. This is significantly less than the spacing of 4 μm between the pancakes and thus the stability of the spatial position of the pancakes does not limit our experiments.

All of the measurements presented so far were still performed before the move to the new laboratories at the University of Heidelberg. Since then, several parts of the setup were optimized to be able to perform more precise tomography measurements. Before we will present these changes to the setup, we will first explain how we perform such a measurement for a mBEC.

Tomography of a mBEC

If we transfer a molecular BEC into the pancake traps, the atoms are bound into diatomic molecules. Therefore, we cannot remove one of the components with a resonant light pulse without strongly affecting the other component that we want to keep in the trap. In order to minimize the heating and loss during the removal process, we ramp to very high magnetic field (> 1000 G). Here, the atoms are not bound into molecules[9] and we remove the atoms in state $|1\rangle$ with a resonant light pulse. This heats the remaining atoms but according to our measurements, they still cannot hop into the next pancake. The remaining one-component Fermi gas is then ramped to the magnetic offset field where we want to perform the tomography which is usually either 527 G or 795 G. The actual RF transition and the application of the magnetic field gradient is done exactly as for the fermionic case. As illustrated in figure 6.4, the atoms are usually distributed over less pancakes when they were transferred from a mBEC. This is owed to the fact that due to the Fermi pressure, a Fermi gas is larger in size than a mBEC with a similar number of atoms.

Optimizing the Stability of the Experiment

As we showed earlier, we could so far not clearly address one single pancake. This was mostly due to fluctuations of the magnetic offset field. Before the optimization, the long-term stability of the magnetic offset field was only about 40 mG for an offset field of about 800 G. Therefore, we took great care to improve the magnetic field stability after moving the experimental setup to the new laboratories at the Physikalisches Institut.

---

[8] This stability is only achieved if the experiment is completely thermalized. This thermalization process usually takes on the order of a few of hours.

[9] For a quasi two-dimensional system there is a bound state for all values of the interparticle interaction. At this field however, the binding energy is $E_{2D,B} \ll k_B 1\,\mathrm{nK}$ and thus the atoms are not bound.

Furthermore, we replaced the power supply of the MOT coils in order to be able to increase the magnetic field gradient further. We will now list all the upgrades and changes made in order to increase the stability of the tomographic RF measurement and to be able to load all atoms into as few pancakes as possible:

- We realigned the foci of the optical dipole trap beams. Now, the foci are exactly at the position where the two beams intersect. This increases the confinement in the vertical direction and leads to smaller cloud sizes in the vertical direction. This allows us to load the gas into fewer pancakes.

- Additionally, we lowered the fan speed of the flow box used to control the temperature of the optical table. The vibrations and the strong draft of the air were causing shot-to-shot fluctuations of the position of the optical dipole trap. Over the course of a tomography measurement this would broaden the atom distribution over more pancakes.

- With the new power supply we are able to increase the applied magnetic field gradient from about 40 G/cm before the move to about 60-65 G/cm.

- For the tomographic measurement, we also independently optimized the PID parameters to create a very stable magnetic offset fields and magnetic field gradients.

- We changed the voltage control input of the Feshbach coils power supply from $0 - 5\,\mathrm{V}$ to $0 - 10\,\mathrm{V}$. This increases the precision of the set value from the PID controller by a factor of 2.

- The ADWIN signal which controls the Feshbach coils was internally increased by a factor 3. After the ADWIN we divide the signal again by exactly the same factor using a voltage divider. This decreases the minimal possible step size of the control voltage by a factor of 3.

- We increased the precision of the control input which measures the current in the Feshbach coils for our digital PID controller. This is achieved by subtracting an offset and subsequently multiplying the signal by a factor of 20. This is done in a box produced by the electronic workshop of the institute. This high precision input is only used when we want to perform a tomography measurement.

After taking all these measures we reevaluated the magnetic field stability and obtained a long-term stability of about 5 mG at an offset field of 800 G. This constitutes an eight-fold improvement and the magnetic field stability is now as good as in the "old"/ few-fermion machine.

Current RF Tomography

With all the above mentioned improvements, we retook the RF tomography measurements. Figure 6.8 shows the results of these measurements both for the transfer of a degenerate Fermi gas (a) and for the transfer of a molecular BEC (b) into the pancake-shaped optical trap.

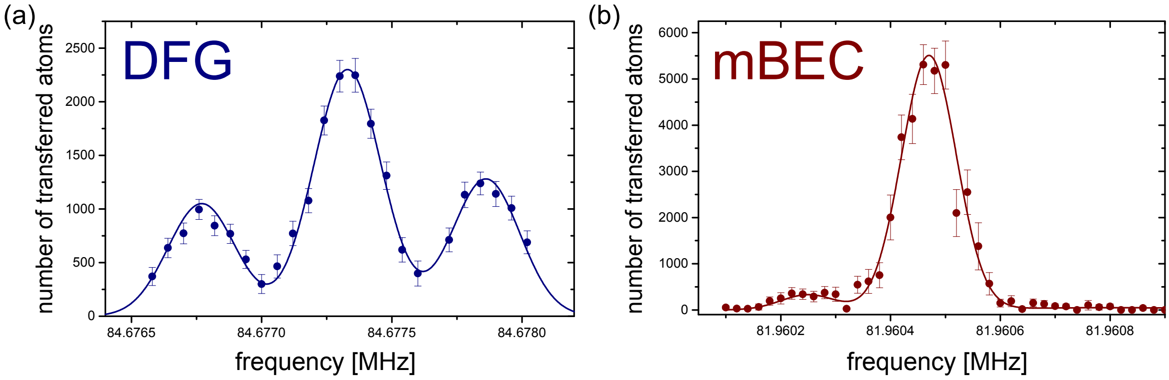

Figure 6.8: Tomographic RF spectroscopy measurement for the transfer of a degenerate Fermi gas (a) and a molecular mBEC (b) into the standing-wave trap. Due to the Fermi pressure, the Fermi gas is larger before the transfer into the pancakes and thus the atoms populate three adjacent pancakes. For the transfer of a mBEC, we can transfer almost all atoms into a single pancake.

As shown in figure 6.8(a), the Fermi gas is now only distributed over about 3 pancakes. For the mBEC, we are even able to load most of the atoms ($\gtrsim 95\%$) into a single pancake. The relative number that we obtain in such a tomography measurement underestimates the fraction of atoms loaded into the center pancake. This is owed to the fact that the magnetic field gradient, which is applied for the tomography, spills atoms from the pancakes. The fraction of atoms spilled from a pancake is larger if there are more atoms in this particular pancake. This means that the gradient removes a larger fraction of atoms from the center pancake than from the adjacent one. Hence, the obtained relative number between the pancakes is even better when no gradient is applied.

When loading into only few pancakes it becomes important to adjust the position of the cloud before we transfer it into the pancakes. This is achieved by moving the position of the atoms in the ODT before the transfer to the pancakes. As shown in figure 6.9, we can control the position of the atoms by applying a force with a magnetic field gradient. By scanning the size of the gradient and performing a tomography measurement for each value, we can optimize the position such that we predominantly load everything into one single pancake. For this optimization however it is helpful to populate more pancakes since this facilitates finding the optimal value for the transfer. Such an optimization of the dipole trap position was already done for the measurement shown in figure 6.8(b). Using this technique we can also populate two pancakes with the same number of atoms. This could for example be used as a starting point for an interference experiment similar to the one presented in [Had06].

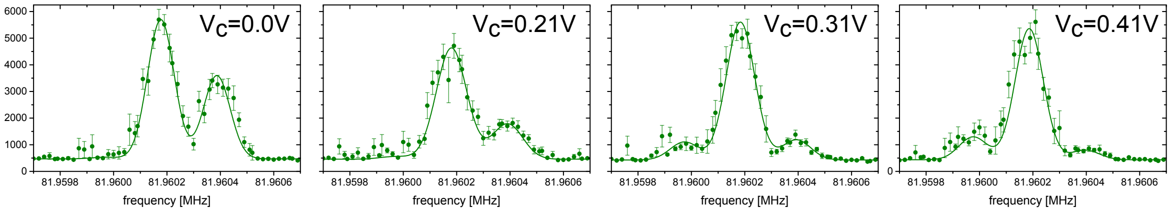

Figure 6.9: RF tomography of a mBEC for different positions of the optical dipole trap before the transfer into the pancakes. V_c is the voltage that controls the strength of the gradient that moves the cloud in the ODT.

Using MW Fields to Empty Single Pancakes

With the improved stability and the larger gradient, the individual pancakes are now almost completely separated. This should allow us to address the pancakes individually, for example using MW fields. We already performed such a tomography measurement with an additional MW pulse which transfers the atoms in state $|2\rangle$ to state $|5\rangle$ (see figure 2.5). The measurement is shown in figure 6.10, but unfortunately it was done before all the improvements on the stability of the setup were finished. Therefore, in this measurement the pancakes are not as clearly separated as now possible. Still, the measurement nicely shows how such a manipulation works in principle.

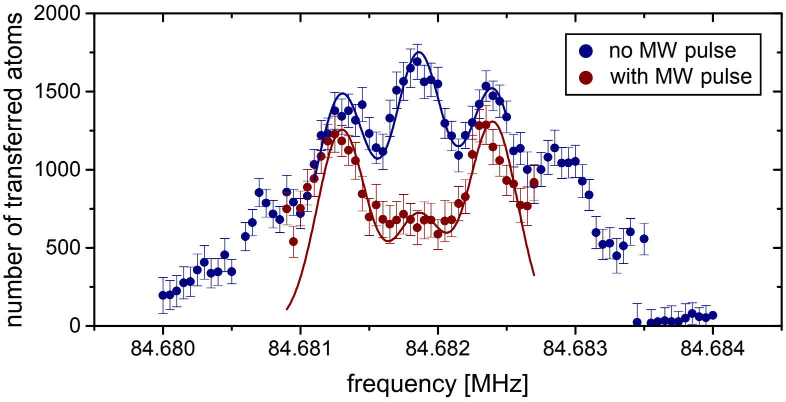

Figure 6.10: RF tomography with and without a MW pulse that transfers most atoms of the center pancake from state $|2\rangle$ to state $|5\rangle$. When the atoms are in state $|5\rangle$ the RF pulse cannot transfer the atoms to state $|3\rangle$. Hence, we observe less transferred atoms at the position of the center pancake.

6.2.3 Trap Frequencies

Another parameter that is very important for the characterization of our pancake-shaped traps is the trap frequency. These frequencies tell us the spacing between the different trap levels. Therefore, we need them to determine how many atoms we can load into our trap while staying quasi two-dimensional. Furthermore, the trap frequency in the tight, vertical axis of the trap, $\omega_z = 2\pi\nu_z$, also strongly influences the interaction strength in the quasi two-dimensional regime.

To record the trap frequencies, we load a mBEC into the pancakes and then remove the atoms in state $|1\rangle$ with a resonant light pulse[10]. The remaining one-component Fermi gas of atoms in state $|2\rangle$ is thus non-interacting. We then jump from a certain trap depth $V_c = U_{\mathrm{trap}}/2$ to twice the control voltage $V_c = U_{\mathrm{trap}}$. This quickly compresses the cloud and after a variable wait time we release the atoms from the trap for a short time-of-flight ($t_{tof} \approx 2\,\mathrm{ms}$). During the wait time the size of the atomic cloud oscillates and during the free expansion in the time-of-flight this oscillation is amplified. We then record the cloud using absorption imaging and determine the size of the cloud in all directions as a function of the wait time. We can then extract the trap frequency from damped sinusoidal fits to the size of the cloud[11]. The resulting trap frequencies for all three directions are shown in figure 6.11.

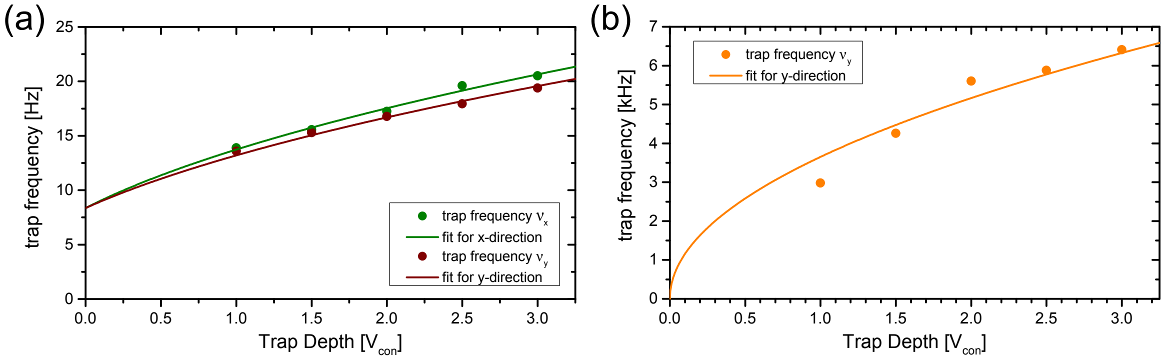

Figure 6.11: Trap frequencies ν_i as a function of the trap depth in the pancakes. We measure the trap frequencies by observing the breathing mode of a non-interacting one-component Fermi gas after a sudden change in the trap depth.

The measured trap frequencies follow the expected scaling with the square root of the trap depth (solid lines). For the vertical direction it becomes difficult to observe the oscillations for shallow trap depths with $V_{con} \leq 1.5\,\mathrm{V}$. This explains the increased discrepancies between the prediction and the measurement for these values. One should note that in the horizontal direction the atoms are not only trapped by the optical potential created by the standing wave. Due to the shape of the magnetic offset field, we

---

[10] This is done according to the procedure described earlier for the RF tomography of a mBEC.

[11] In case of the breathing mode, the cloud size oscillates at twice the trap frequency.

also have a confining magnetic potential (see section 3.3.1). This magnetic confinement tunes with the magnetic offset field. At the offset field of 795 G, where this measurement was performed, we obtain a magnetic trap frequency of $\omega_{x,m} = \omega_{y,m} = 2\pi\,8.36\,\mathrm{Hz}$. From this measurement we can also determine the aspect ratio between the vertical and the horizontal trap frequencies $\eta = \omega_z/\omega_r = 321 \pm 8$, where $\omega_r = \sqrt{\omega_x\,\omega_y}$ is the mean trap frequency in the horizontal directions[12]. This is very close to the projected value of about 300.

6.3 Theoretical Description of Quasi-2D Fermi Gases

In section 2.6, we already presented that the scattering cross section is affected by the dimensionality of the system. In particular, for a two-dimensional Fermi gas there is always a bound state, even for an arbitrarily weak attraction between the particles [Ket08]. The binding energy $E_{B,2D}$ of this confinement induced molecular state is connected to the two-dimensional scattering length a_{2D} by the following relation

$$E_{B,2D} = \frac{\hbar^2}{m a_{2D}^2}. \tag{6.1}$$

Therefore, one can use this binding energy $E_{B,2D}$ as a parameter for the description of the interaction strength of the system. According to [Pet01, Blo08, Kos12], $E_{B,2D}$ can be calculated from the following transcendental equation

$$\frac{a_z}{a_{3D}} = \int_0^\infty \frac{\mathrm{d}u}{\sqrt{4\pi u^3}} \left(1 - \frac{\exp(-E_{B,2D}u/\hbar\omega_z)}{\left[\frac{1}{2u}\left(1-\exp(-2u)\right)\right]^{1/2}}\right), \tag{6.2}$$

where $a_z = \sqrt{\hbar/(m\omega_z)}$ is the harmonic oscillator length and a_{3D} is the three-dimensional scattering length. The resulting binding energy for the two-dimensional molecular state, obtained for a trap frequency of $\omega_z = 2\pi\,5.5\,\mathrm{kHz}$, is shown as a function of the magnetic field in figure 6.12.

At a magnetic field of 690 G the binding energy $E_{B,2D}$ is significantly larger than $\hbar\omega_z$. This means that in the quasi two-dimensional regime the diatomic molecules are so deeply bound that the fact that they consist of two fermionic atoms does not matter. Only when $E_{B,2D}$ becomes similar to the Fermi energy E_F of the system[13], the fermionic nature of the constituents of the molecule will start to become relevant and influence the behavior of the system. For measurements at 690 G, the system can thus be simply treated like a quasi 2D Bose gas of dimers. Therefore, we will now discuss the low temperature phases of two-dimensional Bose gases. For these systems, it is shown in [Mer66, Hoh67, Had11] that the fluctuations destroy the long-range order of the system

---

[12] We only included the measurements for $V_c \geq 2\,\mathrm{V}$ in this determination.

[13] For quasi two-dimensional Fermi systems the Fermi energy must be smaller than $\hbar\omega_z$.

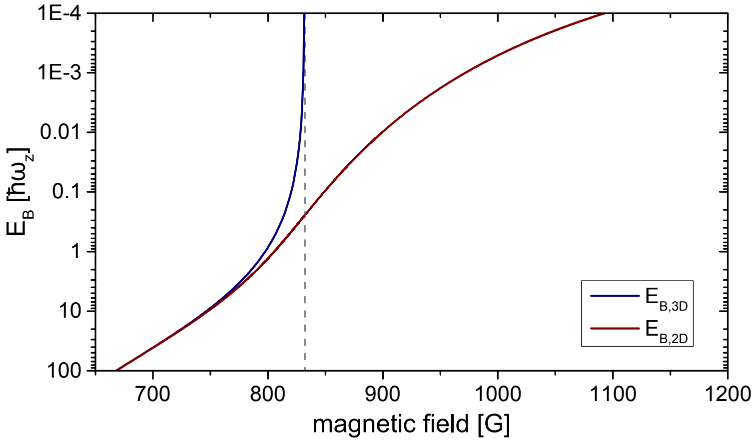

Figure 6.12: Binding energy of the 2D and 3D molecules as a function of the magnetic offset field for a $|1\rangle$-$|2\rangle$ mixture of ^{6}Li atoms. While in the three-dimensional case the molecular state crosses the continuum at the Feshbach resonance (832.17 G, gray dashed line), the confinement induced 2D molecule remains bound. $E_{B,2D}$ was calculated for a vertical trap frequency of $\omega_z = 2\pi\, 5.5\,\mathrm{kHz}$.

for any finite temperature $T > 0$. Therefore, a Bose-Einstein condensate does not exist for a homogeneous two-dimensional system. For low temperatures, there is still a phase transition to a superfluid "quasi condensate". This transition is described by the BKT theory [Ber72, Kos73] and is associated with the emergence of topological order. The superfluid phase below this transition is commonly referred to as a BKT superfluid, or the BKT phase. In [Had06], such a transition was observed using an ultracold bosonic gas confined to a quasi two-dimensional geometry. Only recently, it was possible to directly observe the pairing of vortices with opposite circulation, which is associated with the BKT transition [Cho13].

For the description of these bosonic systems [Pet00, Hun11a, Cho13], one usually defines a dimensionless interaction parameter $\tilde{g} = \sqrt{8\pi}\frac{a_{3D}}{a_z}$. In previous measurements, this coupling parameter, which compares the strength of the confinement with the strength of the interaction, was usually small compared to one ($\tilde{g} \ll 1$). In our case, we need to consider the diatomic bosonic molecules. Therefore, the harmonic oscillator length is given by $a_z = \sqrt{\hbar/(2m_{6Li}\,\omega_z)} \approx 390\,\mathrm{nm}$ for a vertical trap frequency of $\omega_z = 2\pi\, 5.5\,\mathrm{kHz}$. At 690 G where we perform most of our experiments, the molecules interact with $a_{3D,mol} = 0.6\, a_{3D} \approx 44\,\mathrm{nm}$[14]. We thus obtain $\tilde{g}(690\,\mathrm{G}) \approx 0.56$. This value is not small compared to 1 which tells us that the systems we are going to investigate are far from being weakly interacting.

---

[14] Here we used that the scattering length between diatomic molecules is given by 0.6 times the scattering length for the free fermionic atoms [Pet05].

6.4 Phase Coherence and Fluctuations of a Quasi-2D Molecular Bose Gas?

We will now describe the initial stages of our efforts to investigate the phase coherence in a quasi two-dimensional molecular Bose gas. One should note that the studies presented here are not yet concluded. Therefore, all the measurements we will now present are preliminary and especially the first measurement turned out to still have certain issues that need to be addressed in future studies.

One of the first measurements was to transfer a mBEC into one of the pancake-shaped traps. For these measurements, the trap frequencies were $\omega_z = 2\pi\, 5.5\,\mathrm{kHz}$ and $\omega_r = 2\pi\, 29.6\,\mathrm{Hz}$. From a Gaussian fit to the data we obtained a number of atoms of about 30×10^3. These measurements were conducted at a magnetic offset field of 690 G. In the previous section we saw that, for this value of the magnetic field, the binding energy of the two-dimensional confinement induced molecule is still a lot larger than the Fermi energy E_F of the sample. This means that the measurement should not be influenced by the fact that the diatomic molecules consist of fermionic atoms.

We noticed that we observe a clear bimodal distribution after letting the atoms expand for a time-of-flight. From a fit we obtain a ”condensate” fraction of up to about 40%. Figure 6.13(b) shows one of these images taken after a time-of-flight of 8 ms, together with the bimodal fit (solid line). The thermal part of the fit is indicated by the dashed line. For these measurements we did not suddenly switch off the optical trap. This would lead to a very fast expansion in the vertical direction which would make it difficult to extract meaningful information from the images of these highly elongated clouds. In order to alleviate this issue, we ramped the intensity of the pancake trap beam down over a time of 100-200 μs. This time is short compared to the timescale set by the horizontal trap frequency $\tau_r = 1/(2\pi\ 29.6\,\mathrm{Hz}) \approx 5\,\mathrm{ms}$.

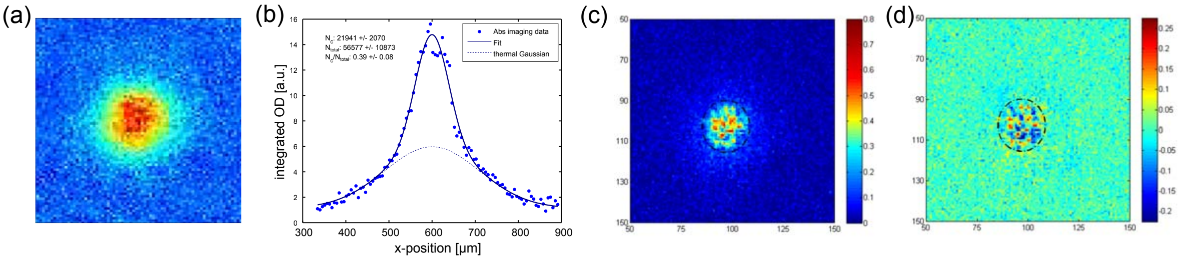

Figure 6.13: (a) Typical single-shot in-situ image of a molecular cloud in one pancake. (b) After releasing the cloud from the trap and letting it expand for 8 ms, we observe a bimodal distribution with a ”condensed” fraction of 0.39. (c) In the absorption image after the time-of-flight we observe strong density fluctuation. (d) After subtracting a 2D bimodal fit from the data, only the fluctuations are left. The black dash-dotted line indicates the radius of the ”quasi-condensed part”.

Figure 6.13(c) shows an absorption image after the 200 μs release and an additional 8 ms of time-of-flight. One can clearly observe strong density fluctuations in the center of the cloud. The black dash-dotted line indicates the radius of the ”condensed” part of the cloud. This radius is obtained from a bimodal fit similar to the one shown in figure 6.13(b). The strong fluctuations become even better visible (see figure 6.13(d)) when we subtract a two-dimensional bimodal fit from the cloud. Then only the fluctuations around the smooth average density remains. In this image, the radius of the ”condensed” part is again indicated by the black dash-dotted line. We attribute these density fluctuations which emerge after a short time-of-flight to phase fluctuations in the initial sample. The size of the individual parts of equal phase are on the order of about $\sim 20\,\mu$m. This indicates a phase coherence that is large compared to the one expected for a thermal system. From measurements with bosonic systems we know that one expects an algebraically decaying phase coherence when the atoms are below the Berezinskii-Kosterlitz-Thouless (BKT) transition [Had06, Had11]. However, to determine whether we are already in that quasi-condensed phase, we need to quantify and evaluate the observed phase coherence and fluctuations.

6.4.1 Quantifying the Fluctuations

We tried several different methods to quantify the observed fluctuation. We will now present these methods and for a better comparison, we will apply all three techniques to the same absorption image (shown in figure 6.13(c)) taken after $t_{tof} = 8$ ms at a magnetic field of 690 G.

The Fourier Power Spectrum The first technique uses the two-dimensional Fourier transformation and investigates the obtained two-dimensional power spectrum. This is the same technique we already used to investigate the spinor systems in section 5.5.5. Figure 6.14(a) shows such a Fourier power spectrum for the absorption image shown in figure 6.13(c). This method was already used in [Cho12c] for a similar measurement with a quasi two-dimensional Bose gas of ^{87}Rb atoms. As pointed out in [Lan13], in this kind of analysis one has to be very careful about the focus of the imaging setup. When we average several of these power spectra we do not observe fluctuations at only certain wavelengths (as described in [Cho12c]). We rather observe a homogeneous signal of fluctuations for almost the whole region we investigate (see figure 6.14(b)[15]). This is possibly due to the fact that the stability of the experimental setup was not yet optimized when we took that data. Hence, the position, temperature and atom number strongly fluctuated from shot to shot. This could maybe explain the homogeneous fluctuation spectrum. The reason why the average over several spectra results in a rhombus shape is so far unclear. This behavior could be caused by imaging aberrations.

---

[15] The large red signal in the center is due to the overall size of the cloud.

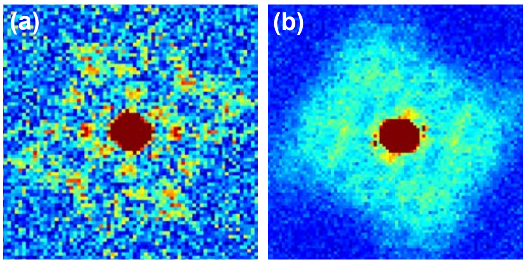

Figure 6.14: (a) Two-dimensional power spectrum of the Fourier transform of the absorption image shown in 6.13(c). (b) Average of 30 power spectra.

Variance Over Mean The second method we used was to analyze the variance over mean for each pixel inside the possibly "quasi condensed" part of the cloud. For this, we compare a large set of a few hundred images and calculate the variance of N over the mean number of atoms for each single pixel $(\mathrm{Var}(N(\mathbf{r}))/\bar{N}(\mathbf{r}))$. This method was already successfully employed in [Hun11b, Hun11a] for the analysis of a quasi two-dimensional Bose gas of ^{133}Cs atoms. For a quantitative application of this analysis technique, one has to calibrate the imaging system to be able to subtract the photon shot noise. This calibration is not yet finished. But even without subtracting the imaging shot noise, the plots of $\mathrm{Var}(N)/\bar{N}$ as a function of the radial distance look promising (see figure 6.16).

Two-Particle Correlation Function The last technique we used to quantify the observed density fluctuations is to define a two-point correlation function of the following form

$$G(\delta\mathbf{r}) = \frac{1}{\#_{\delta\mathbf{r}}} \sum_{r} \frac{\delta n(\mathbf{r}) \cdot \delta n(\mathbf{r}+\delta\mathbf{r})}{\bar{n}(\mathbf{r}) \cdot \bar{n}(\mathbf{r}+\delta\mathbf{r})}, \tag{6.3}$$

where $\mathbf{r}$ is a two-dimensional vector, $\#_{\delta\mathbf{r}}$ is the number of summands for a given $\delta\mathbf{r}$, $\delta n(\mathbf{r}) = n(\mathbf{r}) - \bar{n}(\mathbf{r})$ and $\bar{n}(\mathbf{r})$ is the average density which is usually determined by the average over several shots[16]. In these average images the fluctuations smoothen out. This indicates that the observed fluctuations are not produced by imaging aberrations.

6.4.2 Crossover to the Fermionic Limit

We stated earlier that we want to expand our measurements towards the fermionic limit. The fermionic nature of the particles begins to play a role as soon as the binding energy $E_{B,2D}$ becomes of the order of the Fermi energy E_F. For our system, this occurs for magnetic offset fields $\gtrsim 800\,\mathrm{G}$ (see figure 6.12).

When we let the clouds expand at these fields, we do not observe density fluctuations after a time-of-flight. This is most likely due to the fact that in this regime, the interaction of the system becomes even stronger ($\tilde{g} \rightarrow 1$) and thus the expansion of

---

[16] One can also determine the average density $\bar{n}(r)$ from a two-dimensional bimodal fit to the image.

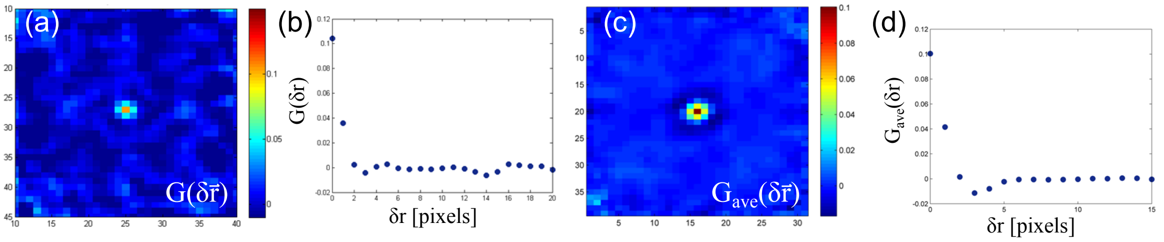

Figure 6.15: (a)Two-dimensional two-point correlation function $G(\delta\mathbf{r})$ of the absorption image shown in 6.13(c) and its radial average (b). (c,d) Average over several two-dimensional correlation functions and its radial average.

the atoms after releasing them from the trap is not ballistic anymore. This means that the individual particles continue to scatter while they are already expanding. These scattering events scramble the phase relation between the particles and thus the density fluctuations of the clouds are destroyed.

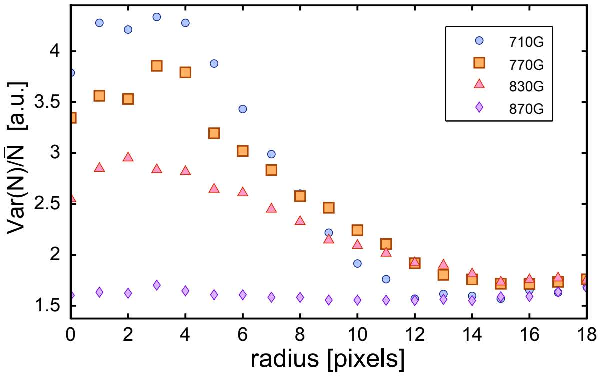

Figure 6.16: Radial average of variance over mean ($\mathrm{Var}(N)/\bar{N}$) as a function of the magnetic field before a quick magnetic field quench to 690 G. One can observe the fluctuations which decrease for larger magnetic fields.

To avoid this, we use a rapid ramping technique. Here, we quickly quench the magnetic field from the values where we want to investigate our sample to a value where the samples expand ballistically (in our case 690 G). A similar method [Reg04, Zwi04] was already used to investigate strongly interacting fermionic systems close to Feshbach resonances. By performing a reference measurement we can show that it takes our systems approximately 5 ms to reach an equilibrated state after a quick quench of the magnetic field from about 800 G to 690 G. The time for our rapid projection ramp is usually about 100 μs. This is significantly shorter than the equilibration timescale and ensures that we are indeed probing the properties of the system before the quench. With this method, we can observe bimodal distributions and some density fluctuations even for higher magnetic fields. As an example for the rapid ramping technique, figure 6.16 shows the obtained radially averaged variance-over-mean values for different magnetic fields. One clearly observes that the phase fluctuations weaken but persist for fields up to about 830 G.

Due to the already mentioned large shot-to-shot fluctuations in the position of the cloud, the atom number and the temperature, we were so far not able to extract quantitative and conclusive results from these measurements. Therefore, we optimized the whole evaporation stage and investigated the causes leading to the shot-to-shot fluctuations. During this time we tried to determine the temperature of the investigated clouds.

6.4.3 Temperature Determination

In order to see if the observed phase coherences are possibly due to the formation of a BKT-like quasi condensate, we then tried to determine the temperature of our system. For this, we recorded in-situ density distributions, both deeply in the bosonic (690 G) and deeply in the fermionic regime (1400 G). At 1400 G the binding energy $E_{B,2D} \ll k_B \times 1\,\mathrm{nK}$ and thus the atoms are not bound to molecules anymore. This means that at this magnetic field value, we can investigate an attractively interacting two-component Fermi gas. Figure 6.17 shows an average over 120 images in-situ images at 690 G (a) and 1400 G (b) and the radial averages for both fields (c). From the Gaussian fit we obtain a number of atoms of about $N \approx 50\,000$ atoms per state. In figure 6.17(a,b), one can nicely observe the effect of quantum statistics. Due to the Pauli pressure, the maximum density of the fermionic cloud is lower but the radius of the distribution is larger. For the bosonic case at 690 G, one observes a more peaked density distribution with a smaller width.

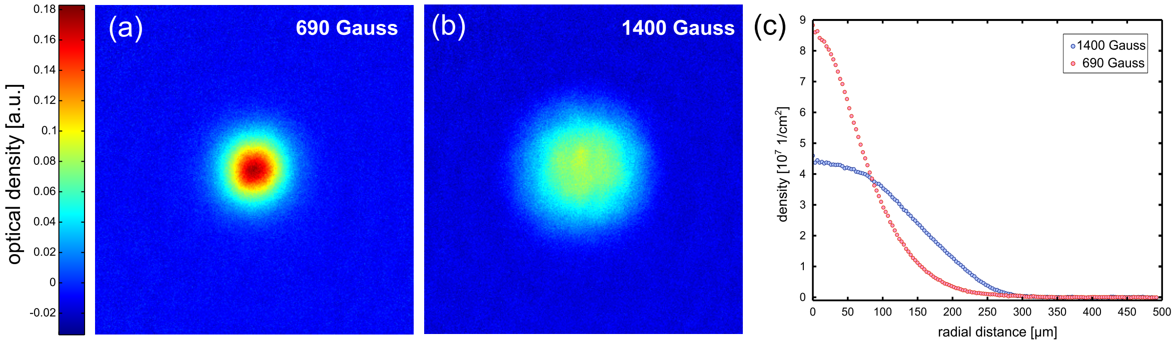

Figure 6.17: Average of about 120 in-situ absorption images in the bosonic limit (a) and the fermionic limit (b). The radial averages for both magnetic field values are shown in (c). One can clearly see that the Pauli pressure between the fermions leads to a larger, less dense sample. The bosonic cloud of molecules is significantly smaller.

When we tried to fit the density distribution with the prediction for non-interacting fermions, we noticed that the cloud is significantly too large for an atom number of

50 000. A more detailed analysis showed that we underestimated the number of atoms in the pancakes. This effect is due to two reasons. First, the atoms start to move due to the absorption of imaging photons during the imaging pulse of 8-10 μs. Due to the Doppler effect, their transition frequency changes and therefore we record a smaller optical density. The second reason is that the intensity we use to image is not significantly smaller than the saturation intensity. Thus, the approximations made when deriving the optical density fail (see equation 3.2) and the results need to be modified. This effect also leads to an underestimation of the number of atoms.

The consequence of this underestimation of the number of atoms in these systems is that most of the performed measurements were not as deeply in the quasi two-dimensional regime as initially thought. This means that a fraction of the atoms were in vertically excited states. As a consequence, some of the results obtained earlier need to be reevaluated or remeasured.

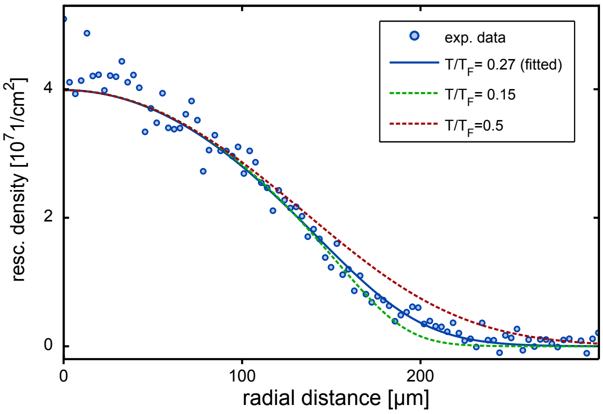

Figure 6.18: Fit to the in-situ density distribution obtained at 1400 G with the prediction for a non-interacting two-dimensional Fermi gas. To account for the underestimation of the atom number, we rescale the obtained densities and number of atoms by a factor of 1.3. Due to known issues like the occupation of vertically excited states, the interactions of the system and the uncertainty in the determination of the number of atoms, the obtained degeneracy temperature of $T/T_F = 0.27$ is just an estimate.

We can still try to determine a temperature from these images. For this, we take a radially averaged in-situ absorption image which was recorded in the fermionic limit at 1400 G. We account for the underestimation of the density and thus the number of atoms in this measurement by scaling these quantities with a factor of 1.3. Figure 6.18 shows the fit to such a rescaled image with the prediction for a two-dimensional non-interacting Fermi gas [17]. From this fit, we obtain a degeneracy temperature of $T/T_F = 0.27$. Furthermore, one can observe that the prediction for higher ($T/T_F = 0.5$) and lower temperature ($T/T_F = 0.15$) do not agree with the experimental data.

---

[17] For the fit, we only consider the data points for $r > 50\,\mu$m.

However, due to known issues, the determination of the temperature from these images is not very reliable. First, we expect the occupation of vertically excited states to influence the density distribution. Second, the effect that the interactions have on the density profile are difficult to predict. Finally, the exact value we have to use to rescale the number of atoms and the density can so far only be estimated and a more precise determination of these effects needs to be made in the future. Still, one can see that the system is in the quantum degenerate regime and it may be possible to reach the temperature predicted for the formation of a BKT-like superfluid which is expected to occur at about $T_{\mathrm{BKT}}/T_F \approx 0.1$ [Pet03]. We are confident that with the optimizations of the sequence and the stability of the setup, we can produce significantly colder samples and therefore reach this regime.

6.4.4 Finding the Quasi-2D Regime

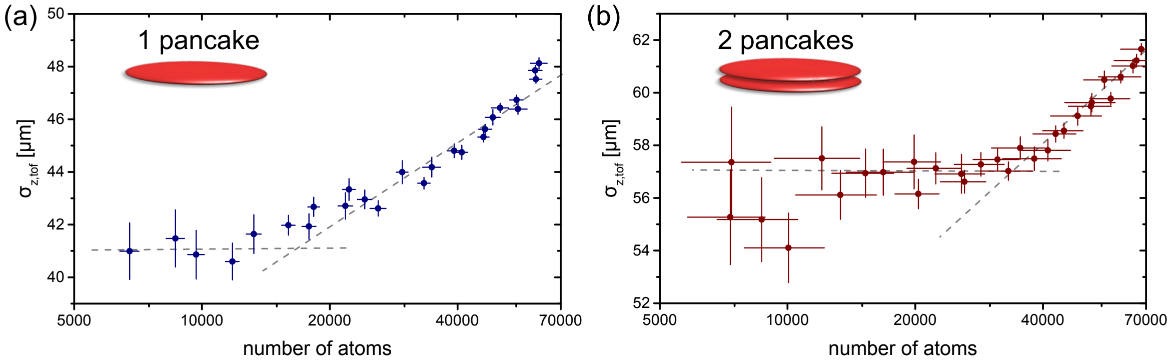

Figure 6.19: Vertical cloud size after 3 ms (4 ms) time-of-flight for one (two) filled pancake-shaped traps. The dashed lines are guides to the eye. For one filled pancake trap (a) the size saturates below ∼ 15 000 atoms. For two pancakes (b) below ∼ 30 000. The number of atoms in this measurement is still not corrected.

To make sure that we are in fact in the quasi two-dimensional regime in future measurements we investigate the size of the cloud as a function of the number of atoms. This measurement was performed according to [Dyk11], which studies how the size of a weakly interacting Fermi gas changes when the system becomes quasi two-dimensional. One expects that the size in the vertical (tightly confined) axis after a time-of-flight saturates at a finite value even if one loads less atoms into the trap. Figure 6.19(a) shows such a measurement when we fill only a single pancake. Below about 15 000 atoms[18], the size after 3 ms time-of-flight stays roughly constant. It is however difficult to observe so few atoms. Therefore, we repeated the measurement but loaded an equal

---

[18] Note that this is still the uncorrected number of atoms. The actual number of atoms is therefore higher.

amount of atoms into two adjacent pancake-shaped traps (see 6.19(b)). In this case, the size saturated below about 30 000 atoms. Due to the larger signal of about twice the number of atoms the kink in the size is better visible.

6.5 Conclusion and Outlook

To conclude, we realized a stack of oblate pancake-shaped optical traps with an aspect ratio of $\eta = \omega_z/\omega_r \approx 300$. We showed that we can measure the distribution of atoms over the pancake-shaped traps using RF tomography. When we begin with a mBEC in the optical dipole trap we can load almost all molecules into one single pancake. For such systems, we started to investigate phase coherence and fluctuations of a system close to the quasi two-dimensional regime. We presented preliminary results and introduced the different analysis methods we want to use to quantify the fluctuations. Using the method described in [Dyk11], we can furthermore determine how many atoms we can load into one pancake without leaving the quasi two-dimensional regime (see section 6.4.4). With the improvements of the stability of the setup that we presented in this chapter, we should be now able to perform quantitative measurements of the fluctuations (section 6.4.1) without and with the fast magnetic ramping technique (see section 6.4.2). As a consequence, the next step of our efforts will therefore be to precisely quantify the phase coherences of the systems as a function of the temperature and of the interactions of the system.

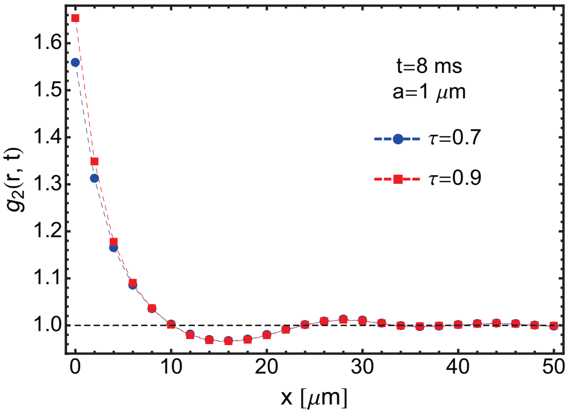

Figure 6.20: Radial average of the two-point correlation function g_2 for a bosonic system of ^{6}Li-dimers after an expansion time of $t = 8\,\mathrm{ms}$. The parameter a describes the interparticle interaction and τ indicates the temperature. τ varies from 1 to 0 as the temperature is decreased from T_{BKT} to 0. Obtained from [Mat13, Sin13]

With the help of theoretical predictions, we hope to be able to clarify if we can reach a quasi-condensed BKT-like phase with our setup. Currently, the group of L. Mathey in Hamburg is theoretically investigating the two-point correlation functions expected for systems above and below the BKT transition. Figure 6.20 shows the calculated correlation function for a system of ^{6}Li-dimers. A comparison to figure 6.15(d), which displays a similarly defined correlation function, shows striking similarities to the calculated behavior. However, further measurements and evaluations are needed to draw clear conclusions.

6.5.1 Towards a Two-Dimensional Optical Lattice

While we were performing these investigations, we also set up two retroreflected optical lattice beams in the horizontal direction [Bec13]. The interference of these lattice beams lead together with the quasi two-dimensional pancake trap to a two-dimensional optical lattice (see 6.21(b)). Our plans are to use this setup to study fermionic quantum gases in an optical lattice. The optical lattice setup was evaluated and optimized using the same Kapitza-Dirac technique we presented in section 6.2.1 and an image of the diffraction of a mBEC on the optical lattice is shown in figure 6.21(a).

Furthermore, a high-resolution objective was tested and prepared for the addition to the existing experimental setup [Kri13]. This objective will allow us to take high-resolution images of the quasi two-dimensional systems or to investigate systems trapped in a 2D optical lattice (see figure 6.21(c)).

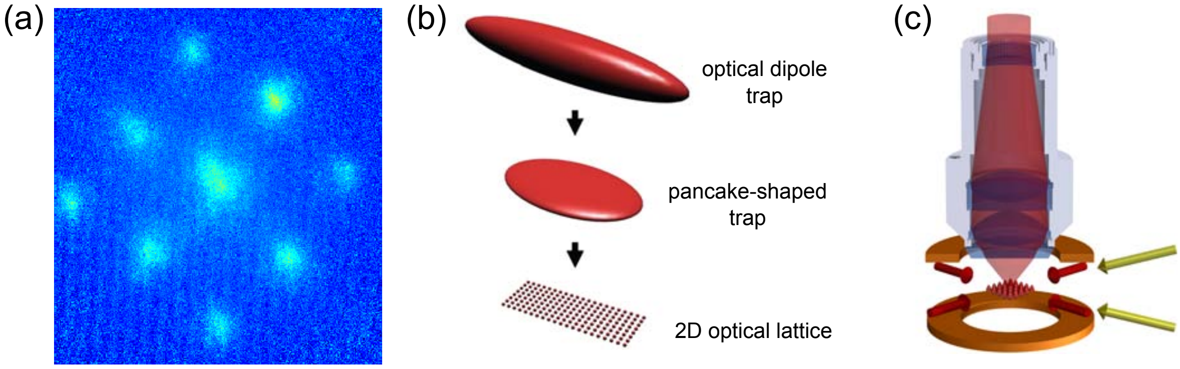

Figure 6.21: (a) Kapitza-Dirac diffraction pattern of a mBEC on the optical lattice standing wave. Taken from [Bec13]. (b) When we transfer the clouds from the optical dipole trap to a single pancake and then turn on the optical lattice beams, we realize a two-dimensional optical lattice. (c) High-resolution objective and trapping beams. The red arrows indicate the optical lattice beams and the yellow ones depict the beams used for the creation of the pancake-shaped optical traps.

7 Conclusion and Outlook

In the course of this thesis ultracold gases have been used to address open questions in quantum many-body physics. These studies ranged from observing a crossover from few to many-body physics, over investigations of the equilibration of bosonic spinor systems to the exploration of quasi long-range order in a two-dimensional Fermi gas. For all three topics, we will summarize the main findings and outline the possibilities for further studies and experiments.

In chapter 4, we presented our ability to prepare few-particle systems with full control over the number of atoms, the motional state and their interactions. We used these systems to access the regime of mesoscopic physics which is located at the interface between few and many-particle systems. Physical systems in this regime are ubiquitous in nature. The most prominent examples for such systems are electrons in the shell of an atom and nucleons in the atomic nuclei. Given the progress of semiconductor technology, the number of doping atoms in the smallest transistors and devices used for computation will also soon reach the mesoscopic scale. This gives these mesoscopic quantum systems an additional technological relevance. In particular, it is interesting to study how many-body properties and behaviors emerge. With the experiments presented in this thesis, we showed that quantitative measurements in this transitional regime between few and many-body physics can now be performed. This paves the way for future studies with these finite ultracold systems. One possible route would be to study how the physics of phase transitions emerges when the size of such a system grows. This could be investigated by measuring the excitation spectrum of ultracold systems in the mesoscopic regime. Additionally, these studies of finite strongly correlated fermions also offer the possibility to mimic phenomena from nuclear physics [Zin08, Zür13b], from high-energy physics [Rap07, Wil07] or from attosecond physics [Kel65, Kra09, Sal13a]. In the latter case, a time-dependent magnetic field gradient can simulate the effects of the oscillating electric field of a short laser pulse [Sal13a].

In chapter 5, we described experiments with bosonic spinor BECs and we could show how one can use spin-echo techniques to determine the three-dimensional vector magnetization. Additionally, we presented how one can calibrate and test high-resolution imaging setups in-situ using the atomic cloud. By measuring the time evolution of initially unmagnetized samples in different initial configurations we could determine the timescale for the equilibration and show the formation and coarsening of ferromagnetic domains. The mechanisms that allow these systems to reach a steady state and that determine the timescale for the equilibration are still far from being understood. These processes and their interplay with the increased role that fluctuations play in lower dimensions would be an interesting route for new studies. By combining these spinor systems with optical lattices and possibly with the full control over the number and state of the atoms (e.g. as shown in chapter 4 or in [Bak09, Bak10, She10, Wei11, Ser11b]), one could use these systems to realize fundamental spin Hamiltonians and study quantum magnetism. This could be especially interesting if one added long-range spin dependent interactions, for example by using particles with a large magnetic or electric dipole moment [Gio02, Gri05, Ni08].

For the quasi two-dimensional Fermi gases presented in chapter 6, we could show that we observe phase coherences for a system close to the expected phase transition to superfluid behavior. It would be interesting to observe this phase transition and determine the dependence of the critical temperature from the limit of bosonic molecules to fermions. In particular, it would be compelling to study the role of the fluctuations in this crossover from bosons to fermions by comparing it to the three-dimensional analogue, the BEC-BCS crossover. Such a system, in particular with an optical lattice, would be ideally suited to emulate simplified versions of high-T_c superconductors or other quasi two-dimensional structures of solid state physics like graphene [Ueh13].

All these experiments, considerations and new directions that are currently emerging show that ultracold quantum gases are a great generic quantum system to test and evaluate theories and approaches. In the 20 years since its beginning, this young field was able to take many textbook examples for quantum systems and realize them in a very pure and clean form in laboratories. Purely academic models and studies could thus be scrutinized using experimental many-body systems and this development is still far from being over. All of the recent advances show that the kind of Hamiltonians that can be emulated with cold atoms is steadily growing; and with the single particle control that is now available, the possibilities to mimic physical systems at different scales and from different fields will increase even more.

Bibliography

[And95] M. H. Anderson, J. R. Ensher, M. R. Matthews, C. E. Wieman, E. A. Cornell, *Observation of Bose-Einstein Condensation in a Dilute Atomic Vapor*, Science **269**, 198–201 (1995).

[And97] M. R. Andrews, C. G. Townsend, H.-J. Miesner, D. S. Durfee, D. M. Kurn, W. Ketterle, *Observation of Interference Between Two Bose Condensates*, Science **275**(5300), 637–641 (1997).

[Arm11] J. R. Armstrong, N. T. Zinner, D. V. Fedorov, A. S. Jensen, *Analytic harmonic approach to the N -body problem*, Journal of Physics B: Atomic, Molecular and Optical Physics **44**(5), 055303 (2011).

[Ast04] G. E. Astrakharchik, D. Blume, S. Giorgini, B. E. Granger, *Quasi-One-Dimensional Bose Gases with a Large Scattering Length*, Phys. Rev. Lett. **92**, 030402 (2004).

[Ast13] G. E. Astrakharchik, I. Brouzos, *Trapped one-dimensional ideal Fermi gas with a single impurity*, Phys. Rev. A **88**, 021602 (2013).

[Bak01] G. A. Baker, *The MBX challenge competition: a neutron matter model*, International Journal of Modern Physics B **15**, 1314–1320 (2001).

[Bak09] W. S. Bakr, J. I. Gillen, A. Peng, S. Folling, M. Greiner, *A quantum gas microscope for detecting single atoms in a Hubbard-regime optical lattice*, Nature **462**(7269), 74–77 (2009).

[Bak10] W. S. Bakr, A. Peng, M. E. Tai, R. Ma, J. Simon, J. I. Gillen, S. Fölling, L. Pollet, M. Greiner, *Probing the Superfluid-to-Mott Insulator Transition at the Single-Atom Level*, Science **329**, 547–550 (2010).

[Bar57] J. Bardeen, L. N. Cooper, J. R. Schrieffer, *Theory of Superconductivity*, Phys. Rev. **108**, 1175–1204 (1957).

[Bar04] M. Bartenstein, A. Altmeyer, S. Riedl, S. Jochim, C. Chin, J. H. Denschlag, R. Grimm, *Collective Excitations of a Degenerate Gas at the BEC-BCS Crossover*, Phys. Rev. Lett. **92**, 203201 (2004).

[Bar05] M. Bartenstein, A. Altmeyer, S. Riedl, R. Geursen, S. Jochim, C. Chin, J. H. Denschlag, R. Grimm, A. Simoni, E. Tiesinga, C. J. Williams, P. S. Julienne, *Precise Determination of* ^{6}Li *Cold Collision Parameters by Radio-Frequency Spectroscopy on Weakly Bound Molecules*, Phys. Rev. Lett. **94**, 103201 (2005).

[Bec13] J. Becher, *A two dimensional optical lattice for ultracold fermions* (2013), Bachelor thesis, Ruprecht-Karls-Universität Heidelberg.

[Ber72] V. L. Berezinskii, *Destruction of long-range order in one-dimensional and two-dimensional systems possessing a continuous symmetry group. II. Quantum systems*, Sov. Phys. JETP **34**, 610 (1972).

[Ber03] T. Bergeman, M. G. Moore, M. Olshanii, *Atom-Atom Scattering under Cylindrical Harmonic Confinement: Numerical and Analytic Studies of the Confinement Induced Resonance*, Phys. Rev. Lett. **91**(16), 163201 (2003).

[Ber13] A. Bergschneider, *Ultracold few-fermion systems in multiwell potentials* (2013), Master thesis, Ruprecht-Karls-Universität Heidelberg.

[Blo75] P. Bloom, *Two-dimensional Fermi gas*, Phys. Rev. B **12**, 125–129 (1975).

[Blo08] I. Bloch, J. Dalibard, W. Zwerger, *Many-body physics with ultracold gases*, Rev. Mod. Phys. **80**, 885 (2008).

[Blu10] Blume, Daily, *Trapped two-component Fermi gases with up to six particles: Energetics, structural properties, and molecular condensate fraction*, cond-mat 1008.3191 (2010).

[Blu12] D. Blume, S. Gharashi, *Numerical calculations using a finite-range model*, private communication (2012).

[Bog47] N. Bogoliubov, *On the theory of superfluidity*, J. Phys. (USSR) **11**, 23 (1947).

[Boh12] J. E. Bohn, *Towards an ultracold three-component Fermi Gas in a two-dimensional optical lattice* (2012), Diploma thesis, Ruprecht-Karls-Universität Heidelberg.

[Bra06] E. Braaten, H.-W. Hammer, *Universality in few-body systems with large scattering length*, Physics Reports **428**, 259 – 390 (2006).

[Bri05] D. Brink, R. Broglia, *Nuclear Superfluidity* (Cambridge University Press, 2005).

[Bro23] L. de Broglie, *Waves and Quanta*, Nature (London) **112**, 540 (1923).

[Bro12] I. Brouzos, P. Schmelcher, *Construction of Analytical Many-Body Wave Functions for Correlated Bosons in a Harmonic Trap*, Phys. Rev. Lett. **108**, 045301 (2012).

[Bro13] I. Brouzos, P. Schmelcher, *Two-component few-fermion mixtures in a one-dimensional trap: Numerical versus analytical approach*, Phys. Rev. A **87**, 023605 (2013).

[Bug13] P. O. Bugnion, G. J. Conduit, *Ferromagnetic spin correlations in a few-fermion system*, Phys. Rev. A **87**, 060502 (2013).

[Bus98] Thomas Busch, B.-G. Englert, K. Rzazewski, M. Wilkens, *Two Cold Atoms in a Harmonic Trap*, Foundations of Physics **28**, 549–559 (1998).

[But97] D. A. Butts, D. S. Rokhsar, *Trapped Fermi gases*, Phys. Rev. A **55**, 4346–4350 (1997).

[Car03] J. Carlson, S.-Y. Chang, V. R. Pandharipande, K. E. Schmidt, *Superfluid Fermi Gases with Large Scattering Length*, Phys. Rev. Lett. **91**, 050401 (2003).

[Cha05] M.-S. Chang, Q. Qin, W. Zhang, L. You, M. S. Chapman, *Coherent spinor dynamics in a spin-1 Bose condensate*, Nature Physics **1**(2), 111–116 (2005).

[Chi04] C. Chin, M. Bartenstein, A. Altmeyer, S. Riedl, S. Jochim, J. H. Denschlag, R. Grimm, *Observation of the Pairing Gap in a Strongly Interacting Fermi Gas*, Science **305**, 1128–1130 (2004).

[Chi05] C. Chin, P. S. Julienne, *Radio-frequency transitions on weakly bound ultracold molecules*, Phys. Rev. A **71**, 012713 (2005).

[Chi10] C. Chin, R. Grimm, P. Julienne, E. Tiesinga, *Feshbach resonances in ultracold gases*, Rev. Mod. Phys. **82**(2), 1225 (2010).

[Cho12a] J. yoon Choi, W. J. Kwon, M. Lee, H. Jeong, K. An, Y. il Shin, *Imprinting Skyrmion spin textures in spinor Bose-Einstein condensates*, New Journal of Physics **14**(5), 053013 (2012).

[Cho12b] J.-y. Choi, W. J. Kwon, Y.-i. Shin, *Observation of Topologically Stable 2D Skyrmions in an Antiferromagnetic Spinor Bose-Einstein Condensate*, Phys. Rev. Lett. **108**, 035301 (2012).

[Cho12c] J.-y. Choi, S. W. Seo, W. J. Kwon, Y.-i. Shin, *Probing Phase Fluctuations in a 2D Degenerate Bose Gas by Free Expansion*, Phys. Rev. Lett. **109**, 125301 (2012).

[Cho13] J.-y. Choi, S. W. Seo, Y.-i. Shin, *Observation of Thermally Activated Vortex Pairs in a Quasi-2D Bose Gas*, Phys. Rev. Lett. **110**, 175302 (2013).

[Cla09] P. Cladé, C. Ryu, A. Ramanathan, K. Helmerson, W. D. Phillips, *Observation of a 2D Bose Gas: From Thermal to Quasicondensate to Superfluid*, Phys. Rev. Lett. **102**, 170401 (2009).

[Cui13] X. Cui, T.-L. Ho, *Ground-State Ferromagnetic Transition in Strongly Repulsive One-Dimensional Fermi Gases*, ArXiv e-prints 1305.6361 (2013).

[D'A13] P. D'Amico, M. Rontani, *Three interacting atoms in a one-dimensional trap: A benchmark system for computational approaches*, ArXiv e-prints 1310.3829 (2013).

[Dal98] J. Dalibard, *Collisional dynamics of ultracold atomic gases*, in M. Inguscio, S. Stringari, C. Wieman (Ed.), *Bose-Einstein Condensation in Atomic Gases*, Vol. Course CXL of *Proceedings of the International School of Physics Enrico Fermi* (IOS Press, Varenna, 1998).

[Dal99] F. Dalfovo, S. Giorgini, L. P. Pitaevskii, S. Stringari, *Theory of Bose-Einstein condensation in trapped gases*, Rev. Mod. Phys. **71**(3), 463–512 (1999).

[Dav95] K. B. Davis, M.-O. Mewes, M. R. Andrews, N. J. van Druten, D. S. Durfee, D. M. Kurn, W. Ketterle, *Bose-Einstein condensation in a gas of sodium atoms*, Phys. Rev. Lett. **75**(22), 3969–3973 (1995).

[DeM99] B. DeMarco, D. S. Jin, *Onset of Fermi Degeneracy in a Trapped Atomic Gas*, Science **285**, 1703–1706 (1999).

[Des12] R. Desbuquois, L. Chomaz, T. Yefsah, J. Leonard, J. Beugnon, C. Weitenberg, J. Dalibard, *Superfluid behaviour of a two-dimensional Bose gas*, Nat Phys **8**(9), 645 (2012).

[Deu13] F. Deuretzbacher, D. Becker, J. Bjerlin, S. M. Reimann, L. Santos, *Quantum magnetism without lattices in strongly-interacting one-dimensional spinor gases*, ArXiv e-prints 1310.3705 (2013).

[Dyk11] P. Dyke, E. D. Kuhnle, S. Whitlock, H. Hu, M. Mark, S. Hoinka, M. Lingham, P. Hannaford, C. J. Vale, *Crossover from 2D to 3D in a Weakly Interacting Fermi Gas*, Phys. Rev. Lett. **106**, 105304 (2011).

[Eag69] D. M. Eagles, *Possible Pairing without Superconductivity at Low Carrier Concentrations in Bulk and Thin-Film Superconducting Semiconductors*, Phys. Rev. **186**, 456–463 (1969).

[Efi70] V. Efimov, *Energy levels arising from resonant two-body forces in a three-body system*, Physics Letters B **33**, 563 – 564 (1970).

[Fel11] M. Feld, B. Fröhlich, E. Vogt, M. Koschorreck, M. Köhl, *Observation of a pairing pseudogap in a two-dimensional Fermi gas*, Nature **480**, 75 (2011).

[Fer28] E. Fermi, *Eine statistische Methode zur Bestimmung einiger Eigenschaften des Atoms und ihre Anwendung auf die Theorie des periodischen Systems der Elemente*, Zeitschrift für Physik **48**(1-2), 73–79 (1928).

[Fer11] F. Ferlaino, A. Zenesini, M. Berninger, B. Huang, H.-C. Nägerl, R. Grimm, *Efimov Resonances in Ultracold Quantum Gases*, Few-Body Systems **51**(2-4), 113–133 (2011).

[Fes58] H. Feshbach, *Unified theory of nuclear reactions*, Annals of Physics **5**(4), 357 – 390 (1958).

[Fet03] A. Fetter, J. Walecka, *Quantum Theory of Many-particle Systems*, Dover Books on Physics (Dover Publications, 2003).

[Fie39] M. Fierz, *Über die relativistische Theorie kräftefreier Teilchen mit beliebigem Spin*, Helvetica Physica Acta **12**, 3–37 (1939).

[Frö11] B. Fröhlich, M. Feld, E. Vogt, M. Koschorreck, W. Zwerger, M. Köhl, *Radio-Frequency Spectroscopy of a Strongly Interacting Two-Dimensional Fermi Gas*, Phys. Rev. Lett. **106**, 105301 (2011).

[Frö12] B. Fröhlich, M. Feld, E. Vogt, M. Koschorreck, M. Köhl, C. Berthod, T. Giamarchi, *Two-Dimensional Fermi Liquid with Attractive Interactions*, Phys. Rev. Lett. **109**, 130403 (2012).

[Geh03] M. Gehm, *Properties of 6Li* (2003), http://www.physics.ncsu.edu/jet/ techdocs/pdf/PropertiesOfLi.pdf.

[Gha12] S. E. Gharashi, K. M. Daily, D. Blume, *Three s-wave-interacting fermions under anisotropic harmonic confinement: Dimensional crossover of energetics and virial coefficients*, Phys. Rev. A **86**, 042702 (2012).

[Gha13] S. E. Gharashi, D. Blume, *Correlations of the Upper Branch of 1D Harmonically Trapped Two-Component Fermi Gases*, Phys. Rev. Lett. **111**, 045302 (2013).

[Gio02] S. Giovanazzi, A. Görlitz, T. Pfau, *Tuning the Dipolar Interaction in Quantum Gases*, Phys. Rev. Lett. **89**, 130401 (2002).

[Gio08] S. Giorgini, L. P. Pitaevskii, S. Stringari, *Theory of ultracold atomic Fermi gases*, Rev. Mod. Phys. **80**, 1215–1274 (Oct 2008).

[Gir60] M. Girardeau, *Relationship between Systems of Impenetrable Bosons and Fermions in One Dimension*, J. Math. Phys. **1**, 516–523 (1960).

[Gir09] S. Giraud, R. Combescot, *Highly polarized Fermi gases: One-dimensional case*, Phys. Rev. A **79**, 043615 (2009).

[Gir10] M. D. Girardeau, *Two super-Tonks-Girardeau states of a trapped one-dimensional spinor Fermi gas*, Phys. Rev. A **82**, 011607 (2010).

[Gor61] L. P. Gorkov, T. K. Melik-Barhudarov, *Contribution to the theory of superfluidity in an imperfect Fermi gas*, Soviet Physics JETP **13**, 1018 (1961).

[Gre98] S. Grebenev, J. P. Toennies, A. F. Vilesov, *Superfluidity Within a Small Helium-4 Cluster: The Microscopic Andronikashvili Experiment*, Science **279**(5359), 2083 (1998).

[Gre02] M. Greiner, O. Mandel, T. Esslinger, T. W. Hänsch, I. Bloch, *Quantum phase transition from a superfluid to a Mott insulator in a gas of ultracold atoms*, Nature (London) **415**(6867), 39–44 (2002).

[Gre03] M. Greiner, C. A. Regal, D. S. Jin, *Emergence of a molecular Bose-Einstein condensate from a Fermi gas*, Nature **426**(6966), 537 (2003).

[Gre05] M. Greiner, C. A. Regal, D. S. Jin, *Probing the Excitation Spectrum of a Fermi Gas in the BCS-BEC Crossover Regime*, Phys. Rev. Lett. **94**, 070403 (2005).

[Gri00] Rudolf Grimm, Matthias Weidemüller, Yurii B. Ovchinnikov, *Optical dipole traps for neutral atoms*, Adv. At. Mol. Opt. Phys. **Vol. 42**, 95–170 (2000).

[Gri05] A. Griesmaier, J. Werner, S. Hensler, J. Stuhler, T. Pfau, *Bose-Einstein Condensation of Chromium*, Phys. Rev. Lett. **94**, 160401 (2005).

[Gri12] M. Gring, M. Kuhnert, T. Langen, T. Kitagawa, B. Rauer, M. Schreitl, I. Mazets, D. A. Smith, E. Demler, J. Schmiedmayer, *Relaxation and Prethermalization in an Isolated Quantum System*, Science **337**, 1318–1322 (2012).

[Grü10] T. Grünzweig, A. Hilliard, M. McGovern, M. F. Andersen, *Near-deterministic preparation of a single atom in an optical microtrap*, Nature Physics **6**, 951 (2010).

[Gua13] X.-W. Guan, M. T. Batchelor, C. Lee, *Fermi gases in one dimension: From Bethe Ansatz to experiments*, ArXiv 1301.6446 (2013).

[Gub13] K. Gubbels, H. Stoof, *Imbalanced Fermi gases at unitarity*, Physics Reports **525**(4), 255 – 313 (2013).

[Gup03] S. Gupta, Z. Hadzibabic, M. W. Zwierlein, C. A. Stan, K. Dieckmann, C. H. Schunck, E. G. M. van Kempen, B. J. Verhaar, W. Ketterle, *Radio-Frequency Spectroscopy of Ultracold Fermions*, Science **300**(5626), 1723–1726 (2003).

[Guz11] J. Guzman, G.-B. Jo, A. N. Wenz, K. W. Murch, C. K. Thomas, D. M. Stamper-Kurn, *Long-time-scale dynamics of spin textures in a degenerate $F = 1$ ^{87}Rb spinor Bose gas*, Phys. Rev. A **84**, 063625 (2011).

[Guz12] J. S. Guzman, *Explorations of Magnetic Phases in F = 1 ^{87}Rb Spinor Condensates*, Dissertation, University of California, Berkeley (2012).

[Had02] Z. Hadzibabic, C. A. Stan, K. Dieckmann, S. Gupta, M. W. Zwierlein, A. Gorlitz, W. Ketterle, *Two-Species Mixture of Quantum Degenerate Bose and Fermi Gases*, Phys. Rev. Lett. **88**(16), 160401–4 (2002).

[Had06] Z. Hadzibabic, P. Krüger, M. Cheneau, B. Battelier, J. Dalibard, *Berezinskii-Kosterlitz-Thouless crossover in a trapped atomic gas*, Nature **441**, 1118 (2006).

[Had11] Z. Hadzibabic, J. Dalibard, *Two-dimensional Bose fluids: An atomic physics perspective*, Rivista del Nuovo Cimento, vol. **34,**, pp.389–434 (2011).

[Hal98] D. S. Hall, M. R. Matthews, C. E. Wieman, E. A. Cornell, *Measurements of Relative Phase in Two-Component Bose-Einstein Condensates*, Phys. Rev. Lett. **81**(8), 1543–1546 (1998), erratum: ibidem, 4532.

[Hal09] E. Haller, M. Gustavsson, M. J. Mark, J. G. Danzl, R. Hart, G. Pupillo, H.-C. Nägerl, *Realization of an Excited, Strongly Correlated Quantum Gas Phase*, Science **325**, 1224–1227 (2009).

[Hal10a] E. Haller, R. Hart, M. J. Mark, J. G. Danzl, L. Reichsollner, M. Gustavsson, M. Dalmonte, G. Pupillo, H.-C. Nagerl, *Pinning quantum phase transition for a Luttinger liquid of strongly interacting bosons*, Nature **466**(7306), 597–600 (2010).

[Hal10b] E. Haller, M. J. Mark, R. Hart, J. G. Danzl, R. Lukas, V. Melezhik, P. Schmelcher, H.-C. Nägerl, *Confinement-Induced Resonances in Low-Dimensional Quantum Systems*, Phys. Rev. Lett. **104**, 153203 (2010).

[Heu11] S. Heupts, *A new radio frequency setup to manipulate spin mixtures of fermionic atoms* (2011), Bachelor thesis, Ruprecht-Karls-Universität Heidelberg.

[Hig05a] J. M. Higbie, *First Steps toward Precision Measurements using Multicomponent Bose-Einstein Condensates of* ^{87}Rb, Dissertation, University of California, Berkeley (2005).

[Hig05b] J. M. Higbie, L. E. Sadler, S. Inouye, A. P. Chikkatur, S. R. Leslie, K. L. Moore, V. Savalli, D. M. Stamper Kurn, *Direct Nondestructive Imaging of Magnetization in a Spin-1 Bose-Einstein Gas*, Phys. Rev. Lett. **95**(5), 050401–4 (2005).

[Ho98] T.-L. Ho, *Spinor Bose Condensates in Optical Traps*, Phys. Rev. Lett. **81**, 742–745 (1998).

[Hof07] S. Hofferberth, I. Lesanovsky, B. Fischer, T. Schumm, J. Schmiedmayer, *Non-equilibrium coherence dynamics in one-dimensional Bose gases*, Nature **449**(7160), 324 (2007).

[Hoh67] P. C. Hohenberg, *Existence of Long-Range Order in One and Two Dimensions*, Phys. Rev. **158**, 383 (1967).

[Hu94] Z. Hu, H. J. Kimble, *Observation of a Single-Atom in a Magnetooptical Trap*, Opt. Lett. **19**, 1888–1890 (1994).

[Hua87] K. Huang, *Statistical Mechanics* (John Wiley & Sons, 1987).

[Huc09] J. H. Huckans, J. R. Williams, E. L. Hazlett, R. W. Stites, K. M. O'Hara, *Three-Body Recombination in a Three-State Fermi Gas with Widely Tunable Interactions*, Phys. Rev. Lett. **102**, 165302 (2009).

[Hun11a] C.-L. Hung, X. Zhang, N. Gemelke, C. Chin, *Observation of scale invariance and universality in two-dimensional Bose gases*, Nature **470**(7333), 236–239 (2011).

[Hun11b] C.-L. Hung, X. Zhang, L.-C. Ha, S.-K. Tung, N. Gemelke, C. Chin, *Extracting density-density correlations from in situ images of atomic quantum gases* 1105.0030 (2011).

[Idz05] Z. Idziaszek, T. Calarco, *Two atoms in an anisotropic harmonic trap*, Phys. Rev. A **71**, 050701 (2005).

[Idz06] Z. Idziaszek, T. Calarco, *Analytical solutions for the dynamics of two trapped interacting ultracold atoms*, Phys. Rev. A **74**, 022712 (2006).

[Ima00] M. Imada, M. Kohno, *Superconductivity from Flat Dispersion Designed in Doped Mott Insulators*, Phys. Rev. Lett. **84**, 143–146 (2000).

[Ino98] S. Inouye, M. R. Andrews, J. Stenger, H.-J. Miesner, D. M. Stamper Kurn, W. Ketterle, *Observation of Feshbach resonances in a Bose-Einstein condensate*, Nature **392**, 151–154 (1998).

[Jac12] D. Jacob, L. Shao, V. Corre, T. Zibold, L. De Sarlo, E. Mimoun, J. Dalibard, F. Gerbier, *Phase diagram of spin-1 antiferromagnetic Bose-Einstein condensates*, Phys. Rev. A **86**, 061601 (2012).

[Jak98] D. Jaksch, C. Bruder, J. I. Cirac, C. W. Gardiner, P. Zoller, *Cold Bosonic Atoms in Optical Lattices*, Phys. Rev. Lett. **81**(15), 3108 (1998).

[Jo12] G.-B. Jo, J. Guzman, C. K. Thomas, P. Hosur, A. Vishwanath, D. M. Stamper-Kurn, *Ultracold Atoms in a Tunable Optical Kagome Lattice*, Phys. Rev. Lett. **108**, 045305 (2012).

[Joc03a] S. Jochim, M. Bartenstein, A. Altmeyer, G. Hendl, C. Chin, J. H. Denschlag, R. Grimm, *Pure Gas of Optically Trapped Molecules Created from Fermionic Atoms*, Phys. Rev. Lett. **91**(24), 240402 (2003).

[Joc03b] S. Jochim, M. Bartenstein, A. Altmeyer, G. Hendl, S. Riedl, C. Chin, J. Hecker Denschlag, R. Grimm, *Bose-Einstein Condensation of Molecules*, Science **302**(5653), 2101–2103 (2003).

[Joc04] S. Jochim, *Bose-Einstein Condensation of Molecules*, Dissertation, Leopold-Franzens-Universität Innsbruck (2004).

[Jul92] P. Julienne, A. Smith, K. Burnett, *Theory of Collisions between Laser Cooled Atoms*, Vol. 30 of *Advances In Atomic, Molecular, and Optical Physics*, 141 – 198 (Academic Press, 1992).

[Kau12] A. M. Kaufman, B. J. Lester, C. A. Regal, *Cooling a Single Atom in an Optical Tweezer to Its Quantum Ground State*, Phys. Rev. X **2**, 041014 (2012).

[Kaw10] Y. Kawaguchi, H. Saito, K. Kudo, M. Ueda, *Spontaneous magnetic ordering in a ferromagnetic spinor dipolar Bose-Einstein condensate*, Phys. Rev. A **82**, 043627 (2010).

[Kel65] L. V. Keldysh, *Ionization in the field of a strong electromagnetic wave*, Soviet Physics JETP **20**, 1307–1314 (1965).

[Kem02] E. G. M. van Kempen, S. J. J. M. F. Kokkelmans, D. J. Heinzen, B. J. Verhaar, *Interisotope Determination of Ultracold Rubidium Interactions from Three High-Precision Experiments*, Phys. Rev. Lett. **88**, 093201 (2002).

[Kes07] J. P. Kestner, L.-M. Duan, *Level crossing in the three-body problem for strongly interacting fermions in a harmonic trap*, Phys. Rev. A **76**, 033611 (2007).

[Ket99] W. Ketterle, D. S. Durfee, D. M. Stamper Kurn, *Making, probing and understanding Bose-Einstein condensates*, in M. Inguscio, S. Stringari, C. Wieman (Ed.), *Bose-Einstein Condensation in Atomic Gases*, Vol. CXL of *Proceedings of the International School of Physics Enrico Fermi*, 67–176 (IOS Press, Amsterdam, 1999).

[Ket08] W. Ketterle, M. W. Zwierlein, *Proc. of the International School of Physics 'Enrico Fermi', Course CLXIV: Making, probing and understanding ultracold fermi gases* (2008).

[Kha01] U. A. Khawaja, H. Stoof, *Skyrmions in a ferromagnetic Bose-Einstein condensate*, Nature **411**(6840), 918–920 (2001).

[Kin04] T. Kinoshita, T. Wenger, D. S. Weiss, *Observation of a one-dimensional Tonks-Girardeau gas*, Science **305**, 1125–1128 (2004).

[Kin06] T. Kinoshita, T. Wenger, D. S. Weiss, *A quantum Newton's cradle*, Nature **440**, 900–903 (2006).

[Kjä09] J. A. Kjäll, A. M. Essin, J. E. Moore, *Magnetic phase diagram of a spin-1 condensate in two dimensions with dipole interaction*, Phys. Rev. B **80**, 224502 (2009).

[Koh12] C. Kohstall, M. Zaccanti, M. Jag, A. Trenkwalder, P. Massignan, G. M. Bruun, F. Schreck, R. Grimm, *Metastability and coherence of repulsive polarons in a strongly interacting Fermi mixture*, Nature **485**, 615 (2012).

[Kos73] J. M. Kosterlitz, D. J. Thouless, *Ordering, metastability and phase transitions in two-dimensional systems*, Journal of Physics C: Solid State Physics **6**(7), 1181 (1973).

[Kos12] Marco Koschorreck, Daniel Pertot, Enrico Vogt, Bernd Fröhlich, Michael Feld, Michael Köhl, *Attractive and repulsive Fermi polarons in two dimensions*, Nature **485**, 619 (2012).

[Kra09] F. Krausz, M. Ivanov, *Attosecond physics*, Rev. Mod. Phys. **81**, 163–234 (2009).

[Kri13] S. Krippendorf, *An optical setup for high-resolution imaging and manipulation of ultracold atoms* (2013), Bachelor thesis, Ruprecht-Karls-Universität Heidelberg.

[Kro06] J. Kronjäger, C. Becker, P. Navez, K. Bongs, K. Sengstock, *Magnetically Tuned Spin Dynamics Resonance*, Phys. Rev. Lett. **97**, 110404 (2006).

[Krü10] P. Krüger, S. Hofferberth, I. E. Mazets, I. Lesanovsky, J. Schmiedmayer, *Weakly Interacting Bose Gas in the One-Dimensional Limit*, Phys. Rev. Lett. **105**, 265302 (2010).

[Ku12] M. J. H. Ku, A. T. Sommer, L. W. Cheuk, M. W. Zwierlein, *Revealing the Superfluid Lambda Transition in the Universal Thermodynamics of a Unitary Fermi Gas*, Science **335**, 563–567 (2012).

[Ku13] Z. M. W. Ku, M., private communication (2013).

[Lam07] A. Lamacraft, *Quantum Quenches in a Spinor Condensate*, Phys. Rev. Lett. **98**, 160404 (2007).

[Lan33] L. D. Landau, *Über die Bewegung der Elektronen in Kristallgitter*, Physik Z. Sowjetunion **3**, 644 (1933).

[Lan81] L. Landau, E. Lifshitz, *Quantum Mechanics: Non-Relativistic Theory*, Vol. 3 (Elsevier Science, 1981).

[Lan96] L. Landau, E. Lifshitz, *Statistical Physics*, Vol. 5 (Elsevier Science, 1996).

[Lan13] T. Langen, *Comment on "Probing Phase Fluctuations in a 2D Degenerate Bose Gas by Free Expansion"*, Phys. Rev. Lett. **111**, 159601 (2013).

[Leg80] A. J. Leggett, *Cooper pairing in spin-polarized Fermi systems*, J. Phys. (Paris) Coll. **41**, C7–19 (1980).

[Les08] S. R. A. Leslie, *On Spinor Condensates as Amplifiers, Sensors and Tunable Quantum Playgrounds for Studies of Spin*, Dissertation, University of California, Berkeley (2008).

[Lia10] Y.-a. Liao, A. S. C. Rittner, T. Paprotta, W. Li, G. B. Partridge, R. G. Hulet, S. K. Baur, E. J. Mueller, *Spin-imbalance in a one-dimensional Fermi gas*, Nature **467**(7315), 567–569 (2010).

[Lin13] E. J. Lindgren, J. Rotureau, C. Forssén, A. G. Volosniev, N. T. Zinner, *Fermionization of two-component few-fermion systems in a one-dimensional harmonic trap*, ArXiv e-prints 1304.2992 (2013).

[Liu10] X.-J. Liu, H. Hu, P. D. Drummond, *Three attractively interacting fermions in a harmonic trap: Exact solution, ferromagnetism, and high-temperature thermodynamics*, Phys. Rev. A **82**, 023619 (2010).

[Lom08] T. Lompe, *An apparatus for the production of molecular Bose-Einstein condensates* (2008), Diploma thesis, Ruprecht-Karls-Universität Heidelberg.

[Lom10a] T. Lompe, T. B. Ottenstein, F. Serwane, K. Viering, A. N. Wenz, G. Zürn, S. Jochim, *Atom-Dimer Scattering in a Three-Component Fermi Gas*, Phys. Rev. Lett. **105**, 103201 (2010).

[Lom10b] T. Lompe, T. B. Ottenstein, F. Serwane, A. N. Wenz, G. Zürn, S. Jochim, *Radio-Frequency Association of Efimov Trimers*, Science **330**, 940–944 (2010).

[Lom11] Thomas Lompe, *Efimov Physics in a three-component Fermi gas*, Dissertation, Ruprecht-Karls-Universität Heidelberg, http://www.mpi-hd.mpg.de/biblio/preprints/2011-023.pdf (2011).

[Mad00] K. W. Madison, F. Chevy, W. Wohlleben, J. Dalibard, *Vortex Formation in a Stirred Bose-Einstein Condensate*, Phys. Rev. Lett. **84**(5), 806–809 (2000).

[Mar10a] G. E. Marti, R. Olf, E. Vogt, A. Öttl, D. M. Stamper-Kurn, *Two-element Zeeman slower for rubidium and lithium*, Phys. Rev. A **81**, 043424 (2010).

[Mar10b] K. Martiyanov, V. Makhalov, A. Turlapov, *Observation of a Two-Dimensional Fermi Gas of Atoms*, Phys. Rev. Lett. **105**, 030404 (2010).

[Mas11] P. Massignan, G. Bruun, *Repulsive polarons and itinerant ferromagnetism in strongly polarized Fermi gases*, Eur. Phys. J. D **65**, 83–89 (2011).

[Mas13] P. Massignan, M. Zaccanti, G. M. Bruun, *Polarons, Molecules, and Itinerant Ferromagnetism in ultracold Fermi gases*, ArXiv e-prints 1309.0219 (2013).

[Mat98] M. R. Matthews, D. S. Hall, D. S. Jin, J. R. Ensher, C. E. Wieman, E. A. Cornell, F. Dalfovo, C. Minniti, S. Stringari, *Dynamical Response of a Bose-Einstein Condensate to a Discontinuous Change in Internal State*, Phys. Rev. Lett. **81**(2), 243–247 (1998).

[Mat99] M. R. Matthews, B. P. Anderson, P. C. Haljan, D. S. Hall, C. E. Wieman, E. A. Cornell, *Vortices in a Bose-Einstein Condensate*, Phys. Rev. Lett. **83**(13), 2498–2501 (1999).

[Mat13] L. Mathey, V. Singh, *Two-point density correlation function for an expanding gas of bosonic* ^{6}*Li-dimers*, private communication (2013).

[McG64] J. B. McGuire, *Study of Exactly Soluble One-Dimensional N-Body Problems*, Journal of Mathematical Physics **5**(5), 622–636 (1964).

[McG65] J. B. McGuire, *Interacting Fermions in One Dimension. I. Repulsive Potential*, J. Math. Phys. **6**, 432 (1965).

[McG66] J. B. McGuire, *Interacting Fermions in One Dimension. II. Attractive Potential*, J. Math. Phys. **7**, 123 (1966).

[Mer66] N. D. Mermin, H. Wagner, *Absence of Ferromagnetism or Antiferromagnetism in One- or Two-Dimensional Isotropic Heisenberg Models*, Phys. Rev. Lett. **17**, 113 (1966).

[Met99] H. J. Metcalf, P. van der Straten, *Laser Cooling and Trapping* (Springer-Verlag, New York, 1999).

[Mig59] A. Migdal, *Superfluidity and the moments of inertia of nuclei*, Nuclear Physics **13**(5), 655–674 (1959).

[Moe95] A. J. Moerdijk, B. J. Verhaar, A. Axelsson, *Resonances in ultracold collisions of* ^{6}Li, ^{7}Li, *and* ^{23}Na, Phys. Rev. A **51**, 4852–4861 (1995).

[Mor04] C. Mora, R. Egger, A. O. Gogolin, A. Komnik, *Atom-Dimer Scattering for Confined Ultracold Fermion Gases*, Phys. Rev. Lett. **93**, 170403 (2004).

[Mor05] H. Moritz, *One-dimensional Atomic Gases*, Dissertation, ETH (2005), supervisor: Tilman Esslinger.

[Muk07] S. Mukerjee, C. Xu, J. E. Moore, *Dynamical models and the phase ordering kinetics of the* $s = 1$ *spinor condensate*, Phys. Rev. B **76**, 104519 (2007).

[Nak11] S. Nakajima, M. Horikoshi, T. Mukaiyama, P. Naidon, M. Ueda, *Measurement of an Efimov Trimer Binding Energy in a Three-Component Mixture of* ^{6}Li, Phys. Rev. Lett. **106**, 143201 (2011).

[Nas09] S. Nascimbène, N. Navon, K. J. Jiang, L. Tarruell, M. Teichmann, J. McKeever, F. Chevy, C. Salomon, *Collective Oscillations of an Imbalanced Fermi Gas: Axial Compression Modes and Polaron Effective Mass*, Phys. Rev. Lett. **103**, 170402 (2009).

[Nas10] S. Nascimbène, N. Navon, K. J. Jiang, F. Chevy, C. Salomon, *Exploring the thermodynamics of a universal Fermi gas*, Nature **463**(7284), 1057–1060 (2010).

[NEG] *NEG: Non Evaporable Getter coating, applied at GSI Darmstadt*, http://est-div-sm.web.cern.ch/est-div-sm/Project-Getter-home.htm.

[Nei13] M. Neidig, *A realization of a two-dimensional Fermi gas in a standing wave trap* (2013), Master thesis, Ruprecht-Karls-Universität Heidelberg.

[Ni08] K.-K. Ni, S. Ospelkaus, M. H. G. de Miranda, A. Pe'er, B. Neyenhuis, J. J. Zirbel, S. Kotochigova, P. S. Julienne, D. S. Jin, J. Ye, *A High Phase-Space-Density Gas of Polar Molecules*, Science **322**(5899), 231 (2008).

[O'H02] K. M. O'Hara, S. L. Hemmer, M. E. Gehm, S. R. Granade, J. E. Thomas, *Observation of a Strongly Interacting Degenerate Fermi Gas of Atoms*, Science **298**(5601), 2179–2182 (2002).

[Ohm98] T. Ohmi, K. Machida, *Bose-Einstein Condensation with Internal Degrees of Freedom in Alkali Atom Gases*, Journal of the Physical Society of Japan **67**(6), 1822–1825 (1998).

[Ols98] M. Olshanii, *Atomic Scattering in the Presence of an External Confinement and a Gas of Impenetrable Bosons*, Phys. Rev. Lett. **81**, 938 (1998).

[Ols03] M. Olshanii, V. Dunjko, *Short-Distance Correlation Properties of the Lieb-Liniger System and Momentum Distributions of Trapped One-Dimensional Atomic Gases*, Phys. Rev. Lett. **91**, 090401 (2003).

[Ott04] H. Ott, E. de Mirandes, F. Ferlaino, G. Roati, G. Modugno, M. Inguscio, *Collisionally Induced Transport in Periodic Potentials*, Phys. Rev. Lett. **92**(16), 160601–4 (2004).

[Ott08] T. B. Ottenstein, T. Lompe, M. Kohnen, A. N. Wenz, S. Jochim, *Collisional Stability of a Three-Component Degenerate Fermi Gas*, Phys. Rev. Lett. **101**(20), 203202 (2008).

[Ott10] T. B. Ottenstein, *Few-body physics in ultracold Fermi gases*, Dissertation, Ruprecht-Karls-Universität Heidelberg, http://www.mpi-hd.mpg.de/biblio/preprints/2010-001.pdf (2010).

[Ovc99] Y. B. Ovchinnikov, J. H. Müller, M. R. Doery, E. J. D. Vredenbregt, K. Helmerson, S. L. Rolston, W. D. Phillips, *Diffraction of a Released Bose-Einstein Condensate by a Pulsed Standing Light Wave*, Phys. Rev. Lett. **83**, 284 (1999).

[Par06] G. B. Partridge, W. Li, R. I. Kamar, Y.-a. Liao, R. G. Hulet, *Pairing and Phase Separation in a Polarized Fermi Gas*, Science **311**(5760), 503 (2006).

[Pas13] B. Pasquiou, A. Bayerle, S. M. Tzanova, S. Stellmer, J. Szczepkowski, M. Parigger, R. Grimm, F. Schreck, *Quantum degenerate mixtures of strontium and rubidium atoms*, Phys. Rev. A **88**, 023601 (2013).

[Pau25] W. Pauli, *Über den Zusammenhang des Abschlusses der Elektronengruppen im Atom mit der Komplexstruktur der Spektren*, Zeitschrift für Physik **31**(1), 765–783 (1925).

[Pau40] W. Pauli, *The Connection Between Spin and Statistics*, Phys. Rev. **58**, 716–722 (1940).

[Peh13] N. Pehoviak, *Laserstabilisierung durch Modulationstransferspektroskopie in 6Li* (2013), Bachelor thesis, Ruprecht-Karls-Universität Heidelberg.

[Pek46] S. I. Pekar, Zh. Eksp. Theor. Fiz **16**, 335 (1946).

[Per05] A. Perali, P. Pieri, G. C. Strinati, *Extracting the Condensate Density from Projection Experiments with Fermi Gases*, Phys. Rev. Lett. **95**, 010407 (2005).

[Pet00] D. S. Petrov, M. Holzmann, G. V. Shlyapnikov, *Bose-Einstein Condensation in Quasi-2D Trapped Gases*, Phys. Rev. Lett. **84**, 2551–2555 (2000).

[Pet01] D. S. Petrov, G. V. Shlyapnikov, *Interatomic collisions in a tightly confined Bose gas*, Phys. Rev. A **64**(1), 012706–14 (2001).

[Pet02] C. J. Pethick, H. Smith, *Bose-Einstein Condensation in Dilute Gases* (Cambridge University Press, 2002).

[Pet03] D. S. Petrov, *Bose-Einstein Condensation in Low-Dimensional Trapped Gases*, Dissertation, Universiteit van Amsterdam (2003).

[Pet04] D. S. Petrov, C. Salomon, G. V. Shlyapnikov, *Weakly Bound Dimers of Fermionic Atoms*, Phys. Rev. Lett. **93**, 090404 (2004).

[Pet05] D. S. Petrov, C. Salomon, G. V. Shlyapnikov, *Scattering properties of weakly bound dimers of fermionic atoms*, Phys. Rev. A **71**, 012708 (2005).

[Pit03] L. Pitaevskii, S. Stringari, *Bose-Einstein Condensation*, International Series of Monographs on Physics - 116 (Oxford University Press, 2003).

[Pro08a] N. Prokof'ev, B. Svistunov, *Fermi-polaron problem: Diagrammatic Monte Carlo method for divergent sign-alternating series*, Phys. Rev. B **77**, 020408 (2008).

[Pro08b] N. V. Prokof'ev, B. V. Svistunov, *Bold diagrammatic Monte Carlo: A generic sign-problem tolerant technique for polaron models and possibly interacting many-body problems*, Phys. Rev. B **77**, 125101 (2008).

[Rap07] A. Rapp, G. Zaránd, C. Honerkamp, W. Hofstetter, *Color Superfluidity and "Baryon" Formation in Ultracold Fermions*, Phys. Rev. Lett. **98**(16), 160405 (2007).

[Reg03] C. A. Regal, C. Ticknor, J. L. Bohn, D. S. Jin, *Creation of ultracold molecules from a Fermi gas of atoms*, Nature **424**(6944), 47–50 (2003).

[Reg04] C. A. Regal, M. Greiner, D. S. Jin, *Observation of Resonance Condensation of Fermionic Atom Pairs*, Phys. Rev. Lett. **92**(4), 040403–4 (2004).

[Rie10] M. G. Ries, *A magneto-optical trap for the preparation of a three-component Fermi gas in an optical lattice* (2010), Diploma thesis, Ruprecht-Karls-Universität Heidelberg.

[Rig08] M. Rigol, V. Dunjko, M. Olshanii, *Thermalization and its mechanism for generic isolated quantum systems*, Nature **452**, 854–858 (2008).

[Ron12] M. Rontani, *Tunneling Theory of Two Interacting Atoms in a Trap*, Phys. Rev. Lett. **108**, 115302 (2012).

[Sad06a] L. E. Sadler, *Dynamics of a Spin 1 Ferromagnetic Condensate*, Dissertation, University of California, Berkeley (2006).

[Sad06b] L. E. Sadler, J. M. Higbie, S. R. Leslie, M. Vengalattore, D. M. Stamper Kurn, *Spontaneous symmetry breaking in a quenched ferromagnetic spinor Bose-Einstein condensate*, Nature **443**(7109), 312–315 (2006).

[Sak94a] J. Sakurai, S. Tuan, *Modern Quantum Mechanics* (Pearson Education, 1994).

[Sak94b] J. J. Sakurai, *Modern Quantum Mechanics* (Addison-Wesley Publishing Company, Inc., 1994).

[Sal13a] S. Sala, J. Förster, A. Saenz, *Ultracold-atom quantum-simulator for attosecond science*, submitted for publication (2013).

[Sal13b] S. Sala, G. Zürn, T. Lompe, A. N. Wenz, S. Murmann, F. Serwane, S. Jochim, A. Saenz, *Coherent Molecule Formation in Anharmonic Potentials Near Confinement-Induced Resonances*, Phys. Rev. Lett. **110**, 203202 (2013).

[Sca] *Scattering lengths of different channels of* ^{6}*Li can be found online*, http://prl.aps.org/supplemental/PRL/v110/i13/e135301.

[Sch91] T. Schneider, Z. Gedik, S. Ciraci, *From low to high-temperature superconductivity: A dimensional crossover phenomenon? A finite size effect?*, Zeitschrift für Physik B Condensed Matter **83**(3), 313–321 (1991).

[Sch99] U. Schünemann, H. Engler, R. Grimm, M. Weidemüller, M. Zielonkowski, *Simple scheme for tunable frequency offset locking of two lasers*, Rev. Sci. Instrum. **70**(1), 242–243 (1999).

[Sch00] F. Schwabl, *Statistische Mechanik*, Springer-Lehrbuch (Springer-Verlag GmbH, 2000).

[Sch01] N. Schlosser, G. Reymond, I. Protsenko, P. Grangier, *Sub-poissonian loading of single atoms in a microscopic dipole trap*, Nature **411**, 1024–1027 (2001).

[Sch07] C. H. Schunck, Y. Shin, A. Schirotzek, M. W. Zwierlein, W. Ketterle, *Pairing Without Superfluidity: The Ground State of an Imbalanced Fermi Mixture*, Science **316**(5826), 867 (2007).

[Sch08a] A. Schirotzek, Y.-i. Shin, C. H. Schunck, W. Ketterle, *Determination of the Superfluid Gap in Atomic Fermi Gases by Quasiparticle Spectroscopy*, Phys. Rev. Lett. **101**, 140403 (2008).

[Sch08b] C. H. Schunck, Y. Shin, A. Schirotzek, W. Ketterle, *Determination of the fermion pair size in a resonantly interacting superfluid*, Nature **454**, 739–743 (2008).

[Sch09] A. Schirotzek, C.-H. Wu, A. Sommer, M. W. Zwierlein, *Observation of Fermi Polarons in a Tunable Fermi Liquid of Ultracold Atoms*, Phys. Rev. Lett. **102**, 230402 (2009).

[Sch10] A. Schirotzek, *Radio-Frequency Spectroscopy of Ultracold Atomic Fermi Gases*, Dissertation, Massachusetts Institute of Technology (2010).

[Sch12a] R. Schmidt, T. Enss, V. Pietilä, E. Demler, *Fermi polarons in two dimensions*, Phys. Rev. A **85**, 021602 (2012).

[Sch12b] U. Schneider, L. Hackermüller, J. P. Ronzheimer, S. Will, S. Braun, T. Best, I. Bloch, E. Demler, S. Mandt, D. Rasch, A. Rosch, *Fermionic transport and out-of-equilibrium dynamics in a homogeneous Hubbard model with ultracold atoms*, Nat Phys **8**(3), 213 (2012).

[Ser07] F. Serwane, *The setup of a Magneto Optical Trap for the preparation of a mesoscopic degenerate Fermi gas*, http://www.mpi-hd.mpg.de/biblio/preprints/2007-031.pdf (2007), Diploma thesis, Ruprecht-Karls-Universität Heidelberg.

[Ser11a] F. Serwane, *Deterministic preparation of a tunable few-fermion system*, Dissertation, Ruprecht-Karls-Universität Heidelberg, http://www.mpi-hd.mpg.de/biblio/preprints/2011-048.pdf (2011).

[Ser11b] F. Serwane, G. Zuern, T. Lompe, T. B. Ottenstein, A. N. Wenz, S. Jochim, *Deterministic Preparation of a Tunable Few-Fermion System*, Science **332**(6027), 336–338 (2011).

[Sha01] J. R. Abo Shaeer, C. Raman, J. M. Vogels, W. Ketterle, *Observation of Vortex Lattices in Bose-Einstein Condensates*, Science **292**(5516), 476–479 (2001).

[She10] J. F. Sherson, C. Weitenberg, M. Endres, M. Cheneau, I. Bloch, S. Kuhr, *Single-atom-resolved fluorescence imaging of an atomic Mott insulator*, Nature **467**(7311), 68–72 (2010).

[Shi06] Y. Shin, M. W. Zwierlein, C. H. Schunck, A. Schirotzek, W. Ketterle, *Observation of Phase Separation in a Strongly Interacting Imbalanced Fermi Gas*, Phys. Rev. Lett. **97**, 030401 (2006).

[Sim03] A. Simoni, F. Ferlaino, G. Roati, G. Modugno, M. Inguscio, *Magnetic Control of the Interaction in Ultracold K-Rb Mixtures*, Phys. Rev. Lett. **90**(16), 163202–4 (2003).

[Sim10] P. Simon, *Apparatus for the preparation of ultracold Fermi gases* (2010), Diploma thesis, Ruprecht-Karls-Universität Heidelberg.

[Sin13] V. Singh, L. Mathey, *Noise correlations of two-dimensional Bose gases*, In preparation (2013).

[Sol11] P. Soltan-Panahi, J. Struck, P. Hauke, A. Bick, W. Plenkers, G. Meineke, C. Becker, P. Windpassinger, M. Lewenstein, K. Sengstock, *Multi-component quantum gases in spin-dependent hexagonal lattices*, Nat Phys **7**(5), 434 (2011).

[Som11] A. Sommer, M. Ku, G. Roati, M. W. Zwierlein, *Universal spin transport in a strongly interacting Fermi gas*, Nature **472**(7342), 201–204 (2011).

[Som12] A. T. Sommer, L. W. Cheuk, M. J. H. Ku, W. S. Bakr, M. W. Zwierlein, *Evolution of Fermion Pairing from Three to Two Dimensions*, Phys. Rev. Lett. **108**, 045302 (2012).

[sor13] *Collins English Dictionary - Complete & Unabridged 10th Edition* (Oct 2013).

[Sow13] T. Sowiński, T. Grass, O. Dutta, M. Lewenstein, *Few interacting fermions in a one-dimensional harmonic trap*, Phys. Rev. A **88**, 033607 (2013).

[Sta98a] D. M. Stamper-Kurn, M. R. Andrews, A. P. Chikkatur, S. Inouye, H.-J. Miesner, J. Stenger, W. Ketterle, *Optical Confinement of a Bose-Einstein Condensate*, Phys. Rev. Lett. **80**(10), 2027–2030 (1998).

[Sta98b] D. M. Stamper-Kurn, H.-J. Miesner, A. P. Chikkatur, S. Inouye, J. Stenger, W. Ketterle, *Reversible Formation of a Bose-Einstein Condensate*, Phys. Rev. Lett. **81**(11), 2194–2197 (1998).

[Sta99] D. M. Stamper-Kurn, A. P. Chikkatur, A. Görlitz, S. Inouye, S. Gupta, D. E. Pritchard, W. Ketterle, *Excitation of Phonons in a Bose-Einstein Condensate by Light Scattering*, Phys. Rev. Lett. **83**, 2876–2879 (1999).

[Sta00] D. Stamper-Kurn, *Peeking and poking at a new quantum fluid: Studies of gaseous Bose-Einstein condensates in magnetic and optical traps*, Dissertation, MIT (2000), supervisor: Wolfgang Ketterle.

[Sta04] C. A. Stan, M. W. Zwierlein, C. H. Schunck, S. M. F. Raupach, W. Ketterle, *Observation of Feshbach Resonances between Two Different Atomic Species*, Phys. Rev. Lett. **93**(14), 143001–4 (2004).

[Sta12] J. Stachurska, *An optical dipole trap for the two-dimensional confinement of Lithium atoms* (2012), Bachelor thesis, Ruprecht-Karls-Universität Heidelberg.

[Ste98] J. Stenger, S. Inouye, D. Stamper-Kurn, H. Miesner, A. Chikkatur, W. Ketterle, *Spin domains in ground-state Bose-Einstein condensates*, Nature **396**(6709), 345–348 (1998).

[Tan08] S. Tan, *Large momentum part of a strongly correlated Fermi gas*, Annals of Physics **323**(12), 2971 – 2986 (2008).

[Tas92] H. Tasaki, *Ferromagnetism in the Hubbard models with degenerate single-electron ground states*, Phys. Rev. Lett. **69**, 1608–1611 (1992).

[Tho27] L. H. Thomas, *The calculation of atomic fields*, Mathematical Proceedings of the Cambridge Philosophical Society **23**, 542–548 (1927).

[Tun10] S. Tung, G. Lamporesi, D. Lobser, L. Xia, E. A. Cornell, *Observation of the Pre-superfluid Regime in a Two-Dimensional Bose Gas*, Phys. Rev. Lett. **105**, 230408 (2010).

[Ueh13] T. Uehlinger, G. Jotzu, M. Messer, D. Greif, W. Hofstetter, U. Bissbort, T. Esslinger, *Artificial graphene with tunable interactions*, ArXiv e-prints 1308.4401 (2013).

[Ven08] M. Vengalattore, S. R. Leslie, J. Guzman, D. M. Stamper-Kurn, *Spontaneously Modulated Spin Textures in a Dipolar Spinor Bose-Einstein Condensate*, Phys. Rev. Lett. **100**, 170403 (2008).

[Ven10] M. Vengalattore, J. Guzman, S. R. Leslie, F. Serwane, D. M. Stamper-Kurn, *Periodic spin textures in a degenerate $F = 1$ $^{87}\mathrm{Rb}$ spinor Bose gas*, Phys. Rev. A **81**, 053612 (2010).

[Vog12] E. Vogt, M. Feld, B. Fröhlich, D. Pertot, M. Koschorreck, M. Köhl, *Scale Invariance and Viscosity of a Two-Dimensional Fermi Gas*, Phys. Rev. Lett. **108**, 070404 (2012).

[Voi95] J. Voit, *One-dimensional Fermi liquids*, Reports on Progress in Physics **58**(9), 977 (1995).

[Voi09] A.-C. Voigt, M. Taglieber, L. Costa, T. Aoki, W. Wieser, T. W. Hänsch, K. Dieckmann, *Ultracold Heteronuclear Fermi-Fermi Molecules*, Phys. Rev. Lett. **102**, 020405 (2009).

[Vol13] A. G. Volosniev, D. V. Fedorov, A. S. Jensen, M. Valiente, N. T. Zinner, *Strongly-interacting fermions in one dimension and microscopic magnetism*, ArXiv e-prints 1306.4610 (2013).

[Wei99] J. Weiner, V. S. Bagnato, S. Zilio, P. S. Julienne, *Experiments and theory in cold and ultracold collisions*, Rev. Mod. Phys. **71**, 1 (1999).

[Wei09] M. Weidemüller, C. Zimmermann, *Cold Atoms and Molecules*, Physics textbook (Wiley, 2009).

[Wei11] C. Weitenberg, M. Endres, J. F. Sherson, M. Cheneau, P. Schausz, T. Fukuhara, I. Bloch, S. Kuhr, *Single-spin addressing in an atomic Mott insulator*, Nature **471**(7338), 319 (2011).

[Wen08] A. Wenz, *Few-Body Physics in a Three-Component Fermi Gas*, http://www.mpi-hd.mpg.de/biblio/preprints/2008-023.pdf (2008), Diploma thesis, Ruprecht-Karls-Universität Heidelberg.

[Wen09] A. N. Wenz, T. Lompe, T. B. Ottenstein, F. Serwane, G. Zürn, S. Jochim, *Universal trimer in a three-component Fermi gas*, Phys. Rev. A **80**, 040702 (2009).

[Wen13] A. Wenz, G. Zürn, S. Murmann, I. Brouzos, T. Lompe, S. Jochim, *From Few to Many: Observing the Formation of a Fermi Sea One Atom at a Time*, Science **342**(6157), 457 (2013).

[Wil07] F. Wilczek, *Quantum chromodynamics: Lifestyles of the small and simple*, Nature Physics **3**(6), 375 (2007).

[Wil08] E. Wille, F. M. Spiegelhalder, G. Kerner, D. Naik, A. Trenkwalder, G. Hendl, F. Schreck, R. Grimm, T. G. Tiecke, J. T. M. Walraven, S. J. J. M. F. Kokkelmans, E. Tiesinga, P. S. Julienne, *Exploring an Ultracold Fermi-Fermi Mixture: Interspecies Feshbach Resonances and Scattering Properties of* ^{6}Li *and* ^{40}K, Phys. Rev. Lett. **100**, 053201 (2008).

[Wil10] S. Will, T. Best, U. Schneider, L. Hackermüller, D.-S. Luhmann, I. Bloch, *Time-resolved observation of coherent multi-body interactions in quantum phase revivals*, Nature **465**(7295), 197 (2010).

[Wil11] S. Will, *Interacting bosons and fermions in three-dimensional optical lattice potentials*, Dissertation, Johannes Gutenberg-Universität Mainz (2011).

[Zer42] F. Zernike, *Phase contrast, a new method for the microscopic observation of transparent objects*, Physica **9**(7), 686 – 698 (1942).

[Zin08] N. T. Zinner, A. S. Jensen, *Common concepts in nuclear physics and ultracold atomic gasses*, Journal of Physics: Conference Series **111**(1), 012016 (2008).

[Zür09] G. Zürn, *Realization of an Optical Microtrap for a Highly Degenerate Fermi Gas* (2009), Diploma thesis, Ruprecht-Karls-Universität Heidelberg.

[Zür12a] G. Zürn, *Few-fermion systems in one dimension*, Dissertation, Ruprecht-Karls-Universität Heidelberg (2012).

[Zür12b] G. Zürn, F. Serwane, T. Lompe, A. N. Wenz, M. G. Ries, J. E. Bohn, S. Jochim, *Fermionization of Two Distinguishable Fermions*, Phys. Rev. Lett. **108**, 075303 (2012).

[Zür13a] G. Zürn, T. Lompe, A. N. Wenz, S. Jochim, P. S. Julienne, J. M. Hutson, *Precise Characterization of* ^{6}Li *Feshbach Resonances Using Trap-Sideband-Resolved RF Spectroscopy of Weakly Bound Molecules*, Phys. Rev. Lett. **110**, 135301 (2013).

[Zür13b] G. Zürn, A. N. Wenz, S. Murmann, A. Bergschneider, T. Lompe, S. Jochim, *Pairing in Few-Fermion Systems with Attractive Interactions*, Phys. Rev. Lett. **111**, 175302 (2013).

[Zwe03] W. Zwerger, *Mott-Hubbard transition of cold atoms in optical lattices*, Journal of Optics B: Quantum and Semiclassical Optics **5**(2), S9 (2003).

[Zwe11] W. Zwerger, *The BCS-BEC Crossover and the Unitary Fermi Gas*, Lecture Notes in Physics (Springer, 2011).

[Zwi04] M. W. Zwierlein, C. A. Stan, C. H. Schunck, S. M. F. Raupach, A. J. Kerman, W. Ketterle, *Condensation of Pairs of Fermionic Atoms near a Feshbach Resonance*, Phys. Rev. Lett. **92**, 120403 (2004).

[Zwi05] M. W. Zwierlein, J. R. Abo Shaeer, A. Schirotzek, C. H. Schunck, W. Ketterle, *Vortices and superfluidity in a strongly interacting Fermi gas*, Nature **435**, 1047–1051 (2005).

[Zwi06a] M. W. Zwierlein, *High-Temperature Superfluidity in an Ultracold Fermi Gas*, Dissertation, Massachusetts Institute of Technology (2006).

[Zwi06b] M. W. Zwierlein, A. Schirotzek, C. H. Schunck, W. Ketterle, *Fermionic Superfluidity with Imbalanced Spin Populations*, Science **311**(5760), 492 (2006).

[Zwi06c] M. W. Zwierlein, C. H. Schunck, A. Schirotzek, W. Ketterle, *Direct observation of the superfluid phase transition in ultracold Fermi gases*, Nature **442**(7098), 54 (2006).

Acknowledgments

Thanks to everyone who made this thesis and the work presented here possible and so much fun.

In particular, I would like to thank…

Selim Jochim for his enthusiasm and great guidance and supervision. It is a pleasure to work for someone as fascinated by and dedicated to our experiments. It is hard not to get infected by the way you make experimental physics and research so much fun;

and the whole Jochim group: (in order of appearance[1]) Friedhelm ”Peacehelmet/fried ham” Serwane, Timo ”the first part of Dr. Ottenstenz” Ottenstein, Thomas ”Laser-” Lompe, Gerhard ”mit T und Rotation, aber ohne Schulter” Zürn, Matthias Kohnen, Martin Ries, Philipp Simon, Johanna Bohn, Andrea Bergschneider, Juliana Stachurska, Sebastian Heupts, Mathias ”Mr. Hybernation/Matlab Master” Neidig, Simon ”Mürmann” Murmann, Jan-Hendrik Becher, Puneeth Murthy, Sebastian Pres, Sven Krippendorf

for filling an empty lab with experiments, laughter, chair-chair collisions, music, beeping Arduinos, fun, Tischfussball, help with this thesis, proof-reading, Blödsinn/Lötzinn, Laubsperren, spranks & clamps, 1400 ballons, ridiculous PhD ”helmets”, moving, cleaning up every friday, coffee, telling me to talk more quietly and all the other stuff that made my time in this group so much fun.

Furthermore, I would like to thank…

Dan Stamper-Kurn for the opportunity to work in his group in Berkeley, his razor-sharp mind which allows him to solve problems we have been dealing with for hours and days with one quick look;

and the ultracold atoms group in Berkeley: Jennie Guzman, Kater ”see what happens Larry” Murch, Gyu-Boong ”GB” Jo, Ed Marty, Ryan ”the name song singer” Olf, Dan ”little Dan” Brooks, Nathan Brahms, Thierry Botter, Anton ”Toni” Öttl, Tom ”TPP” Purdy, Sydney Schreppler and all the others who made my stay in Berkeley such a great time

for coffee runs, Nefeli, pressing the ”close excess pictures” button, Frisbee sessions, group snow trip, potluck, 1am donut and donut-hole runs, proof-reading, burgers & beers, CTM at House of Curries, E5 because it is awesome, Friedhelm for setting stuff up before I started and the Rugby crew for being my family replacement.

---

[1] At some places I am not quite sure.

Many thanks as well to all theorists: Richard Schmidt, Stefan Flörchinger, José D'Incao, Eric Braaten, Hans-Werner Hammer, Ioannis Brouzos, Dörte Blume, Massimo Rontani, Simon Sala, Alejandro Saenz, Jeremey Hudson, Paul Julienne, Jim McGuire, Thomas Busch, Nikolai Zinner, Gareth Conduit, Xi-Wen Guan, Ludwig Matthey and many others, whose collaboration, calculations, publications and explanations helped me to learn something.

I would also like to thank all other groups (the Ullrich group and the Blaum at group the MPIK, the Weidemüller group and the Pan group at the PI, the Oberthaler group at the KIP, the Müller and Häffner group at UC Berkeley) and all their members for helping out with knowledge, parts, lasers, bits, drills and other things necessary to keep a laboratory running. It is great that to be surrounded by nice and helpful people. Particular thanks to Matthias Weidemüller for reading this thesis.

Additionally, I want to thank all the workshop and administrative staff at the MPIK, the PI and UC Berkeley for helping me to focus on research and dealing with everything else. In particular, I would like to thank Florian Säubert, Stephan Flicker and Michael Solarz for unbureaucratic help and knowledge when it comes to machining and designing parts; Ralf Ziegler and his staff at the PI workshop for helping us with the move to the new labs and everything that was associated to it.

I would also like to thank...
everyone who helped me through the studies in Heidelberg, in particular Andreas Vogel, Falk von Seggern, Stefan Schoch, Philipp Schröder and Silvan Eppinger;
my high school teacher Mr. Reich and my cousin Kaline Coutinho to spark my interest for physics;
all other friends who supported me, freed my mind on holidays, trip, weekends and evenings and endured my bad mood when stuff in lab did not go well.

Last but not least, I need to thank my family and my girlfriend Nele for being there for me and supporting me in all possible ways. I love you.